ARO 25478.19-PH

LASER SPECTROSCOPY CHARACTERIZATION OF MATERIALS FOR FREQUENCY AGILE SOLID STATE LASER SYSTEMS

Richard C. Powell, Ph.D.
Principal Investigator

Center for Laser Research
OKLAHOMA STATE UNIVERSITY
Stillwater, Oklahoma 74078-0444

FINAL REPORT

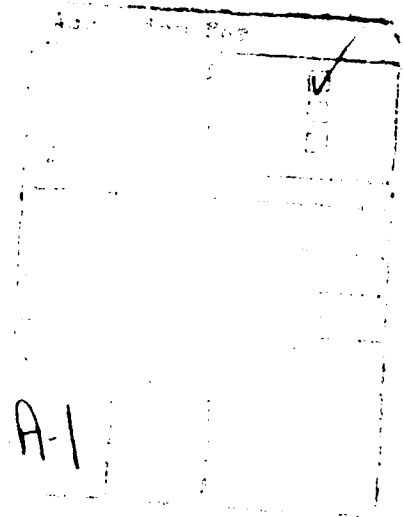January 15, 1988 - January 14, 1991

REPORT DOCUMENTATION PAGE

Public reporting burden for this collection of information is estimated to average 1 hour per response, including the time for reviewing instructions, searching existing data sources, gathering and maintaining the data needed, and completing and reviewing the collection of information. Send comments regarding this burden estimate or any other aspect of this collection of information, including suggestions for reducing this burden, to Washington Headquarters Services, Directorate for Information Operations and Reports, 1215 Jefferson Davis Highway, Suite 1204, Arlington, VA 22202-4302, and to the Office of Management and Budget, Paperwork Reduction Project (0704-0188), Washington, DC 20503

1. AGENCY USE ONLY (Leave blank)	2. REPORT DATE 3/15/91	3. REPORT TYPE AND DATES COVERED Final: 1/15/88- 1/14/91

4. TITLE AND SUBTITLE
Laser Spectroscopy Characterization of Materials for Frequency Agile Solid State Laser Systems

5. FUNDING NUMBERS
DAAL03-88-K-0025

6. AUTHOR(S)

Richard C. Powell, Ph.D.

7. PERFORMING ORGANIZATION NAME(S) AND ADDRESS(ES)
Center for Laser Research
OKLAHOMA STATE UNIVERSITY
Stillwater, Oklahoma 74078-0444

8. PERFORMING ORGANIZATION REPORT NUMBER

9. SPONSORING/MONITORING AGENCY NAME(S) AND ADDRESS(ES)

U. S. Army Research Office
P. O. Box 12211
Research Triangle Park, NC 27709-2211

10. SPONSORING/MONITORING AGENCY REPORT NUMBER

ARO 25478.19-PH

11. SUPPLEMENTARY NOTES
The view, opinions and/or findings contained in this report are those of the author(s) and should not be construed as an official Department of the Army position, policy, or decision, unless so designated by other documentation.

12a. DISTRIBUTION/AVAILABILITY STATEMENT

Approved for public release; distribution unlimited.

12b. DISTRIBUTION CODE

13. ABSTRACT (Maximum 200 words)

This research involves the use of laser spectroscopy techniques to investigate materials which include laser crystals such as Cr^{3+}-doped alexandrite, emerald, garnets, and glass ceramics as well as Nd^{3+}-doped garnets and germinates and Ho^{3+}-doped fluorides. In addition, photorefractive processes were studied in potassium niobate crystals and in rare earth doped glasses. Some of the results of major importance from this work are: (1) The characterization of the properties of laser-induced gratings in glasses; (2) The elucidation of the effects of dopant ions on the photorefractive response of potassium niobate; (3) The observation of a new type of picosecond nonlinear optical response in potassium niobate associated with scattering from a Nb hopping mode; (4) The characterization of the properties of energy migration and radiationless relaxation processes in Cr^{3+}-doped laser crystals; (5) The characterization of the pumping dynamics and lasing properties of Ho^{3+} in $BaYb_2F_8$; and (6) The characterization of the pumping dynamics and lasing properties of several Nd^{3+}-doped crystals.

14. SUBJECT TERMS

15. NUMBER OF PAGES

16. PRICE CODE

17. SECURITY CLASSIFICATION OF REPORT	18. SECURITY CLASSIFICATION OF THIS PAGE	19. SECURITY CLASSIFICATION OF ABSTRACT	20. LIMITATION OF ABSTRACT
UNCLASSIFIED	UNCLASSIFIED	UNCLASSIFIED	UL

NSN 7540-01-280-5500

Standard Form 298 (Rev 2-89)
Prescribed by ANSI Std Z39-18
298-102

LASER SPECTROSCOPY CHARACTERIZATION OF MATERIALS FOR FREQUENCY AGILE SOLID STATE LASER SYSTEMS

Richard C. Powell, Ph.D.
Principal Investigator

Center for Laser Research
OKLAHOMA STATE UNIVERSITY
Stillwater, Oklahoma 74078-0444

A-1

FINAL REPORT

January 15, 1988   January 14, 1991

ABSTRACT

This report summarizes the research done in the Center for Laser Research at Oklahoma State University supported by the U.S. Army Research Office under Contract Number DAAL03-88-K-0025 from January 15, 1988 - January 14, 1991. The research involves the use of laser spectroscopy techniques such as four-wave mixing, high power picosecond pulse pumping, and time-resolved site-selection spectroscopy to characterize dynamical optical processes such as energy migration, multiphoton absorption, radiationless relaxation, and the photorefractive effect in materials with potential applications in optical technology. The materials investigated include laser crystals such as Cr^{3+}-doped alexandrite, emerald, garnets, and glass ceramics as well as Nd^{3+}-doped garnets and germinates and Ho^{3+}-doped fluorides. In addition, photorefractive processes were studied in potassium niobate crystals and in rare earth doped glasses. Some of the results of major importance from this work are: (1) The characterization of the properties of laser-induced gratings in glasses; (2) The elucidation of the effects of dopant ions on the photorefractive response of potassium niobate; (3) The observation of a new type of picosecond nonlinear optical response in potassium niobate associated with scattering from a Nb hopping mode; (4) The characterization of the properties of energy migration and radiationless relaxation processes in Cr^{3+}-doped laser crystals; (5) The characterization of the pumping dynamics and lasing properties of Ho^{3+} in $BaYb_2F_8$; and (6) The characterization of the pumping dynamics and lasing properties of several Nd^{3+}-doped crystals.

CONTENTS

IV. NONLINEAR OPTICAL PROPERTIES OF CRYSTALS AND GLASSES

4

I.   INTRODUCTION

Optical technology has emerged as a vitally important area for research and development related to military applications. This technology has made important contributions to the development of "smart weapons", communications, surveillance, and display systems. The basis of this technology is optical devices such as laser sources, light modulation devices (frequency, intensity, direction, etc.), light guides (fibers, waveguides, etc.), and detectors. All-solid-state systems have the advantage of ruggedness for field operation. However, the development of these systems is currently limited by the lack of availability of materials with the optimum device operational parameters. The goal of this research project was to enhance our understanding of the fundamental physical processes in optical materials relevant to device operation. Only through an understanding of these processes will it be possible to design optical devices with predictable operational characteristics.

This research focused on laser sources and nonlinear optical materials for modulating laser beams. The physical processes of interest are those affecting the pumping dynamics of solid state lasers and those contributing to the formation of transient and permanent holographic gratings in nonlinear optical materials. The materials of interest included rare earth- and chromium-doped laser crystals, rare earth-doped glasses, and potassium niobate. Laser spectroscopy techniques were used to characterize the properties of these materials. These techniques included four-wave mixing, picosecond pulse-probe measurements, and time-

resolved site-selection spectroscopy, as well as laser-pumped-laser measurements.

The project was divided into three thrust areas according the type of materials being investigated: rare earth-doped laser crystals; chromium-doped laser crystals; and photorefractive crystals and glasses. The important results obtained during the three years of this contract are briefly outlined in this section and presented in detail in the remainder of the report.

I.1 SUMMARY OF RESEARCH ACCOMPLISHMENTS

The first research area of this contract focused on rare earth-doped laser materials. This work involved two types of projects: characterizing Nd-doped laser materials and characterizing Ho-doped laser materials. Using a tunable alexandrite laser as an excitation source to simulate diode laser pumping, the lasing properties of Nd^{3+} were studied as a function of pump wavelength. The lasing threshold and slope efficiency were measured as well as the spectral, spatial, and temporal beam properties. It was found that excited state absorption of pump photons plays a critical role in determining the lasing properties of a material excited by monochromatic pumping. In addition, the spectroscopic and lasing properties were characterized for Nd^{3+} in several host crystals with potential for diode laser pumping. These included $Ba_2MgGe_2O_7$, $Ba_2Zn_2Ge_2O_7$, and $La_3Lu_2Ga_3O_{12}$. A comprehensive study was made of the spectral dynamics and lasing properties of Ho^{3+} in $BaYb_2F_8$ crystals. Time-resolved site-selection spectroscopy measurements were used to characterize the energy transfer and upconversion processes that

6

lead to channel switching of the laser output.

The second research area involves vibronic laser materials based on chromium ions. The most important project in this area involved the continuation of our use of four-wave mixing (FWM) to characterize the spectral dynamics of a series of Cr^{3+}-doped laser crystals. This has provided an understanding of the origin of FWM signal in these materials and demonstrated how the polarizability change of the optically-pumped Cr^{3+} ions can cause "population lensing" of laser beams passing through the sample. In addition, the dynamics of energy transfer among the Cr^{3+} ions was characterized for different types of laser crystals and found to depend significantly on the concentration and distribution of dopant ions as well as the intrinsic properties of the host material. Information was also obtained on the radiationless relaxation processes involved in pumping these materials. All of this information is relevant to understanding the operation of these materials as solid state lasers. FWM experiments were also performed on a Cr-doped glass ceramic and the results compared to those obtained on Cr-doped crystals.

The third research area focused on the characterization of photorefractive materials for nonlinear optical applications. Two classes of materials were studied: displacive ferroelectrics represented by $KNbO_3$ crystals and rare earth doped glasses. The studies of laser-induced holographic gratings in rare earth doped glass focused on trying to enhance our understanding of the physical mechanism responsible for this effect. A theoretical model was developed based on a two-level system associated with the structural environment of the rare earth ion. This model was

7

applied to interpret experimental results obtained on a series of silicate glasses with different monovalent alkali modifier ions and a series of silicate glasses with different divalent alkaline modifier ions. This work has lead to an increased understanding of this phenomena and how to alter the material composition in order to maximize the effect. In addition, applications for optical storage, frequency demultiplexing, and laser beam modulation were demonstrated. A comprehensive study was made of the nonlinear optical properties of undoped and doped $KNbO_3$ since it has the highest photorefractive figure of merit for any material of its class. Using c.w. laser techniques, the properties of photorefractive beam coupling, four-wave mixing, and the dynamics of holographic grating formation and decay were studied. In addition, picosecond pulse-probe techniques were used to investigate the fast nonlinear optical response of this material. The results of this study provide a thorough understanding of the nonlinear optical properties of this material. Of special interest is the fast conjugate signal observed on the picosecond time scale. A model was developed that attributed this fast response to stimulated scattering from a niobium hopping mode.

I.2 PUBLICATIONS AND PERSONNEL

The work performed during the three years of this contract resulted in 21 publications, three doctoral theses, two masters theses, and numerous unpublished presentations and colloquia. These are listed in Table I.

The personnel making major contributions to this research

include the principal investigator, Richard C. Powell, and several visiting scientists and graduate students. The visiting scientists were:

Dr. Frederic M. Durville, CNRS, Lyon, France;

Dr. Mahendra G. Jani, OSU Post-Doctoral Research Associate;

Prof. Dhiraj K. Sardar, University of Texas, San Antonio;

Prof. Bahaeddin Jassemnejad, Central State University, OK;

Dr. Roger J. Reeves, University of Christ's Church, New Zeland;

Dr. Andrzej Suchocki, Polish Academy of Sciences, Poland.

The graduate students support by this contract include G.J. Quarles, G.D. Gilliland, E.G. Behrens, M.L. Kliewer, James D. Allen, Michael J. Ferry, V.A. French, F.M. Hashmi, and K.W. Ver Steeg. Gilliland, Behrens and Kliewer all three received their doctoral degrees from this research. They are now working at IBM Watson Research Laboratories, Fibercek, and Schwartz Electro Optics, respectively. Allen and Ferry received their masters degrees from this research and are working at Texas Instruments and the Army Center for Night Vision and Electro-Optics, respectively. The other three students are continuing their graduate studies for their doctoral degrees here at Oklahoma State University.

It is a pleasure to acknowledge the collaboration with a number of colleagues. Important contributions to this research were made by:

Prof. Georges Boulon, University of Lyon, France;

Mr. Douglas H. Blackburn, NIST;

Dr. David C. Cranmer, NIST;

Mr. Greg J. Mizell, Virgo Optics;

Dr. Leon Esterowitz, Naval Research Laboratory;

Dr. Toomas H. Allik, Science Applications International;

Dr. M.R. Kokta, Union Carbide Corp.;

Dr. Shui Lai, Allied Signal;

Dr. Donald F. Heller, Allied Signal;

Finally, this work benefited greatly from collaboration with U.S. Army personnel. Dr. Al Pinto and his group at CNVEO worked closely with us on several of these projects and provided an important degree of relevance to this fundamental research program.

TABLE I

THESES, PUBLICATIONS, AND PRESENTATIONS

THESES

"Properties and Applications of Laser Induced Gratings in Rare Earth Doped Glasses", E.G. Behrens, Ph.D Thesis, Oklahoma State University, July 1989.

"Spectral Dynamics of Two Frequency Agile Laser Materials: Alexandrite and $BaYb_2F_8:Ho^{3+}$", G.D. Gilliland, Ph.D Thesis, Oklahoma State University, May 1988.

"Investigation of the Dynamics of Solid State Laser Crystals", M.L. Kliewer, Ph.D. Thesis, Oklahoma State University, December 1989.

"Spectroscopic and Laser Properties of Nd:BMAG", M.J. Ferry, M.S. Thesis, Oklahoma State University, August 1989.

"Optical Spectroscopy in $Li_4Ge_5O_{12}:Mn^{4+}$ and the Photorefractive Effect in $Bi_{12}SiO_{20}$", J.D. Allen, M.S. Thesis, Oklahoma State University, December 1988.

PUBLICATIONS

G.D. Gilliland, Richard C. Powell, and Leon Esterowitz, "Spectral and Up-Conversion Dynamics and Their Relationship to the Laser Properties of $BaYb_2F_8:Ho^{3+}$", Phys. Rev. B $\underline{38}$, 9958 (1988).

M.L. Kliewer and R.C. Powell, "Excited State Absorption of Pump Radiation as a Loss Mechanism in Solid-State Lasers", IEEE J. Quant. Electron. $\underline{25}$, 1850 (1989).

T.H. Allik, S.A. Stewart, D.K. Sardar, G.J. Quarles, R.C. Powell, C.A. Morrison, G.A. Turner, M.R. Kokta, W.W. Hovis, and A.A. Pinto, "Preparation, Structure, and Spectroscopic Properties of $Nd^{3+}:(La_{1-x}Lu_x)_3[Lu_{1-y}Ga_y]_2Ga_3O_{12}$ Crystals", Phys. Rev. B. $\underline{37}$, 9129 (1988).

M.J. Ferry, M.L. Kliewer, R.J. Reeves, R.C. Powell, and T.H. Allik, "Site-Selection Spectroscopy, Energy Transfer, and Laser Emission in Nd^{3+}-Doped $Ba_2MgGe_2O_7$", J. Appl. Phys. $\underline{68}$, 6372 (1990).

T.H. Allik, M.J. Ferry, R.J. Reeves, R.C. Powell, W.W. Hovis, D.P. Caffey, R.A. Utano, L. Merkle, and C.F. Campana, "Crystallography, Spectroscopic Analysis, and Lasing Properties of $Nd^{3+}:Ba_2ZnGe_2O_7$", J. Opt. Soc. Am. B $\underline{7}$, 1190, (1990).

R.C. Powell and M.L. Kliewer, "Investigation of Pumping Dynamics in Rare Earth Doped Solid State Laser Materials", in SPIE Proc. Vol. 1062, "Laser Applications in Meteorology and Earth and Atmospheric Remote Sensing", ed. M.M. Sokoloski (SPIE, Bellingham, 1989), p. 65.

G.D. Gilliland, A. Suchocki, K.W. Ver Steeg, R.C. Powell, and D.F. Heller, "Laser-Induced Grating Spectroscopy of Alexandrite Crystals", Phys. Rev B $\underline{38}$, 6227 (1988).

G.J. Quarles, A. Suchocki, R.C. Powell, and S. Lai, "Optical Spectroscopy and Four-Wave Mixing in Emerald", Phys. Rev. B $\underline{38}$, 9996 (1988).

F.M. Durville, R.C. Powell, G. Boulon, and B. Champagnon, "Four-Wave Mixing Spectroscopy of a Cr^{3+}-Doped Transparent Glass Ceramic", Phys. Rev. B $\underline{37}$, 1435 (1988).

A. Suchocki and R.C. Powell, "Laser-Induced Grating Spectroscopy of Cr^{3+}-Doped $Gd_3Ga_5O_{12}$ and $Gd_3Sc_2Ga_3O_{12}$ Crystals", Chem. Phys. $\underline{128}$, 59 (1988).

F.M. Hashmi, K.W. Ver Steeg, F. Durville, R.C. Powell, and G. Boulon, "Four-Wave Mixing Spectroscopy of Cr-Doped Garnet Crystals", Phys. Rev. B $\underline{42}$, 3818 (1990).

R.C. Powell, "Four-Wave Mixing Spectroscopy of Transition Elements in Solids", in "Proc. Int. School on Excited States of Transition Elements", eds. B. Jezowska-Trzebiatowska, J. Legendziewicz, and W. Strek, (World Scientific, Singapore, 1989), p. 452.

R.C. Powell, "Spectroscopy of Chromium Doped Tunable Laser Materials", in "Proc. of the Topical Meeting on Laser Materials and Laser Spectroscopy", eds. Wang Zhijiang and Zhang Zhiming, (World Scientific, Singapore, 1989), p. 6.

E.G. Behrens, R.C. Durville, R.C. Powell, and D.H. Blackburn, "Properties of Laser-Induced Gratings in Eu-Doped Glasses", Phys. Rev. B $\underline{39}$, 6076 (1989).

E.G. Behrens, R.C. Powell, and D.H. Blackburn, "Characteristics of Laser-Induced Gratings in Pr^{3+}- and Eu^{3+}-Doped Silicate Glasses", J. Opt. Soc. Am. B $\underline{7}$, 1437 (1990).

E.G. Behrens, R.C. Powell, and D.H. Blackburn, "Optical Applications of Laser-Induced Gratings in Eu Doped Glasses", Appl. Opt. $\underline{29}$, 1619 (1990).

V.A. French, R.C. Powell, D.H. Blackburn, and D.C. Cranmer, "Refractive Index Gratings in Rare-Earth-Doped Alkaline Earth Glasses", J. Appl. Phys. $\underline{69}$, 913 (1991).

G.J. Quarles, A. Suchocki, and R.C. Powell, "A Comparison of the Spectroscopic Properties of Eu^{3+}-Doped Fluoride and Oxide Glasses Under High-Power, Picosecond-Pulse Excitation", J. Appl. Phys. 63, 861 (1988).

R.C. Powell, E.G. Behrens, and F.M. Durville, "Laser-Induced Gratings in Rare Earth-Doped Glasses", Materials Science Forum 50, 115 (1989).

R.J. Reeves, M.G. Jani, R.C. Powell, and G.J. Mizell, "J. Luminescence 45, 419 (1990).

R.J. Reeves, M.G. Jani, B. Jassemnejad, R.C. Powell, G.J. Mizell, and W. Fay, "Photorefractive Properties of $KNbO_3$", Phys. Rev. B 43, 71 (1991).

INVITED PRESENTATIONS

R.C. Powell, "Laser-Induced Grating Spectroscopy of Ions in Solids", Physics Department Colloquium, University of Missouri-Rolla, February 1988.

R.C. Powell, "Laser-Induced Grating Spectroscopy of Ions in Solids", Physics Department Colloquium, University of Iowa, February 1988.

R.C. Powell, "Laser Spectroscopy of Rare Earth-Doped Glasses", Research Colloquium, Rome Air Development Center, February 1988.

R.C. Powell, "Transient Grating Spectroscopy of Transition Metal Ions in Solids", Physics Colloquium, Polish Academy of Sciences, Warsaw, Poland, June 1988.

R.C. Powell, "Four-Wave Mixing of Transition Metal Ions in Solids", International School on Transition Metal Ions in Solids, Wroclaw, Poland, June 1988.

R.C. Powell, "Spectroscopy of Chromium Doped Tunable Laser Materials", International Meeting on Laser Materials and Laser Spectroscopy, Shanghai, China, July 1988.

R.C. Powell, "Permanent Laser-Induced Gratings in Glass", Hoya Glass Company", Freemont, CA, September 1988.

R.C. Powell, "The Future of Solid State Lasers", panal discussion at the Fourth International Laser Science Conference, Atlanta, GA, October 1988.

R.C. Powell, "Laser-Induced Grating Spectroscopy of Solids", Quantum Electronics Colloquium, Stanford University, Feb. 1989.

R.C. Powell, "Photorefractive Effects in Oxides and
    Semiconductors", Research Colloquium, IBM Research
    Laboratories, April 1989.

R.C. Powell, "Laser-Induced Picosecond Gratings", Research
    Colloquium, Sandia National Laboratories, April 1989.

R.C. Powell, "Some Aspects of Optically Pumped Nd-Doped Laser
    Materials", Nova Laser Technology Seminar, Lawrence
    Livermore National Laboratories, May 1989.

R.C. Powell, "Picosecond Four-Wave Mixing Measurements of
    Photorefractive Materials", Int. Laser Science Conf.-V,
    Stanford, August 1989. BAPS 34, 1654 (1989).

R.C. Powell, "Four-Wave Mixing of Ions in Solids", U.S.-Japan
    Exchange Seminar on Dynamical Processes of Ions in Solids,
    East-West Exchange Center, Hawaii, November 1989.

R.C. Powell, "Four-Wave Mixing of Ions in Solids", Am. Phys. Soc.
    Meeting, March 1990, Anaheim. BAPS 63, 1364 (1990).

CONTRIBUTED PRESENTATIONS

E.G. Behrens, and R.C. Powell, "Laser-Induced Gratings in Eu^{3+}-
    Doped Glasses", Am. Phys. Soc. Meeting, New Orleans, March
    1988. BAPS 33, 810 (1988).

R.C. Powell, F.M. Hashmi, A. Suchocki, F. Durville, and G.
    Boulon, "Laser-Induced Grating Spectroscopy of Cr^{3+}-Doped
    Garnets", Opt. Soc. Am. Meeting, Santa Clara, 1988.

R.C. Powell and M.L. Kliewer, "Investigation of Pumping Dynamics
    in Rare Earth Doped Solid State Laser Materials", SPIE O-E
    Lase Meeting, Los Angeles, January 1989.

R.J. Reeves, M.G. Jani, R.C. Powell, and G. Mizell, "The
    Photorefractive Effect in $KNbO_3$", Am. Phys. Soc. Meeting,
    St. Louis, March 1989. BAPS 34, 837 (1989).

E.G. Behrens and R.C. Powell, "Investigation of Laser-Induced
    Gratings in Rare-Earth Doped Glasses", Am. Phys. Soc.
    Meeting, St. Louis, March 1989. BAPS 34, Supp. N99 (1989).

R.C. Powell, R.J. Reeves, M.G. Jani, M.S. Petrovic, A. Suchocki,
    and E. G. Behrens, "Characteristics of Nonlinear Optical
    Materials for Use in Optical Limiting", SPIE Meeting on
    Optoelectronic Materials and Devices, Orlando, March 1989.

M.L. Kliewer and R.C. Powell, "Properties of Nd^{3+}-Doped
    Crystalline Lasers Pumped by an Alexandrite Laser", QELS
    '89, Baltimore, April 1989.

R.C. Powell and M.L. Kliewer, "Excited State Absorption of Pump Radiation as a Loss Mechanism", Conference on Tunable Solid State Lasers, North Falmouth, MA, May 1989.

S.A. Payne, R.C. Powell, S.C. Weaver, and L.L. Chase, "Degenerate Four-Wave Mixing of Cr^{3+} and Nd^{3+} Impurities in Solids", Int. Laser Science Conf.-V, Stanford, August 1989. BAPS 34, 1672 (1989).

R.R. Reeves, M. Jani, and R.C. Powell, "Picosecond Photorefractive Effect in $KNbO_3$", Int. Conf. on Dynamical Processes of Excited States in Solids, Athens, GA, August 1989.

R.J. Reeves, M. Jani, R.C. Powell, L.L. Chase, and G. J. Mizell, "Photorefractive Properties of $KNbO_3$", Opt. Soc. America Meeting, Orlando, Oct. 1989.

T.H. Allik, M.J. Ferry, R.J. Reeves, R.C. Powell, W.W. Hovis, D.P. Caffey, and R. Utano, "Spectroscopic Analysis and Diode Array Side-Pump Lasing Properties of BZAG:Nd", Opt. Soc. America Meeting, Orlando, Oct. 1989.

M.J. Ferry, M.L. Kliewer, R.J. Reeves, R.C. Powell, and T.H. Allik, "Lasing Properties and Excited State Absorption of Nd:BMAG", Opt. Soc. America Meeting, Orlando, Oct. 1989.

R.C. Powell, R.J. Reeves, M.S. Petrovic, "Nonlinear Optical Interactions in II-VI Semiconductors and Displacive Ferroelectrics, SPIE Conference, Orlando, April 1990.

S.A. Payne, L.L. Chase, and R.C. Powell, "Four-Wave Mixing of Nd^{3+} Impurities in Glasses and Crystals", XVII Int. Quantum Electronics Conf., Anaheim, May 1990.

F.M. Hashmi, K.W. Ver Steeg, R.C. Powell, and G. Boulon, "Four-Wave Mixing Spectroscopy of Cr-Doped Garnet Crystals", Int. Conf. on Luminescence, Lisbon, Portugal, July 1990.

F.M. Hashmi and R.C. Powell, "Four-Wave Mixing in Cr- and Nd-Doped Garnet Crystals", Sixth Interdisciplinary Laser Science Conference, Minneapolis, Sept. 1990. (BAPS 35, 1499, 1990).

V. French, E.G. Behrens, R.C. Powell, D.H. Blackburn, and D.C. Cranmer, "Laser-Induced Gratings in Rare Earth Doped Glasses", Annual Meeting of the Optical Soc. of Am., Boston, November 1990.

15

II. SPECTRAL DYNAMICS OF RARE EARTH LASER CRYSTALS

The following five manuscripts present details of the results obtained on several rare earth doped laser crystals. The first involves a Ho^{3+} laser in a fluoride host. Holmium lasers are becoming very important for near infrared laser applications. Because of weak absorption transitions, it is best to sensitize the holmium ions with energy transfer from other ions. This study extensively documents the details of the spectral dynamics of host-sensitized pumping in a fluoride host. It is the most extensive investigation that has been reported on a laser material of this class and the results provide a model for predicting the properties of other sensitized holmium lasers.

The next four papers document the properties of Nd^{3+}-doped laser crystals. The first paper focuses on problems associated with the excited state absorption of pump photons that can occur with monochromatic pumping. This is important for diode laser-pumped solid state lasers which is emerging as a very important class of lasers. The results show how important it is to select exactly the right wavelength for the diode laser pump source for maximum pumping efficiency. The other papers document the spectral and lasing properties of Nd^{3+} in three different crystal hosts. This work is part of a survey we are doing to identify host materials for Nd^{3+} lasers with enhanced absorption properties for diode laser pumping and with enhanced properties for Q-switching. The results demonstrate how the spectral properties change for different hosts and help provide a data base for the choice of the best host for a specific system.

Spectral and up-conversion dynamics and their relationship to the laser properties of $BaYb_2F_8:Ho^{3+}$

Guy D. Gilliland and Richard C. Powell

Department of Physics, Oklahoma State University, Stillwater, Oklahoma 74078-0444

Leon Esterowitz

Naval Research Laboratory, Washington, D.C. 20375-5000

The optical spectroscopic properties, energy transfer, up-conversion transitions, and lasing dynamics of $BaYb_2F_8:Ho^{3+}$ crystals are reported here. The positions of the various Stark components of the different J manifolds of Ho^{3+} are identified, and the branching ratios and radiative decay rates were calculated for the Ho^{3+} levels from the Judd-Ofelt theory. The fluorescence-decay kinetics of the Ho^{3+} emission originating on the $^5F_3$ and $^5S_2,^5F_4$ levels and of the Yb^{3+} emission were measured and analyzed with two energy-transfer theories. These calculations show that the Ho^{3+}-Yb^{3+} interaction is greater for ions initially in the $^5F_3$ level and that the diffusion of excitation energy among Yb^{3+} ions is a thermally assisted incoherent hopping process with a diffusion constant of 1.1×10^{-10} cm^2/sec at 300 K. The kinetics of the up-conversion processes were modeled with rate equations. It was necessary to include the effects of stimulated emission at 551.5 nm and three successive energy transfers from Yb^{3+} to Ho^{3+} to adequately describe the spectral dynamics of the up-conversion. The efficiencies of the different laser transitions were found to be dependent upon the pump power used. The output of the shorter-wavelength transition (0.55 μm) increases at the expense of the longer-wavelength transition (2.9 μm) as the pump power is increased. The 2.9-μm laser action was found to have a 15% energy conversion efficiency and a slope efficiency of 4.5% when pumped at 1.047 μm.

I. INTRODUCTION

The phenomenon of "frequency up-conversion," the conversion of infrared light to visible light, has been extensively studied in systems containing rare-earth ions, and up-conversion pumping of rare-earth laser systems has been demonstrated.[1-18] This can be an important technique for switching lasing channels. Important factors in the choice of a host material which affect the efficiency of emission for this type of the up-conversion process are the ability of the host material to accept a large concentration of the optically active ions, and weak electron-phonon interaction so the radiative rates for the visible emitting states of the activator ion are large in comparison to the nonradiative rates.[15,19]

It is well known that holmium ions can produce stimulated emission at several wavelengths in the infrared portion of the spectrum [2.4,[3] 2.0,[3,4] and 2.9 μm (Refs. 5 and 6)] and also in the green region.[3] When co-doped with ytterbium, holmium can also convert infrared radiation into green emission efficiently enough for stimulated emission to occur.[1,2]

In this paper we report the results of an extensive investigation of the spectral, energy-transfer, up-conversion, and lasing properties of $BaYb_2F_8:Ho^{3+}$ crystals. The energy levels and some of the relevant transitions for Ho^{3+} and Yb^{3+} are shown in Fig. 1. The results of measurements of the absorption and emission spectra at various temperatures as well as the results of a Judd-Ofelt analysis[15,20-22] are presented. The important features of two different up-conversion processes have

been analyzed and related to the stimulated emission at 2.9, 2.0, and 0.55 μm.

II. EXPERIMENT

The sample used for this investigation was a single crystal of $BaYb_2F_8$ containing 7.0 at. % Ho^{3+} ions (9.0×10^{20} cm^{-3}) and 93 at. % Yb^{3+} ions (1.2×10^{22}

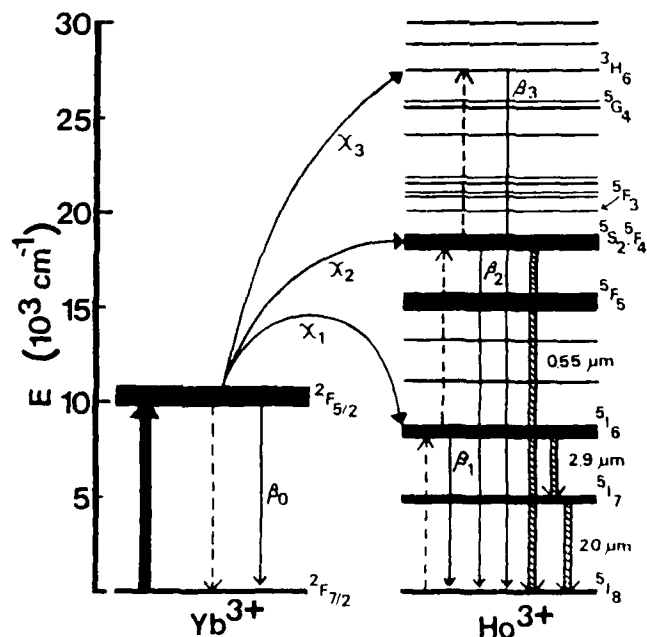FIG. 1. Energy levels and model for up-conversion of infrared light.

cm⁻¹). It had a diameter of 5.0 mm and a length of 7.0 mm. The host crystal has the same structure as BaTm₂F₈, which crystallizes in the monoclinic syngony with two molecules per unit cell.[23] The space group is C_{2h}^3 (C_{2h}),[23,25] with lattice parameters $a = 6.894$ Å, $b = 10.53$ Å, $c = 4.346$ Å, and $\beta = 99°18'$.[26] The Yb³⁺ ions sit in a site of eightfold coordination with F anions and form a slightly distorted Thomson cube.[25] The Ho³⁺ ions substitute for the Yb³⁺ ions. The host crystal is a single-center system, and the low symmetry of this site implies that all degeneracy in the electronic energy levels is removed except Kramers's degeneracy.[24]

The absorption and fluorescence spectra were obtained with standard spectroscopic equipment. For time-resolved energy-transfer studies, the excitation was provided by a nitrogen-laser-pumped dye laser with either Coumarin-540A or DCM dyes. For stimulated-emission measurements, the primary output from a passively mode-locked Nd:YAG (YAG denotes yttrium aluminum garnet) laser having a pulse width of 50 psec was used to pump the sample. The laser-performance measurements at 2.9 μm were done using the primary output of a Nd:YLF (YLF denotes yttrium lithium fluoride) laser at 1.047 μm with a 60-μsec pulse width as a pump source.

III. ABSORPTION AND EMISSION SPECTRA

Figure 2 shows the various regions of the absorption spectrum at 12 K. The spectrum is characterized by sharp lines in the visible region due to transitions within the $4f^{10}$ configuration of the Ho³⁺ ions, a broadband with structure in the nearinfrared due to the $^2F_{7/2}$-$^2F_{5/2}$

transition of the Yb³⁺ ions, and several absorption bands between 1.1 and 2.0 μm due to transitions to the lower-lying energy levels of the Ho³⁺ ions. Figures 3(a)–3(h) show the spectra of the visible and infrared emission of Ho³⁺ ions and the near-infrared emission of Yb³⁺ ions at 12 K. Figure 3(i) shows the 2.8-μm emission of Ho³⁺ at room temperature since it was too weak to detect at 12 K. The additional lines in the spectra at higher temperatures are due to absorption from the thermally populated higher Stark components of the $^5I_8$ ground-state multiplet of Ho³⁺.

A comparison of the emission spectrum of Yb³⁺ at 12 K shown in Fig. 3(f) with the absorption spectrum at 12 K shown in Fig. 2(b) demonstrates that both have the same general shape. From this we conclude that the splitting of the ground-state manifold $^2F_{7/2}$ of the Yb³⁺ ions is about 760 cm⁻¹. In C_{2h} point-group symmetry each J manifold of Ho³⁺ is split by the crystal field into $2J + 1$ non-Kramers levels, while each J manifold of Yb³⁺ is split into $J + \frac{1}{2}$ Kramers doublets. The crystal-field levels of Ho³⁺ have been identified from the absorption and emission spectra of BaYb₂F₈:Ho³⁺ and are shown in Table I. It was impossible to identify the crystal-field levels of Yb³⁺ due to the lack of resolution of the broad, overlapping levels.

The Judd-Ofelt theory[20,21] was applied to the room-temperature absorption spectrum of this sample to determine the radiative decay rates and branching ratios of the transitions. The oscillator strength of a transition of average frequency ν from a level J to the level J' is expressed as
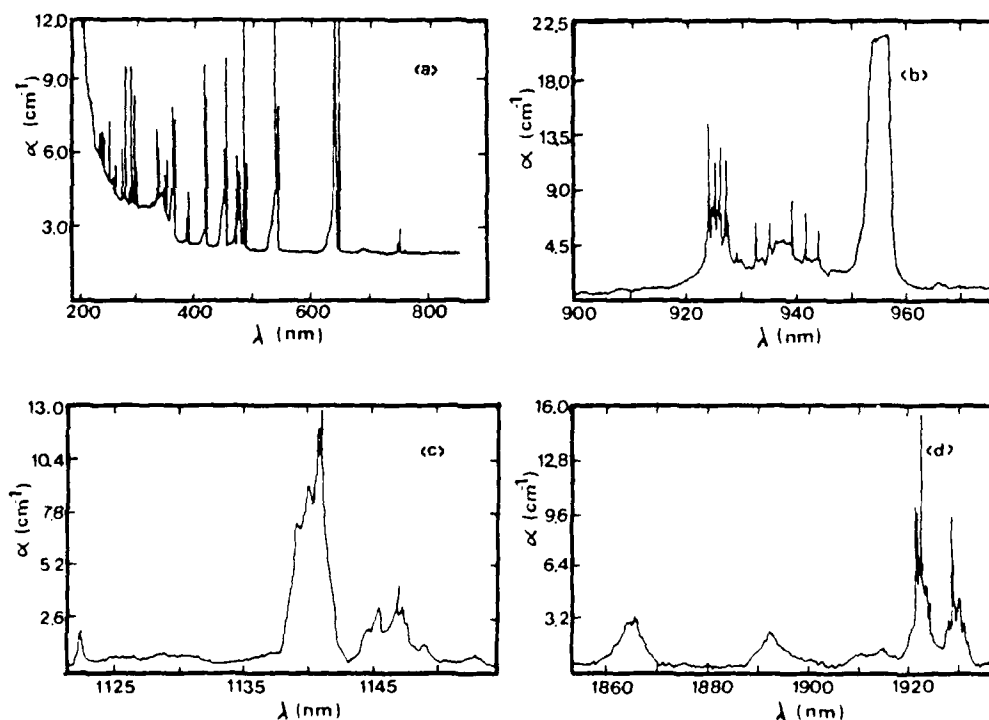
FIG. 2. Absorption spectra of BaYb₂F₈:Ho³⁺ at 12 K. (a) Transitions to the $^5I_4$ and higher levels of Ho³⁺; (b) transitions to the $^2F_{5/2}$ levels of Yb³⁺; (c) transitions to the $^5I_6$ levels of Ho³⁺; (d) transitions to the $^5I_7$ levels of Ho³⁺.
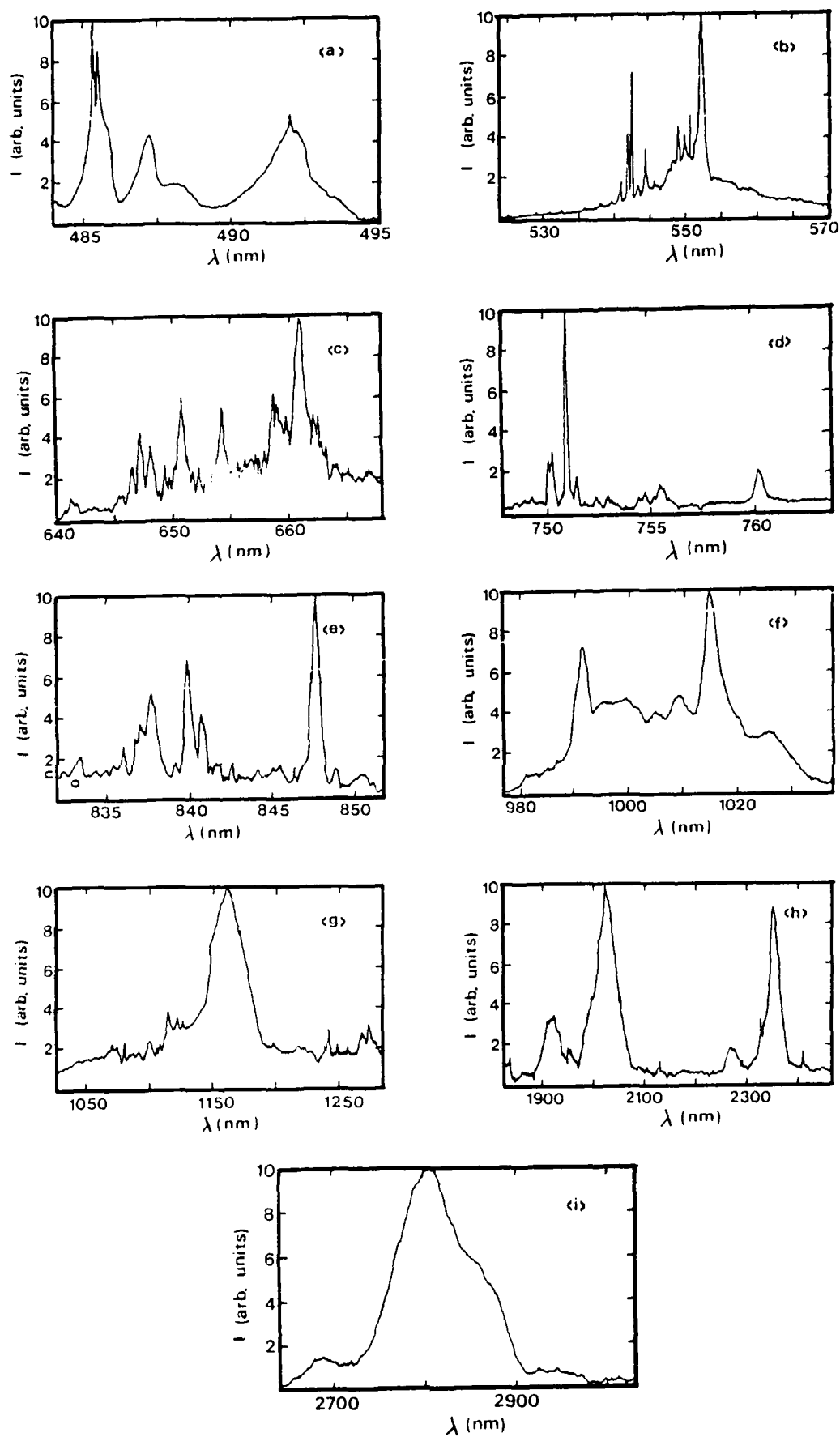
FIG. 3. Ho³⁺ and Yb³⁺ emission in BaYb₂F₈Ho³⁺: (a)–(h) at 12 K and (i) at 300 K. (a) ⁵F₃-⁵I₈ transitions; (b) ⁵S₂,⁵F₄-⁵I₈ transi-tions; (c) ⁵G₅-⁵I₀ transitions; (d) ⁵S₂,⁵F₄-⁵I₇ transitions; (e) ⁵F₅-⁵I₆ transitions; (f) ⁵S₂,⁵F₄-⁵I₆ transitions; (g) ⁵I₆-⁵I₈ transitions; (h) ⁵I₅-⁵I₈ and ⁵F₅-⁵I₅ transitions; (i) ⁵I₆-⁵I₇ transitions.

$$f(aJ;bJ') = (8\pi^2 m \nu)/[3h(2J+1)e^2]$$

$$\times [S_{ED}(aJ;bJ') + S_{MD}(aJ;bJ')], \quad (1)$$

where the electric-dipole and magnetic-dipole line strengths are

$$S_{ED}(aJ;bJ') = e^2 \sum_{t=2,4,6} \Omega_t \, |\langle f^n J \| U^{(t)} \| f^n J' \rangle |^2, \quad (2a)$$

TABLE I. Energy levels of Ho^{3+} ions in $BaYb_2F_8$.

	Energy (cm^{-1})		Energy (cm^{-1})
$^5I_8$	0	$^5F_5$	15 506
	31		15 538
	45		15 545
	75		15 586
	78		15 630
	115		15 662
	125		15 696
	141		15 701
	155		15 703
	173		15 713
	205		15 715
	243	$^5S_2, ^5F_4$	18 515
	255		18 549
	270		18 560
	317		18 608
	360		18 622
$^5I_7$	5166		18 660
	5175		18 681
	5178		18 695
	5181		18 702
	5187		18 713
	5198		18 718
	5200		18 723
	5204		18 730
	5222		18 755
	5254	$^5F_3$	20 602
	5284		20 619
	5361		20 648
	5364		20 683
$^5I_6$	8673		20 734
	8703		20 747
	8713		20 777
	8716	$^3H_6$	27 563
	8719		27 609
	8731		27 655
	8736		27 732
	8764		27 778
	8767		27 840
	8773		27 871
	8779		27 933
	8910		28 011
$^5I_5$	13 221		28 121
	13 257		28 329
	13 348		28 450
	13 364		
	13 371		
	13 378		
$^5I_4$	13 380		
	13 416		
	13 514		

$$S_{MD}(aJ;bJ') = [(e^2 h^2)/(4m^2 c^2)]$$

$$\times |\langle f^n J \| L + 2S \| f^n J' \rangle |^2, \quad (2b)$$

respectively. Here, a and b represent the other quantum numbers designating the states, f^n represents the electronic configuration, $U^{(t)}$ is the tensor operator for electric-dipole transitions, $L+2S$ is the operator for magnetic-dipole transitions, and Ω_t are the phenomenological parameters associated with the crystal-field environment of the ion in the host. The reduced matrix elements in Eqs. (2a) and (2b) have been calculated elsewhere[22,27] and are essentially invariant from host to host. The oscillator strength of a transition can be calculated from the absorption spectrum at room temperature using the equation

$$f = (mcn^2)/(\pi e^2 N \chi) \int \sigma(\nu) d\nu, \quad (3)$$

where m and e are the mass and charge of the electron, c is the speed of light, N is the concentration of absorbing centers, and $\int \sigma(\nu)d\nu$ is the integrated absorption cross section. χ is the correction term for the effective field in the crystal and is approximated by $\chi_{ED} = n(n^2+2)^2/9$ for electric-dipole transitions and $\chi_{MD} = n^3$ for magnetic-dipole transitions where n is the refractive index of the host. Measurements of the dispersion curves have not been performed on the host at this time. A value of $n = 1.6$ was used, which is similar to values of the index of refraction for other fluoride materials. It was found that varying n over a reasonable range of values did not significantly alter the results of the Judd-Ofelt analysis.

By combining Eqs. (1)–(3) and using the reduced matrix elements calculated by Weber[22] for Ho^{3+}, the phenomenological parameters Ω_t were determined from a least-squares fit to the absorption spectrum. These were found to be $\Omega_2 = 0.96 \times 10^{-20}$ cm^2, $\Omega_4 = 2.12 \times 10^{-20}$ cm^2, and $\Omega_6 = 3.25 \times 10^{-20}$ cm^2. Using these results, the spontaneous-emission probability can be obtained for each transition from

$$A(aJ;bJ') = (64\pi^4 \nu^3)/[3(2J+1)hc^3]$$

$$\times (\chi_{ED} S_{ED} + \chi_{MD} S_{MD}). \quad (4)$$

The radiative lifetimes and branching ratios can be determined by

$$\tau_{Ri}^{-1} = \sum_j A(i,j), \quad (5)$$

$$\beta(i,j) = A(i,j)/\tau_{Ri}, \quad (6)$$

where the summation is over transitions to final states j. The results of this analysis are summarized in Table II and are estimated to have an accuracy of $\pm 10\%$.

IV. ENERGY-TRANSFER PROCESSES

Many theories have been developed to describe energy migration and transfer between ions. Each of these theories is limited to a specific range of parameters for which it is valid.[28–33] The results obtained in this work are analyzed with two models which are valid fo

TABLE II. Radiative decay rates and branching ratios for Ho^{3+} transitions in $BaYb_2F_8{:}Ho^{3+}$ crystals.[a]

Initial level	Terminal level	$A(i,j)$ (sec^{-1})	$\beta(i,j)$	τ_R
$^5I_7$	$^5I_8$	120.44	1.00	8.3 msec
$^5I_6$	$^5I_7$	25.87	0.09	3.5 msec
	$^5I_8$	262.63	0.91	
$^5I_5$	$^5I_6$	7.32	0.035	4.7 msec
	$^5I_7$	122.15	0.579	
	$^5I_8$	81.50	0.386	
$^5I_4$	$^5I_5$	4.52	0.044	9.7 msec
	$^5I_6$	38.77	0.376	
	$^5I_7$	49.65	0.481	
	$^5I_8$	10.30	0.099	
$^5F_5$	$^5I_4$	0.055	2.43×10^{-5}	422 μsec
	$^5I_5$	8.31	0.0037	
	$^5I_6$	110.48	0.049	
	$^5I_7$	429.39	0.190	
	$^5I_8$	1818.20	0.757	
$^5S_2, {}^5F_4$	$^5F_5$	2.13	0.0004	190 μsec
	$^5I_4$	48.70	0.009	
	$^5I_5$	146.70	0.028	
	$^5I_6$	283.67	0.054	
	$^5I_7$	800.35	0.152	
	$^5I_8$	3981.90	0.756	

[a] $\Omega_2 = 0.96 \times 10^{-20}$ cm^2; $\Omega_4 = 2.12 \times 10^{-20}$ cm^2; $\Omega_6 = 3.25 \times 10^{-20}$ cm^2.

different circumstances. The Ho^{3+}-Yb^{3+} energy transfer is consistent with a single-step process while the Yb^{3+}-Ho^{3+} energy transfer is consistent with a model in which energy transfer between sensitizer and activator ions acts as a weak perturbation on the strong diffusion among sensitizers.

The typical ion-ion interaction mechanisms involving rare-earth ions are the electric multipolar mechanisms.[30,31] The strength of the interaction depends on the distance between sensitizer and activator ions as R^{-s}, where $s = 6, 8$, or 10 for dipole-dipole, dipole-quadrupole, and quadrupole-quadrupole interactions, respectively. Inokuti and Hirayama have derived an expression for the time dependence of the sensitizer fluorescence in the presence of energy transfer to randomly distributed activator ions,[28]

$$I(t) = A \exp[-t/\tau - \Gamma(1 - 3/s)C/C_0(t/\tau)^{3/s}] , \qquad (7)$$

where τ is the intrinsic lifetime of the sensitizer in the absence of activator ions, C is the concentration of activators, C_0 is called the "critical transfer concentration," Γ is the gamma function, and A is a normalization constant. The critical transfer distance R_0 can be determined from C_0 by[30,31]

$$R_0 = (3/4\pi C_0)^{1/3} . \qquad (8)$$

A. Ho^{3+}-Yb^{3+} energy transfer

As a first approximation, we assume that the excitation energy residing on the Ho^{3+} ions does not migrate between Ho^{3+} ions, but is capable of being transferred to Yb^{3+} ions. Thus for this case the Ho^{3+} ions play the role

of sensitizer ions while Yb^{3+} ions play the role of activator ions. Justification for the assumption of no Ho^{3+}-Ho^{3+} interaction is based on the relative concentrations of sensitizer and activator ions. Because Yb^{3+} is a stoichiometric component of $BaYb_2F_8$ and there are approximately ten Yb^{3+} ions for every Ho^{3+} ion, the nearest-neighbor environment of optically active ions surrounding the Ho^{3+} ions consists almost completely of Yb^{3+} ions (assuming no clustering of Ho^{3+} ions). The Ho^{3+}-Yb^{3+} energy transfer can involve two sets of electronic-emission transitions, $^5S_2, {}^5F_4 \rightarrow {}^5I_6$ and $^5F_5 \rightarrow {}^5I_7$, which are both resonant with the $^2F_{7/2} \rightarrow {}^2F_{5/2}$ absorption transition of Yb^{3+}. Therefore, the branching ratios for each of these transitions need to be considered to determine the effects of competing processes. If the Ho^{3+}-Ho^{3+} interaction is present, it will involve resonant emission and absorption transitions between the excited state, $^5S_2, {}^5F_4$ or $^5F_5$, and the ground state, $^5I_8$, of Ho^{3+}. By assuming only nearest-neighbor interactions and using the branching ratios listed in Table II, we estimate that the Ho^{3+}-Yb^{3+} interaction is 3.3 times more probable than the Ho^{3+}-Ho^{3+} interaction for ions in the $^5F_5$ state of Ho^{3+} (see Fig. 4), and in the case of ions in the $^5S_2, {}^5F_4$ states it is 1.1 times as probable. For randomly distributed Ho^{3+} ions the Ho^{3+}-Ho^{3+} interaction would be over distances much greater than nearest-neighbor separations and thus the interaction strength will be significantly less than the estimates given above. Therefore, the Ho^{3+}-Yb^{3+} interaction strength is greater than the Ho^{3+}-Ho^{3+} interaction strength, and as a first approximation, the theory of Inokuti and Hirayama can be used to characterize this case.
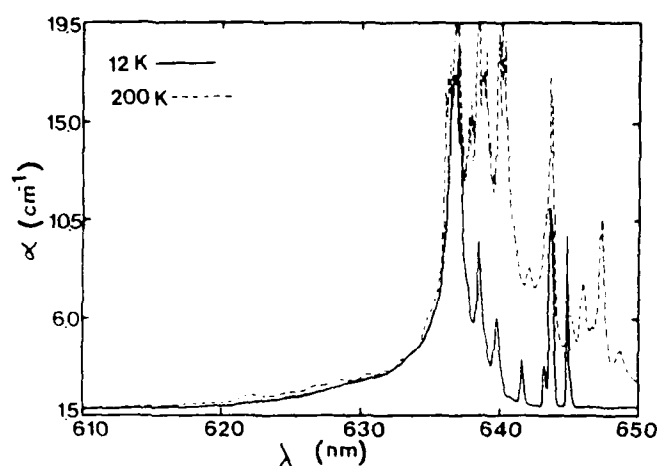
FIG. 4. Comparison of the absorption spectra at 12 and 200 K for the $^5F_5$ level of Ho^{3+}.

To characterize the energy-transfer processes, the kinetics of the fluorescence transitions between the initially excited states and the ground state of the Ho^{3+} ions was monitored. The fluorescence decay from the $^5S_2, ^5F_4$ levels of Ho^{3+} was measured by monitoring the transitions terminating on the ground state at several temperatures ranging from 12 to 300 K. Figure 5 shows the decay of the fluorescence intensity at 12 K along with least-squares fits to the data using Eq. (7) for different multipolar interactions. The best fit for all temperatures is for the dipole-dipole interaction. The decay curves are all clearly nonexponential at short times for all temperatures and tend asymptotically toward an exponential at long times. The intrinsic decay rate of the Ho^{3+} ions was determined from the exponential part of the decay curves approached at long times. The theoretical curves gen-
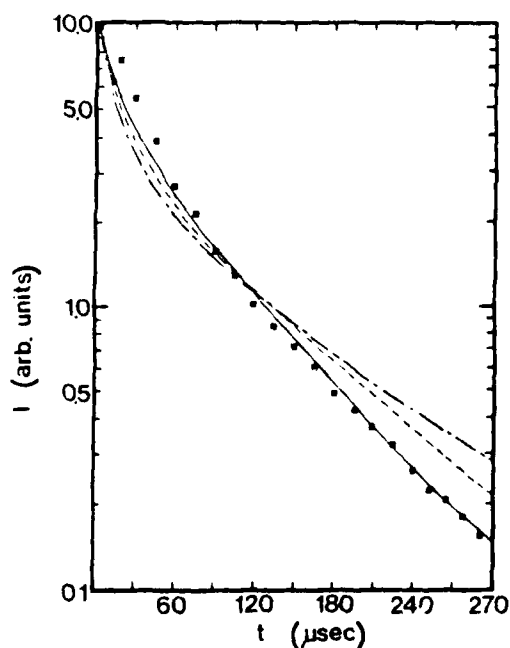
erated from Eq. (7) were fitted to the data by treating C/C_0 as an adjustable parameter for each type of interaction $(s = 6, 8,$ or $10)$, and values for R_0 were determined using Eq. (8). The temperature dependence of R_0 for these initial conditions is plotted in Fig. 6.

The coupling between the Ho^{3+} and Yb^{3+} ions with the former initially in the $^5F_5$ state was also investigated using Eq. (7) to fit the fluorescence-decay curves. The intrinsic decay rate in this case was again determined from the exponential tail of the decay kinetics and was found to be in substantial agreement with the measured value obtained in a sample of $BaY_2F_8:Ho^{3+}$ which contains no Yb^{3+}.[24] The interaction mechanism in this case was again found to be electric-dipole–dipole. However, the strength of the interaction, as well as its temperature dependence, is different. The strength of the interaction, which is reflected in the magnitude of the critical interaction distance R_0, is shown as a function of temperature in Fig. 6.

Examination of Fig. 6 shows that the interaction strength between Ho^{3+} and Yb^{3+} ions is slightly greater when the Ho^{3+} ions are in the $^5F_5$ excited state than when they are in the $^5S_2, ^5F_4$ excited state. The value of R_0 for the former case is close to the nearest-neighbor distance between Ho^{3+} and Yb^{3+} ions, which is approximately 2.7 Å, whereas the value of R_0 is slightly smaller than this for ions in the $^5S_2, ^5F_4$ states. If the Ho^{3+} ions are directly excited, the temperature dependence of the interaction strength can affect the temperature dependence of the integrated fluorescence intensity of the Yb^{3+} ions. Figure 7 shows the temperature dependence of the integrated fluorescence intensity at 1.0 μm due to Yb^{3+} emission after two types of excitation. After pumping the $^5F_5$ state of Ho^{3+}, the interaction strength is independent of temperature and the Yb^{3+} fluorescence decreases monotonically with temperature due to some quenching mechanism in the Yb^{3+} ion, possibly energy transfer to the $^5I_6$ state of Ho^{3+}. The situation is quite different in the case of excitation into the $^5S_2, ^5F_4$ states of Ho^{3+}. The temperature dependence of the Yb^{3+} emission for this case increases to a maximum at approximately 50 K and then decreases. The interaction strength depicted in

FIG. 5. $^5S_2, ^5F_4$ emission at 12 K (dots), along with theoretical fits from Inokuti-Hirayama theory $(s = 6,$ solid line; $s = 8,$ short-dashed line; $s = 10,$ long-dashed line).
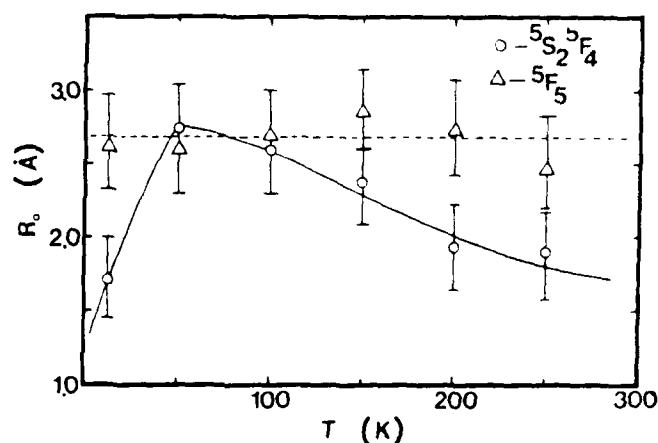

FIG. 6. Temperature dependence of R_0 for $^5F_5$ and $^5S_2, ^5F_4$ states calculated from Inokuti-Hirayama theory.
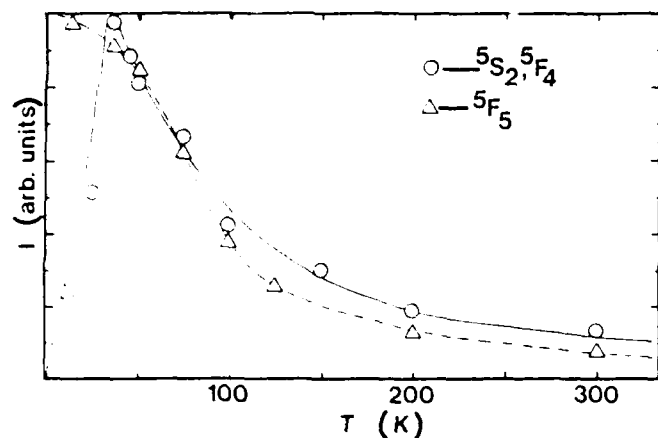
FIG. 7. Temperature dependence of integrated Yb^{3+} emission for $^5F_5$ and $^5S_2,^5F_4$ excitation.

Fig. 6 shows the same type of temperature dependence for this excitation. Thus the increase in the fluorescence intensity at 1.0 μm up to 50 K is due to the increase in the interaction strength between the Ho^{3+} and Yb^{3+} ions, and the decrease in the fluorescence intensity above 50 K is due to both the decrease in the interaction strength and the quenching of the Yb^{3+} emission mentioned above.

B. Yb^{3+}-Ho^{3+} energy transfer

Because of the large concentration of Yb^{3+} ions, 93 at. %, when the Yb^{3+} ions play the role of sensitizers the multistep diffusion among sensitizers is dominant over the single-step direct transfer from an excited Yb^{3+} ion to an unexcited Ho^{3+} ion. For weak diffusion the theory of Yokota and Tanimoto[33] describes the energy

Here, a is the activator trapping radius, and the lower limits of the integrals do not extend to zero due to the finite nearest-neighbor distance between the sensitizer and activators. The relation between a and R_0 is

$$R \sim (a\tau_s)^{1/6},$$ (12)

where τ_s is the intrinsic decay time of the sensitizer. The integrals appearing in Eq. (11) were evaluated numerically and the sensitizer-activator interaction constant α, diffusion coefficient D, and trapping radius a were determined by performing a nonlinear least-squares fit to the data. The intrinsic decay time of the $^5F_5$ Yb^{3+} emission has been determined previously to be 1.8 msec,[34] in-

transfer kinetics, while for strong diffusion the theory developed by Chow and Powell[29] gives the appropriate description. Both theories were fitted to the data obtained here and it was found that the parameters describing the energy transfer are consistent with the strong-diffusion model.

The equation governing the excited sensitizer concentration $n(r,t)$ is[29]

$$\frac{\partial n(r,t)}{\partial t} = -\beta n(r,t) + D\nabla^2 n(r,t) - \sum_i v(r-R_i)n(r,t) .$$ (9)

Here, β is the intrinsic decay rate of the sensitizer ions, D is the diffusion coefficient describing the energy migration among the sensitizer ions, R_i is the position vector for a given activator ion, r is the position vector for the sensitizer ions, and $v(r-R_i)$ is the interaction strength for a given sensitizer-activator pair. The second term on the right-hand side of Eq. (9) describes diffusion among the sensitizers, while the third term describes the sensitizer-activator interaction. The solution of Eq. (9) was obtained by Chow and Powell for a dipole-dipole interaction, where $v(r-R_i) = \alpha/|r-R_i|^6$, which is weaker than energy transfer by diffusive migration. The solution of Eq. (9) was then averaged over a uniformly random activator distribution. Most theories, including this one, assume a uniformly distributed lattice of sensitizers, so that a single average hopping time can be used to describe the random walk of the excitation energy, "exciton." This situation should be valid for the "host-sensitized" energy transfer in this crystal.

The intensity of sensitizer fluorescence given by Chow and Powell is[29]

$$I_s(t) = A \exp[-t/\tau - w_{sa}(t)t] ,$$ (10)

where the energy-transfer rate is given by

$$w_{sa}(t) = 4\pi D a n_a [1 + a(\pi Dt)^{-1/2}] + [4\pi n_a(\alpha/3a^3) + 2\pi n_a a^2 \int_a^\infty dr(\alpha/r^6)]\text{erfc}[(r-a)/\sqrt{4Dt}]]^2$$
$$- 8\pi n_a a \int_a^\infty dr(\alpha/r^5)\text{erfc}[(r-a)/\sqrt{4Dt}] .$$ (11)

dependent of temperature. For each set of data the validity of the Chow-Powell theory was examined. The assumptions made in deriving Eq. (10) lead to the condition[29] $\pi D a^4 \alpha^{-1} > 1$. This restriction was found to be valid for every set of data examined, typically giving a value of 31.8 for the left-hand side of the inequality. An example of the best fit to the decay kinetics of Yb^{3+} emission at 12 K is shown in Fig. 8.

The temperature dependencies of the diffusion constant D and sensitizer-activator interaction strength α obtained from the Chow-Powell theory are shown in Fig. 9. The diffusion constant increases with temperature and is 1.1×10^{-10} cm^2/sec at one. The long lifetime of $^5I_6$, 4 msec, ensures that there is sufficient population in this state for the resonant cross-relaxation process from Yb^{3+} to Ho^{3+} to occur on the time scale of the Yb^{3+} emission.
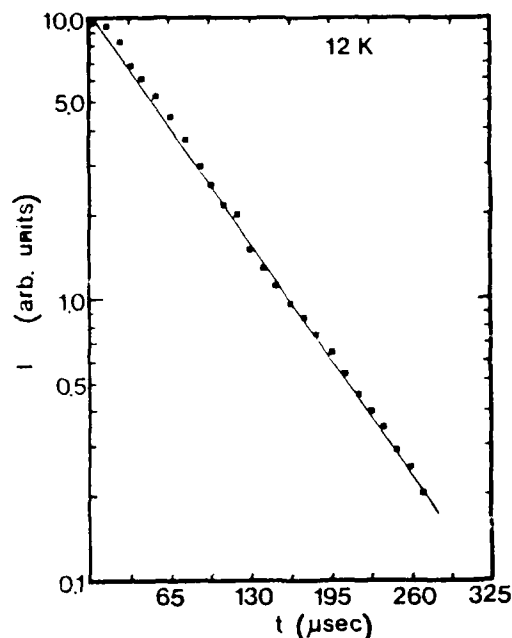
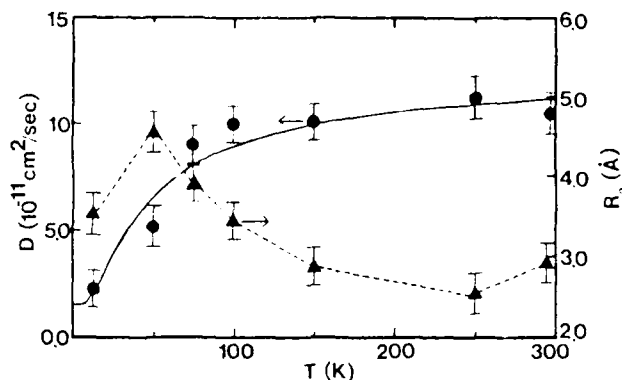FIG. 8 Yb³⁺ emission with Chow-Powell fit (solid line) at 12 K

FIG. 9. Temperature dependence of diffusion constant and sensitizer-activator interaction strength calculated from Chow-Powell theory (solid line is theoretical fit for D, dashed line just shows trend of data).

V. UP-CONVERSION AND STIMULATED-EMISSION PROCESSES

Materials containing both Yb^{3+} and Ho^{3+} ions can efficiently convert 1.0-μm radiation into visible radiation.[9,14,18,16-19] As can be seen from the energy-level diagram for Yb^{3+} and Ho^{3+} shown in Fig. 1, Ho^{3+} has several nearly equally spaced energy levels giving rise to transitions which are coincident in energy with the $^2F_{5/2} \rightarrow ^2F_{7/2}$ Yb^{3+} transition near 1.0 μm. The green emission corresponding to the $^5S_2,^5F_4 \rightarrow ^5I_8$ transition of Ho^{3+} is seen when the sample is excited with either of two longer wavelengths as discussed below, but the mechanism for the up-conversion in each case is different.

There are several multiphoton mechanisms which can

be responsible for the up-conversion.[7,8,17] One possible mechanism is the sequential absorption of two pump photons by a single ion. Another possible mechanism is the absorption of pump photons by more than one ion with the subsequent energy transfer to the emitting ion.[7,8] The following results indicate that the latter mechanism is the dominant up-conversion mechanism responsible for the green emission in $BaYb_2F_8:Ho^{3+}$ for both types of excitation.

The kinetics of up-conversion processes can be modeled using rate equations. The emission from $^5S_2,^5F_4 \rightarrow ^5I_8$ transition of Ho^{3+} after excitation into the $^5F_5$ level of Ho^{3+} state can be modeled as shown in Fig. 10. The first step in the up-conversion 300 K. The diffusion length can be determined from

$$L_d = (2D\tau)^{1/2} \qquad (13)$$

and these values are listed in Table III. The accuracy of these energy-transfer parameters is estimated to be $\pm 10\%$. Figure 9 shows that the sensitizer-activator in-

TABLE III. Energy-transfer parameters.

	12 K		250 K	
	R_0 (Å)	Rate at 2.7 Å (sec⁻¹)	R_0 (Å)	Rate at 2.7 Å (sec⁻¹)
		$Ho^{3+} \rightarrow Yb^{3+}$ transfer		
$^5F_5$	2.6	1.3×10^4	2.3	4.9×10^3
$^5S_2,^5F_4$	1.7	1.0×10^3	2.1	3.0×10^3

12 K		250 K	
	$Yb^{3+} \rightarrow Ho^{3+}$ transfer		

$D = 2.1 \times 10^{-11}$ cm²/sec
$R_0 = 3.56$ Å $(S-A)$
$R_0 = 10.3$ Å $(S-S)$
$L_d = 27.5$ Å

$D = 1.5 \times 10^{-10}$ cm²/sec
$R_0 = 2.54$ Å $(S-A)$
$R_0 = 13.8$ Å $(S-S)$
$L_d = 84.9$ Å

$D(0) = 1.55 \times 10^{-11}$ cm²/sec
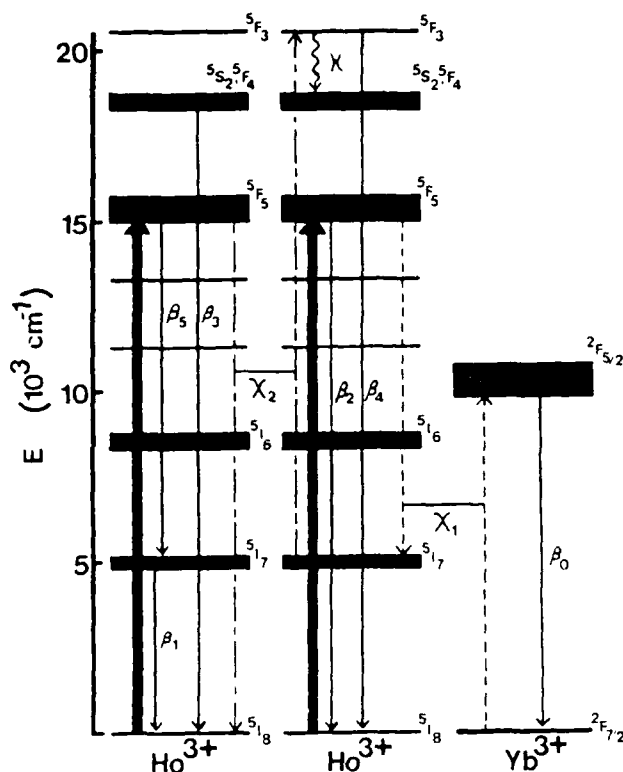$B = 1.10 \times 10^{-10}$ cm²/sec
$\Delta E = 27.3$ cm⁻¹

FIG. 10. Energy levels and model for up-conversion of red light.

teraction strength has the same temperature dependence as that calculated for the Ho^{3+}-Yb^{3+} transfer from the theory of Inokuti and Hirayama. The major difference is that the role of the sensitizer and activator ions are reversed in these two cases. For resonant processes the interaction strength is contained in the overlap integral between the sensitizer emission and activator absorption. The magnitude of the spectral overlap changes depending on which ion acts as sensitizer and activator due to the energy shift for emission for both Ho^{3+} and Yb^{3+} ions. However, the variation of the spectral overlap with temperature is essentially the same for both cases.

The actual measurement was performed by pumping the $^5S_2,^5F_4$ states of Ho^{3+} and monitoring the Yb^{3+} emission. The population of the Yb^{3+} excited state is achieved by the resonant cross-relaxation process

$$| Ho^{3+}(^5S_2,^5F_4),Yb^{3+}(^2F_{7/2}) \rangle$$
$$\rightarrow | Ho^{3+}(^5I_6),Yb^{3+}(^2F_{5/2}) \rangle .$$
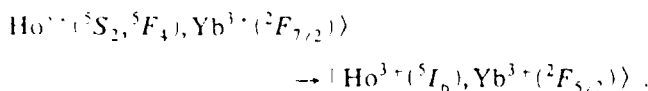
Initially the population of $^5I_6$ *is equal to that of the* $^2F_{5/2}$ state of Yb^{3+}. Therefore the energy transfer from Yb^{3+} to Ho^{3+} can take place via two types of processes. The first is transfer to the $^5I_6$ state via a phonon-assisted energy transfer. The second is the resonant cross relaxation

$$| Yb^{3+}(^2F_{5/2}),Ho^{3+}(^5I_6) \rangle$$
$$\rightarrow | Yb^{3+}(^2F_{7/2}),Ho^{3+}(^5S_2,^5F_4) \rangle .$$
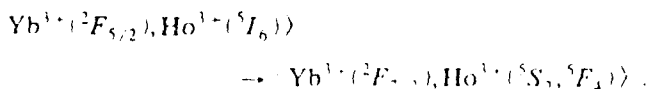
The temperature dependence and difference in rates between resonant and nonresonant processes, calculated

below, point to the second mechanism as the dominant is the resonant cross-relaxation process

$$| Ho^{3+}(^5F_5),Yb^{3+}(^2F_{7/2}) \rangle$$
$$\rightarrow | Ho^{3+}(^5I_7),Yb^{3+}(^2F_{5/2}) \rangle .$$
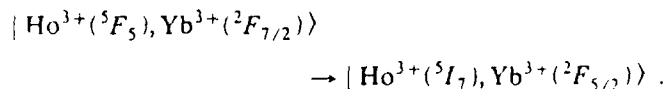
The relative probability of this process is related to the branching ratio for the Ho^{3+} transition, which is listed in Table II as 0.19. Therefore, this transition is one-fourth as probable as the transition originating from this excited level and terminating on the ground state. A rate-equation analysis of the energy-transfer rate between sensitizers and activators, when two energy levels are taken to characterize these ions, gives a relationship between the energy-transfer rate and the risetime of the activator emission[40]

$$t_{max} = (P_A^r - P_S^r - P_{SA})^{-1} \ln[P_A^r /(P_S^r + P_A^r)] \qquad (14)$$

where P_A^r and P_S^r are the radiative rates of the sensitizer and activator, respectively, and P_{SA} is the energy-transfer rate. The Yb^{3+} emission has a risetime of 4 μsec for this excitation which implies that the Ho^{3+}-Yb^{3+} transfer occurs with a rate of 1.5×10^5 sec^{-1}. Thus this first step in the up-conversion process also explains the observed Yb^{3+} emission. The second step in the up-conversion process can proceed by one of two mechanisms. The first is a resonant cross-relaxation between two Ho^{3+} ions,

$$| Ho^{3+}(^5F_5),Ho^{3+}(^5I_7) \rangle \rightarrow | Ho^{3+}(^5I_8),Ho^{3+}(^5F_3) \rangle ,$$
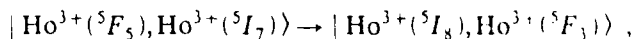
and the second is the absorption of an excitation photon by a Ho^{3+} ion that has already participated in the first step and is in the $^5I_7$ level. The last step involves both weak fluorescence from the $^5F_3$ level followed by fast nonradiative decay to the $^5S_2,^5F_4$ states and the green emission.

If a second cross-relaxation process is responsible for the excitation into the $^5F_3$ state, then it will originate on the $^5I_7$ level of a Ho^{3+} ion which has already undergone the first cross-relaxation process. The reason for this is that the radiative lifetime of the $^5I_7$ level is 9 msec while that of the $^5F_5$ level is 420 μsec. If a single ion were to absorb a photon, undergo cross relaxation, and then absorb another photon, it would require that the cross-relaxation process be faster than the duration of the pump pulse. This rules out the sequential two-photon mechanism because the pulse width of the laser excitation is 10 nsec, and the cross-relaxation time, reflected in the risetime of the $^2F_{5/2}$ Yb^{3+} emission, is 4 μsec at 12 K.

The rate equations used to analyze the spectral dynamics are

$$\frac{ds_1}{dt} = Y_1 n_2 (S - s_1) - \gamma_1 s_1 n_1 - \beta_0 s_1 , \qquad (15a)$$

$$\frac{dn_1}{dt} = Y_1 n_2 (S - s_1) - \gamma_1 s_1 n_1 - Y_2 n_1 n_2$$

$$+ \gamma_2 n_4 (N - n_1 - n_2 - n_3 - n_4) - \beta_1 n_1 + \beta_3 n_3 , \qquad (15b)$$

$$\frac{dn_2}{dt} = W_p(N - n_1 - n_2 - n_3 - n_4) - \beta_2 n_2$$
$$- X_1 n_2(S - s_1) + \gamma_1 s_1 n_1 - X_2 n_2 n_2$$
$$+ \gamma_2 n_4(N - n_1 - n_2 - n_3 - n_4) - \beta_5 n_2 , \quad (15c)$$

$$\frac{dn_3}{dt} = \kappa n_4 - \beta_3 n_3 , \quad (15d)$$

$$\frac{dn_4}{dt} = X_2 n_1 n_2 - \gamma_2 n_4(N - n_1 - n_2 - n_3 - n_4)$$
$$- (\kappa + \beta_4) n_4 , \quad (15e)$$

where $S = s_1 + s_0$ and $N = n_0 + n_1 + n_2 + n_3 + n_4$. s_i and n_i are the populations of the ith energy levels of the Yb^{3+} ions, $^2F_{7/2}$ and $^2F_{5/2}$, and Ho^{3+} ions, $^5I_8$, $^5I_7$, $^5F_5$, $^5S_2$, $^5F_4$, and $^5F_3$, respectively. S and N are the total concentrations of Yb^{3+} and Ho^{3+} ions, W_p is the pumping rate for absorbing photons from the laser excitation, X_i $(i = 1,2)$ is the energy-transfer coefficient, γ_i $(i = 1,2)$ is the back-transfer coefficient, β_0 is the fluorescence-decay rate of the $^2F_{5/2}$ level of Yb^{3+}, β_i $(i = 1-5)$ is the fluorescence-decay rate of each Ho^{3+} level as shown in the figure, and κ is the nonradiative-decay rate from $^5F_3$ to $^5S_2, ^5F_4$.

These equations were solved numerically on a DEC Micro-Vax II microcomputer using a fourth-order Runge-Kutta method in order to find the transient solutions. A δ-function excitation was assumed and the four transfer coefficients were treated as adjustable parameters. The observed fluorescence intensity from each level will be proportional to the population of the level. The time evolution of the fluorescence emissions from the $^2F_{5/2}$ level of Yb^{3+} and the $^5S_2, ^5F_4$ levels of Ho^{3+} are shown in Fig. 11. The solid and dashed lines represent the computer-generated least-squares fit to the data using the theoretical model described above. The data taken at 12 K were analyzed because the $^5F_3$ emission is too weak to detect at higher temperatures due to the increase in the multiphonon emission rate with temperature, and the Yb^{3+} emission is strongest at 12 K, as shown in Fig. 7. This analysis provides a fit of two sets of data with the same set of adjustable parameters. The best-fit parameters are listed in Table IV and are estimated to be accu-
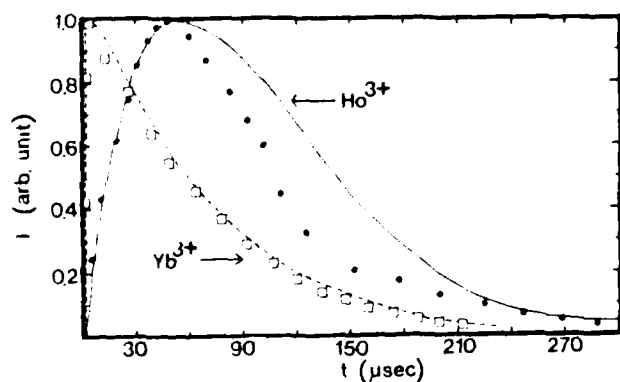
TABLE IV. Parameters obtained from the rate-equation analyses.

Activator level	Coefficient (cm³/sec)	Transfer rate (sec⁻¹)
Up-conversion of red pump light at 12 K		
X_1 (s_0)	2.1×10^{-17}	2.5×10^5
γ_1 (n_1)	3.0×10^{-8}	3.0×10^5
X_2 (n_1)	5.0×10^{-9}	5.0×10^4
γ_2 (s_0)	5.7×10^{-18}	6.8×10^4
κ	2.0×10^4 sec⁻¹	
Up-conversion of infrared pump light at 300 K		
X_1 (n_0)	7.0×10^{-18}	6.3×10^3
γ_1 (s_0)	1.0×10^{-21}	12.0
X_2 (n_1)	3.1×10^{-8}	1.5×10^5
γ_2 (s_0)	1.4×10^{-17}	1.7×10^5
X_3 (n_2)	1.0×10^{-7}	1.0×10^5
γ_3 (s_0)	2.0×10^{-17}	2.4×10^5
ϕ_1	1.00 cm³/sec	
ϕ_2	0.05 cm³/sec	
τ_1	10 psec	
τ_2	10 psec	

rate to ±10%. The intensity of the green emission as a function of laser-pump power is found to be almost quadratic, as shown in Fig. 12. This is expected for any two-photon process. Figure 13 shows the excitation spectra for the green up-conversion along with the absorption spectra in the region of the $^5F_5$ state of Ho^{3+}. The excitation spectra have been corrected for variations in laser power and the penetration depth into the sample. This shows a one-to-one correspondence with the positions of the peaks in the absorption spectra.

The kinetics leading to the green emission from the $^5S_2, ^5F_4$ levels after excitation into the inhomogeneously broadened $^2F_{5/2}$ state of the Yb^{3+} ion can be modeled as shown in Fig. 1. The first step in the up-conversion is the energy transfer from Yb^{3+} to Ho^{3+},

$$| Yb^{3+}(^2F_{5/2}), Ho^{3+}(^5I_8)\rangle \rightarrow | Yb^{3+}(^2F_{7/2}), Ho^{3+}(^5I_6)\rangle .$$

FIG. 11. Decay kinetics of emission from $^2F_{5/2}$ level of Yb^{3+} and $^5S_2, ^5F_4$ level of Ho^{3+} at 12 K with rate-equation fits.
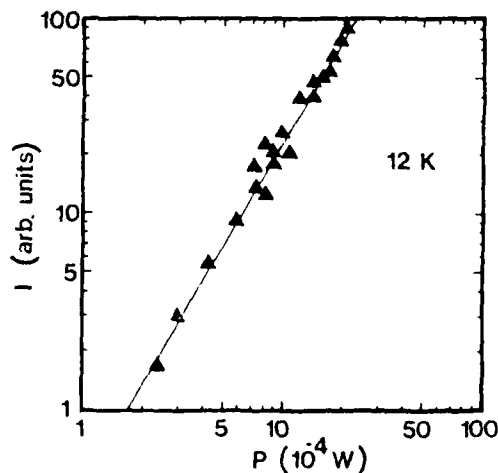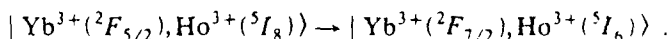

FIG. 12. Power dependence of green up-conversion, obtained by pumping $^5F_5$ and observing green emission from $^5S_2, ^5F_4$ at 12 K.
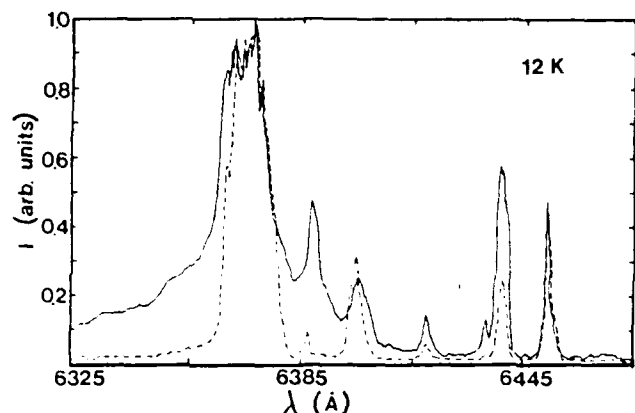
FIG. 13. Excitation spectra for green up-conversion in the region of $^5F_5$ level of Ho^{3+} at 12 K (dashed line) along with absorption spectra in the same region at 12 K (solid line).

This is a nonresonant process and the difference in energy is made up by the emission of phonons. As can be seen from the energy-level diagram, Fig. 1, the energy mismatch is about 1700 cm^{-1}. The phonons in this material have a maximum energy of approximately[41] 450 cm^{-1}; therefore the phonon-assisted energy transfer takes place with the emission of at least four phonons. The back-transfer rate from Ho^{3+} to Yb^{3+} should be smaller than the forward-transfer rate by a factor of[3] $[\exp(\Delta E/k_B T)]^4$, where ΔE is the energy of the phonons absorbed. This difference in rates is approximately 3 orders of magnitude at room temperature. The next step in the total scheme is the resonant cross-relaxation

$$Yb^{3+}(^2F_{5/2}), Ho^{3+}(^5I_6))$$

$$\rightarrow | Yb^{3+}(^2F_{7/2}), Ho^{3+}(^5S_2, ^5F_4)) .$$
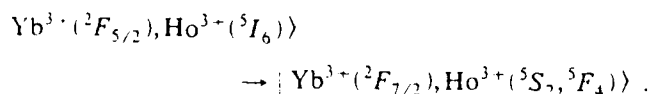
The third step, which is necessary in order to explain the observed dependence of the green-emission intensity on infrared pump power as discussed below, is also resonant. This process is

$$Yb^{3+}(^2F_{5/2}), Ho^{3+}(^5S_2, ^5F_4))$$

$$\rightarrow | Yb^{3+}(^2F_{7/2}), Ho^{3+}(^3H_6)) .$$
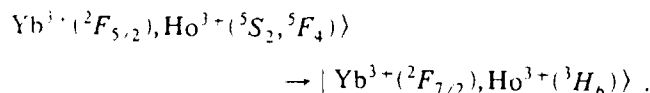
In both of these resonant processes, back-transfer cannot be neglected. The presence of back-transfer was confirmed experimentally by the observation of the emission at 1.0 μm due to Yb^{3+} after pumping the $^5S_2, ^5F_4$ and $^3H_6$ states of Ho^{3+}. The risetime for the Yb^{3+} emission was measured to be 15 μsec at 12 K.

The rate equations for this model are

$$\frac{ds_1}{dt} = W_p(S - s_1) - Y_1 s_1(N - n_1 - n_2 - n_3)$$

$$+ \gamma_1 n_1(S - s_1) - Y_2 s_1 n_1 + \gamma_2 n_2(S - s_1)$$

$$- Y_3 s_1 n_2 + \gamma_3 n_3(S - s_1) - \beta_0 s_1 , \quad (16a)$$

$$\frac{dn_1}{dt} = Y_1 s_1(N - n_1 - n_2 - n_3) - \gamma_1 n_1(S - s_1)$$

$$- Y_2 s_1 n_1 + \gamma_2 n_2(S - s_1) - \beta_1 n_1 - \phi_1 n_1 p_1 , \quad (16b)$$

$$\frac{dn_2}{dt} = X_2 s_1 n_1 - \gamma_2 n_2(S - s_1) - X_3 s_1 n_2$$

$$+ \gamma_3 n_3(S - s_1) - \beta_2 n_2 - \phi_2 n_2 p_2 , \quad (16c)$$

$$\frac{dn_3}{dt} = X_3 s_1 n_2 - \gamma_3 n_3(S - s_1) - \beta_3 n_3 , \quad (16d)$$

$$\frac{dp_1}{dt} = \phi_1 n_1 p_1 + \beta_1 n_1 - p_1/\tau_1 , \quad (16e)$$

$$\frac{dp_2}{dt} = \phi_2 n_2 p_2 + \beta_2 n_2 - p_2/\tau_2 , \quad (16f)$$

where the definitions of the parameters are as described following Eqs. (15). Here, s_i and n_i are the populations of the ith energy levels of the Yb^{3+} ions, $^2F_{7/2}$ and $^2F_{5/2}$, and Ho^{3+} ions, $^5I_8$, $^5I_6$, $^5S_2^5F_4$, and $^3H_6$, respectively. Terms representing stimulated-emission transitions from levels n_1 and n_2 are included in the model. Stimulated emission from n_1 occurs at[5,6] 2.9 μm, and p_1 represents the total number of photons at this wavelength in the sample. ϕ_1 represents the stimulated-emission parameter which is related to the stimulated-emission threshold, and τ_1 represents losses in the sample at this wavelength.[45] Stimulated emission from n_2 occurs at[1] 551.5 nm, and p_2, ϕ_2, and τ_2 represent the same parameters for this transition. As shown below, it is necessary to include stimulated emission at 551.5 nm in order to explain the observed power dependence of the green up-conversion and the observed lifetime shortening. The stimulated emission from n_1 must be included because we have determined the threshold for laser action at[5] 2.9 μm to be 80 mJ corresponding to a pumping rate of 4.3×10^{21} photons/sec. This threshold occurs at a considerably lower pumping rate than that used in our spectroscopic measurements ($10^{24}-10^{27}$ photons/sec). Omission of this term will lead to nonphysical values for the energy-transfer coefficients, tending to overestimate the forward-transfer coefficients Y_i.

Figure 14 shows the power dependence of the intensity of the green fluorescence versus the power of the infrared pump laser. The data show the presence of saturation effects since the slope is much less than quadratic, as is usually expected for a two-photon process. At a pumping rate of 4.0×10^{26} photons/sec the slope of the curve shows a significant increase which is due to stimulated emission. The change in slope corresponds to the threshold for this process and is consistent with the onset of the observed lifetime shortening discussed below. This power dependence was modeled using the rate equations given in Eqs. (16). These equations were solved numerically using the same computer procedure described above. A δ-function excitation was assumed and the transfer coefficients Y_2, Y_3, γ_3, and the stimulated-emission parameter ϕ_2 were treated as adjustable parameters. Y_1 can be estimated from the risetime of the 1.2-μm emission and γ_1 was chosen to be approximately 3 orders of magnitude smaller, as discussed earlier. Y_1 was chosen to be 7.0×10^{-18} cm^3/sec, agreeing with earlier estimates,[14,37] and γ_1 was chosen to be 1.0×10^{-21} cm^3/sec. γ_2 can be measured by exciting Ho^{3+} in the $^5S_2, ^5F_4$ levels and measuring the risetime of the $^2F_{5/2}$ Yb^{3+} emission.
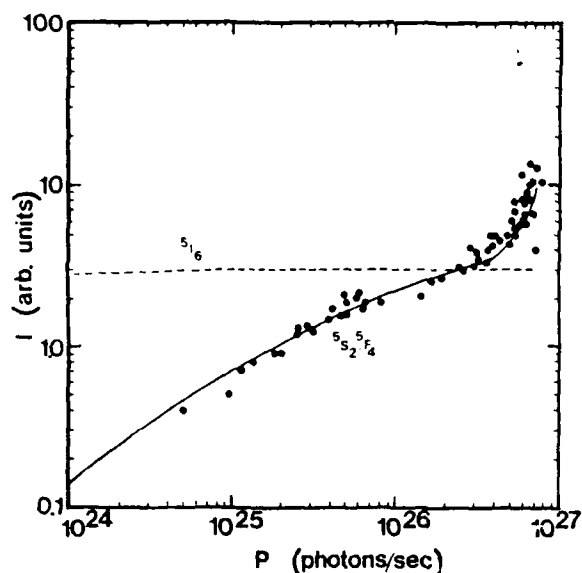
FIG. 14. Power dependence of green up-conversion, obtained by pumping $^2F_{5/2}$ level of Yb^{3+} at room temperature.

becoming limited by experimental resolution. The time evolution of the green emission below this threshold was also calculated from the rate equations and is shown along with the experimentally measured data in Fig. 15.

Under the condition of low-power infrared excitation the lifetime of the green transition is measured to be approximately 47 μsec. When the excitation power is increased to the threshold value of 4.0×10^{26} photons/sec and above, the shape of the decay curve abruptly changes. The short-time emission decays much faster than at low excitation powers, and the long-time decay is the same as for the low-power excitation. The $1/e$ value of the decay curve is plotted as a function of pump power in Fig. 16. The general shape of these data is similar to that reported in Refs. 42 and 43 and shows a definite excitation threshold. The fact that the intensity of the green emission increases instead of decreases above this threshold value confirms that we are observing a gain and not a loss mechanism. The increase in intensity is a result of the stimulated emission which causes the emission of photons at earlier times (lifetime shortening), thereby inhibiting the third energy-transfer step.

The model presented here has one more energy-transfer step than is necessary to explain the population of the $^5S_2, ^5F_4$ states by the up-conversion mechanism. The additional energy-transfer process to the $^3H_6$ level must be included in order to explain the observed power dependence shown in Fig. 14. This level acts as a "sink" for the excitation since population can accumulate in this level or decay into levels other than n_1 or n_2 without being recycled into these metastable levels on the time scale of the green emission. Without this additional energy level the green-emission intensity dependence on pump power cannot become sublinear.[44] In this case the model is essentially a closed system, on the time scale of the experiment, because the decay times are much longer than the observed risetimes at which the data were taken. The saturation behavior of the population of n_2 would, at

From these measurements γ_2 was calculated to be 1.4×10^{-17} cm^3/sec. The measured fluorescence-decay rates were used for the transition rates. τ_1 and τ_2 were chosen to be 10 psec, the time it takes light to pass through the sample.[42] ϕ_1 was chosen to agree with the threshold for the 2.9-μm laser action using the equation

$$n_1 = (\tau_1 \phi_1)^{-1} . \tag{17}$$

This is obtained by defining the threshold as when the gain terms equals the loss term in Eq. (16e). The resulting best fit to the data is shown as a solid line in Fig. 14. The values for the adjustable parameters obtained from this fit are listed in Table IV and estimated to have an accuracy of $\pm 10\%$.

The peak intensities of green emission plotted in Fig. 14 and in the theoretical fit were chosen at the peak of the rise in the number of photons, p_2, in the sample. This time was about 1.5 μsec for pump powers below the threshold for stimulated emission in the green transition and became shorter above the threshold, eventually
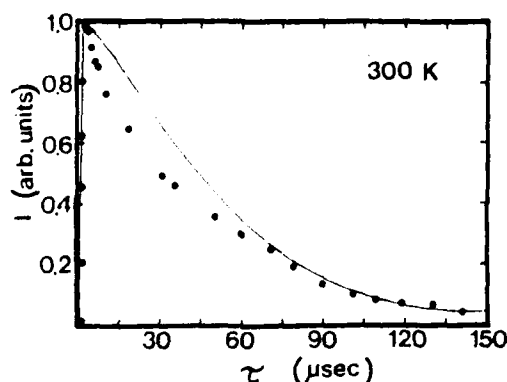

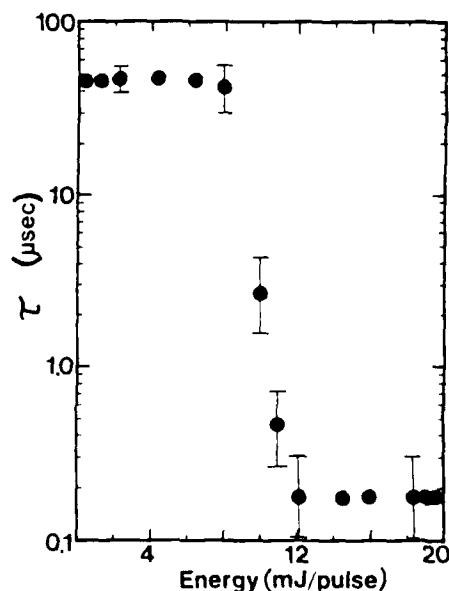FIG. 15. $^5S_2, ^5F_4$ decay kinetics with rate-equation fit.

FIG. 16. Decay time of $^5S_2, ^5F_4$ at room temperature as a function of excitation power showing lifetime shortening.
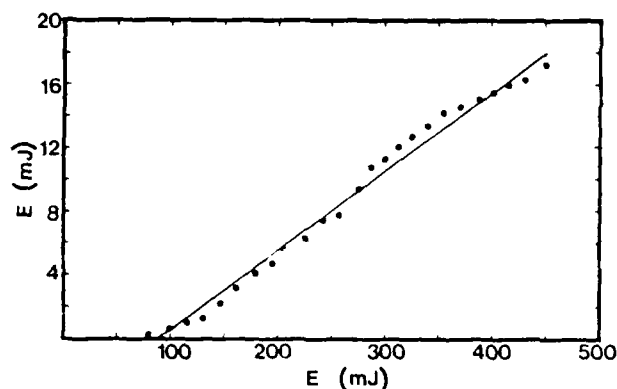
FIG. 17. Conversion efficiency of 2.9-μm laser output, pumping with the 1.047-μm output of a Nd:YLF laser.

best, decrease from a quadratic to a linear dependence on pump power, and the slope could not become any smaller without this additional level.

Figure 17 shows the laser output energy at 2.9 μm as a function of the energy input into the crystal at room temperature. Laser action was achieved by end-pumping the laser rod with a Nd:YLF laser constructed in-house. The pump laser had a wavelength of 1.047 μm and a pulse width of 60 μsec. The YLF laser was operated in the long-pulse regime with no mode-selective elements and a 30% output coupler. Output energies up to 750 mJ are obtainable from the pump laser. The 2.9-μm laser cavity consisted of a flat high reflector (greater than 99% reflecting at 2.9 μm) and a flat output coupler (approximately 90% reflecting at 2.9 μm), separated by 5 cm. An energy-conversion efficiency of 15% is obtained with a slope efficiency of 4.5% and a fractional pump light absorption in the rod of 0.33 times the incident energy on the laser rod. The threshold for 2.9-μm lasing action was found to be 80 mJ of incident pump energy. Antipenko et al.[6] have reported a conversion efficiency of 7.5% using the 1.061-μm emission from a Nd:GSGG (GSGG denotes gadolinium scandium gallium garnet) laser as a pumping source. The increased efficiency obtained here is a result of the larger Yb^{3+} absorption coefficient at 1.047 μm. Similar results were obtained using an 80% reflecting output coupler, suggesting that the threshold and extraction efficiency are dominated by scattering losses in the rod.

The saturation of the $^5I_6$ population mentioned earlier in connection with the rate equations is not evident in these results. This is because the pumping power is not large enough for the second energy-transfer process in Fig. 1 to become dominant over the first energy-transfer process.

VI. DISCUSSION

To interpret the data presented above, a theoretical estimate must be obtained for the magnitude and temperature dependence of D, and relationships between the various energy-transfer parameters must be established. The physical meaning of the stimulated-emission parameter must also be determined.

A theoretical calculation of the magnitude of the

diffusion constant is difficult since the details of the exciton band shape are not known. A rough theoretical estimate for D can be obtained by considering the rate of energy transfer between two Yb^{3+} ions. Assuming that the interaction mechanism between Yb^{3+} ions is dipole-dipole in nature, the energy-transfer rate between two ions separated by a distance R is[28,31]

$$P(R) = 1/\tau(R_0/R)^6 , \tag{18}$$

where R_0 is again the critical interaction distance. For multistep energy migration, the diffusion coefficient can be expressed in terms of the interaction rate between ions as[45]

$$D = \frac{1}{6} \int_0^\infty R^2 P(R) \rho(R) dR , \tag{19}$$

where $\rho(R)$ is the probability of finding an ion at a distance R from the ion at the origin, and for a random distribution is given by[45]

$$\rho(R) = 4\pi N_s R^2 \exp(-4\pi N_s R^3/3) . \tag{20}$$

With these expressions the diffusion constant becomes

$$D = \frac{2}{3}(\pi N_s R_0^6/\tau_s) \int_d^\infty R^{-2} \exp(-4\pi N_s R^3/3) dR . \tag{21}$$

Note that the lower limit of the integral is taken to be the smallest distance between Yb^{3+} ions. Using the value of $d = 2.7$ Å along with the concentration and intrinsic decay rate of Yb^{3+} ions, $N_s = 1.2 \times 10^{22}$ cm^{-3} and $\tau_s^{-1} = 555$ sec^{-1}, the integral in Eq. (21) can be evaluated numerically to give a value of 1.23×10^6, yielding the result

$$D = 1.7 \times 10^{31} R_0^6 . \tag{22}$$

Using the values of D calculated from the Chow-Powell theory, the value of R_0 can be calculated. At 12 K, R_0 equals to 10.3 Å, while at 250 K, R_0 equals 13.8 Å. These values are listed in Table III.

The temperature dependence of D, shown in Fig. 9, can give some qualitative information about the exciton motion in the Yb^{3+} system. Figure 9 shows that D increases with temperature, which implies that the exciton motion is a thermally assisted incoherent process. This can be represented by

$$D(T) = D(0) + B \exp(-\Delta E/k_B T) , \tag{23}$$

where $D(0)$ is the diffusion constant at zero temperature, ΔE is the activation energy of the thermally assisted process, and k_B is Boltzmann's constant. $D(0)$ is the resonant contribution to the diffusion, and B is the parameter describing the nonresonant contribution to the diffusion. The best-fit parameters obtained from a least-squares-fitting procedure are listed in Table III.

As shown previously, the results of the Inokuti-Hirayama analysis of the Ho^{3+}-Yb^{3+} energy transfer and the Chow-Powell analysis of the Yb^{3+}-Ho^{3+} energy transfer are related in terms of transfer and back-transfer processes. The differences in the magnitudes of the energy-transfer rates are associated with the changes in the role of the sensitizer and activator ions, which change the spectral overlap due to the energy shift between absorption and emission transitions. Because most of the

energy-transfer processes take place with the activator ion initially in an excited state, it is not possible to calculate the overlap integral since there is no excited-state absorption information available on this material. For this reason it is not possible to correlate the transfer rates with the spectral data.

The computer models used to explain the two different types of up-conversion also provide values for the energy-transfer rates. In order to correlate the transfer coefficients with the transfer rates obtained from the two energy-transfer theories, it is necessary to multiply the transfer coefficients by the concentration of the initial activator energy level.[17] The appropriate levels for each transfer coefficient are listed .in Table IV. Because the pumping rates used in these experiments do not deplete the ground states to any appreciable extent, the excited-state populations of Ho^{3+} are quite low compared to the ground-state populations. Therefore, in order for the forward- and back-transfer rates to be equal for the resonant transitions, the transfer coefficients must be several orders of magnitude different. In addition, the transfer rates for two different resonant transitions may be equal, but the corresponding transfer coefficients may not be equal. Previous studies[3,11,12,14,37] using similar rate-equation models have assumed that the resonant transfer coefficients are equal, instead of the resonant transfer rates, as done here.

The risetimes of Yb^{3+} emission after pumping the $^5Y_5$ and $^5S_2, ^5F_4$ states of Ho^{3+} are 4 and 15 μsec at 12 K, respectively, in agreement with the difference in the interaction strengths. The risetime of the $^5S_2, ^5F_4$ emission after pumping the $^5F_5$ level of Ho^{3+} is 48 μsec. From these results and Eq. (14) the rate of the second transfer process in Fig. 10 can be calculated to be approximately 2.0×10^4 sec^{-1}. This is in good agreement with our rate-equation results listed in Table IV $(5.0 \times 10^4$ sec$^{-1})$. The nearest-neighbor energy-transfer rates predicted from the Inokuti-Hirayama theory are smaller than the rates predicted from the rate-equation models. This is a result of the neglect of back-transfer. The energy-transfer rate predicted for the Yb^{3+}-Ho^{3+} interaction from the Chow-Powell theory is also smaller than the rate predicted from just the Y_2 term in Eqs. (16). Both energy-transfer models suffer as a result of neglecting the back-transfer of excitation energy, whereas the rate-equation approach properly takes back-transfer into account at the expense of using time-independent transfer rates. Neglecting back-transfer causes the sensitizer-activator strength to be underestimated.

The rate-equation models were used to fit the time dependence of the up-conversion emission. The results are shown as solid and dashed lines in Figs. 11 and 15. The theoretical calculations agree well with the risetime and asymptotic $(t \rightarrow \infty)$ behaviors of the data, but the fits are poor in the the time region just after the maximum population of the level has been reached. The reason for this is that the transfer coefficients used in the rate equations were time independent, and hence the only time dependence in the transfer rate was contained in the concentration of acceptor ions in the specific level involved. The decay kinetics shown in Figs. 5 and 8 can be inter-
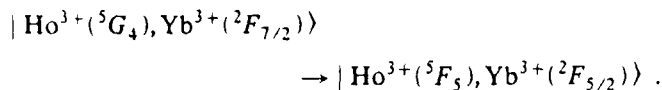
preted accurately by models with time-dependent transfer rates, such as those of Inokuti-Hirayama and Chow-Powell. These time-dependent transfer rates manifest themselves predominantly in the early portions of the decay, where the constant transfer coefficients give a poor fit, leading to nonexponential decays. The parameters obtained from these models should be taken as approximate average values of the real time-dependent values of the energy-transfer rates.

The stimulated-emission parameters used in this model of the infrared up-conversion are related to the threshold for stimulated emission. The spontaneous-emission term in Eq. (16f), $\alpha_2 n_2$, acts as a feeding mechanism for the total number of photons of a particular wavelength in the sample. The other two terms in this equation are competitive in nature. When the gain term $\phi_2 n_2 p_2$ equals the loss term p_2 / τ_2, then threshold has been reached. Substitution of the values from Table IV into Eq. (17) gives a value for n_2 of 2.0×10^{12} cm^{-3}. This implies a threshold of 1.5×10^4 W/cm^3 for direct pumping of this level, and consequently a higher value for the threshold for infrared excitation of Yb^{3+}. For a pure two-photon process without losses, the threshold would be 3.0×10^4 W/cm^3. However, losses in this system are not negligible, as discussed earlier in connection with the saturation behavior and inclusion of a third energy-transfer process. As a result, the actual threshold for stimulated emission in the green after infrared excitation would be still higher. Experimentally the threshold was observed to be 75 MW/cm^3 for infrared excitation. The simplified model used to describe the stimulated emission is largely responsible for the discrepancy in threshold values.[43]

At the high pumping powers used here, the efficiency of the infrared excitation of the green emission is not as high as at lower pump powers. This is reflected in the saturation of the power dependence shown in Fig. 14, and in the population of n_2 obtained from the computer fits. This is a result of the third transfer process becoming more effective at higher pump powers.[4,44] The saturation of the population of the $^5I_6$ level shown in Fig. 14 is also evident in the laser output at 2.9 μm when large pump powers are used.[4] This is a result of the difference in transfer rates obtained from Eqs. (16), $Y_1(n_0)$ and $Y_2(n_1)$. Because the first transfer from Yb^{3+} is nonresonant while the second one is resonant, the population of $^5I_6$ starts to level off at a specific pump power,[4] ≈ 1 kW/cm^3, as a result of the second transfer becoming more efficient at this power level. The saturation of $^5I_6$ has been observed[44] at a pump energy of 0.6 J/cm^3 or 2.7×10^{23} photons/sec for a crystal containing 0.5 at. % Ho^{3+}. This is slightly larger than the value calculated here due to the difference in concentration of Ho^{3+} ions.

Another mechanism for decreasing the 2.9-μm laser output at high pump powers is population of the terminal level of the 2.9-μm emission,[44] $^5I_7$. The $^5I_7$ state is metastable, having a lifetime of 9 msec, so that population of this level decreases the inversion for the 2.9-μm stimulated-emission transition. There are two effective mechanisms for populating the $^5I_7$ level after 1.0-μm pumping. The first, which is the dominant process at low pump powers, is nonradiative decay from $^5I_6$ to $^5I_7$. The

second process, which only becomes effective at high pump powers, is a result of two cross-relaxation processes after the third transfer from Yb^{3+} to Ho^{3+}. The third transfer populates $^3H_6$ and then nonradiative decay to $^5G_4$ occurs.[44] The first cross-relaxation is

$$| Ho^{3+}(^5G_4), Yb^{3+}(^2F_{7/2}) \rangle$$

$$\rightarrow | Ho^{3+}(^5F_5), Yb^{3+}(^2F_{5/2}) \rangle .$$

The second cross-relaxation is

$$| Ho^{3+}(^5F_5), Yb^{3+}(^2F_{7/2}) \rangle$$

$$\rightarrow | Ho^{3+}(^5I_7), Yb^{3+}(^2F_{5/2}) \rangle .$$
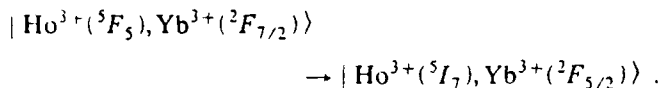
Both are resonant processes. The second cross-relaxation is exactly the first step in the up-conversion of 640-nm radiation into 551.5-nm radiation, Fig. 10. This is the connection between the two up-conversion models. This process is only effective in populating $^5I_7$ at high pump powers, because the third transfer from Yb^{3+} to Ho^{3+} is only effective at high pump powers. A result of the increase in population of the $^5I_7$ level is an increase in the output at 2.0 μm. This mechanism should become effective in populating $^5I_7$ at the pump powers at which it becomes necessary to include the third transfer from Yb^{3+} to Ho^{3+}.

VII. CONCLUSIONS

The characteristics of the interaction between the rare-earth ions in $BaYb_2F_8:Ho^{3+}$ crystals in several energy levels has been calculated and it has been shown that the interaction is electric-dipole–dipole. The coupling between Ho^{3+} and Yb^{3+} ions is greater for the $^5F_5$ state of Ho^{3+} than it is for the $^5S_2, ^5F_4$ states. The multistep migration of energy among Yb^{3+} ions is much stronger than the Yb^{3+}-Ho^{3+} interaction, having a mean free path of 85 Å at 250 K. This justifies the treatment of the Yb^{3+} ions as always being able to transfer their energy to nearest-neighbor Ho^{3+} ions since energy migrates from one Yb^{3+} to another until a Ho^{3+} ion is close enough for the transfer from Yb^{3+} to Ho^{3+} to take place.

Multiple energy-transfer processes were shown to lead to up-conversion, switching of lasing channels, and saturation. An important conclusion is that a model with just two transfers from Yb^{3+} to Ho^{3+} is insufficient to explain the observed data.[4,44] Energy transfer from Yb^{3+} to Ho^{3+} in the $^5S_2, ^5F_4$ states resulting in excitation of the Ho^{3+} ion to the $^3H_6$ state must be included for the high pumping powers used here. Therefore, as the pump power is increased the efficiency of the short-wavelength stimulated emission, 0.55 μm, increases, while the efficiency of the longer-wavelength stimulated emission, 2.9 μm, decreases. At still larger pump powers the third energy transfer causes the 0.55μm stimulated emission to be less efficient.

The laser-performance results for the 2.9-μm laser action have shown that the efficiency of the laser action can be significantly increased by pumping into a Yb^{3+} spectral region with a larger absorption coefficient. Since the Yb^{3+} absorption peaks at approximately 960 nm at room temperature, diode pumping should be an effective method of achieving improved efficiency in the 2.9-μm laser action. However, as we have shown in connection with the rate-equation analysis, the efficiency of this laser channel is limited by saturation effects, and therefore the very large difference in the absorption coefficient at 960 nm as opposed to 1047 nm (greater than an order of magnitude) may not be reflected in the increased efficiency of the 2.9-μm laser action.

[1] L. F. Johnson and H. J. Guggenheim, Appl. Phys. Lett. 19, 44 (1971).

[2] S. A. Pollack, D. B. Chang, and N. L. Moise, J. Appl. Phys. 60, 4077 (1986).

[3] L. F. Johnson, H. J. Guggenheim, T. C. Rich, and F. W. Ostermayer, J. Appl. Phys. 43, 1125 (1972).

[4] B. M. Antipenko, I. V. Vorykhalov, B. V. Sinitsyn, and T. V. Uvarova, Kvantovaya Elektron. (Moscow) 7, 197 (1980) [Sov. J. Quantum Electron. 10, 114 (1980)].

[5] P. Lacovara, G. D. Gilliland, and L. Esterowitz, Proc. SPIE (to be published).

[6] B. M. Antipenko, B. V. Sinitsyn, and T. V. Uvarova, Kvantovaya Elektron. (Moscow) 7, 2019 (1980) [Sov. J. Quantum Electron. 10, 116B (1980)].

[7] F. Auzel, Phys. Rev. B 13, 2809 (1976).

[8] F. Auzel, Proc. IEEE 61, 758 (1973).

[9] R. A. Hewes and J. F. Sarver, Phys. Rev. 182, 427 (1969).

[10] R. A. Hewes, J. Lumin. 1,2, 778 (1970).

[11] F. W. Ostermayer, Jr. and L. G. Van Uitert, Phys. Rev. B 1, 4208 (1970).

[12] F. W. Ostermayer, Jr., J. P. van der Ziel, H. M. Marcos, L. G. Van Uitert, and J. E. Geusic, Phys. Rev. B 3, 2698 (1972).

[13] L. F. Johnson, J. E. Geusic, H. J. Guggenheim, T. Kushida, S. Singh, and L. G. Van Uitert, Appl. Phys. Lett. 15, 48 (1969).

[14] R. K. Watts, J. Chem. Phys. 53, 3552 (1970).

[15] D. C. Yeh, W. A. Sibley, M. Suscavage, and M. G. Drexhage, J. Appl. Phys. 62, 266 (1987).

[16] T. C. Rich and D. A. Pinnow, J. Appl. Phys. 43, 2357 (1972).

[17] J. C. Wright, Top. Appl. Phys. 15, 239 (1976).

[18] J. D. Kingsley, J. Appl. Phys. 41, 175 (1970).

[19] L. F. Johnson and H. J. Guggenheim, Appl. Phys. Lett. 23, 96 (1973).

[20] B. R. Judd, Phys. Rev. 127, 750 (1962).

[21] G. S. Ofelt, J. Chem. Phys. 37, 511 (1962).

[22] M. J. Weber, B. H. Matsinger, V. L. Donlan, and G. T. Surratt, J. Chem. Phys. 57, 562 (1972).

[23]A. A. Kaminskii, B. P. Sobolev, and T. V. Uvarova, Phys. Status Solidi A **78**, K13 (1983).

[24]L. F. Johnson and H. J. Guggenheim, IEEE J. Quantum Electron. **QE-10**, 442 (1974).

[25]O. E. Izotova and V. B. Aleksandrov, Dokl. Akad. Nauk SSSR **192**, 1037 (1970) [Sov. Phys.—Dokl. **15**, 525 (1970)].

[26]*Landolt-Börnstein, New Series, Crystal Structure Data of Inorganic Compounds, Key Elements: F, Cl, Br, I* (Springer-Verlag, New York, 1973), Vol. III/7a, p. 170.

[27]W. T Carnall, P. R. Fields, and K. Rajank, J. Chem. Phys. **49**, 4424 (1968).

[28]M. Inokuti and F. Hirayama, J. Chem. Phys. **43**, 1978 (1965).

[29]H. C. Chow and R. C. Powell, Phys. Rev. B **21**, 3785 (1980).

[30]D. L. Dexter, J. Chem. Phys. **21**, 836 (1953).

[31]T. Forster, Ann. Phys. (Leipzig) **2**, 55 (1948); Z. Naturforsch. **4a**, 321 (1949); Discuss. Faraday Soc. **27**, 7 (1959).

[32]M. Yokota and O. Tanimoto, J. Phys. Soc. Jpn. **22**, 779 (1967).

[33]C. M. Lawson, E. E. Freed, and R. C. Powell, J. Chem. Phys. **76**, 4171 (1982).

[34]R. K. Watts and H. J. Richter, Phys. Rev. B **6**, 1584 (1972).

[35]M. J. Weber, Phys. Rev. B **4**, 2932 (1971).

[36]B. M. Antipenko, Opt. Spektrosk. **56**, 72 (1984) [Opt. Spectrosc. (USSR) **56**, 44 (1984)].

[37]R. K. Watts and W. C. Holton, Solid State Commun. **9**, 137 (1971).

[38]H. J. Guggenheim and L. F. Johnson, Appl. Phys. Lett. **15**, 51 (1969).

[39]G. F. De Sa, P. A. Santa Cruz, and F. Auzel, J. Lumin. **31,32**, 693 (1984).

[40]R. C. Powell and G. Blasse, in *Structure and Bonding,* edited by J. D. Dunitz, J. B. Goodenough, P. Hemmerich, J. A. Ibers, C. K. Jorgensen, J. B. Neilands, D. Reinen, and R. J. P. Williams (Springer, Berlin, 1980), Vol. 42, p. 43; M. D. Shinn and W. A. Sibley, Phys. Rev. B **29**, 3834 (1984).

[41]B. M. Antipenko, S. P. Voronin, Sh. N. Gifeisman, R. V. Dubravyanu, Yu. E. Perlin, T. A. Privalova, and O. B. Raba, Opt. Spectrosk. **58**, 1270 (1985) [Opt. Spectrosc. (USSR) **58**, 780 (1985)].

[42]G. M. Loiacono, M. F. Shone, G. Mizell, R. C. Powell, G. J. Quarles, and B. Elouadi, Appl. Phys. Lett. **48**, 622 (1986).

[43]M. L. Kliewer, A. B. Suchocki, and R. C. Powell (unpublished).

[44]B. M. Antipenko, Pis'ma Zh. Tekh. Fiz. **6**, 968 (1980) [Sov. Tech. Phys. Lett. **6**, 417 (1980)].

[45]S. Chandrasekhar, Rev. Mod. Phys. **15**, 1 (1943).

Excited State Absorption of Pump Radiation as a Loss Mechanism in Solid-State Lasers

MICHAEL L. KLIEWER AND RICHARD C. POWELL

Abstract—The characteristics of optical pumping dynamics occurring in laser-pumped rare earth-doped, solid-state laser materials were investigated by using a tunable alexandrite laser to pump $Y_3Al_5O_{12}:Nd^{3+}$ in an optical cavity. It was found that the slope efficiency of the Nd laser operation depends strongly on the wavelength of the pump laser. For pump wavelengths resulting in low slope efficiencies, intense fluorescence emission is observed from the sample in the blue-green spectral region. This is attributed to the excited state absorption of pump photons which occurs during radiationless relaxation from the pump band to the metastable state. This type of process will be an important loss mechanism for monochromatic pumping of laser systems at specific pump wavelengths.

I. INTRODUCTION

SELECTIVELY pumping rare earth-doped solid-state lasers in pump bands only slightly higher in energy than the lasing metastable state is desirable because there is less pump energy converted to heat than there is in broad-band pumping throughout the spectral region much higher in energy. The small quantum defect associated with this type of low-energy monochromatic pumping can increase the efficiency of laser operation and decrease problems arising from thermal lensing. The development of diode lasers as pump sources has led to the construction of compact, solid-state laser systems [1]-[6]. However, the powers and wavelengths presently available from diode laser pump sources are limited. Pumping with a tunable alexandrite laser can be useful in simulating diode laser pumping and extending potential laser pumping to higher power and different wavelength regions. In addition, for some high-power laser applications, an alexandrite laser may be an ideal pump source for a rare earth-doped solid-state laser.

The results of an investigation of the spectral dynamics of a $Y_3Al_5O_{12}:Nd^{3+}$ (Nd-YAG) laser pumped by an alexandrite laser are presented here. These results show important differences between broad-band frequency pumping and monochromatic pumping, demonstrate the importance of completely characterizing the pumping dynamics of laser systems, and show the effects of excited state absorption (ESA) of pump photons from levels above the lasing transition on the slope efficiency of the laser operation.

II. ALEXANDRITE LASER PUMPING OF Nd-YAG

An alexandrite laser with an output tunable between 725 and 790 nm was used to pump an Nd-YAG crystal. The pulse width of the alexandrite was about 60 μs FWHM and the maximum power obtainable was 20 W at a reception rate of 20 Hz. The spectral width of the laser is approximately 1 nm FWHM.

The crystal was mounted in a cavity consisting of a 100 percent reflector with a 50 cm radius of curvature and a flat 85 percent output coupler. Transverse pumping was employed with cylindrical and convex lenses used to focus the pump laser beam in a line along the length of the Nd-YAG sample. In this way, an efficient pumping configuration was achieved. The power incident on the Nd-YAG crystal and the power output from the Nd-YAG laser were measured simultaneously with two calibrated power meters. The Fresnel reflections and absorption of the material were considered when calculating the power absorbed by the crystal. The fluorescence emission from the sample was sent through a 1/4 m monochromator, detected with an RCA C31034 photomultiplier tube, analyzed by a boxcar integrator, and recorded on a chart recorder. The experimental setup shown in Fig. 1 made it possible to measure the fluorescence emission both while the sample was lasing at 1.06 μm and in the absence of lasing. The sample was 0.28 cm long and contained approximately 1×10^{20} Nd^{3+} ions/cm³.

Fig. 2 shows the energy levels of Nd^{3+} and the relevant electronic transitions when pumping with 737 nm. Fig. 3 shows the absorption spectrum of Nd^{3+} in YAG in the tuning region of the alexandrite laser. The structure is due to the transitions to various Stark components of the $^4S_{3/2}$ + $^4F_{7/2}$ levels. The alexandrite laser output is tuned over the absorption transitions shown in Fig. 2, after which radiationless relaxation occurs to the $^4F_{3/2}$ metastable state. Fluorescence occurs from the $^4F_{3/2}$ level to the levels belonging to the ^4I term and, above threshold, lasing occurs in the $^4F_{3/2} \rightarrow {}^4I_{11/2}$ transition.

Figs. 4 and 5 show the room temperature fluorescence spectra between 300 and 900 nm of Nd-YAG pumped by an alexandrite laser at 734.0 and 748.6 nm, respectively. In recording these spectra, a filter was used to eliminate scattered laser light, and this also eliminates from the recorded spectra some of the emission transitions occurring between 600 and 770 nm. A neutral density filter rated at 4.0 O.D. was used when recording the fluorescence emis-

Fig. 1. Experimental setup used for measuring slope efficiencies and fluorescence. The abbreviations are beam splitter (BS), cylindrical lens (CL), and convex lens (L).

Fig. 2. Energy level diagram of Nd^{3+} in YAG.

Fig. 3. Absorption spectrum of Nd-YAG in the spectral region of alexandrite laser pumping. The vertical lines give the spectral position of the pump wavelength needed for absorption from the $^4F_{3/2} + ^2H_{9/2}$ level to the P energy level.

Fig. 4. Fluorescence of Nd-YAG when pumped with the 734 nm emission of an alexandrite laser. Cutoff and neutral density filters were used.

Fig. 5. Fluorescence of Nd-YAG when pumped with the 748 nm emission of an alexandrite laser. Cutoff and neutral density filters were used.
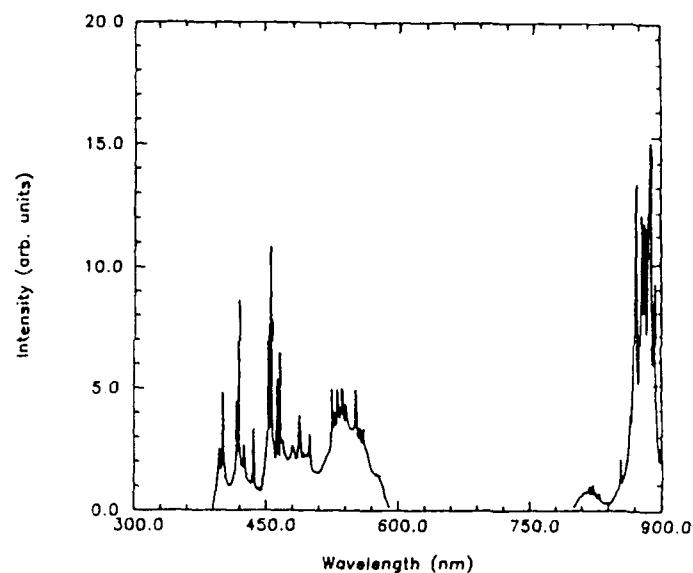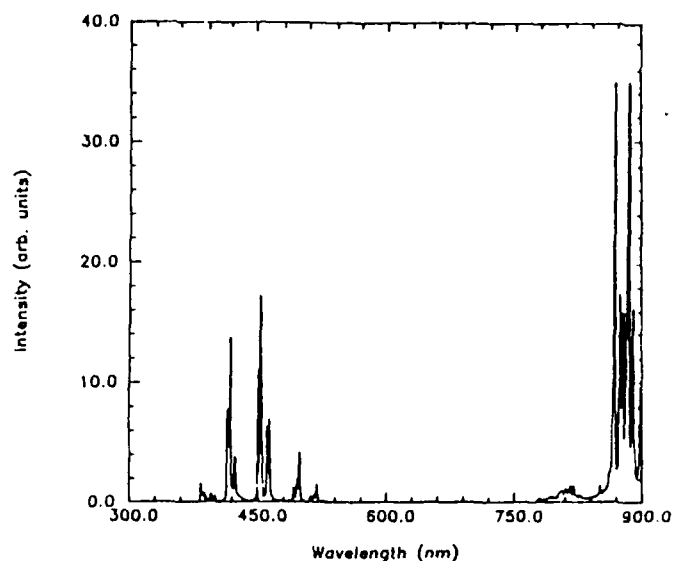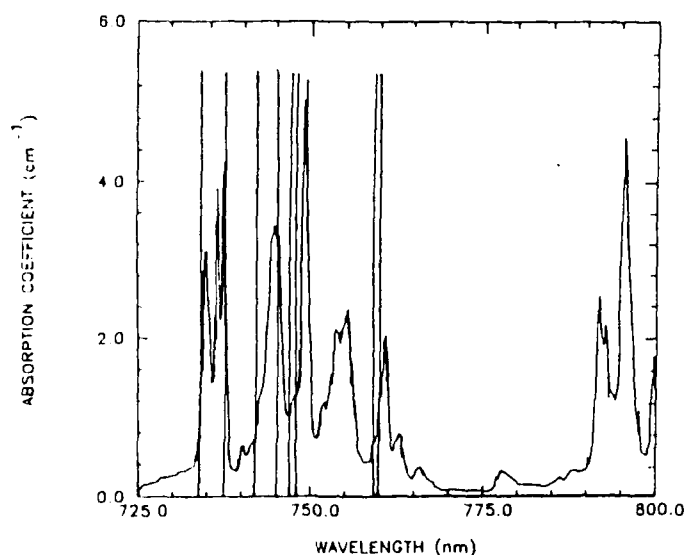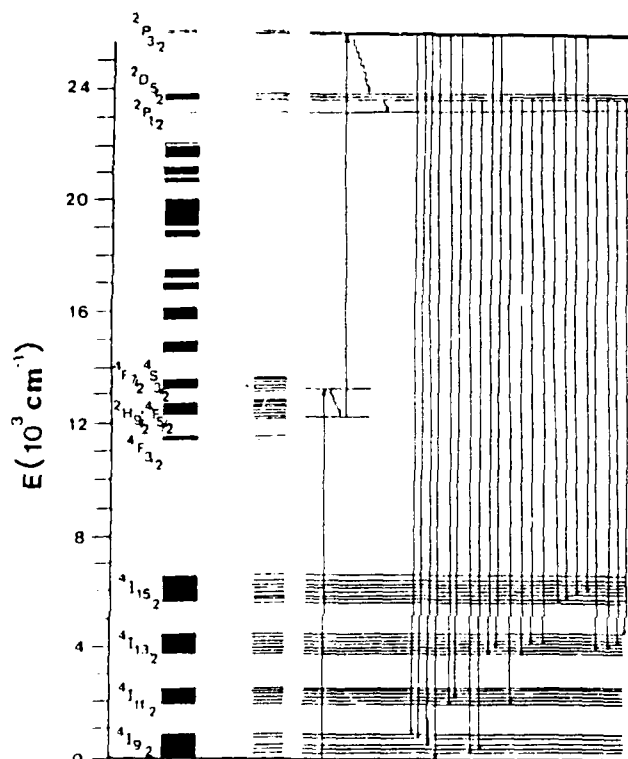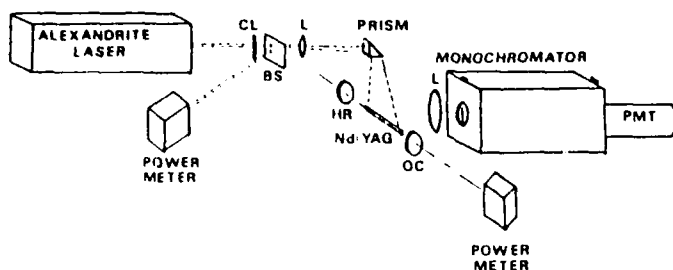
sion in the spectral region from 770 to 900 nm. Along with the normal fluorescence from the $^4F_{3/2}$ level in the near-infrared spectral region, strong emission lines appear at higher energies between about 380 and 600 nm. These transitions must be associated with multiphoton absorption processes. The specific transitions that appear in this spectral region and their relative intensities depend on the wavelength and the power of the pump pulse. Transitions between levels having energy differences matching the observed spectral lines of Fig. 4 are shown in Fig. 2. It appears that these transitions originate from the $^2P_{3/2}$, $^2D_{5/2}$, and $^2P_{1/2}$ levels and terminate on the various multiplets of the ground term. The spectrum shown in Fig. 5 is also a result of a multiphoton excitation process and the fluorescence in the green is a result of transitions originating from the $^4G_{7/2}$ level and terminating on various components of the ground term.

In order to excite the higher lying fluorescence levels producing the emission shown in Fig. 4, it is necessary for two pump photons to be absorbed. For energy to be conserved, the energy of the transition from the ground state to the final level must match the sum of the energies of the two photons minus any energy lost through radiationless decay processes. By studying the energy level diagram in Fig. 2, it is clear that the only path for the required two-photon excitation process under these pumping conditions is for the first photon to be absorbed by a transition to one of the Stark components of the $^4F_{7/2} + {}^4S_{5/2}$ levels followed by radiationless relaxation to the levels of the $^2H_{9/2} + {}^4F_{5/2}$ manifold. The second photon is absorbed before the ion can continue relaxing down to the $^4F_{3/2}$ metastable state. Depending on the exact energy of the pump photons, there is a good energy match to transitions terminating on the two Stark components of the $^2P_{3/2}$ level. In this level, there is a branching ratio for fluorescing and radiationless relaxation to the lower $^2D_{5/2}$ and $^2P_{1/2}$ levels from which some fluorescence also occurs.

Excitation spectra of the emission in the 420 nm spectral region was taken in an attempt to verify the above interpretation and the results are shown in Fig. 6. The peaks in the 420 nm excitation spectrum are different from the absorption peaks in Fig. 3 and correspond spectrally to the energy differences between the different Stark components of the $^4F_{5/2} + {}^2H_{9/2}$ manifold and the Stark levels of the $^2P_{3/2}$ multiplet. The excitation spectrum of the 870 nm emission was also measured and found to contain the same features as the absorption spectra shown in Fig. 3.

III. EFFECT OF PUMP PHOTON ESA ON SLOPE EFFICIENCIES

Fig. 7 shows the results of measuring lasing thresholds and slope efficiencies for Nd-YAG pumped at different wavelengths by an alexandrite laser. It should be noted that no attempt was made to optimize the sample or cavity parameters to obtain the best possible operational characteristics of an Nd-YAG laser. The purpose of this work is to demonstrate how these characteristics vary as a function of pump wavelength. The results show only small changes in the lasing threshold as a function of pump wavelength, whereas the slope efficiency varies significantly as the pump laser is tuned across the absorption band of Nd-YAG shown in Fig. 3.

The vertical lines in Fig. 3 identify the spectral positions of the pump wavelengths resulting in excited state absorption from the $^4F_{5/2} + {}^2H_{9/2}$ levels to the $^2P_{1/2}$ energy levels. For 753.6 nm excitation, no ESA of pump photons occurs and a slope efficiency of 10 percent is obtained, while for 737.0 nm excitation, ESA of pump photons reduces the slope efficiency to only 6 percent. For the pumping conditions resulting in high values of the slope efficiency, there is no change in the slope of the measured power output versus power absorbed curve over
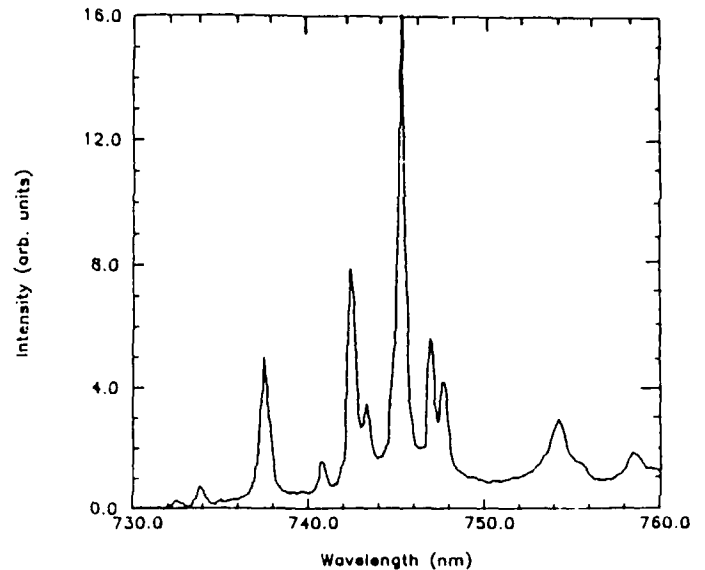
Fig. 6. 420 nm excitation of Nd-YAG when pumped with the emission of a tunable alexandrite laser.
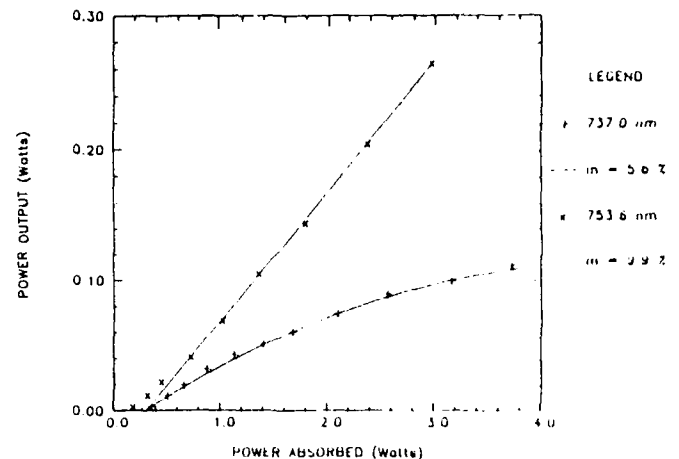
Fig. 7. Power threshold and slope efficiency for Nd-YAG pumped by an alexandrite laser. The dotted line is the fit to the slope efficiency curve at 737 nm pumping.

the entire range of pumping powers. However, for the pumping conditions resulting in low values of the slope efficiency, the slope of the curve of measured power output versus power absorbed decreases at high pump powers. This is associated with the pump power dependence of the ESA loss mechanism.

The slope efficiency η_s is defined as [9], [10]

$$\eta_s = \frac{\lambda_p}{\lambda_o} \cdot \frac{C_o}{C + L} \cdot \eta_p \tag{1}$$

where λ_p and λ_o are the pump and output wavelengths, C_o is the output coupler transmission, L is the sample loss per pass, and C is the total transmission of the cavity mirrors. η_p is the pumping efficiency and is defined as the number of ions excited to the origin of the lasing transition produced per photon absorbed.

The ESA of pump photons found to occur in levels above the upper level of the lasing transition can be taken into account by redefining the pumping efficiency as

$$\eta_p = \eta_p''(1 - \eta_{ESA}). \tag{2}$$

Equation (2) is valid when the excited state absorption cross section is much greater than the ground state absorption cross section and the rate of nonradiative relaxation downward is much greater than the rate upward due to excited state absorption. The slope efficiency can be expanded as

$$\eta_s = \eta_s''(1 - \eta_{ESA}) \tag{3}$$

where η_s'' is given in (1) with η_p replaced by η_p'' and η_{ESA} is the excited state absorption efficiency defined as

$$\eta_{ESA} = N_t \sigma_{ESA} d. \tag{4}$$

N_t and σ_{ESA} are the excited state density and excited state absorption cross section, respectively, of the levels above the upper level of the lasing transition from which the ESA processes occur. d is the depth of absorption of the pump light in the sample.

The effects ESA of pump photons present at various pump wavelengths can be described by (3). For 753.6 nm excitation, there is no blue emission detected and the maximum slope efficiency is obtained. Thus, it is assumed that there is no ESA of pump photons from levels above the upper level of the lasing transition and the value of 10 percent obtained for the slope efficiency under these pumping conditions is taken as the maximum value for η_s''. η_p'' is assumed to be one in the absence of ESA of pump photons, but will vary with pump wavelength. The ESA efficiency and the excited state absorption cross section can be determined by fitting (3) to the slope efficiency curves shown in Fig. 7. An example of this type of fitting is shown as a solid line in the figure for 737.0 nm pumping. In thermal equilibrium, a Boltzmann distribution predicts that about 2.5 percent of the population of the excited state will be in the specific Stark component of the $^4H_{9/2}$, $^4F_{3/2}$ levels from which ESA occurs. Fitting (3) to the results obtained for 737.0 nm excitation yields a value for η_{ESA} of 0.108 at the pumping threshold. η_{ESA} increases linearly with the power absorbed by the material because of N_t's linear dependency on power absorbed. Using the value for η_{ESA} with (4) gives an excited state absorption cross section of 4.6×10^{-19} cm^2. This is consistent with results found from two-photon absorption studies of Nd^{3+} ions in solids [11]. The reason for this relatively large value is probably due to strong admixture of the d wavefunctions in the high lying $^2P_{3/2}$ level.

IV. DISCUSSION AND CONCLUSIONS

The results discussed above show that alexandrite laser pumped Nd–YAG lasers can have a pump wavelength-dependent loss mechanism associated with the excited state absorption of pump photons. This loss mechanism is

negligible for some pump wavelengths, while for other wavelengths, this loss mechanism dominates the pumping dynamics to the extent that the slope efficiency is greatly decreased. This is the first observation of a loss mechanism in lasers due to excited state absorption of pump photons taking place during relaxation from the pump band to the metastable state. This will not be as significant a loss mechanism for broad-band pumping because the pump photons are spread over a wide range of the energies. However, for monochromatic pumping by laser sources with all the pump photons having the same energy, this can be the dominant loss mechanism. Since multiphoton absorption is power-dependent process, this loss mechanism will be most important for high-power pumping situations. However, even for low-power diode laser pumping, the loss via this mechanism may not be negligible.

Other types of excited state absorption processes are well known as loss mechanisms in laser systems. These include up-conversion energy transfer through ion-ion interactions [8] and the excited state absorption of photons that are part of the laser emission [10]. It is not surprising that excited state absorption of pump photons can become important under the conditions of high-power laser pumping. However, it is surprising that the second step in the two-photon absorption process occurs before the ion has completely relaxed to the lowest lying metastable state. This allows many different transitions to take place in the excited state absorption process, and therefore enhances the effect of this loss mechanism. The effectiveness of this loss mechanism depends on the relative rate of the nonradiative relaxation of the ions in the initial state of the transition compared to the rate of excited state absorption. The exponential energy gap law [12] predicts a multiphonon decay rate for the $^4F_{5/2}$ term on the order of 10^6 s^{-1}, whereas the ESA pump rate at threshold

$$(W_{ESA})_{th} = \sigma_{ESA}\left(\frac{I}{\hbar\omega}\right) \tag{5}$$

is on the order of 10^5 s^{-1}.

It should also be pointed out that we have observed this new type of loss mechanism when pumping into the $^4F_{5/2}$ energy levels [13], in a large number of Nd-doped laser materials and in laser materials based on other rare earth ions such as Er^{3+}. Thus, it appears that this is a general loss mechanism that may be in all laser-pumped solid-state laser systems based on rare earths ions.

REFERENCES

[1] B. Zhou, T. J. Kane, G. J. Dixon, and R. L. Byer, "Efficient, frequency-stable laser-diode pumped Nd:YAG laser," Opt. Lett., vol. 10, pp. 62–64, 1985.

[2] F. Hanson and D. Haddock, "Laser diode side pumping of neodymium laser rods," Appl. Opt., vol. 27, pp. 80–83, 1988.

[3] R. L. Byer, "Diode laser-pumped solid-state lasers," Science, vol. 239, pp. 742–747, 1988.

[4] T. Y. Fan and R. L. Byer, "Diode laser-pumped solid-state lasers," IEEE J. Quantum Electron., vol. 24, pp. 895–912, 1988.

[5] G. T. Maker, S. J. Keen, and A. I. Ferguson, "Mode-locked and Q-

switched operation of a diode laser pumped Nd : YAG laser operating at 1.064 μm," *Appl. Phys. Lett.*, vol. 53, pp. 1675-1677, 1988.

[6] J. Berger, D. F. Welch, D. R. Scifres, W. Streifer, and P. S. Cross, "High power, high efficient neodymium : yttrium aluminum garnet laser end pumped by a laser diode array," *Appl. Phys. Lett.*, vol. 51, pp. 1212-1214, 1987.

[7] W. Koechner, *Solid-State Laser Engineering.* New York: Springer-Verlag, 1976, p. 87.

[8] G. D. Gilliland, R. C. Powell, and L. Esterowitz, "Spectral and up-conversion dynamics and their relationship to the laser properties of BaYb₂F₈: Ho³⁺," *Phys. Rev. B*, vol. 38, pp. 9958-9970, 1988.

[9] M. L. Shand and S. T. Lai, "CW laser pumped emerald laser," *IEEE J. Quantum Electron.*, vol. 20, pp. 105-108, 1984.

[10] J. A. Caird, S. A. Payne, P. R. Staver, A. J. Ramponi, L. L. Chase, and W. F. Krupke, "Quantum electronic properties of the Na₃Ga₂Li₃F₁₂: Cr³⁺ laser," *IEEE J. Quantum Electron.*, vol. 24, pp. 1070-1099, 1988.

[11] G. J. Quarles, G. E. Venikouas, and R. C. Powell, "Sequential two-photon excitation processes of Nd³⁺ ions in solids," *Phys. Rev. B*, vol. 31, pp. 6935-6940, 1985.

[12] L. A. Riseberg and M. J. Weber, "Relaxation phenomena in rare-earth luminescence," *Progr. Opt.*, vol. 14, pp. 89-159, 1977.

[13] M. L. Kliewer and R. C. Powell, to be published.

Michael L. Kliewer, photograph and biography not available at the time of publication.

Richard C. Powell, photograph and biography not available at the time of publication.

Preparation, structure, and spectroscopic properties
of Nd^{3+}:$\{La_{1-x}Lu_x\}_3[Lu_{1-y}Ga_y]_2Ga_3O_{12}$ crystals

Toomas H. Allik and Susan A. Stewart

Science Applications International Corporation, 1710 Goodridge Drive, P.O. Box 1303, McLean, Virginia 22102

Dhiraj K. Sardar,* Gregory J. Quarles, and Richard C. Powell

Department of Physics, Oklahoma State University, Stillwater, Oklahoma 74078-0444

Clyde A. Morrison and Gregory A. Turner

Harry Diamond Laboratories, U.S. Army Laboratory Command (LABCOM), Adelphi, Maryland 20783-1197

Milan R. Kokta

Union Carbide Corporation, 750 South 32nd Street, P.O. Box 6381, Washougal, Washington 98671

Wayne W. Hovis and Albert A. Pinto

*Center for Night Vision & Electro-Optics, U.S. Army Electronics Research and Development Command (ERDCOM),
Fort Belvoir, Virginia 22060-5567*

(Received 30 November 1987; revised manuscript received 29 January 1988)

Single crystals of lanthanum lutetium gallium garnet (LaLuGaG) were grown by the Czochralski pulling technique. X-ray diffraction and elemental analysis performed on these samples indicate that these garnets do not form with simple stoichiometry described as $\{La\}_3[Lu]_2Ga_3O_{12}$ but with increased Lu concentration in the dodecahedral site and Ga occupancy in the octahedral site. Optical absorption and fluorescence spectra confirm these results, showing inhomogeneous broadening of the spectral lines of Nd^{3+}. Various laser gain measurements were performed on $\{La_{1-x}Lu_x\}_3[Lu_{1-y}Ga_y]_2Ga_3O_{12}$ crystals containing 4.3 and 1.3 at. % Nd^{3+} to determine the usefulness of this material as a laser. No optical gain was observed. Time-resolved, site-selection spectroscopy measurements were performed to determine the effects of ion-ion interaction, and show the presence of very weak energy transfer between ions in nonequivalent crystal-field sites. Two-photon excitation spectroscopy measurements demonstrate the presence of very strong two-photon–absorption transitions, which prevents lasing in this garnet.

I. INTRODUCTION

Although Nd-doped $Y_3Al_2(AlO_4)_3$ (YAG) has become a standard laser material, there is still significant interest in characterizing the properties of other types of Nd-doped materials that can be pumped with $Ga_{2-x}Al_xAs$ laser diodes emitting radiation at 800±20 nm. The spectral emission of laser diodes at 800 nm is resonant with the $^4F_{5/2}$ and $^2H_{9/2}$ Nd^{3+} absorption bands. The advantage derived from the spectral match leads to a reduction of the amount of heat which is deposited in the medium, thus reducing the thermomechanical requirements of the laser host. With the commercial availability of single laser diodes with powers exceeding 1 W and two-dimensional arrays producing 4.0 kW/cm², it is useful to determine if other materials can be found with spectral and thermo-optic properties leading to improved laser characteristics. Desirable properties of new laser-diode-pumped solid-state lasers include a longer fluorescence lifetime, a broader absorption band, and a higher absorption coefficient as compared to Nd:YAG. We report here the results of x-ray diffraction, elemental and spectroscopic analysis, and gain measurements obtained on Nd^{3+}-doped $\{La_{1-x}Lu_x\}_3[Lu_{1-y}Ga_y]_2Ga_3O_{12}$ (LaLu-

GaG) crystals.

$Y_3Al_2(AlO_4)_3$ is not the ideal garnet structure for doping with Nd^{3+} ions. The ionic radius of Nd^{3+} is too large to give polyhedra sides that match the sides of Al^{3+} polyhedra. This mismatch imposes difficulties in forming a solid solution of $Nd_3Al_2(AlO_4)_3$ with $Y_3Al_2(AlO_4)_3$ that would limit the amount of Nd^{3+} that can be incorporated into the YAG lattice to only a few atomic percent. In addition, the distances between cation lattice positions for the aluminum garnets are small enough to allow for strong enough ion-ion interaction to produce concentration quenching of the Nd^{3+} fluorescence.[1] On the other hand, neodymium may be substituted completely into gallium-based garnet systems. The largest lattice parameters in the gallium garnet group may be realized in garnets formed with lanthanum occupying the dodecahedral positions. For such garnets to be synthesized, the structure must be expanded by substitution of ions larger than gallium into the dodecahedral sites. When such substitutions were made, it was found[2] that compounds do not form with simple stoichiometry described as $\{La\}_3[Lu]_2Ga_3O_{12}$, but that the octahedral and tetrahedral substituents are distributed between two crystallographic sites, with the distribution corresponding to

the formula $\{La_{1-x}Lu_x\}_3[Lu_{1-y}Ga_y]_2Ga_3O_{12}$.

The study of mixed garnet crystals began in the late 1960s. Mixed garnets are those in which additional additives have been introduced into the $\{A\}_3[B]_2(C)_3O_{12}$ garnet crystal, causing multiple ions to occupy crystallographic sites. Numerous laboratories have studied the optical spectroscopy of mixed garnets, in particular Lu-compensated $Nd:Y_3Al_2(AlO_4)_3$. Holton *et al.*[3] showed inhomogeneous broadening of the spectral lines of Nd^{3+}, attributed to a distribution of Nd ions among sites with different crystalline fields. The resulting broadening is attributed to Nd ions residing in Lu-rich and Y-rich sites with slightly different crystal fields. Voron'ko and Sobol',[4] in a more comprehensive study of this mixed garnet system, investigated the dependence of the width and intensity of the spectral lines with respect to varying concentrations of Y and Lu in the dodecahedral sites. A slight broadening, by 2–10 times, was seen in these garnets, with no change of the intensities.

Doped with Nd, these mixed garnets are intermediate-gain laser materials, exhibiting gain higher than Nd:glass but lower than Nd:YAG. These materials would exhibit higher energy storage and lower amplified spontaneous emission at high pump powers.[5]

II. EXPERIMENTAL RESULTS

A. Crystal growth

The lanthanum lutetium gallium garnets of the above composition were grown by the standard Czochralski pulling technique. The raw materials were dried at 200 °C, and La_2O_3 and Lu_2O_3 were fired at 1100 °C for 12 h so that they would be free of absorbed water and carbon dioxide. The oxide was then mixed in the desired ratio, pressed in an isostatic press, and loaded into a 5×5 cm iridium crucible. rf power at a 9.8-kHz frequency was coupled via copper coil to the crucible, heating the crucible and melting the charge. The crucible was insulated with a stabilized zirconia sleeve, and the entire assembly (coil, insulation, and crucible) was enclosed in a water-cooled bell jar equipped with nitrogen and oxygen supply lines, providing a growth atmosphere of N_2 with 1 vol. % of O_2. The pulling rates employed were 1 mm/h. The fluid flow in the melt was aided by rotating of the crystal at the rate of 15 rpm. The crystal diameter was controlled at a programmed rate by regulating the weight of the growing crystal. The crystal grown in the [111] direction displayed typical garnet morphology, that is, faceting and core formation due to growth with a convex interface. The crystals were 1 in. in diameter and between 2 and 4 in. long. Numerous growth runs of these LaLuGaG crystals were performed with either or both Cr^{3+} and Nd^{3+}. The samples studied were two Nd-doped boules with 3.3 and 1.0 at. % added to the melt and one sample with 0.4 at. % Cr^{3+}. Spectroscopic samples of high optical quality were cut and polished from these boules.

B. X-ray diffraction

The spectroscopic characteristics of optically active ions in garnet crystals are closely related to the properties of the crystal structure. Originally determined by Menser[6] for naturally occurring minerals such as grossularite, spessartine, or pyrope, the garnet structure is cubic and belongs to space group $Ia\bar{3}d$. All the cations are in special positions with no degree of freedom, while the oxygen atoms are in general positions. Each oxygen atom is at a shared corner of four polyhedra: one tetrahedron surrounding a "d" ion; one octahedron surrounding an "a" ion; two dodecahedra surrounding "c" ions.

The positions of the oxygen ions in the structure are defined by three general parameters: x, y, and z. The values of these parameters change with the chemical composition of the garnets and depend mainly on the radii of the cations. When oxygen ions are shifted from their ideal positions, distortions of polyhedra result. These distortions change the length of the edges of the polyhedron, while the distances between the center and the corners of the polyhedron are given by cation-oxygen ionic radii. Thus, freedom in substitution of various cations in the garnet structure is greatly restricted by the requirement of matching the length of the shared edges among the three polyhedron types. On the other hand, expanding one polyhedron by proper selection of substituting cations may allow extending the selection of other cations for substituting into the garnet structure. This approach has been successful in doped lanthanum garnets.[2]

The crystal structure analysis was performed on an automated Nicolet R3m/μ diffractometer equipped with an incident-beam graphite monochromator and Mo $K\alpha$ radiation ($\lambda = 0.7107$ Å). Lattice parameters were determined for 20 centered reflections within $3.0° < 2\theta < 60.0°$. Data were corrected for Lorentz-polarization effects and absorption correction. The structure of $\{La_{1-x}Lu_x\}_3[Lu_{1-y}Ga_y]_2Ga_3O_{12}$ was solved by direct methods by varying x and y until the R factors (or residuals) were minimized.[7] Low R factors indicate that the structure is correct and that the structure model based on atomic positions agrees well with the experimentally measured intensities. Table I shows the essential details of the structure; detailed structure information can be found in Ref. 8.

C. X-ray fluorescence

Elemental analysis was performed on three samples of LaLuGaG doped with impurities. These included two spectroscopic samples doped with Nd^{3+} and Cr^{3+}. The third sample was a 10-cm-long by 3-cm-diameter Nd^{3+}:LaLuGaG boule. The analysis was performed with a Kevex 770/8000 x-ray fluorescence spectrophotometer. This instrument uses the energy dispersive technique, where radiation from a primary x-ray tube is directed upon a secondary target, generating monochromatic x-ray fluorescent radiation at the characteristic $K\alpha$ and $K\beta$ energy levels of the target material. This secondary radiation is then directed upon the sample to be analyzed. The subsequent x-ray fluorescence from the sample is

TABLE I. Summary of single-crystal x-ray diffraction results of $\{La_{1-x}Lu_x\}_3[Lu_{1-y}Ga_y]_2Ga_3O_{12}$ for $x=0.25$ and $y=0$. Atom coordinates $(\times 10^4)$ and thermal coefficients $(\text{Å}^2 \times 10^3)$ of LaLuGaG. Space Group: $Ia\bar{3}d$ (cubic) (No. 230). Unit cell axis length: 12.930(3) Å. Observed data $[I \geq 3\sigma(I)]$: 236. Refinement: $R=4.07\%$; $wR=3.02\%$.

Atom	$10^4 x$	$10^4 y$	$10^4 z$	U $(10^{-3}$ Å$^2)$
Lu(1)	0	0	0	21(1)[a]
La(2)	0	2500	1250	20(1)[a]
Lu(2)	0	2500	1250	20(1)[a]
Ga(3)	0	2500	3750	22(1)[a]
O	300(3)	576(3)	6569(3)	23(1)[a]

[a]Equivalent isotropic U defined as one third of the trace of the orthogonalized U_{ij} tensor. Parenthetical values are estimated standard deviations.

detected and recorded on a multichannel analyzer. The chief advantage of the energy dispersive system is that secondary targets can be chosen whose secondary x-ray fluorescence will most efficiently excite the analytes in question. Such efficient monochromatic excitation results in a high signal to background ratio and provides the ideal conditions for accurate quantification routines.

Film standards of known concentration and mass thickness were obtained from Micromatter Co.[9] to obtain a known intensity-concentration ratio. This known ratio is compared with the sample fluorescence intensities and is used in conjunction with excitation efficiencies and matrix effects to calculate analyte concentrations and the elemental composition of the sample.

In our analysis of these samples, we selected secondary targets which would most efficiently excite the analytes of interest with minimum peak overlapping. Other parameters such as tube voltage and current, counting time, and atmosphere were selected to provide a statistically valid number of counts and reduce atmospheric effects. The composition of three LaLuGaG single crystals is shown in Table II. The results in Table II clearly indicate the added presence of lutetium in positions other than that of the octahedral site. Based on size constraints, Lu undoubtedly occupies the dodecahedral site. These results were confirmed by x-ray diffraction. In addition, the Ga concentration was found to be slightly larger than three formula units, which would indicate occupancy in the octahedral site.

The segregation constant,[1] k, for Nd^{3+}:LaLuGaG can be determined from the data in Table II. At equilibrium,

the concentration in the solid is given by[10]

$$c_s = kc_0(1-g)^{k-1} , \qquad (1)$$

where c_0 is the initial concentration of the dopant ion and g is the fraction of melt that has been crystallized. For Nd^{3+} in LaLuGaG, k is 1.3.

D. Index of refraction

The refractive indices of Nd:LaLuGaG were measured using the method of minimum deviation,[11] in which a polished prism of Nd^{3+}:LaLuGaG was fabricated and mounted on a goniometer, and monochromatic light (in this case, from multiline argon ion and helium neon lasers) was passed through it. The point of least deflection is recorded as the angle of minimum deviation, and the index of refraction is calculated according to the formula

$$n = \sin[(\tfrac{1}{2})(\alpha + \eta_m)]/\sin(\tfrac{1}{2}\alpha) , \qquad (2)$$

where α is the prism angle and η_m is the angle of minimum deviation. The results appear in Table III.

The accuracy of the refractive index calculated from the data was limited by the accuracy with which the angle of minimum deviation was measured, in this case 5″ of arc. Thus there existed an inherent error of ± 0.0025. The actual average error was ± 0.0035.

These experimental data were subsequently fit to Sellmeier's dispersion equation

$$n^2(\lambda) = 1 + S\lambda^2/(\lambda^2 - \lambda_0^2) . \qquad (3)$$

TABLE II. LaLuGaG crystal composition in formula units.

Sample	Chemical analysis	Nd^{3+} concentration in LaLuGaG composition (at. %) Crystal	Melt
Nd:LaLuGaG boule (top)	$Nd_{0.04}La_{2.32}Lu_{2.57}Ga_{3.07}O_{12.00}$	1.37±0.05	1.0
Nd:LaLuGaG boule (bottom)	$Nd_{0.04}La_{2.26}Lu_{2.63}Ga_{3.07}O_{12.00}$	1.30±0.05	1.0
Spectroscopic sample Nd:LaLuGaG	$Nd_{0.13}La_{2.14}Lu_{2.53}Ga_{3.20}O_{12.00}$	4.31±0.17	3.3
Spectroscopic sample Cr:LaLuGaG	$Cr_{0.4}La_{2.32}Lu_{2.61}Ga_{3.07}O_{12.00}$		

TABLE III. Indices of refraction of Nd^{3+}:LaLuGaG. Sellmeier coefficients: $n^2(\lambda) = 1 + S\lambda^2/(\lambda^2 - \lambda_0^2)$; $S = 2.3891$; $\lambda_0 = 194.46$ nm.

Wavelength (nm)	$n_{experimental}$
632.8	1.9070
611.9	1.9174
594.1	1.9221
543.0	1.9304
514.5	1.9376
496.5	1.9537
488.0	1.9632
476.5	1.9665

FIG. 1. Room-temperature absorption spectrum of Nd^{3+}:LaLuGaG (1.3 at. % Nd^{3+}). The sample thickness is 6.61 mm.

Appropriate values of S and λ_0, given in Table III, were calculated from this formula by averaging all the possible values extracted from the data. The index of refraction of maximum fluorescence in the $^4F_{3/2}$-$^4I_{11/2}$ transition, 1059 nm, was found to be 1.8634.

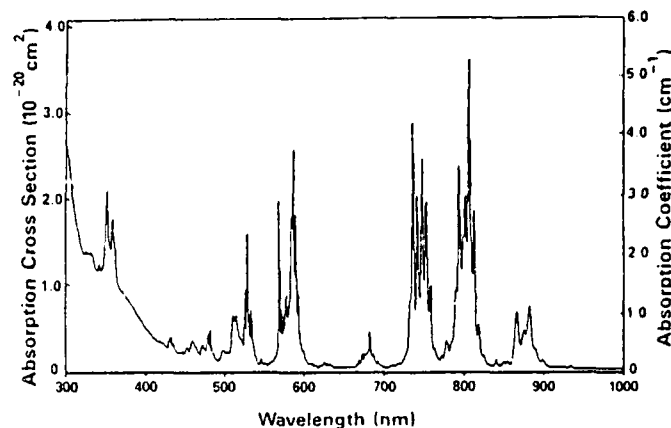### E. Nd^{3+} absorption spectra

The absorption spectrum of neodymium-doped LaLuGaG was investigated in the range of 200–6000 nm at room temperature and 10 K. These data were recorded

TABLE IV. Experimental (E) and theoretical (T) (the crystal-field parameters given in Table IX were used in the calculation of the energy levels) crystal-field splittings of Nd^{3+} ion manifolds in LaLuGaG.

State[a]		Stark-level positions (cm^{-1})
$^4I_{9/2}$	E	0, 102, 187, 287, 710
313	T	−6, 103, 191, 287, 711
$^4I_{11/2}$	E	1962, 2003, 2097, 2129, 2347, 2416
2177	T	1964, 2001, 2097, 2123, 2343, 2422
$^4I_{13/2}$	E	3899, 3920, 4040, 4059, 4315, 4338, 4407
4148	T	3901, 3915, 4039, 4051, 4317, 4337, 4412
$^4I_{15/2}$	E	5783, 5818, 5959, 6009, 6450, 6481, 6526, 6603
6190	T	5784, 5824, 5963, 6006, 6454, 6473, 6525, 6588
$^4F_{3/2}$	E	11 417, 11 534
11517	T	11 414, 11 531
$^2H_{9/2}$	E	12 402, 12 477, 12 567, 12 598, 12 625, 12 659,
$^4F_{5/2}$		12 817, 12 850
12383	T^b	12 192, 12 268, 12 314, 12 452, 12 478, 12 581,
12652		12 622, 12 656
$^4F_{7/2}$	E	13 375, 13 462, 13 582, 13 587,
$^4S_{3/2}$		13 602, 13 648
13501	T	13 368, 13 452, 13 564, 13 586,
13592		13 597, 13 659
$^4F_{9/2}$	E	14 645, 14 717, 14 775, 14 852, 14 964
14770	T	14 652, 14 723, 14 771, 14 834, 14 952
$^2H_{11/2}$	E	15 901, 15 926, 15 991, 16 093, 16 129
15969	T^b	15 908, 15 939, 15 961, 15 968, 16 011, 16 054,
$^4G_{5/2}$	E	16 951, 17 042, 17 116, 17 324, 17 586
$^2G_{7/2}$		
17091	T	16 963, 17 043, 17 104, 17 367,
17353		17 434, 17 465, 17 653
$^2G_{9/2}$	E	18 825, 18 917, 18 935, 19 032, 19 361, 19 410,
$^4G_{7/2}$		19 469, 19 599, 19 650
$^2P_{1/2}$	E	23 217

[a] The multiplet in Russell-Saunders notation and centroids of that multiplet are given.
[b] Experimental energy levels not used in the crystal-field calculations. The aqueous centroids were used instead.

in the ultraviolet, visible, and near infrared on a Perkin-Elmer Lambda 9 spectrophotometer with a maximum resolution of 0.01 nm. A Perkin-Elmer 983G infrared spectrophotometer having an accuracy of 0.1 cm^{-1} was used to obtain spectra beyond 3200 nm.

A closed-cycle refrigerator, CTI-Cryogenics Model 21, was used to obtain spectra at 10 K. Sample temperatures were measured with a silicon diode calibrated to <1 K below 50 K. Typical cooldown times were 1 h.

Figure 1 shows the absorption spectrum at room temperature of Nd^{3+}:LaLuGaG between 300 and 1000 nm for a 0.661-cm-thick sample with a Nd^{3+} concentration of 1.45×10^{20} ions/cm^3. This spectrum is very typical of Nd^{3+} in other crystalline hosts, showing strong transitions from the $^4I_{9/2}$ ground-state multiplet to the $^2H_{9/2}$ and $^4F_{5/2}$ (800 nm), $^4F_{7/2}$ and $^4S_{3/2}$ (750 nm), and $^4G_{5/2}$ and $^2G_{7/2}$ (590 nm) states. The experimentally determined Stark levels of the Nd^{3+} ions in the dodecahedral sites are listed in Table IV.

The peak absorption (emission) cross section for the $^4F_{3/2}$-$^4I_{11/2}$ ($Y_3 \rightarrow R_2$) transition was measured. The peak absorption cross section, given in Eq. (4), is equal to the absorption coefficient divided by the lower-level population

$$\sigma_p(Y_3 \rightarrow R_2) = \alpha_p(Y_3 \rightarrow R_2)/N(Y_3) . \quad (4)$$

The absorption coefficient for the 10.13-cm-long Nd:LaLuGaG boule was measured to be 6.34×10^{-4} cm^{-1}. With the Nd^{3+} concentration of the Nd:LaLuGaG boule equal to 1.45×10^{20} Nd^{3+} ions/cm^3 (determined by x-ray fluorescence), and the partition function equal to 2.488 (data taken from Table IV), the population in the Y_3 Stark level at 2097 cm^{-1} is 2.32×10^{15} Nd^{3+}/cm^3 at 298 K. Substitution of these values into Eq. (4) yields a cross section of 2.73×10^{-19} cm^2. This value is 2.4 and 0.9 times smaller than the values for Nd:YAG and Nd:GSGG, respectively.[12]

F. Branching ratios and radiative lifetimes of Nd^{3+}:LaLuGaG

The branching ratios and the radiative lifetimes of the $^4F_{3/2}$-^4I_J ($J = \frac{9}{2}, \frac{11}{2}, \frac{13}{2}, \frac{15}{2}$) were determined in two independent ways. The first method is a direct application

of the Judd-Ofelt theory[13,14] and has been used by many authors.[15-17] Data analysis was performed similar to that of Krupke[17] and is briefly described below.

The integrated absorption coefficient, $\int k(\lambda)d\lambda$, emanating from the ground state $|(SL)J\rangle$ $^4I_{9/2}$ manifold to excited $|(S'L')J'\rangle$ manifolds was measured for 11 absorption bands in Fig. 1. The integrated absorption coefficient in turn is related to the line strength S by Eq. (5):[1]

$$\int k(\lambda)d\lambda = \frac{8\pi^3 N_0 \bar{\lambda} e^2}{3ch(2J+1)} \left[\frac{(n^2+2)^2}{9n} \right] S , \quad (5)$$

where J is the total angular momentum quantum number of the initial level, $\bar{\lambda}$ is the mean wavelength that corresponds to the J-J' transition, n is the index of refraction, and N_0 is the Nd^{3+} concentration. Values for n were taken from Sellmeier's dispersion equation, Eq. (3), and N_0 was 1.45×10^{20} ions/cm^3. The Judd-Ofelt theory predicts that the line strength S may be written in the form

$$S([SL]J,[S'L']J')$$

$$= \sum_{t=2,4,6} \Omega_t \, | \, \langle 4f^n[SL]J \| U^{(t)} \| 4f^n[S'L']J' \rangle \, |^2 , $$

$$(6)$$

where $\langle 4f^n[SL]J \| U^{(t)} \| 4f^n[S'L']J' \rangle$ is a reduced-matrix element of the irreducible tensor operator of rank t, and Ω_t are the Judd-Ofelt parameters. The numerical values of the squares of the reduced-matrix elements for Nd^{3+} (aquo) ions for transitions from the ground state were taken from Carnall, Fields, and Rajnak.[18] When the absorption band was a superposition of lines assigned to several intermultiplet transitions, the matrix element was taken to be the sum of the corresponding squared matrix elements.[1] A least-squares fitting of S_{calc} to S_{meas} yields values for $\Omega_{2,4,6}$. Table V shows the measured and calculated line strengths for 11 absorption bands. The Judd-Ofelt parameters and the branching ratios are given in Table VI.

TABLE V. Measured and calculated line strengths of Nd^{3+} in LaLuGaG.

Russell-Saunders state $[S'L']J'$	Wavelength (nm)	Index of refraction n	Line strengths $(10^{-20}$ cm$^2)$	
			S_{meas}	S_{calc}
$^4F_{3/2}$	882	1.8738	0.424	0.749
$^4F_{5/2} + ^2H_{9/2}$	807	1.8805	2.137	1.984
$^4F_{7/2} + ^4S_{3/2}$	748	1.8874	1.741	1.842
$^4F_{9/2}$	683	1.8973	0.144	0.133
$^2H_{11/2}$	625	1.9092	0.014	0.034
$^4G_{5/2} + ^2G_{7/2}$	587	1.9193	1.594	1.594
$^2K_{11/2} + ^4G_{7/2} + ^4G_{9/2}$	526	1.9410	0.886	0.898
$^2K_{15/2} + ^4G_{9/2} + (^2D,^2P)_{1/2}$	479	1.9648	0.130	0.176
$^4G_{11/2}$	459	1.9778	0.084	0.016
$^2P_{1/2} + ^2D_{5/2}$	433	1.9982	0.041	0.103
$^2P_{3/2} + ^2D_{3/2} + ^4D_{3/2} + ^4D_{5/2}$	356	2.0988	0.980	0.789

TABLE VI. Experimental and theoretical Judd-Ofelt parameters and predicted branching ratios in Nd^{3+}:LaLuGaG.

Parameters	Experimental value	Theoretical value
	Judd-Ofelt	
Ω_2	0.84×10^{-20} cm^2	0.31×10^{-20} cm^2
Ω_4	2.64×10^{-20} cm^2	1.21×10^{-20} cm^2
Ω_6	2.61×10^{-20} cm^2	5.19×10^{-20} cm^2
	Radiative lifetime	
$^4F_{3/2}$	362 μs,[a] 295 μs[b]	286 μs
	Branching ratios	
$\beta(^4F_{3/2}-^4I_{9/2})$	43.6%	26.0%
$\beta(^4F_{3/2}-^4I_{11/2})$	47.2%	59.5%
$\beta(^4F_{3/2}-^4I_{13/2})$	8.8%	13.8%
$\beta(^4F_{3/2}-^4I_{15/2})$	0.4%	0.7%

[a]From Judd-Ofelt calculations.
[b]From fluorescence lifetime experiments.

The second method of determining the branching ratios and radiative lifetimes uses the point charge model. In these calculations, the Stark-level positions of Nd^{3+} given in Table IV were used along with the free-ion Russell-Saunders $[SL]J$ states with the free-ion Hamiltonian containing the Coulomb, spin-orbit, L^2, $G(G_2)$, and $G(R_7)$ interactions.[19] The free-ion parameters chosen, from Carnall, Fields, and Rajnak,[18] are $E^{(1)}=4739.3$, $E^{(2)}=23.999$, $E^{(3)}=485.96$, $\zeta=884.58$, $\alpha=0.5611$, $\beta=-117.15$, and $\gamma=1321.3$ (all in cm^{-1}). In the crystal-field analysis we assume a crystal electric field (CEF) of D_2 symmetry of the form

$$H_{CEF} = \sum_{ikq} B_{kq}^* C_{kq}(\hat{r}_i) , \qquad (7)$$

where the B_{kq} are the crystal-field parameters and the $C_{kq}(\hat{r})$ are spherical tensors related to the spherical harmonics by

$$C_{kq}(\hat{r}_i) = \sqrt{4\pi/(2k+1)}\, Y_{kq}(\theta_i,\phi_i) . \qquad (8)$$

The sum on i in Eq. (7) runs over the three electrons in the $4f^3$ configuration of Nd^{3+}, and the sum on k (k even) covers the range 2–6 with q even and in the range $-k \le q \le k$. Since we assume that the Nd^{3+} ions occupy the dodecahedral site with D_2 symmetry, the crystal-field parameters can be chosen real; thus there is a total of nine even-k B_{kq}. The procedure we use in the analysis of the experimental data is to obtain the free-ion wave functions using the free-ion parameters. We then use these free-ion wave functions to evaluate the energy levels in a crystal using the Hamiltonian given in Eq. (7). The crystal-field parameters B_{kq} are then determined by minimizing the squared difference of the calculated energies from the experimental energies. The centroids of each $[SL]J$ multiplet are allowed to vary freely during this fitting and are considered experimental data in the final analysis.

To obtain starting values of B_{kq} for our fitting of the experimental energy levels, we use point-charge lattice sum A_{kq}. The A_{kq} are related to the B_{kq} by[20]

$$B_{kq} = \rho_k A_{kq} , \qquad (9)$$

where

$$\rho_k = \tau^{-k} \langle r^k \rangle_{HF} (1-\sigma_k) . \qquad (10)$$

τ is an ion-dependent radial expansion parameter,[20] $\langle r^k \rangle_{HF}$ are Hartree-Fock expectation values,[21] and σ_k are shielding factors.[22] Values of ρ_k for Ce^{3+} through Yb^{3+} are given by Morrison and Leavitt.[23] The values of A_{kq} were calculated by a point-charge lattice sum using the x-ray data of Table I. In performing the lattice sum, the material is assumed to be $La_3Lu_2Ga_3O_{12}$, and for the starting parameters the charges on the individual ions are assumed to be the valence charges $q_{La}=3$, $q_{Lu}=3$, $q_{Ga}=3$, and $q_0=-2$ (in units of the electron charge). Later A_{kq} were calculated using an effective charge on the oxygen site q_0 such that $q_{Ga}=-5-4q_0$ and varying q_0 to obtain the best fit of calculated B_{kq} to experimental B_{kq}. The resulting A_{kq} for even k were obtained from the lattice sums; the B_{kq} obtained by using Eq. (9) are given in column 3 of Table VII. These values of B_{kq} were used in the least-squares fitting as starting parameters.

The crystal-field parameters that gave the best fit to the experimental data are given in Table VII, as well as the point-charge B_{kq} computed using $q_0=-1.64$ (the value of the oxygen charge that gave the best agreement to the experimental B_{kq}). In this fitting a number of experimental levels were discarded because attempts to fit these levels were unsuccessful. The odd-k A_{kq} (cm^{-1}/$\mathring{A}^k$) using $q_0=-1.64$ were calculated and are $A_{32}=1520$, $A_{52}=-1500$, $A_{54}=867$, $A_{72}=54.2$, $A_{74}=88.0$, and $A_{76}=-129$. (All odd-k A_{kq} are imaginary.)

The B_{kq} of Table VII along with the odd-k A_{kq} values were used to calculate the intensity of electric and magnetic dipole transitions for the rare-earth series. A detailed discussion of this calculation is given by Leavitt

TABLE VII. Experimental and calculated crystal-field parameters, B_{kq}. Note: Odd-k A_{kq} (cm^{-1}/Å^k) for $q_0 = -1.64$ are $A_{32} = 1520$, $A_{52} = -1500$, $A_{54} = 867$, $A_{72} = 54.2$, $A_{74} = 88.0$, and $A_{76} = -129$.

kq	Best-fit experimental B_{kq}^a (cm^{-1})	Point charge B_{kq}^b (cm^{-1})
20	879	843
22	206	338
40	-80.4	68.6
42	-1650	-2370
44	-782	-1087
60	-1345	-1485
62	-608	-732
64	629	736
66	-613	-614

^{a}Best-fit experimental B_{kq} for all data; rms = 5.658 cm^{-1}.
^{b}Point charge B_{kq} using $q_0 = -1.64$; rms = 50.38 cm^{-1}.

and Morrison.[24] The resulting Judd-Ofelt intensity parameters are given in Table VI for Nd^{3+} and the other rare earths in Table VIII.

G. Nd^{3+}:LaLuGaG fluorescence and lifetime measurements

The fluorescence spectrum of Nd^{3+}:LaLuGaG was recorded with a Spex F222 spectrometer. Figures 2 and 3 show the fluorescence spectrum in the region of the $^4F_{3/2}$-$^4I_{11/2}$ and $^4F_{3/2}$-$^4I_{9/2}$ transitions. The fluorescence lifetime and time-resolved, site-selection spectroscopy measurements were made using a nitrogen laser-pumped tunable dye laser with rhodamine 6G for the excitation source. This provided pulses of about 10 ns in duration and less than 0.04 nm half-width. The 4.3 at. % Nd^{3+} sample was mounted in a cryogenic refrigerator with temperature variable between 10 and 300 K. The fluorescence was analyzed by a 1-m monochromator, detected by a cooled RCA C31034 photomultiplier tube, processed by an EGG-PAR boxcar integrator triggered by the laser, and displayed on an x-y recorder.

The fluorescence lifetime of Nd^{3+} in LaLuGaG after

TABLE VIII. Calculated Judd-Ofelt (JO) intensity parameters Ω_k of rare-earth ions in the La site of La$_3$Lu$_2$Ga$_3$O$_{12}$.

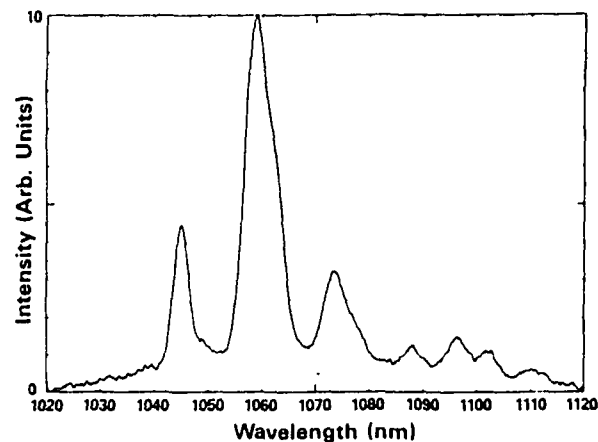| Ion	JO intensity parameters (10^{-20} cm^2)		
	Ω_2	Ω_4	Ω_6
Ce	0.5872	3.734	22.17
Pr	0.3286	1.884	9.449
Nd	0.3167	1.206	5.186
Pm	0.1833	0.9318	3.986
Sm	0.1599	0.7902	3.300
Eu	0.1265	0.6060	2.333
Gd	0.0990	0.4588	1.610
Tb	0.1729	0.8314	3.913
Dy	0.1271	0.5830	2.428
Ho	0.1038	0.4601	1.772
Er	0.0995	0.4352	1.671
Tm	0.0968	0.4190	1.615
Yb	0.0817	0.3417	1.230

FIG. 2. Fluorescence of Nd^{3+}:LaLuGaG at room temperature in the region of the $^4F_{3/2}$-$^4I_{11/2}$.

lower power dye laser excitation varies from 290 μs at 11 K to 205 μs at room temperature, as shown in Fig. 4. The solid line in Fig. 4 represents the best fit to the data using an expression of the form

$$\tau_f^{-1} = \tau_r^{-1} + C\{\exp[\Delta E/(k_B T)]-1\}^{-1}, \qquad (11)$$

where τ_f and τ_r are the fluorescence and radiative lifetimes, respectively. The last term describes the quenching of the lifetime due to radiationless processes involving the absorption of phonons of energy ΔE. C is a constant containing the matrix element for these transitions. The values obtained from fitting Eq. (11) to the experimental data are listed in Table IX. Several types of processes can lead to this type of lifetime quenching and will be discussed in Sec. II I.

II. Laser gain measurements

The laser-pumped, single-pass gain measurements using the frequency-doubled output of a mode-locked Nd-YAG laser as the pump source were performed at Oklahoma State University. This provided a 25-ps excitation pulse with a few millijoules of energy at 532 nm.
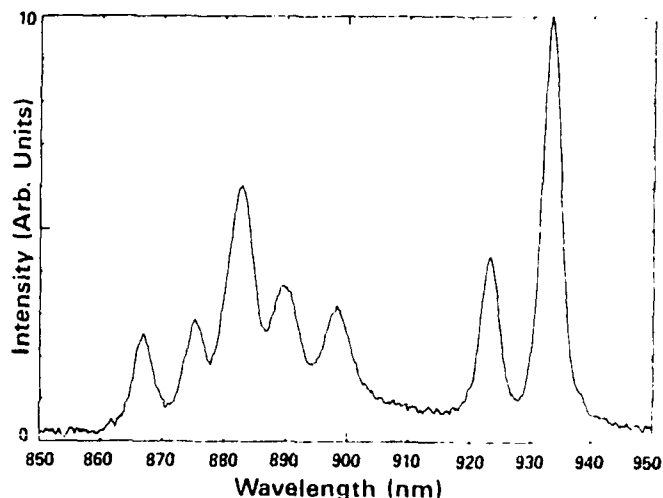

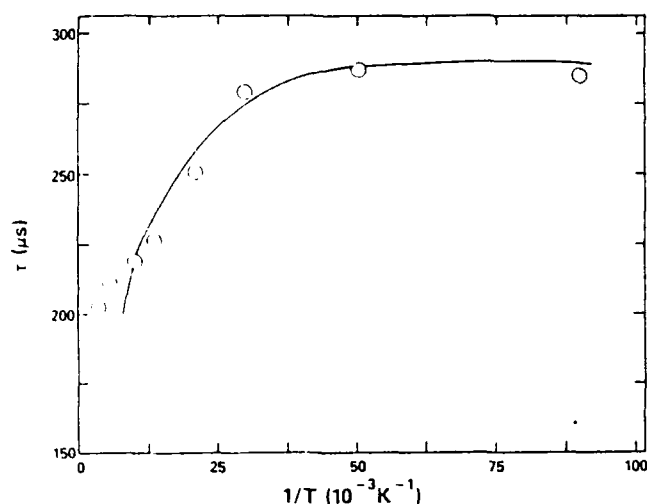FIG. 3. Fluorescence of Nd^{3+}:LaLuGaG at room temperature in the region of the $^4F_{3/2}$-$^4I_{9/2}$.

FIG. 4. Temperature dependence of the fluorescence lifetime of the $^4F_{3/2}$ metastable state of Nd^{3+}:LaLuGaG. (See text for explanation of the theoretical line.)

The probe beam was the collimated output of a xenon lamp passed through a 0.5-m monochromator. The change in the probe beam transmission through the sample under pumped conditions was monitored using a 0.25-m monochromator and photomultiplier tube with the output photographed on a storage scope. Multiphoton excitation studies were made using the same laser for excitation, and the fluorescence emission was monitored with a 0.25-m monochromator with an EGG-PAR silicon array detector and optical multichannel analyzer (OMA) combination. Fluorescence lifetimes under these excitation conditions were again measured with the boxcar integrator.

The attempt to observe single-pass gain was made with the probe beam tuned to the emission peak at 1059 nm while the pump beam at 532 nm was in resonance with one of the strong absorption transitions. Although these experimental conditions resulted in easily observable gain for several different types of Nd-doped crystal and glass

TABLE IX. Summary of results.

Parameter	Value
Fluorescence lifetime	
τ_f $^4F_{3/2}$ (10 K)	290 μs
τ_f $^4F_{3/2}$ (300 K)	205 μs
τ_f $^2P_{3/2}$ (300 K)	0.32 μs
τ_f $^2(F2)_{5/2}$ (300 K)	2.52 μs
Fluorescence rise time	
τ_{rt} $^2P_{3/2}$ (300 K)	317 ns
τ_{rt} $^2(F2)_{5/2}$ (300 K)	200 ns
Radiative lifetime	
τ_r $^4F_{3/2}$	295 μs
Energy transfer	
C	1538 μs
ΔE	30 cm^{-1}
α (100 K)	392 μs
ΔE_s	29 cm^{-1}

materials, no gain was observed for the 4.3 at. % Na^{3+}:LaLuGaG sample at room temperature. Since the optical quality (and thus the scattering losses per pass) was approximately the same for each of the samples investigated, the lack of optical gain indicates the presence of some type of loss process occurring for Nd^{3+} in the LaLuGaG host.

Direct lasing of two Nd:LaLuGaG samples was attempted at the Center for Night Vision and Electro-Optics. Two experiments were performed with different wavelengths of excitation and different pumping geometries. A laser diode array capable of producing 80 mJ per pulse at 20 Hz was used as a pump at 808 nm in a side-pump geometry. Typical outputs for Nd:YAG using this scheme are 25 mJ.[25] When a Nd:LaLuGaG sample was inserted in the resonator, no lasing was detected at 1059 nm. End-pumping of the same crystal was also attempted with a Coherent 699-29 ring dye laser producing 1.3 W with rhodamine 6G. Lasing was again not detected at 1059 nm. A focused dye laser beam at 595 nm produced an intense purple fluorescence at the focal point. This is indicative of two-photon absorption to higher lying levels, which prevents lasing in this material. This is consistent with the experimental results shown in Sec. III.

I. Multiphoton excitation measurements

For low excitation powers, the fluorescence emission originates from the $^4F_{3/2}$ metastable state at wavelengths longer than 850 nm. After high-power picosecond pulse pumping, fluorescence emission extends throughout the visible region of the spectrum to about 800 nm, as shown in Fig. 5. This demonstrates the presence of multiphoton excitation processes and subsequent emission from higher energy metastable states. The spectral dynamics occurring under these pumping conditions have been studied for Nd^{3+} in YAG, $Y_3Ga_5O_{12}$ (YGG), and lithium silicate glass.[26,27] The transitions have been shown to originate on the $^2P_{3/2}$ and $^2F_{5/2}$ metastable states with lifetimes of about 0.3 and 3.0 μs, respectively. The fluorescence lines shown in Fig. 5 can be divided into one set having a lifetime of 0.3 μs and another set having a lifetime of 2.5 μs. In comparison to the previous results, we assign these transitions to lines originating on the $^2P_{3/2}$ and $^2(F2)_{5/2}$, respectively.

One important difference between the results obtained on Nd^{3+}:LaLuGaG and those obtained on other hosts is that strong emission from the $^4F_{3/2}$ level was observed for the other samples under these pumping conditions[26,27] but not for LaLuGaG. This implies that multiphoton excitation transitions lead to relaxation channels that bypass the $^4F_{3/2}$ metastable state and thus act as a loss mechanism for pumping the $^4F_{3/2}$-$^4I_{11/2}$ laser transition. The multiphoton processes in the other hosts have been shown to be sequential two-photon excitation processes (STEP's) involving a real intermediate state,[27] and we assume that the same mechanism is active in LaLuGaG. The effects of the STEP mechanism appear to be stronger in the LaLuGaG sample than in the other hosts. One important spectral difference that may account for this is
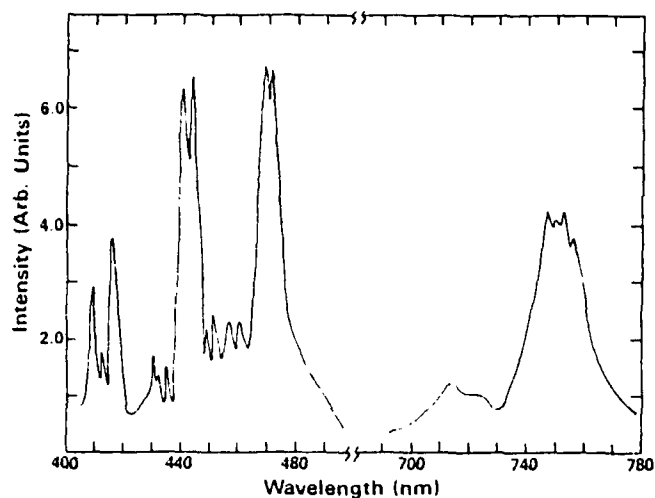
FIG. 5. Fluorescence of Nd^{3+}:LaLuGaG at room temperature after pumping at 532 nm with a 25-ps laser pulse.

that the 532-nm pump wavelength is almost exactly in resonance with an absorption transition in LaLuGaG, whereas for the other hosts investigated this wavelength is on the wing of the absorption band.

J. Energy transfer measurements

Dye laser, time-resolved spectroscopy techniques were used to investigate the characteristics of energy transfer between Nd^{3+} ions in nonequivalent crystal-field sites in the region from 560 to 600 nm. The fluorescence in the 880-nm spectral region was monitored in this investigation and is shown in Fig. 6 for two temperatures. At 11 K these transitions are associated with emission from the $^4F_{3/2}$ metastable state to the various Stark components of the $^4I_{9/2}$ ground-state manifold. At room temperature, emission from higher excited states is present and the transitions broaden because of both electron-phonon interactions and energy transfer to ions in spectrally inequivalent sites.
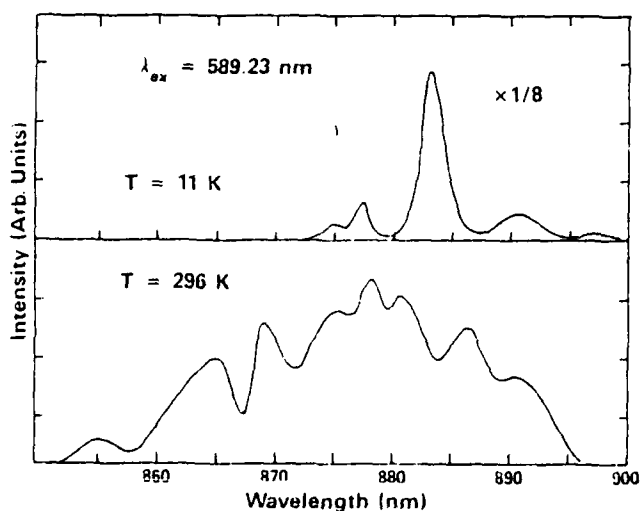
Microscopic strains produce slightly different crystal fields at the site of each Nd^{3+} ion in the lattice, resulting in inhomogeneous broadening of the spectral lines. In addition, Nd^{3+} ions occupying sites having significantly different crystal-field environments produce transitions that are easily resolvable in the optical spectra. Ions in a specific type of site can be selectively excited by tuning the dye laser into resonance with one of the absorption transitions associated with these ions. The results of doing this are shown in Fig. 7. As the excitation wavelength is tuned over 0.41 nm, the maximum emission of this transition shifts from peak a to peak b, indicating a change in the type of ion being excited. Note that the energy separation of the transitions originating from the ions in these two types of sites is $\Delta E_s = 29$ cm^{-1}.

In order to study the energy transfer between Nd^{3+} ions in these two major types of sites, the time evolution of the relative fluorescence intensities of peaks a and b was monitored as a function of time after the excitation pulse for both excitation wavelengths. These time-resolved measurements were carried out at several temperatures between 11 and 100 K, above which the thermal broadening of the lines prevented the spectral resolution necessary for accurate measurements. In this temperature range, no variation was observed in the ratios of the intensities of peaks a and b as a function of time. This indicates that energy transfer between Nd^{3+} ions in these two different types of sites is a very weak

FIG. 6. Fluorescence of Nd^{3+}:LaLuGaG at two temperatures in the region of the $^4F_{3/2}$-$^4I_{9/2}$ transition after pumping near 589 nm with a 10-ns laser pulse.

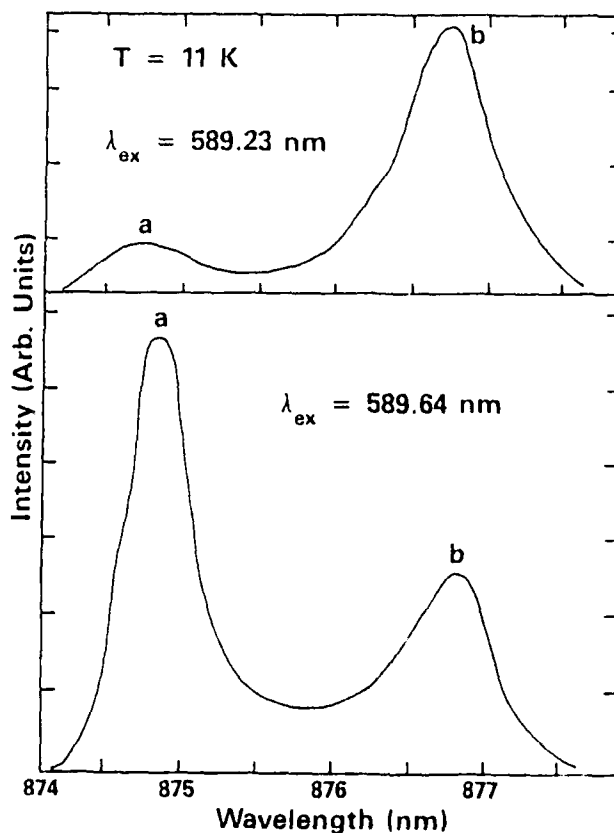

FIG. 7. Fluorescence of Nd^{3+}:LaLuGaG at 11 K in the region of one of the $^4F_{3/2}$-$^4I_{9/2}$ transitions for two different excitation wavelengths.
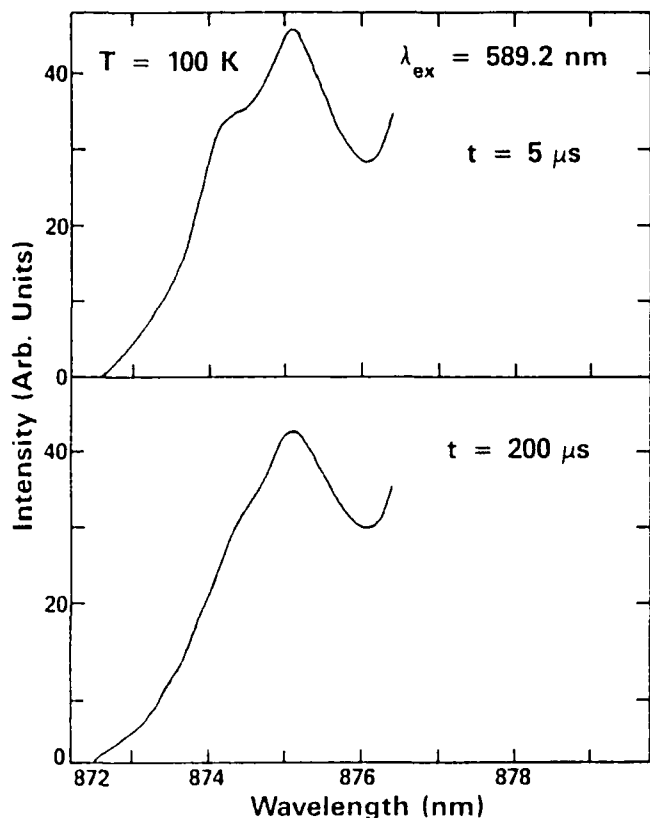
FIG. 8. Fluorescence of Nd^{3+}:LaLuGaG at 100 K in the 875 nm spectral region at two different times after the excitation pulse.
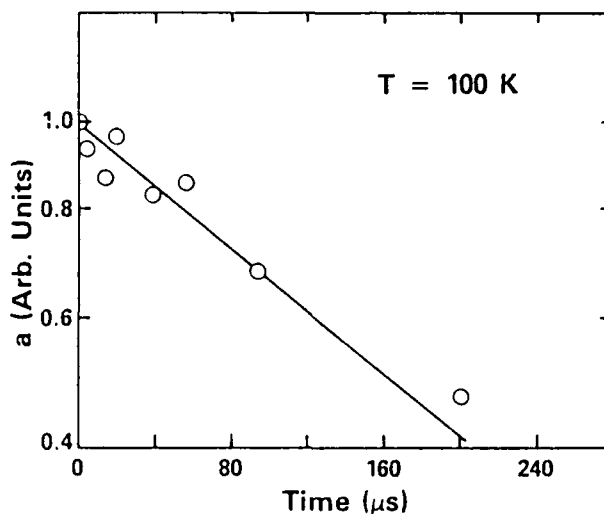

FIG. 9. Time dependence of the energy-transfer function $a(t)$ at 100 K obtained from Eq. (13) by monitoring the time evolution of the shape of the fluorescence band at 875 nm.

$$a(t) = \int_{\omega_1}^{\omega_2} [I(\omega,t) - I(\omega,\infty)] d\omega$$
$$\times \left[\int_{\omega_1}^{\omega_2} [I(\omega,0) - I(\omega,\infty)] d\omega \right]^{-1}. \quad (13)$$

The results of this analysis at 100 K are plotted in Fig. 9. The energy transfer function decreases exponentially with time, having a characteristic *time constant of* $\alpha = 392$ μs. The energy transfer parameters are summarized in Table IX.

III. SUMMARY AND CONCLUSIONS

The lifetime results summarized in Table IX indicate that Nd^{3+} ions in LaLuGaG have a quantum efficiency near 98%, which is significantly higher than that for Nd:YAG crystals with this doping concentration.[1] In addition, the rate of energy transfer between ions in the two major types of nonequivalent crystal-field sites is much smaller than in the YAG host.[29] Since the quantum efficiency of $^4F_{3/2}$ fluorescence in Nd^{3+}-doped materials is generally attributed to cross-relaxation processes between neighboring Nd^{3+} ions which can be enhanced by energy migration among the Nd^{3+} ions, these results are indicative of weak ion-ion interaction processes in the LaLuGaG host. This observation is consistent with the increased ion-ion separation in the LaLuGaG crystal.

The origin of the two major types of nonequivalent crystal-field sites in LaLuGaG has not been identified. However, in comparison with the results of previous site-selection spectroscopy investigations of mixed garnet crystals,[3,29] it is reasonable to assume that the different sites are associated with different lutetium environments around the Nd^{3+} ions. In the YAG host, the energy transfer between ions in the different types of sites has been attributed to a two-phonon assisted process with a real intermediate state.[26,27] This leads to an activation energy associated with the energy level splitting of the lowest two ground-state Stark components which is

process. However, the similarity of the activation energy for thermal quenching of the fluorescence lifetime and the energy difference between peaks a and b may indicate that at higher temperatures energy transfer between ions in these two major types of sites does occur and results in the quenching of the decay time.

Even though energy transfer between ions in the two major types of sites is negligible at low temperatures, time-resolved spectroscopy measurements do reveal spectral energy transfer across an inhomogeneously broadened line. An example of this is shown in Fig. 8 where the shape of fluorescence transition a is shown for two times after the laser pulse at 100 K. A distinct high-energy shoulder appears on this line at short times and disappears at long times. This can be attributed to the presence of energy transfer between Nd^{3+} ions in type a sites with differences in transition energies due to local perturbations of their surrounding crystal fields. This type of energy transfer can be treated quantitatively in the formalism developed for analyzing spectral energy transfer in doped glasses.[28] In this model, the time evolution of the fluorescence intensity at frequency ω is expressed as

$$I(\omega,t) = a(t)I(\omega,0) + [1 - a(t)]I(\omega,\infty), \quad (12)$$

where $a(t)$ is the function describing the energy transfer. This can be integrated to give

significantly greater than the measured activation energy in the Nd^{3+}:LaLuGaG crystal. This implies the presence of different types of energy transfer mechanisms in the two types of hosts.

The point-charge calculation of the odd-fold crystal fields (k = odd A_{kq}) was used to calculate the Judd-Ofelt intensity parameters, Ω_k, for all the rare-earth experimental values. For Nd^{3+}:LaLuGaG the radiative lifetime of the $^4F_{3/2}$ level was calculated and compares favorably with experiment. The branching ratios from a line-to-line intensity calculation for the $^4F_{3/2}$ to ^4I_J manifold were determined. The agreement of the crystal-field calculations with the experimental data was excellent for the ^4I_J and ^4F_J multiplets as well as the $^4S_{3/2}$ and $^4G_{5/2}$ energy levels.

The ability to incorporate high concentrations of Nd^{3+} in the lattice without degrading the optical quality and maintaining a high level of quantum efficiency would make LaLuGaG an attractive host for a Nd^{3+} laser material. However, the inability to observe lasing under pumping conditions producing gain in other Nd-doped materials, due to the presence of strong multiphoton transitions in this host, reduces the potential of Nd^{3+}:LaLuGaG as a replacement for Nd^{3+}:YAG or Nd^{3+}:Cr^{3+}:GSGG as an efficient 1-μm laser.

ACKNOWLEDGMENTS

*Permanent address: Division of Earth and Physical Sciences, The University of Texas at San Antonio, San Antonio, TX 78285.

[1] A. A. Kaminskii, Laser Crystals (Springer-Verlag, Berlin, 1981).

[2] M. Kokta and M. Grasso, J. Solid State Chem. 8, 357 (1973).

[3] L. A. Riseberg and W. C. Holton, J. Appl. Phys. 43, 1876 (1972); L. A. Riseberg, R. W. Brown, and W. C. Holton, Appl. Phys. Lett. 23, 127 (1973); L. A. Riseberg and W. C. Holton, Opt. Commun. 9, 298 (1973).

[4] Yu. K. Voron'ko and A. A. Sobol', Trudy Ordena Lenima Fizicheskogo Instituta Im. P. N. Lebedeva, 98:39 (1982).

[5] W. Koechner, Solid State Laser Engineering (Springer-Verlag, New York, 1976), Vol. 1, p. 35.

[6] G. Menser, Z. Kristallogr. 63, 157 (1926).

[7] J. D. Dunitz, X-Ray Analysis and the Structure of Organic Molecules (Cornell University Press, New York, 1979), pp. 183–222.

[8] C. F. Campana and T. H. Allik, Science Applications International Corporation, Report No. 164-450-043, 1988 (unpublished).

[9] Micromatter Co., Rt. 1, Eastsound, WA 98245.

[10] B. R. Pamplin, Crystal Growth (Pergamon, Oxford, 1980), Vol. 16, p. 289.

[11] W. L. Bond, J. Appl. Phys. 36, 1674 (1965).

[12] W. F. Krupke, M. D. Shinn, J. E. Marion, J. A. Caird, and S. E. Stokowski, J. Opt. Soc. Am. B 3, 102 (1986).

[13] B. R. Judd, Phys. Rev. 127, 750 (1962).

[14] G. S. Ofelt, J. Chem. Phys. 37, 511 (1962).

[15] M. J. Weber, T. E. Varitimos, and B. H. Matsinger, Phys. Rev. B 8, 47 (1973).

[16] W. F. Krupke, IEEE J. Quantum Electron. QE-10, 450 (1974).

[17] W. F. Krupke, IEEE J. Quantum Electron. QE-7, 153 (1971).

[18] W. T. Carnall, P. R. Fields, and K. Rajnak, J. Chem. Phys. 49, 4412 (1968); 49, 4424 (1968); 49, 4434 (1968); 49, 4444 (1968); 49, 4450 (1968).

[19] B. G. Wybourne, Spectroscopic Properties of Rare Earths (Wiley, New York, 1965).

[20] C. A. Morrison, N. Karayianis, and D. E. Wortman, Harry Diamond Laboratories, Report No. HDL-TR-1816, 1977; U.S. National Technical Information Service, Report No. A042447, 1977.

[21] A. J. Freeman and R. E. Watson, Phys. Rev. 127, 2058 (1962).

[22] P. Erdos and J. H. Kang, Phys. Rev. B 6, 3393 (1972).

[23] C. A. Morrison and R. P. Leavitt, J. Chem. Phys. 71, 2366 (1979).

[24] R. P. Leavitt and C. A. Morrison, J. Chem. Phys. 73, 749 (1980).

[25] D. Caffey (private communication).

[26] G. E. Venikouas, G. J. Quarles, J. P. King, and R. C. Powell, Phys. Rev. B 30, 2401 (1984).

[27] G. J. Quarles, G. E. Venikouas, and R. C. Powell, Phys. Rev. B 31, 6935 (1985).

[28] S. A. Brawer and M. J. Weber, Appl. Phys. Lett. 35, 31 (1979).

[29] L. D. Merkle and R. C. Powell, Phys. Rev. B 20, 75 (1979); M. Zokai, R. C. Powell, G. F. Imbusch, and B. DiBartolo, J. Appl. Phys. 50, 5930 (1979).

Site-selection spectroscopy, energy transfer, and laser emission in Nd^{3+}-doped Ba$_2$MgGe$_2$O$_7$

Michael J. Ferry,[a] Michael L. Kliewer, Roger J. Reeves, and Richard C. Powell
Center for Laser Research, Oklahoma State University, Stillwater, Oklahoma 74078-0444

Toomas H. Allik
Science Applications International Corporation, 1710 Goodridge Drive, McLean, Virginia 22102

A detailed spectroscopic and pump wavelength dependent laser study has been performed on Nd^{3+} ions in Ba$_2$MgGe$_2$O$_7$. Site-selection spectroscopy experiments reveal fifteen distinct crystal field sites for the Nd^{3+} ions. At room temperature, excitation of ions in any one of these sites is followed by efficient, thermally activated energy transfer to ions in a site having a laser emission transition at 1054 nm. Laser-pumped laser experiments were performed to determine the pumping threshold and slope efficiency of laser action in this material for different monochromatic pump wavelengths. The measured slope efficiencies were found to be pump wavelength dependent and ranged from 6% to 22%. Excited-state absorption of pump photons was shown to be responsible for this variation in the slope efficiency.

I. INTRODUCTION

The development of high power GaAlAs laser diodes has renewed the interest in rare-earth doped solid-state hosts. For Nd^{3+} doped materials, diode excitation at 800 nm has been shown to be more efficient than flashlamp pumping in generating 0.9, 1.0, and 1.3 μm lasers. In addition, monochromatic pumping in the near-infrared has produced visible (upconversion) emission and new laser wavelengths. Therefore, it is worthwhile reinvestigating materials that do not possess superior flashlamp-pump characteristics but can be reconsidered as materials for diode pumping. We have chosen to study one such material Ba$_2$MgGe$_2$O$_7$:Nd^{3+}, which has many attractive features.

Ba$_2$MgGe$_2$O$_7$:Nd^{3+} (Nd:BMAG) was first studied in the late 1960's and early 1970's as a flashlamp-pumped laser material.[1-3] The host crystal possesses the Åkermanite crystal structure with space group $P\bar{4}2_1m$ (tetragonal)[4] and is a subset of the melilite series of minerals. The Nd^{3+} ions are believed to occupy the Ba^{2+} site (C_s symmetry) and charge compensation is provided by interstitial anions, cation vacancies and monovalent ions such as K$^+$ or Na$^+$. When doped with Nd^{3+} this crystal exhibits inhomogeneously broadened absorption and fluorescence spectra. The room-temperature fluorescence lifetime of 450 μs for the $^4F_{3/2}$ metastable state[1] and the high thermal conductivity of the crystal compared to a glass make Nd:BMAG an attractive material for a diode-array pumped laser system. Spectroscopic measurements have recently been reported on a similar material Ba$_2$ZnGe$_2$O$_7$:Nd^{3+}.[5]

We present here the results of time-resolved, site-selection spectroscopy experiments on Ba$_2$MgGe$_2$O$_7$:Nd^{3+}. The results provide information on the electronic transition wavelengths of Nd^{3+} ions in different crystal field sites and on the energy transfer between ions in these sites. In addition, the characteristics of laser-pumped laser operation of this material are reported. All of these results are relevant to understanding the dynamics involved in monochromatic pumping of this material.

II. ABSORPTION AND SITE-SELECTION SPECTROSCOPY

The crystal used in this study was grown by Linz using the top-seeded-solution growth technique.[6] The sample was obtained from the same growth runs as those used for the previous studies of this material.[1-3] The size of the sample was 0.56×0.83×1.02 cm^3 with the long dimension parallel to the c-axis of the crystal. The absorption spectra were recorded with a Perkin–Elmer Lambda 9 spectrophotometer equipped with a polarizing attachment. Figure 1 shows the polarized absorption spectrum of Nd:BMAG between 300 and 1000 nm at room temperature with the Fresnel losses removed. The two salient features of the spectra are that at most wavelengths the absorption coefficient for $E\perp c$ is greater than $E\|c$, and the sample exhibits broad absorption features for the manifold-to-manifold transitions. The large inhomogeneous broadening is primarily caused by the variation of the crystal field around the rare-earth ions due to the mismatch in electronic charges between Nd^{3+} and Ba^{2+}. In addition to known Nd^{3+} absorption transitions, a broad absorption band from 320 to 420 nm has been detected and could be attributable to a germinate complex.

Fluorescence, excitation, and site-selection spectroscopy measurements were performed using a molectron nitrogen laser-pumped dye laser that provided excitation pulses of 10 ns duration, 0.5 Å bandwidth, and energy of 100 mJ/pulse. The dyes used were Coumarin 440 with output tunable from 420 to 465 nm for excitation into the $^2P_{1/2}$ manifold, and Rhodamine 590 with output tunable from 560 to 630 nm for excitation into the $^4G_{5/2}$ and $^2G_{7/2}$ manifolds. The sample was mounted in a cryogenic refrigerator capable

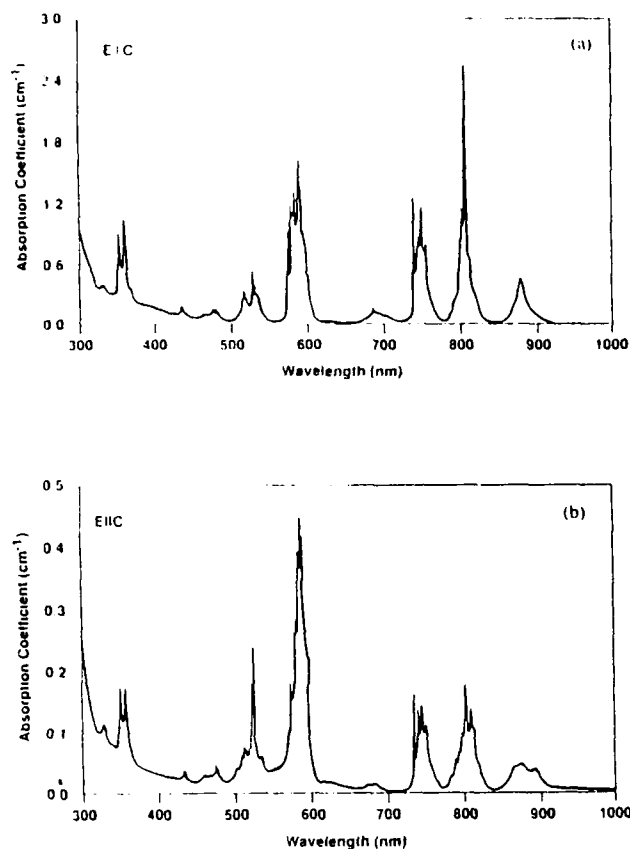[a] Present address: Center for Night Vision and Electro-Optics, Fort Belvoir, VA 22060-5677.

FIG. 1. Absorption spectra of Nd³⁺ in BMAG at room temperature with (a) $E\perp c$ and (b) $E\|c$ polarizations.

Stark manifold	Peak (cm⁻¹)	α_a (cm⁻¹)	FWHM (cm⁻¹)
$^4D_{7/2}$ $^2I_{13/2}$	30 377	0.543	737
$^4D_{1/2}$	28 514	0.790	342
$^4D_{5/2}$ $^2I_{11/2}$	27 964	0.884	422
$^4D_{3/2}$	27 405	0.477	286
$^2P_{3/2}$	26 788	0.424	108
	26 504	0.411	112
	26 110	0.411	212
	25 826	0.399	147
$^2D_{5/2}$	23 776	0.337	266
$^2P_{1/2}$	23 218	0.354	129
	23 010	0.366	243
$^4G_{11/2}$	22 026	0.333	141
	21 763	0.358	142
	21 622	0.358	164
$^2D_{3/2}$	21 182	0.382	216
$^4G_{9/2}$	20 995	0.395	185
$^2G_{9/2}$	19 569	0.613	84
	19 478	0.691	83
	19 353	0.625	86
$^4G_{7/2}$	19 030	1.020	145
	18 868	0.687	78
	18 761	0.629	92
$^4G_{5/2}$	17 501	1.200	75
$^2G_{7/2}$	17 483	0.851	83
	17 209	1.300	92
	17 103	1.440	73
	17 030	1.68	58
	16 972	1.52	55
	16 846	1.09	105
	16 711	0.80	87
$^2H_{11/2}$	16 271	0.321	50
	16 171	0.329	78
	16 067	0.321	57
	15 946	0.313	84
$^4F_{9/2}$	14 550	0.387	188
	14 409	0.370	73
	14 296	0.366	135
$^4F_{7/2}$	13 567	1.380	50
$^4S_{3/2}$	13 460	1.200	73
	13 382	1.470	59
	13 289	1.130	62
	13 154	0.559	73
$^4F_{5/2}$	12 750	0.382	44
$^2H_{9/2}$	12 679	0.485	40
	12 553	0.929	35
	12 505	1.170	39
	12 429	2.040	42
	12 334	0.880	52
	12 252	0.621	50
$^4F_{3/2}$	11 533	0.572	52
	11 399	1.070	49
	11 307	0.588	47
	11 ?1	0.428	84
	11 046	0.325	68
$^4I_{15/2}$	6242	0.169	.4
	6156	0.154	47
	6062	0.156	69
	5961	0.154	48
$^4I_{13/2}$	4359	0.160	35
	4278	0.177	51
	4225	0.193	34
	4170	0.284	77
	4102	0.251	27

of reaching temperatures as low as 10 K and oriented such that the laser pump pulses propagated along the c-axis. The unpolarized fluorescence was monitored perpendicular to the pump beam and focused on the entrance slit of a Spex 1 meter monochrometer. A filter was used to attenuate the scattered pump laser light. It is well known that strong fluorescence from Nd³⁺ ions in solids occurs in the near-infrared region and corresponds to transitions from the $^4F_{3/2}$ manifold to the lower energy ^4I manifolds. This fluorescence signal was detected with a liquid nitrogen cooled RCA 7102 photomultiplier tube and processed by a boxcar integrator. The output of the boxcar was recorded on a strip chart recorder.

The room-temperature energy levels of Nd³⁺ in BMAG were determined from absorption and fluorescence spectra and are listed in Table I. The full width at half maximum (FWHM) was estimated from constructed Gaussian fits to the absorption and fluorescence bands. Reported absorption coefficients, α_a, are those measured at the band maxima. No attempt was made to separate hot band transitions or to deconvolute the multisite contributions when determining the energy levels.

Figure 2 shows the excitation spectrum of the near-infrared emission of Nd:BMAG from 429 to 437 nm at 10 K. The spectrum has been corrected for the filter response but not for the dye laser intensity. The peaks observed in this

TABLE I. (continued)

Stark manifold	Peak (cm^{-1})	α_J (cm^{-1})	FWHM (cm^{-1})
	4057	0.280	35
	4017	0.226	38
$^4I_{11/2}$	2176		67
	2093		74
	2029		76
	1933		47
$^4I_{9/2}$	683		78
	364		101
	235		97
	102		96
	0		70

excitation range correspond to absorption transitions to the $^2P_{1/2}$ manifold of Nd^{3+}.[7] Since this energy level consists of a single Stark component, each peak observed in Fig. 2 is associated with a transition to the $^2P_{1/2}$ level for Nd^{3+} ions in different crystal field sites of BMAG. The excitation spectrum was observed to be comprised of four groups of lines that were well separated in wavelength. These major site categories, labeled with a letter in Fig. 2, were composed of "subsites" which were numbered with ascending integers indicating descending energy. In total, fifteen individual sites were identified. While a direct correlation is not possible with the available data, the major sites appear to be different crystal field centers associated with the different types of charge compensation for the Nd^{3+} in Ba^{2+} positions.[8] The subsites having the same letter designation (i.e., A1, A2, A3, ...) are thought to be distinguished by perturbations in the local crystal field due to lattice defects.[8] The intensity of an excitation peak depends on the absorption coefficient at the excitation wavelength, the emission cross sections for the

transitions of the ions in that particular site, and the dye response at the pump wavelength. In the excitation region covered in Fig. 2, the dye laser response is essentially flat and site A2 is the strongest emitter, followed closely by sites D5 and C4.

With the transitions for the sites identified in the $^2P_{1/2}$ excitation spectrum, it was possible to selectively excite ions in individual sites and observe the fluorescence emitted. Figure 3 shows the $^4F_{3/2} \rightarrow {}^4I_{11/2}$ fluorescence spectra at 10 K associated with pumping the $^2P_{1/2}$ level of sites A2, C4, and D5. Time-resolved studies showed that energy transfer between sites was negligible at 10 K and the fluorescence observed is solely due to ions in the site pumped. The shortest wavelength peaks of the different sites are the highest intensity transitions and are the common laser transitions for Nd^{3+} ions. These transitions appear at distinctly different wavelengths for ions in the different major sites. A rough rule of thumb is 1050, 1060, 1070, and 1080 nm for sites A, B, C, and D, respectively.

Optically pumping the different excitation peaks in the $^2P_{1/2}$ spectral region leads to the identification of many of the Stark levels of the $^4F_{3/2}$, $^4I_{11/2}$, and $^4I_{9/2}$ manifolds for the fifteen sites of Nd:BMAG. Similar measurements were made pumping into the $^4G_{5/2} + {}^2G_{7/2}$ manifold. The results of the spectroscopic energy level identification for the sites of Nd:BMAG at 10 K are presented in Fig. 4. Only those energy levels that could be unambiguously identified are shown in the figure. The energies of the levels generally decrease from sites A to D.

III. ENERGY TRANSFER

Energy transfer between the different crystal field sites in Nd:BMAG was predicted from the appearance of the room-temperature fluorescence spectrum. It was found that excitation of any one of the crystal field sites at room temperature produced the same fluorescence spectrum which is shown in Fig. 5. The fluorescence bands observed in this

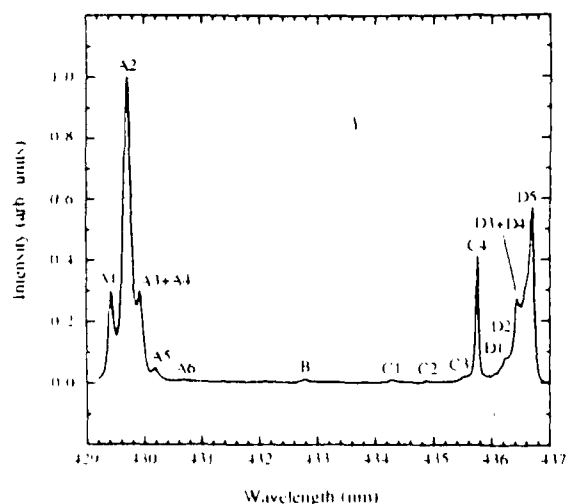
FIG. 2 Excitation spectrum of the near-infrared emission for Nd:BMAG at 10 K for transitions terminating on the $^2P_{1/2}$ energy level.
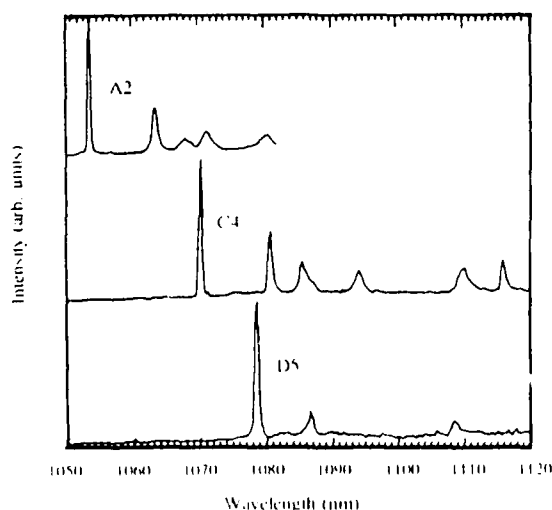

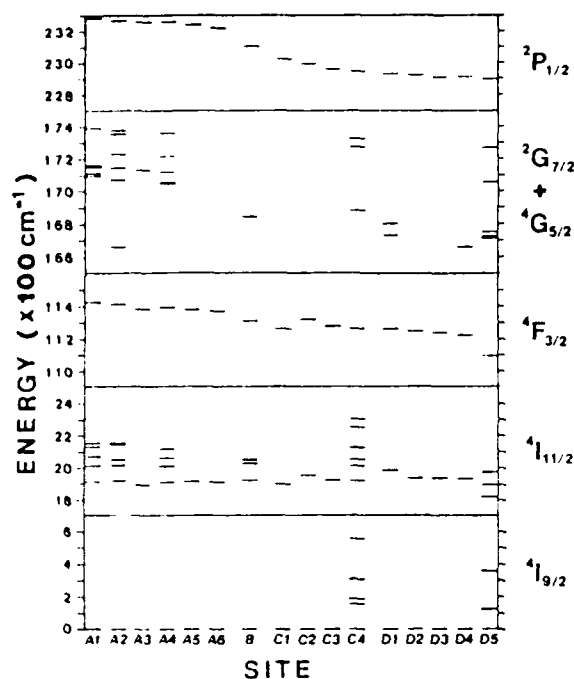FIG. 3 Fluorescence from the $^4F_{3/2}$ level to $^4I_{11/2}$ level for ions in different sites at 10 K.

FIG. 4 Partial energy level diagram for the different crystal field sites in Nd:BMAG at 10 K. Site labels appear on the bottom.

spectrum are indicative of transitions from ions in the A type sites, implying that energy is completely transferred to these ions at room temperature. The energy transfer was investigated by selectively exciting the $^2P_{1/2}$ level of Nd^{3+} ions in a particular site and monitoring the fluorescence in the $^4F_{3/2} \rightarrow {}^4I_{11/2}$ transition region from all other sites.

Sites D5 and C4 were selectively excited at various temperatures and the fluorescence spectra recorded are shown in Figs. 6(a) and 6(b). The peak at 1078 nm in Fig. 6(a) is associated with emission from ions in site D5 while the peak at 1054 nm is associated with site A2. These peaks corre-

FIG. 6. Temperature dependence of the fluorescence for (a) site D5 and (b) site C4 pumping in Nd:BMAG. Each spectra has been normalized, and was recorded at a delay of 200 μs after the excitation pulse.
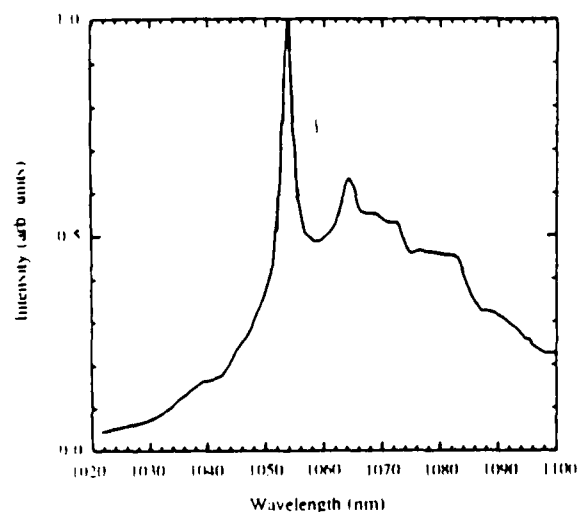
FIG. 5. Fluorescence at room temperature of Nd:BMAG for transitions between the $^4F_{3/2}$ and $^4I_{11/2}$ manifolds.

spond to the transition between the lowest crystal field levels of the $^4F_{3/2}$ and $^4I_{11/2}$ multiplets. The results show the intensity of the line from site A2 growing at the expense of the line from site D5 as the temperature is increased. Thus, energy is being transferred from sensitizer ions in D5 to activator ions in A2 sites and the transfer process is thermally activated.

Fluorescence spectra were recorded at delay times ranging from 10 μs to 1 ms after the excitation pulse but no time dependence of the relative line strengths could be observed at

any temperature. This leads to the conclusion that the transfer is completed prior to the $^4F_{3/2}$ emission.

Similar results were obtained for excitation of the C4 crystal field sites. The intensity of the emission peak at 1070 nm for site C4 decreased as the temperature was increased [Fig. 6(b)]. The energy was transferred to the same activator site A2 and again there was no time dependence of the relative line strengths. Note that the transfer from site C4 is thermally activated at a lower temperature than the transfer from site D5.

The temperature dependence of the energy transfer arises as higher lying Stark components of a metastable state become populated through a Boltzmann distribution. Energy is transferred due to the spectral overlap between the thermally activated levels of the optically pumped ions, and levels of the ions in site A2. An exact resonance of the levels is not required as some degree of mismatch can be compensated by absorption or emission of lattice phonons.

A simple rate equation model can be used to qualitatively explain the observed results. Figure 7 depicts the energy levels involved in the dynamical processes taking place. The sensitizer S, is the ion that is optically pumped (site C4 or D5) and the activator, A, is the ion in the site to which energy is transferred (site A2). The population of ions in the ith level of the sensitizers and activators is designated by S_i or A_i, respectively.

The population of the metastable state S_2 involves absorption of excitation laser photons from $^4I_{9/2}$ to $^2P_{1/2}$ and then rapid nonradiative relaxation from $^2P_{1/2}$ to S_2. Therefore, the rate of population of S_2 is effectively W_p, the optical pumping rate. W_s and W_a are the rates of population loss from the metastable levels S_2 and A_2, and B_u and B_d are nonradiative transition rates between the two Stark components of the sensitizer multiplet involved in the transfer. These Stark components are separated by an energy gap of ΔE_s. Energy transfer between ions occurs through the spectral overlap of the activator level A_2 and the sensitizer level S_3 that is thermally activated. Any energy mismatch between the levels can be compensated by lattice phonons and the transfer will still activate with the Stark splitting
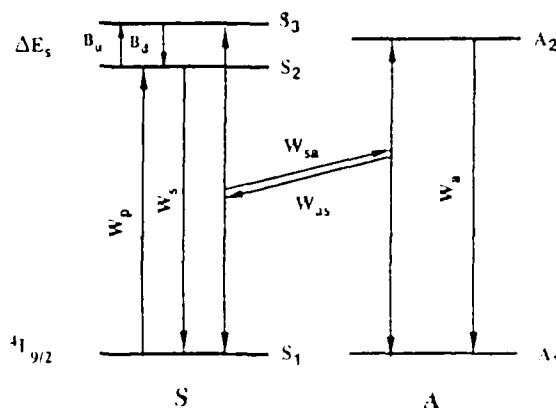
ΔE_s. The transfer is described by a forward rate, W_{sa} (from sensitizer to activator), and a back transfer rate, W_{as} (from activator to sensitizer).

The observed ratio of the fluorescence intensities of the sensitizer and activator emission is proportional to the ratio of level populations,

$$\frac{I_a}{I_s} = \beta(A_2/S_2) \tag{1}$$

where the proportionality factor β includes parameters compensating for possible differences in the radiative decay rates of the fluorescing levels of the sensitizer and activator ions. The ratio A_2/S_2 can be obtained from the rate equation describing the population dynamics of level S_3.

$$\dot{S}_3 = B_u S_2 + W_{as} A_2 - B_d S_3 - W_{sa} S_3. \tag{2}$$

At thermal equilibrium,

$$\frac{S_3}{S_2} = \exp(-\Delta E_s/kT) = \frac{B_u}{B_d}. \tag{3}$$

Since no time dependence of the energy transfer was observed, steady state conditions can be applied and $\dot{S}_3 = 0$. Using this assumption Eq. (2) can be solved for the ratio A_2/S_2 obtaining

$$\frac{I_a}{I_s} = \beta \frac{W_{sa}}{W_{as}} \exp(-\Delta E_s/kT) \tag{4}$$

for the ratio of the fluorescence intensities.

Figure 8 shows the natural log of the ratio of the integrated fluorescence intensity of activator and sensitizer as a function of inverse temperature for C4 and D5 site pumping. The results obtained by fitting Eq. (4) to the data are shown as solid lines in Fig. 8 and the parameters obtained from these fits are given in Table II. ΔE_s is the activation energy determined by the slope of the linear fit to the data in Fig. 8 and the intercept is associated with the constant $\beta(W_{sa}/W_{as})$.

With the available data, identification of the metastable sensitizer level involved in the transfer is not conclusive but the most probable candidate is the $^4F_{3/2}$ level. The energy
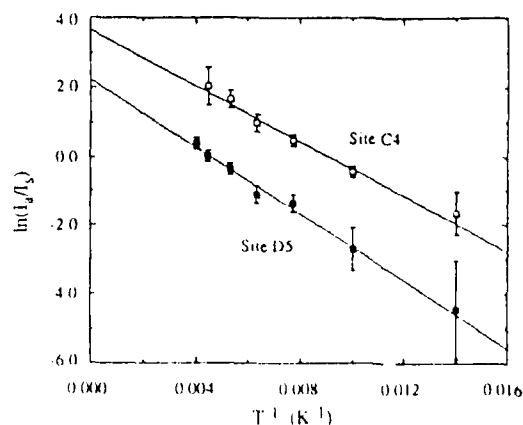

FIG. 7. Model used to explain the temperature dependent energy transfer observed in Nd:BMAG

FIG. 8. Temperature dependence of the fluorescence intensity ratios for A2 activators with C4 or D5 sensitizers.

Sensitizer	ΔE_t	$\beta\dfrac{W_{io}}{W_{ai}}$	ΔE_{mm}
C4	278 ± 33 cm^{-1}	38 ± 18	151 cm^{-1}
D5	338 ± 51 cm^{-1}	9 ± 4	319 cm^{-1}

difference between the lowest Stark component of this multiplet for the activator site, A2, and the sensitizers, C4 and D5, is given in Table II as ΔE_{mm}. For the D5→A2 transfer there is a reasonable agreement between the activator energy required for energy transfer and the site-to-site energy difference, ΔE_{mm}, of the $^4F_{3/2}$ level. The difference between ΔE_t and ΔE_{mm} for the C4→A2 transfer indicates that phonons with energy of 120 cm^{-1} would be released in this transfer process.

IV. LASER-PUMPED LASER STUDIES

Laser action was obtained at room temperature in Nd:BMAG using an alexandrite laser as the excitation source. The alexandrite laser output was tunable from 725 to 790 nm and consisted of a series of pulses of duration 300 ns within a 60 μs envelope. The maximum power at the peak of the gain curve was 20 W at a repetition rate of 20 Hz and the spectral width was approximately 1 nm.

The crystal was mounted in a 23-cm long cavity consisting of a 50 cm radius of curvature high reflector and a flat 85% reflective output coupler. Transverse pumping was employed ($E\mathbin{\perp}c$) with cylindrical and convex lenses used to focus the pump laser beam in a line the length (0.56 cm) of the Nd:BMAG sample. An iris was positioned in the cavity to limit the number of oscillating modes. The power incident on the Nd:BMAG crystal and the power output from the Nd:BMAG laser were measured with two calibrated power meters. The Fresnel reflections and absorption within the cavity mode volume of the material were considered when calculating the power absorbed by the crystal.

Figure 9 shows the absorption spectrum in the pumping region used in these experiments. The spectral structure is associated with absorptions\transitions terminating on the various Stark components of the $^4F_{7/2}$ and $^4S_{3/2}$ manifolds. For all the excitation wavelengths used, Nd:BMAG lased at a wavelength of 1054 nm. As discussed in the previous sections this wavelength corresponds to the $^4F_{3/2}(R_1)\to$ $^4I_{11/2}(Y_1)$ transition of the A2 site in Nd:BMAG. Lasing was observed for pump wavelengths from 736.7 to 758.8 nm, which covers most of the absorption spectrum shown in Fig. 9. Lasing could not be obtained for excitation wavelengths shorter than 736.7 nm because the gain curve of the alexandrite laser limited the available pump power.

The laser power output of Nd:BMAG at 1054 nm was monitored as a function of the incident pump power for several excitation wavelengths and the results were used to determine the laser threshold and slope efficiency. Figure 10 shows the data obtained in this work. Above absorbed power
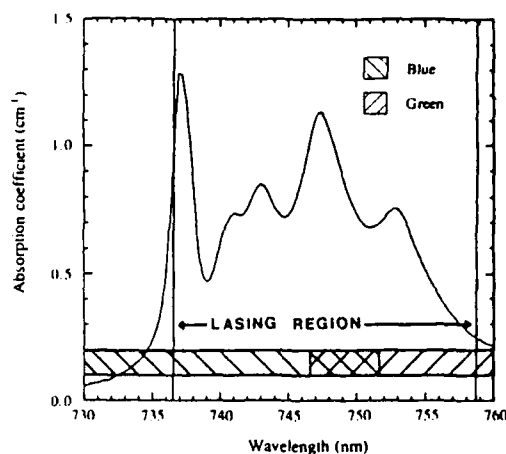
FIG. 9. Absorption spectrum ($E\mathbin{\perp}c$) for the region used in laser pumped laser experiments. The spectral pumping region for which lasing was obtained is marked. Also, spectral pumping regions resulting in blue and green fluorescence are indicated.

levels of 150 mW the Nd:BMAG laser power output levels off due to saturation of absorption in the laser mode volume (waist diameter, $d \doteq 0.069$ cm). The threshold for lasing varies only a small amount with changes in pump wavelength but there are significant changes observed in the slope efficiency. Pumping at 749.5 nm results in the highest slope efficiency (22%) and the lowest power threshold.

Blue and green fluorescence was apparent to the eye for alexandrite pumping of Nd:BMAG. As observed by eye, the intensity of this fluorescence did not significantly change when the sample was lasing. Moreover, the fluorescence showed changes with excitation wavelength suggesting excited state absorption of pump laser photons may be occurring. For excitation between 729 and 752 nm the fluorescence appeared as an intense blue and then a weaker green as the alexandrite laser was tuned to longer wavelengths. The pump wavelength yielding the highest laser slope efficiency
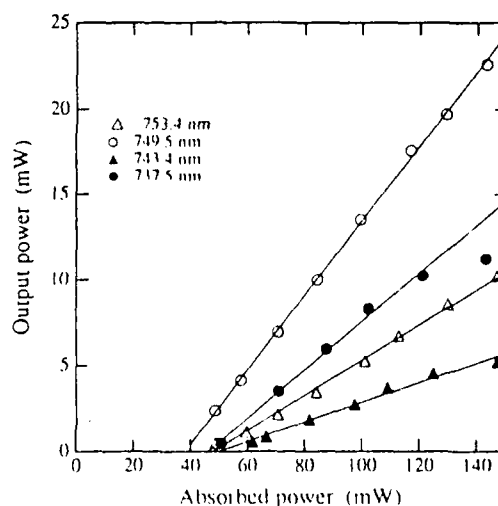
FIG. 10. Laser output power at 1054 nm vs the calculated absorbed pump power in the mode volume of the cavity for different pump wavelengths.

(749.5 nm) also was associated with a minimal amount of upconverted emission. This suggests that the processes producing upconverted emission may be limiting the efficiency of the Nd:BMAG laser at some pump wavelengths.

Excited state absorption (ESA) of pump photons is possible when the pump wavelength is tuned to the transition energy between any populated excited level and a higher level. Additionally, the incident pump photon rate must be comparable to the decay rate of the initial excited level. Because of the high energy and short duration of the spiked alexandrite laser pulses, this condition may be satisfied for some of the intermediate levels of the Nd^{3+} ion. An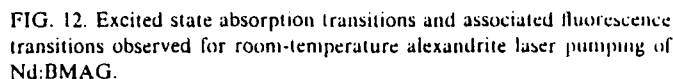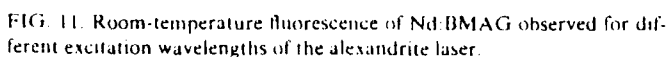 efficient ESA process also requires a resonance for absorption from the ground state. Excitation frequencies that exactly match both resonance conditions may not be possible but transitions involving vibronic levels will extend the range of wavelengths available for ESA.

The fluorescence in the blue-green spectral region was recorded for three alexandrite excitation wavelengths and the results are shown in Fig. 11. The spectra are corrected for both detector and filter response and each spectrum was normalized to the highest peak in the scan range. The absolute intensity for the 738.6 nm excitation is at least an order of magnitude greater than for the 743.2 and 753.6 nm excitations. Using the room-temperature energy levels for Nd:BMAG it was possible to determine the origin of the upconverted transitions observed in these spectra and this is shown in Fig. 12 with respect to the energy level diagram.

The most probable excited level for ESA is the metastable $^4F_{3/2}$ state due to its long lifetime. However, for alexandrite pumping of Nd:BMAG there are no terminating levels within the pump wavelength range and it is concluded that this level is not involved in the processes occurring. Additionally, there were no significant changes in the intensity of the upconverted emission when the crystal was lasing which would be expected if this state was involved. The transition

FIG. 12. Excited state absorption transitions and associated fluorescence transitions observed for room-temperature alexandrite laser pumping of Nd:BMAG.

$^4F_{3/2} \rightarrow ^4G_{9/2}$ labeled transition 2 in Fig. 12, is a close match to the wavelength of the lasing photons at 1054 nm. This ESA transition will be present for all pump laser wavelengths and is not responsible for the pump wavelength dependent effects observed here.

The excitation wavelengths 743.2 and 738.6 nm producing blue fluorescence are a good match to the ESA transitions $^4F_{5/2} \rightarrow ^2P_{3/2}$ and $^4F_{7/2} \rightarrow ^4D_{3/2}$, respectively. These processes, indicated by transitions 3 and 4 in Fig. 12, decrease the number of ions reaching the upper laser level $^4F_{3/2}$ and thus reduce the efficiency of the laser. The two levels taking part, $^4F_{5/2}$ and $^4F_{7/2}$, are known to have very fast decay rates and ESA effects may only be associated with the high energy, fast pulse excitation of alexandrite laser pumping. Also, cross-relaxation between Nd^{3+} ion pairs may enhance ESA effects by changing the single-ion decay rates from these levels. Models describing ESA of pump photons have been discussed recently by Kliewer and Powell[9] and Petrin et al.[10] The nonlinear, coupled differential equations describing the level populations were solved numerically. The results show that excited state absorption of pump photons can decrease the slope efficiency but the model does not yet describe the full extent of the effect.

V. SUMMARY AND CONCLUSIONS

The results obtained in this work show that Nd^{3+} ions occupy several different crystal field sites in BMAG crystals. This produces large inhomogeneous broadening of the spectral transitions which influences the cross sections involved

Wavelength (nm)

FIG. 11. Room-temperature fluorescence of Nd:BMAG observed for different excitation wavelengths of the alexandrite laser.

in optical pumping and laser emission. Efficient energy transfer was observed at room temperature between ions in the different types of sites. The fluorescence observed at room temperature occurs from ions in one type of site indicating that energy transfer can be used to enhance laser pumping. The mechanism for energy transfer was not determined since this depends critically on the concentration of ions in the different types of sites. The efficiency of the energy transfer suggests that the sensitizer-activator separations are less than would be expected if the ions were distributed uniformly between the sites. Thus, it is highly probable that the ions are not uniformly distributed but are preferentially distributed in pairs or larger groups.

Strong blue and green fluorescence was observed when the Nd^{3+} ions were excited with an alexandrite laser. This upconverted emission was pump wavelength dependent and was attributed to excited state absorption processes. The lasing thresholds and slope efficiencies were determined for Nd:BMAG at several excitation wavelengths. The lasing slope efficiency was found to be reduced at the pumping wavelengths associated with excited state absorption. A pump wavelength was identified that minimized this type of loss mechanism.

[1] M. Alam, K. H. Gooen, B. DiBartolo, A. Linz, E. J. Sharp, L. Gillespie, and G. Janney, J. Appl. Phys. 39, 4728 (1968).

[2] M. Munasinghe and A. Linz, Phys. Rev. B 4, 3833 (1971).

[3] E. J. Sharp and J. E. Miller, J. Appl. Phys. 40, 4680 (1969).

[4] S. F. Bartram, Acta Cryst. B 25, 791 (1969).

[5] T. H. Allik, M. J. Ferry, R. J. Reeves, R. C. Powell, W. W. Hovis, D. P. Caffey, R. A. Utano, L. D. Merkle, and C. F. Campana, J. Opt. Soc. B 7, 1190 (1990).

[6] A. Linz, V. Behruss, and C. S. Naiman, J. Electrochem. Soc. 112, 60c (1965).

[7] G. H. Dieke, Spectra and Energy Levels of Rare Earth Ions in Crystals (Wiley, New York, 1968).

[8] L. G. Van Uitert, Luminescence of Inorganic Solids (Academic, New York, 1966), p. 484.

[9] M. L. Kliewer and R. C. Powell, IEEE J. Quantum Electron. 25, 1850 (1989).

[10] R. R. Petrin, M. L. Kliewer, R. C. Powell, I. D. Aggarwal, and R. G. Ginther, presented at the conference on Advanced Solid State Lasers, Salt Lake City, March 1990, proceedings to be published.

Crystallography, spectroscopic analysis, and lasing properties of $Nd^{3+}:Ba_2ZnGe_2O_7$

Toomas H. Allik

Science Applications International Corporation, 1710 Goodridge Drive, McLean, Virginia 22102

Michael J. Ferry,* Roger J. Reeves, and Richard C. Powell

Department of Physics, Oklahoma State University, Stillwater, Oklahoma 74078-0444

Wayne W. Hovis, David P. Caffey, Richard A. Utano, and Larry Merkle

*Center for Night Vision and Electro-Optics, U.S. Army Communications-Electronics Command, Fort Belvoir,
Virginia 22060-5677*

Charles F. Campana

Siemens Analytical X-Ray Instruments, Inc., 6300 Enterprise Lane, Madison, Wisconsin 53719

$Nd^{3+}:Ba_2ZnGe_2O_7$ (BZAG) is an attractive material to be pumped by laser diodes because its fluorescence lifetime is 305 μsec and it has a broad absorption centered at 806 nm. In addition, $Nd^{3+}:BZAG$ has a broad fluorescence spectrum and offers the potential for tunable laser output wavelengths centered at 1.05 and 1.34 μm. Time-resolved, site-selection spectroscopy measurements revealed ten different crystal-field sites for Nd^{3+} in BZAG, but strong energy transfer between nonequivalent ions at room temperature results in emission from only one major site. Diode-array side pumping of 5-mm-diameter rods produced optical slope efficiencies of 22.8%. Crystal structure, Judd–Ofelt analysis, and laser performance are discussed.

INTRODUCTION

For many years, Nd^{3+} doped in $Y_3Al_5O_{12}$ (YAG) has been the most common solid-state flash-lamp-pumped laser owing to its high stimulated-emission cross section, thermal conductivity, and mechanical strength. In the search for improved laser materials, many materials have been studied that possess theoretically better Q-switch properties than $Nd^{3+}:YAG$.[1] Unfortunately, many of these materials were generally unable to tolerate the thermal stress produced by the UV radiation that is present with flash-lamp pumping.[2] Today, with efficient and long-lived GaAlAs diodes operating at ideal pump wavelengths for Nd^{3+} ($^4F_{5/2}$, $^2H_{9/2}$ levels) in the near IR, it is possible to consider host materials with less stringent thermomechanical requirements than $Nd^{3+}:YAG$ has. Desirable properties for a diode-pumped Q-switched laser material include a longer fluorescence lifetime and a broader absorption band compared with $Nd^{3+}:YAG$. A long fluorescence lifetime would increase the storage capacity of the material and reduce the number of diodes needed to produce a given output energy. A broader absorption band would permit a greater wavelength tolerance for an array, thereby reducing system cost.

Flash-lamp-pumped laser action of $Nd^{3+}:Ba_2ZnGe_2O_7$ (BZAG) was demonstrated by the U.S. Army Night Vision Laboratory in 1972.[3] BZAG possesses the akermanite (melilite) structure and congruently melts at 1320°C, which allows these crystals to be grown by the Czochralski method.[4] The salient conclusions of the Night Vision study were that $Nd^{3+}:BZAG$ is a medium-gain laser material, with a stimulated-emission cross section, a fluorescence linewidth, and thermomechanical properties intermediate between those of YAG and most glasses.[3] $Nd^{3+}:BZAG$ possesses a longer fluorescence lifetime than $Nd^{3+}:YAG$ and exhibits a broader absorption and fluorescence spectrum than those of Nd^{3+}-doped YAG, YAlO₃, and YLiF₄.[1] In this study we report the results of x-ray diffraction, detailed spectroscopic analysis, and the lasing properties of Nd-doped BZAG under diode-array, alexandrite, and dye-laser pumping.

EXPERIMENTAL RESULTS AND DISCUSSION

Crystal Growth and Elemental Analysis

The BZAG crystals used in this study were grown in the late 1960's by A. Linz (Massachusetts Institute of Technology), who used the top-seeded solution technique with a nominal 2 mol % Nd^{3+} added to the melt. These samples are the same as those used by Horowitz et al.[3] in the previous study of this laser host. A spectroscopic sample was analyzed for elemental composition by Galbraith Laboratories, Knoxville, Tennessee. Analysis of the sample gave the following results (in weight percent): Nd, 0.14; Ba, 45.82; Zn, 10.74; Ge, 23.61; K, <0.010, and Na, <0.010. The corresponding Nd density was determined to be $2.9 \times 10^{-19} cm^2$.

Table 1. Summary of Single-Crystal X-Ray Diffraction Results for $Ba_2ZnGe_2O_7$[a]

Atom	x	y	z	$U(eq)$[b]
Ba	0.1651(1)	−0.3349(1)	0.4927(2)	28(1)
Zn	0.00000	0.00000	0.00000	26(1)
Ge	0.3591(2)	−0.1409(2)	0.0383(5)	25(1)
O(1)	0.0826(16)	0.1873(14)	0.8105(22)	41(4)
O(2)	−0.1393(16)	−0.3607(16)	0.2717(35)	48(6)
O(3)	0.00000	0.50000	0.8404(40)	26(4)

[a] All 281 reflections were considered observed on the basis that $F_0 > 6\sigma_i(F_0)$. A full-matrix least-squares refinement minimized $\Sigma_w(|F_0| - |F_c|)^2$, $w = \sigma^2(F_0) + 0.0066F_0^2$. For all reflections, refinement converged to $R = 0.0495$, $wR = 0.0721$, $S = 1.02$, and $(\Delta/\sigma)_{max} = 0.013$. Atomic coordinates ($\times 10^4$) are equivalent isotropic displacement parameters (Å $\times$ 10^3) are listed below

[b] Equivalent isotropic U defined as one third of the trace of the orthogonalized U_{ij} tensor. Parenthetical values are estimated standard deviations
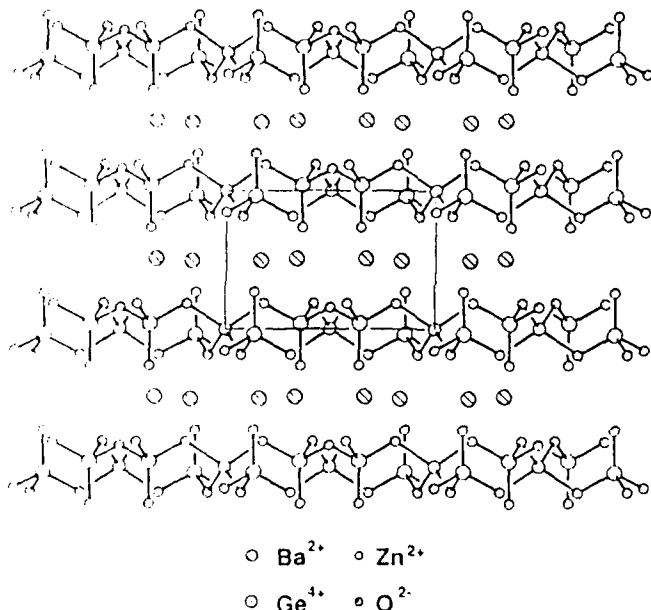

$\circ$ Ba^{2+} $\circ$ Zn^{2+}

$\circ$ Ge^{4+} $\circ$ O^{2-}

Fig. 1. Crystal structure and unit cell of $Ba_2ZnGe_2O_7$ (akermanite). The *c* axis is vertical.

X-Ray Diffraction

The crystal structure analysis was performed at 22°C, on a 0.25-mm-diameter ground sphere with an automated Nicolet R3m/V diffractometer equipped with an incident-beam graphite monochromator and Mo K-α radiation ($\lambda = 0.71073$ Å). A least-squares refinement of 20 centered reflections within $10.0° \leq 2\theta \leq 27.5°$ yielded the lattice parameters $a = 8.347(2)$ Å and $c = 5.554(3)$ Å, within reasonable agreement with the published values of Sirazhiddinov *et al.*[5] X-ray structure investigations showed that Nd:BZAG has tetragonal symmetry with a space group $P\bar{4}2_1m$ (No. 113), with $Z = 2$. Intensity data were collected in the 2θ mode (3.5° to 45.0°), with variable scan rates from 3.9 to 14.6° min^{-1}. The two standard reflections, measured for every 50 reflections, showed no significant change during data collection (<1%). The 2114 measured reflections had Miller indices of $-8 \leq h \leq 6$, $-6 \leq k \leq 8$, and $-6 \leq l \leq 8$. Equivalent reflections were averaged to give 281 unique reflections, $R_{int} = 7.49\%$. The structure was solved and refined by direct

methods with the Nicolet computer routine SHELXTL PLUS (MicroVax II). The atomic positions of the various ions in the unit cell are given in Table 1.

Figure 1 shows the BZAG unit cell. Four equivalent Ba ions occupy distorted square O antiprisms in the unit cell. Ge ions reside in distorted tetrahedra linked at one corner to form double Ge_2O_7 oriented upward and downward relative to the optic axis.[6] Both the Ba^{2+} and the Ge^{4+} sites possess C_s symmetry. Nd^{3+} ions substitute with charge compensation at the large Ba^{2+} site. Since the Zn^{2+} site (S_4) lacks inversion symmetry, it may be doped with large-oscillator-strength divalent transition metals, with the potential of creating a tunable vibronic laser material.

Absorption and Refractive-Index Measurements

The absorption spectra were recorded with a Perkin-Elmer Lambda 9 spectrometer equipped with the polarizer attachment and the 7500 computer. Figures 2 and 3 are the polarized absorption spectra of Nd^{3+}:BZAG between 300 and 1000 nm at room temperature. For most wavelengths, the absorption coefficient for light having its E vector normal to the c axis (E_σ) is greater than that for radiation with E parallel to the c axis (E_π). These observations are consistent with results for an analogous material, Nd^{3+}:$Ba_2MgGe_2O_7$.[7,8] The absorption cross section at the peak of the $^2F_{5/2}$ transition at 806 nm is five times higher for E_σ than for E_π. Another salient feature of the spectra is the inhomogeneous broadening occurring in Nd^{3+}:BZAG, which produces absorption linewidths inter-

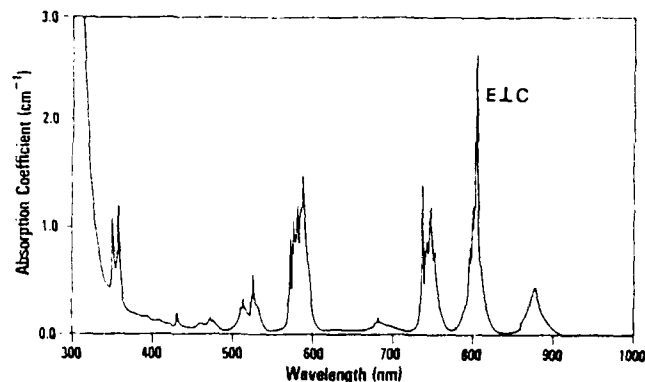Fig. 2. Absorption spectrum of Nd^{3+}:BZAG at room temperature with E perpendicular to C. The Nd concentration is 2.9×10^{19} cm^{-3}.
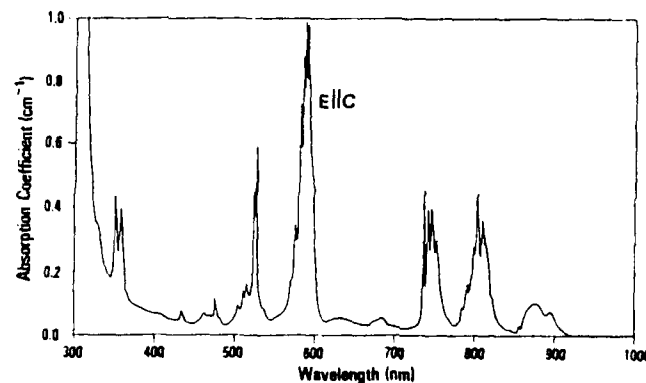

Fig. 3. Absorption spectrum of Nd^{3+}:BZAG at room temperature with E parallel to C.

Table 2. Indices of Refraction of Nd^{3+}:BZAG

Wavelength	n_π	n_σ
632.8	1.760	1.747
611.9	1.767	1.752
594.1	1.764	1.752
543.0	1.764	–
514.5	1.776	1.762
501.7	1.772	1.762
496.5	1.775	1.762
488.0	1.773	1.756
476.5	1.781	1.762
457.9	1.790	1.777
441.6	1.796	1.756
Sellmeier Coefficients		
A	2.012	2.000
B (μm^2)	0.01662	0.01168

mediate between those of YAG and glasses. This is due primarily to the distortion of the crystal field around the Nd^{3+} ions caused by charge compensation. Since no monovalent ions were detected in the sample, the substitution of Nd^{3+} for Ba^{2+} requires the use of interstitial anions or cation vacancies for charge compensation.[9]

The refractive indices, $n_{\sigma,\pi}$, of Nd:BZAG were measured by the method of minimum deviation. A polished prism was fabricated with an angle of 30°59′ perpendicular to the optic axis. He–Ne, He–Cd, and Ar-ion lasers provided polarized monochromatic light from 442 to 632 nm. The measured refractive indices are tabulated in Table 2. These experimental data were least-squares fitted to Sellmeier's dispersion equations, yielding

$$n_\pi{}^2 = 1 + \frac{2.012\lambda^2}{\lambda^2 - 0.01662 \ \mu m^2}, \tag{1}$$

$$n_\sigma{}^2 = 1 + \frac{2.000\lambda^2}{\lambda^2 - 0.01168 \ \mu m^2}. \tag{2}$$

Nd^{3+}:BZAG Fluorescence

The fluorescence spectrum of the $^4F_{3/2}$ metastable state in Nd^{3+}:BZAG was recorded with a Spex F222 spectrometer equipped with a liquid-N_2-cooled Ge or room-temperature Si detector. Figures 4–6 show the polarized fluorescence spectra in the region of the $^4F_{3/2} \to {}^4I_{9/2}$, $^4F_{3/2} \to {}^4I_{11/2}$, and $^4F_{3/2} \to {}^4I_{13/2}$ transitions and were corrected for detector response, grating efficiency, and polarization effects. The fluorescence spectra for transitions terminating to $^4I_{9/2}$ were not corrected for reabsorption. In all cases, the fluorescence intensity is stronger for E_σ than for E_π. These spectra are different from those published, and the differences are attributed to the lack of correction factors in the previous study.[3] The broad nature of these fluorescence curves shows the potential for continuously tunable laser output, which is not obtainable in Nd^{3+}:YAG.

In addition to the typical emission from Nd^{3+}, fluorescence was also seen at higher energies. Fluorescence and excitation spectra were recorded in this spectral region with the Perkin-Elmer MPF-66 fluorescence spectrophotometer. Figure 7 shows the room-temperature fluorescence spectrum of a band at 805 nm that is characteristic of emission from the $^4F_{5/2}$, $^2H_{9/2}$ manifold to $^4I_{9/2}$. It should

be noted that the fluorescence spectrum has not been corrected for the wavelength response of the R928 photomultiplier used. Detection of the fluorescence with a 750-nm blazed grating and an RCA 7102 (S-1) photomultiplier, and thus with nearly constant sensitivity between
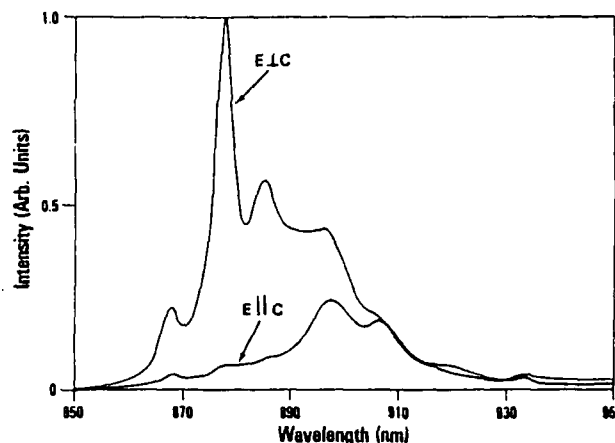

Fig. 4. Fluorescence spectrum at room temperature of the $^4F_{3/2} \to {}^4I_{9/2}$ transition.
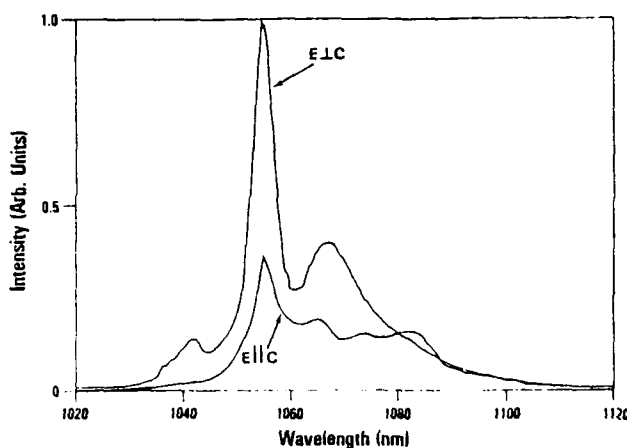

Fig. 5. Fluorescence spectrum at room temperature of the $^4F_{3/2} \to {}^4I_{11/2}$ transition.
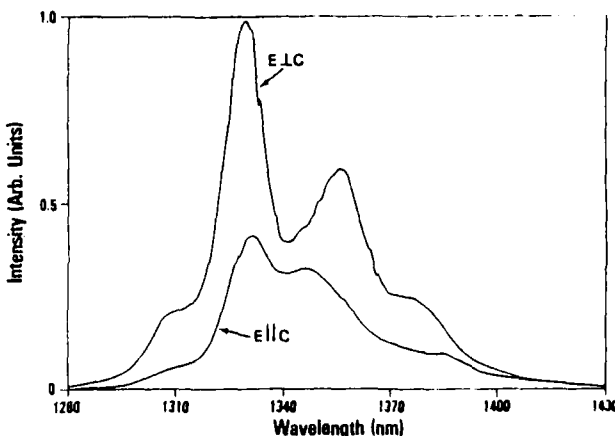

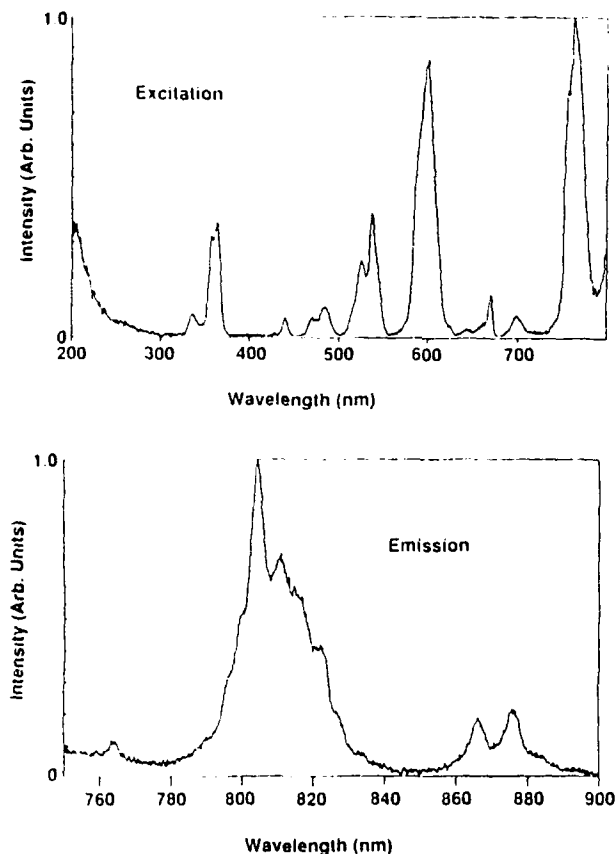Fig. 6. Fluorescence spectrum at room temperature of the $^4F_{3/2} \to {}^4I_{13/2}$ transition.

Fig. 7. The excitation and fluorescence spectra of Nd^{3+}:BZAG showing the emission from the $^4F_{5/2}$, $^2H_{9/2}$ manifold. For the emission spectrum the excitation wavelength was 587 nm and the resolution of the emission monochromator was 2 nm. For the excitation spectrum the emission wavelength was 804 nm, both monochromators had a 5-nm resolution, and the spectrum was corrected to 600 nm with a quantum counter.

800 and 900 nm, showed the $^4F_{5/2}$. $^2H_{9/2}$ emission to be weaker than the $^4F_{3/2}$ by approximately a factor of 50 at room temperature. The room-temperature fluorescence lifetime at 800 nm when frequency-doubled Nd^{3+}:YAG excitation is used is equal to that of the $^4F_{3/2}$ state to within experimental error. Given the rather small energy gap ($\sim$1000 cm^{-1}) between the $^4F_{5/2}$, $^2H_{9/2}$ and $^4F_{3/2}$ manifolds, we conclude that these manifolds reach thermal equilibrium in a time scale shorter than the room-temperature fluorescence lifetime. In view of the weakness of the $^4F_{5/2}$, $^2H_{9/2}$ fluorescence relative to that from $^4F_{3/2}$, this higher-energy manifold fluorescence should have a minimal effect on laser performance.

Figure 7 also shows the excitation spectrum of the germanium oxide fluorescence, which clearly agrees with the absorption spectra except for the absence of the strong UV absorption edge near 320 nm with a tail extending into the visible region.

Figure 8 shows the room-temperature fluorescence and excitation spectra in the UV/visible region. These spectra are characteristic of the host (presumably from a germanium oxide center)[10] and not of Nd^{3+} ($4f^3$) states. This broad fluorescence can also be excited by the doubled Nd^{3+}:YAG laser (532 nm). With this pump source the

fluorescence lifetime was observed to be shorter than 50 nsec.

Site-Selection Spectroscopy and Energy Transfer

With dye-laser excitation we were able to excite Nd ions selectively in specific crystal-field sites. Absorption and fluorescence spectra below 35 K were significantly narrow, enabling us to determine the energy-level positions of the Nd^{3+} ions. An excitation spectrum was generated by using Coumarin 440 dye pumping in the region of the $^2P_{1/2}$ energy level since it is nondegenerate with respect to the electric field (it has only one Stark component) and is relatively isolated from other energy levels. The laser provided pulses of less than 10-nsec duration and less than 0.5-Å FWHM. The excitation spectrum of Nd^{3+}:BZAG appears in Fig. 9, which shows five crystal field sites (labeled A through E), with the majority of Nd^{3+} occupying A sites. These sites are due to dramatically different crystal-field interactions with Nd^{3+}. Three of these sites are found to be composed of distinct subsites (A_1–A_4, $D_{1,2}$, and $E_{1,2}$) for a total of ten crystal-field sites. These transitions are attributable to weaker crystal-field variations and exhibit changes in wavelengths and intensities (concentrations) resulting from Nd^{3+} ions' residing in the Ba^{2+} site with different nearest neighbors.

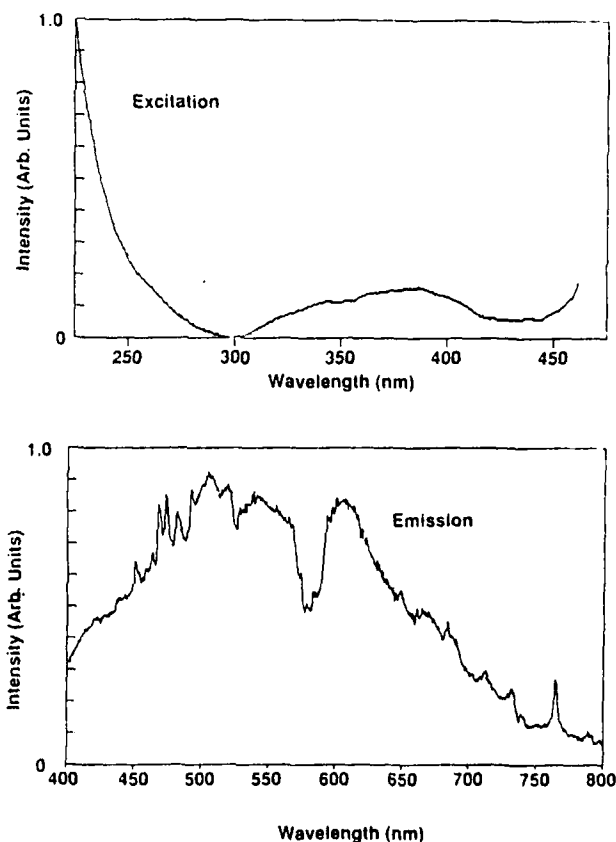Low-temperature fluorescence spectra indicate that the

Fig. 8. Excitation and fluorescence spectra at room temperature of the host. For the emission spectrum the excitation wavelength was 220 nm and the resolution of the emission monochromator was 2 nm. For the excitation spectrum the emission wavelength was 500 nm, and the spectrum has been corrected with a quantum counter.
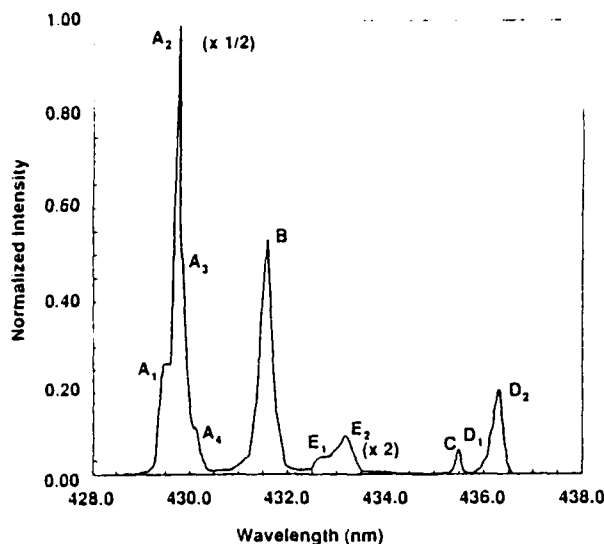
Fig. 9. Excitation spectrum at 35 K in the region of the $^4I_{9/2} \rightarrow$ $^2P_{1/2}$ transition. The excitation peaks correspond to different crystal-field sites.

most intense transition from $^4F_{3/2}$ to $^4I_{11/2}$ is site dependent and ranges from 1052.5 nm for A_1 to 1078.0 nm for D_1. The Stark levels for $^4I_{9/2}$, $^4I_{11/2}$, the lower state of $^4F_{3/2}$, and $^2P_{1/2}$ have been spectroscopically determined for sites A_1, B, C, D_1, and D_2 and appear in Fig. 10. Line overlap of the various subsites is responsible for the multisite fluorescence observed at low temperatures and inhibits the clear identification of the Stark levels of all sites. Room-temperature fluorescence at different excitation wavelengths exhibits only type A fluorescence, which implies rapid energy transfer and an enhancement in laser pumping. In Nd^{3+}:$Ba_2MgGe_2O_7$ the energy transfer is thermally activated and occurs on a time scale much faster than 10 μsec.[8]

The low-temperature fluorescence lifetimes of $^4F_{3/2}$ for the various sites also appear in Fig. 10. The fluorescent lifetime of the A site was measured between 10 and 350 K and was temperature independent for this sample concentration.

Branching Ratios and Radiative Lifetimes of Nd^{3+}:$BZAG$
The branching ratios and radiative lifetimes of $^4F_{3/2} \rightarrow {}^4I_J$ (J = 9/2, 11/2, 13/2, 15/2) for Nd^{3+} in BZAG were determined by direct application of the Judd–Ofelt theory.[11,12] Judd–Ofelt analysis has been performed with a high degree of accuracy to determine Nd^{3+} laser parameters. Numerous authors have described the data-reduction procedures for isotropic materials, and the procedures will not be given here.[13,14] The measured polarized absorbances were averaged spatially by the method of Lomheim and DeShazer[15] since the absorption coefficient for Nd^{3+}:$BZAG$ varies dramatically with the polarization of the incident light. The spatially averaged integrated absorbance, $\bar{\Gamma}$, is

$$\bar{\Gamma} = -(1/L) \int_{band} \ln\{1/3 \exp[-\alpha_\pi(\lambda)L] + 2/3$$

$$\times \exp[-\alpha_\sigma(\lambda)L]\} \, d\lambda, \qquad (3)$$

where L is the sample length and $\alpha(\lambda)$ is the absorption coefficient. To determine $\bar{\Gamma}$, the π and σ transmittance spectra (with the Fresnel loss removed) were merged together and integrated as given by Eq. (3). The absorbances were converted to line strengths, S_{meas}, by using Eq. (4):

$$S_{meas} = \frac{3ch(2J + 1)}{8\pi^3 e^2 \bar{\lambda}\rho} \left[\frac{9n}{(n^2 + 2)^2} \right] \bar{\Gamma}, \qquad (4)$$

where $\bar{\lambda}$ is the mean wavelength of the band, J = 9/2 is the angular momentum of the ground $^4I_{9/2}$ manifold, and ρ is the Nd^{3+} concentration (2.9×10^{19} cm^{-3}). Values for the index of refraction were taken from Sellmeier's dispersion equations (1) and (2) and were averaged in the same manner as the integrated absorbances. Table 3 shows the spatially averaged absorbances and line strengths for nine absorption bands. A least-squares fitting of S_{calc} to S_{meas} yields values for the Judd–Ofelt parameters of $\Omega_{2,4,6}$. The radiative lifetime and the branching ratios of the $^4F_{3/2}$ state along with $\Omega_{2,4,6}$ are given in Table 4.

It is worthwhile pointing out two prominent features from this analysis. First, the branching ratio to $^4I_{9/2}$ is significantly larger in Nd^{3+}:$BZAG$ (41%) than in Nd^{3+}:YAG ($\sim$30%),[1] which enhances the stimulated-emission cross section down to the ground-state manifold. This feature has been observed in another melilite crystal, Nd^{3+}:$SrGdGa_3O_7$,[16] and is desirable for generating 0.9-μm
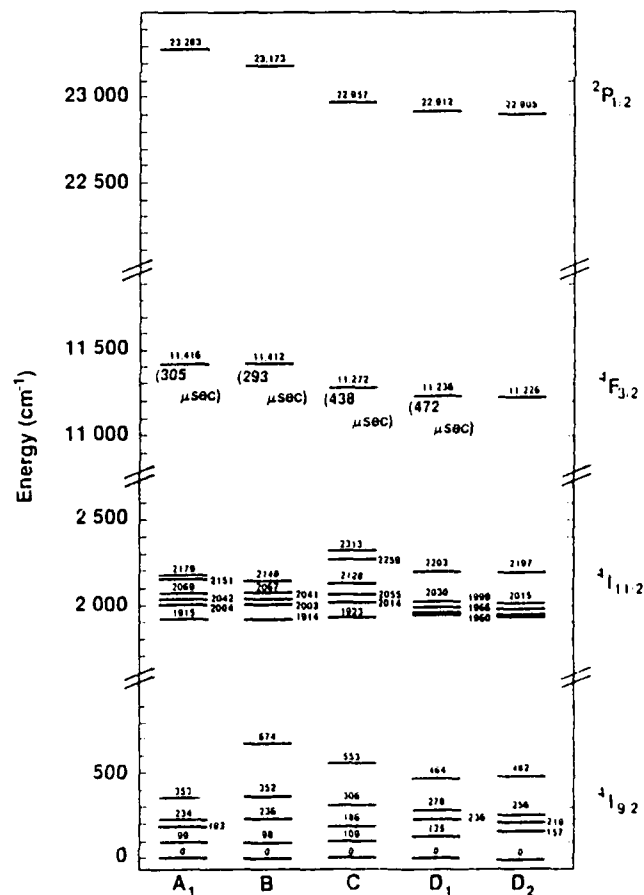

Fig. 10. Energy levels and fluorescence lifetimes for Nd^{3+}:$BZAG$.

Table 3. Spatially Averaged Absorbances and Line Strengths (Measured and Calculated) for Nd^{3+}:BZAG

Excited J Manifold	λ (nm)	$\bar{\Gamma}$ (nm/cm)	S_{meas}[a]	S_{calc}[a]	$(\Delta S)^2$
$^4F_{3/2}$	877	3.910	0.83	1.12	0.0841
$^4F_{5/2}$, $^2H_{9/2}$	804	14.434	3.34	3.20	0.0196
$^4F_{7/2}$, $^4S_{3/2}$	746	11.642	2.90	3.03	0.0169
$^4F_{9/2}$	685	1.029	0.28	0.21	0.0049
$^2H_{11/2}$	627	0.110	0.03	0.06	0.0009
$^4G_{5/2}$, $^2G_{7/2}$	585	18.019	5.69	5.70	0.0001
$^2K_{13/2}$, $^4G_{7/2}$, $^4G_{9/2}$	529	5.223	1.82	1.62	0.0400
$^2K_{15/2}$, $^2G_{9/2}$, $^2D_{3/2}$, $^2G_{11/2}$	467	1.132	0.44	0.34	0.0100
$^2P_{1/2}$	431	0.279	0.12	0.16	0.0016

[a]10^{-20} cm^2; rms line strength, 2.50×10^{-20} cm^2; $\Delta S_{rms} = 0.17 \times 10^{-20}$ cm^2; rms error, 6.8%.

Table 4. Judd–Ofelt Parameters and Predicted Optical Properties of Nd^{3+} in BZAG

Judd–Ofelt parameters	$\Omega_2 = 3.22 \times 10^{-20}$ cm^2
	$\Omega_4 = 3.86 \times 10^{-20}$ cm^2
	$\Omega_6 = 4.31 \times 10^{-20}$ cm^2
$^4F_{3/2}$ Radiative lifetime	280 μsec
Branching ratios	
$^4F_{3/2} \rightarrow {}^4I_{9/2}$	41.1%
$^4F_{3/2} \rightarrow {}^4I_{11/2}$	49.1%
$^4F_{3/2} \rightarrow {}^4I_{13/2}$	9.4%
$^4F_{3/2} \rightarrow {}^4I_{15/2}$	0.4%

radiation from Nd^{3+}-doped laser materials. Second, the radiative lifetime of the $^4F_{3/2}$ state has been calculated to be 280 μsec and is within experimental error of the fluorescence lifetime of the majority A site. This implies that the quantum efficiency of the $^4F_{3/2}$ state of Nd^{3+}:BZAG, $\eta_q = \tau_f/\tau_r$, is near unity.

Laser Measurements

Room-temperature laser action was achieved in Nd^{3+}:BZAG at 1.054 μm in both the side- and end-pump geometries with three different laser sources. In the side-pump configuration the pump source was a laser-diode array operating at 806 nm that was close-coupled to the rod; it was described in a previous publication.[17] The end-pump sources were an Allied Technologies MS500 alexandrite laser (1.6 W) operating at 755 nm and a 1-W Coherent 699-29 Rhodamine 6G dye laser operating near 590 nm. For alexandrite end pumping, the alexandrite laser was collimated to a 5-mm diameter and operated long pulse (100 μsec) at 4 Hz. The cw dye laser was focused into the rod with a 3-cm focal-length lens and chopped at a 50% duty cycle to prevent damage to the coatings. Pulsed output energy was measured with Laser

Precision RjP-734(6) pyroelectric joulemeters, and the temporal output was monitored with a Si photodiode. A Lexel Model 504 power meter was used to measure the dye-laser pump power.

The laser rods were fabricated from a 5-mm-diameter × 27-mm-long sample with the c axis nearly perpendicular to the rod faces. The optical quality of the material was excellent, and the optical finishes showed no water absorption damage after more than 15 years of storage. An interferogram of this stock material produced a peak-to-valley distortion of 0.156 wave, with a rms deviation of 0.027 wave at 632 nm. Two rods were fabricated to a length of 11 mm and were broadband antireflection coated at one end (centered at 1.05 μm) and highly reflection coated on a 5-m convex radius of curvature on the other. The barrel of the rod was polished and was antireflection coated for the 806-nm pump wavelength on 240° of the barrel for efficient side pumping. The rod was mounted in a polished Cu block and was rotated to maximize absorption and laser performance at 1.05 μm.

Table 5 summarizes the experimental results for these three pump wavelengths. The optical slope efficiencies in Table 5 for alexandrite pumping were normalized for absorbed power in the crystal since the coating was partially reflective for the pump radiation. Figure 11 shows a comparison between alexandrite end-pumped Nd^{3+}-doped BZAG and YAG made with the same cavity length and output coupler. The slope efficiencies for Nd^{3+}:YAG and Nd^{3+}:BZAG were 59% and 16%, respectively. The diode-array side-pumping performance for Nd^{3+}:BZAG appears in Fig. 12. The slope efficiency of 22.8% is significantly less than Nd^{3+}:YAG's value of 47.7% in this setup.[17] The lower efficiency of Nd^{3+}:BZAG is attributable to higher resonator losses and to a reduced upper-state efficiency[18] compared with those of Nd^{3+}:YAG. The round-trip Findlay–Clay losses for multimode operation of Nd^{3+}:BZAG were measured to be 4%, which are 33% higher

Table 5. Laser Performance of Nd^{3+}:BZAG (1054 nm) at Three Excitation Wavelengths

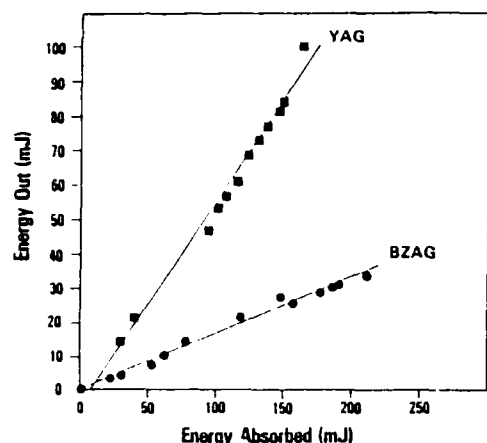| Pump Laser Wavelength (nm)	Pump Geometry	Cavity Length (cm)	Pulse Duration	Outcoupler Reflectivity (Radius of Curvature)	Slope Efficiency (%)
Diode array (806)	Transverse	10	300 μsec	0.975 (64 cm)	22.8
Alexandrite (755)	Longitudinal	15	100 μsec	0.975 (57 cm)	16.4
Rhodamine 6G (590)	Longitudinal	3	cw	0.97 (6 cm)	18.0

Fig. 11. Laser performance of Nd^{3+}:YAG and Nd^{3+}:BZAG when alexandrite laser end pumping is used.
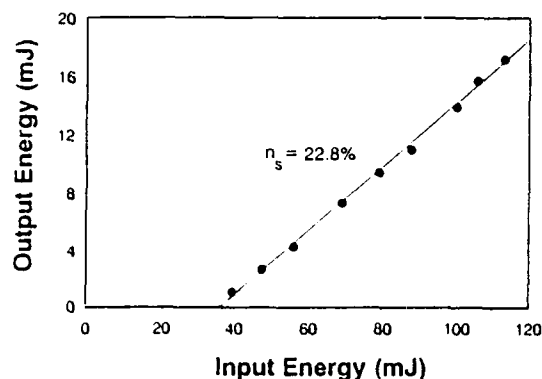

Fig. 12. Multimode laser output as a function of input energy for a 5-mm-diameter, 11-mm-long Nd^{3+}:BZAG rod. The diode-array pulse duration is 300 μsec.

than those for Nd^{3+}:YAG.[17] YAG doped at its typical Nd concentration of 0.72 wt. % has a larger absorption coefficient than Nd^{3+}:BZAG used in this study (0.14 wt. %). In addition, a larger-diameter (6.35-mm) rod of Nd^{3+}:YAG was used, enabling a larger portion of the input energy to be absorbed.

The laser performance of Nd^{3+}:BZAG has been measured at three excitation wavelengths. Normalization for the quantum defect for the three pump wavelengths in Table 5 results in comparable quantum slope efficiencies at 806 nm (30.0%) and 590 nm (32.2%) but is significantly lower at 755 nm (22.9%). Pumping into the $^4F_{7/2}$, $^4S_{3/2}$ band with an alexandrite laser has been shown to cause low lasing slope efficiencies owing to pump-wavelength-dependent losses in Nd^{3+}-doped BMAG.[8] Excited-state absorption of the pump photons can excite Nd^{3+} ions to high-lying $^4D_{3/2}$ and $^2D_{3/2}$ states from initial levels above $^4F_{3/2}$. This creates a loss mechanism in BMAG and possibly may well do so in BZAG.

CONCLUSIONS

A spectroscopic analysis and laser study of Nd^{3+}:BZAG has been performed. The broad absorption spectrum at 800 nm makes BZAG an attractive material to be pumped by laser diodes. The 305-μsec fluorescence lifetime is beneficial for high-energy storage and efficient Q-switch

operation. The diode-array-pumped slope efficiency was 22.8%, which is less than the 47.7% value determined for Nd^{3+}:YAG. This smaller efficiency is attributed to less efficient pump coupling owing to the smaller-diameter Nd^{3+}:BZAG rod and higher scattering losses. Diode-array-pump efficiency can be increased by improvement in crystal quality, along with an increase in the Nd concentration or absorption path length and more efficient pump coupling.

ACKNOWLEDGMENTS

REFERENCES

1. A. A. Kaminskii, *Laser Crystals* (Springer-Verlag, New York, 1981), Vol. 14.
2. W. Koechner, *Solid State Laser Engineering*, 2nd ed. (Springer-Verlag, Berlin, 1988), pp. 28–34.
3. D. J. Horowitz, L. F. Gillespie, J. E. Miller and E. J. Sharp, "Laser action of Nd^{3+} in a crystal $Ba_2ZnGe_2O_7$," J. Appl. Phys. **43**, 3527–3530 (1972).
4. M. R. Kokta, Union Carbide Corporation, Washougal, Washington 98671 (personal communication).
5. N. A. Sirazhiddinov, N. N. Mirbabaeva, and R. G. Grebenshchikov, "Solid solutions in the $Ba_2ZnGe_2O_7$–$Sr_2ZnGe_2O_7$ system," Russ. J. Inorg. Chem. **19**, 576–578 (1974).
6. S. F. Bartram, "Crystal structure of $Y_2SiBe_2O_7$," Acta Cryst. B **25**, 791–795 (1969).
7. M. Alam, K. H. Gooen, B. Di Bartolo, A. Linz, E. Sharp, L. Gillespie, and G. Janney, "Optical spectra and laser action of neodymium in a crystal $Ba_2MgGe_2O_7$," J. Appl. Phys. **39**, 4728–4730 (1968).
8. M. J. Ferry, M. L. Kliewer, R. J. Reeves, R. C. Powell, and T. H. Allik, "Lasing properties and excited state absorption of $Nd:Ba_2MgGe_2O_7$," in *Digest of the OSA 1989 Annual Meeting* (Optical Society of America, Washington, D.C., 1989), paper FV4.
9. L. G. Van Uitert, *Luminescence of Inorganic Solids* (Academic, New York, 1966), pp. 470–475.
10. G. Blasse and A. Bril, "Observations on the luminescence of some oxides containing post-transition metal ions," Mat. Res. Bull. **5**, 231–242, 1970.
11. B. R. Judd, "Optical absorption intensities of rare-earth ions," Phys. Rev. **127**, 750–761 (1962).
12. G. S. Ofelt, "Intensities of crystal spectra of rare-earth ions," J. Chem. Phys. **37**, 511–520 (1962).
13. W. F. Krupke, M. D. Shinn, J. E. Marion, J. A. Caird, and S. E. Stokowski, "Spectroscopic, optical, and thermomechanical properties of neodymium- and chromium-doped gadolinium scandium gallium garnet," J. Opt. Soc. Am. B **3**, 102–113 (1986).
14. W. F. Krupke, "Induced emission cross-sections in neodymium laser glasses," IEEE J. Quantum Electron. QE-10, 450–457 (1974).
15. T. S. Lomheim and L. G. DeShazer, "Optical-absorption intensities of trivalent neodymium in the uniaxial crystal yttrium orthovanadate," J. Appl. Phys. **49**, 5517–5522 (1978).

16. H. R. Verdun, L. R. Black, G. de la Fuente, and D. M. Andrauskas, "Growth and characterization of Nd-doped aluminates and gallates with the melilite structure," in *Tunable Solid State Lasers*, M. L. Shand and H. P. Jenssen, eds,. Vol. 5 of OSA Proceedings Series (Optical Society of America, Washington, D.C., 1989), pp. 405–407.

17. T. H. Allik, W. W. Hovis, D. P. Caffey, and V. King, "Efficient diode-array-pumped Nd:YAG and Nd:Lu:YAG lasers," Opt. Lett. 14, 116–118 (1989).

18. W. Koechner, *Solid State Laser Engineering*, 2nd ed. (Springer-Verlag, Berlin, 1988), pp. 95–96.

III. SPECTROSCOPIC PROPERTIES OF CHROMIUM-DOPED LASER CRYSTALS

The five manuscripts in this section document the results of four-wave mixing studies of Cr^{3+}-doped laser crystals. The first paper describes results obtained on alexandrite. One important aspect of this work is the theoretical development that was done to understand the properties of four-wave mixing signals of ions in solids. This has resulted in the characterization of long range energy transfer among the chromium ions which can affect the saturation properties of the material during optical pumping. In addition, this work reports the identification of the relaxation channel between the pump band and the metastable state which has not been previously investigated.

Similar properties were studied in chromium-doped emerald, several garnet crystals, and a glass ceramic host. The work on emerald and the garnet hosts focused on characterizing the energy migration and on the identification of ions in different local crystal field sites. Laser-induced color centers were also reported in the garnets. In the class ceramic host the investigation focused on relaxation processes.

This work is a continuation of previous studies of Cr^{3+} laser materials. The data base being established from this study is providing information that can be used to predict the spectral properties Cr^{3+} ions in other laser crystals. On important observation from this work is that non-random distributions of Cr^{3+} ions are present in most materials and play an important role in determining spectral dynamics.

Laser-induced grating spectroscopy of alexandrite crystals

Guy D. Gilliland, Andrzej Suchocki,* Keith W. Ver Steeg, and Richard C. Powell

Department of Physics, Oklahoma State Univeristy, Stillwater, Oklahoma 74078-0444

Donald F. Heller

Allied-Signal, Inc., Morristown, New Jersey 07960
(Received 18 February 1988)

Four-wave-mixing techniques were used to establish and probe population gratings of Cr^{3+} ions in alexandrite crystals at temperatures between 10 and 300 K. The results were interpreted in terms of the interaction of the laser radiation with a two-level atomic system. They provide information about the characteristics of four-wave-mixing signals for this physical situation as well as being useful in characterizing the properties of energy transfer and dephasing within the ensemble of Cr^{3+} ions. The patterns of the transient four-wave-mixing signals are consistent with a model based on the pumping dynamics of ions in the mirror and inversion crystal-field sites. The variation of the signal intensity with laser power is strongly affected by beam depletion. The characteristics of exciton migration among Cr^{3+} ions in mirror sites were determined from the results of measuring the variation of the signal decay rate with grating spacing. The temperature dependences of the ion-ion interaction rate, the exciton-phonon scattering rate, and the diffusion coefficient were determined. These are found to be essentially the same for pumping into the $^4T_2$ and ^2E levels, but the effects of scattering from a grating of ions in inversion sites is much stronger for $^4T_2$ pumping. The dephasing times for the atomic system were found from analyzing the variation of the signal intensity with grating spacing. For pumping into the $^4T_2$ level the dephasing is dominated by radiationless decay processes. A model is presented for the decay channel that provides a theoretical explanation for the decay process which is consistent with the measured temperature and frequency dependences of the results as well as their variation with crystal-field strength. For pumping into the ^2E level the dephasing is dominated by dephasing processes associated with the inhomogeneous linewidth of the transition.

I. INTRODUCTION

Four-wave mixing (FWM) can be used as a spectroscopic technique by establishing excited-state, spatial population gratings in an ensemble of atoms or molecules.[1-4] We have recently applied this laser-induced-grating (LIG) spectroscopy method to the study of dynamical processes in several Cr^{3+}-doped laser crystals.[5-8] The results have been useful in characterizing the general properties of energy transfer, radiationless relaxation, and excited-state absorption in these materials under specific pumping conditions. The work reported here extends this study on one particular material, alexandrite, in two ways: The first involves the development of theoretical models to understand the properties of the LIG signal for this specific type of physical situation; the second involves additional investigations of energy transfer and radiationless relaxation, including both the use of different pumping conditions and the development of more rigorous theoretical models, which results in a more detailed understanding of the characteristics of these processes.

Alexandrite is an important, tunable, solid-state laser material consisting of Cr^{3+} ions substituted for Al^{3+} ions in a chrysoberyl host crystal, $BeAl_2O_4$.[9] The sample used in this investigation contained 1.14×10^{19} cm^{-3} Cr^{3+} ions. There are two nonequivalent crystal field sites for the aluminum ions in the chrysoberyl lattice, one having mirror symmetry and one with inversion symmetry. Approximately 78% of the Cr^{3+} ions occupy mirror sites and 22% occupy inversion sites.[10] The optical spectroscopic properties of Cr^{3+} ions in each type of site have been reported previously.[11-13]

Previous LIG results on alexandrite demonstrated the ability to establish gratings in either mirror or inversion-site ions by pumping into the $^4T_2$ levels of the ions in these two types of sites.[5,8] The gratings were found to be dominated by the difference in the dispersion contribution to the refractive index when the Cr^{3+} ions are in the excited state versus the ground state, with the contribution due to the difference in the ground- and excited-state absorption cross sections consistent with the results of direct excited-state absorption measurements.[14] The presence of exciton diffusion among the Cr^{3+} ions in mirror sites was observed below 150 K and the diffusion coefficient was found to increase as temperature was lowered. The dephasing times of the LIG signals were attributed to radiationless relaxation processes occurring after pumping into the $^4T_2$ level and the rate of these processes was found to be different with different local crystal fields for the Cr^{3+} ions. Although these results demonstrated the general properties of laser-induced population gratings in alexandrite crystals, they left several unanswered questions about the observed transient and

equilibrium LIG signal characteristics and did not provide complete details of the exciton dynamics and radiationless relaxation processes in this material. Some of these questions are addressed in the following sections.

The detailed description of the LIG experimental setup was reported previously.[8] The two excitation beams of the same frequency were provided by either an argon-ion laser or an argon-ion-laser-pumped dye laser. A He-Ne laser was used for the probe beam. The dynamical response of the LIG signal was monitored by using a mechanical chopper to interrupt the pump beams while processing the signal beam with an EG&G Princeton Applied Research (PAR) signal averager. For measurements of the steady-state LIG signal, the probe beam was chopped and an EG&G PAR lock-in amplifier was utilized to improve the signal-to-noise ratio.

II. EQUILIBRIUM POWER DEPENDENCE AND LIG SIGNAL TRANSIENTS

In order to fully understand the characteristics of signals observed in LIG spectroscopy involving population gratings, two theoretical models are required. The first involves the formalism describing the mixing of the four electromagnetic fields in the sample due to coupling through the nonlinear complex refractive index of the material. The second involves the formalism describing the pumping dynamics of the atomic system interacting with the laser beams. The laser pump beams interact with the atomic ensemble through a resonant electronic transition, thus changing the population distribution of atoms in different electronic levels. Since the complex refractive index of the system depends on the relative occupation of the various energy levels, this pumping provides the laser-induced modulation of the refractive index, which gives the coupling mechanism for the electric fields. The interference pattern of the two crossed laser pump beams results in a sine-wave spatial distribution of the excited-state population, and thus in a refractive index grating of the same shape. The model for the nonlinear interaction of the laser beams with the atomic system is essentially the same for all FWM applications. This is important in describing LIG spectroscopy results obtained under equilibrium pumping conditions such as the power dependence of the signal strength as described in this section and the dephasing time of the signal as described in Sec. IV. The additional model describing the pumping dynamics of the atomic system is required to explain the transient response of the LIG signal as described in this section and to characterize the effects of transient physical processes such as energy transfer or radiationless relaxation as described in the following two sections.

A. Equilibrium power dependence

The pump power dependence of the FWM scattering efficiency is important in understanding the observed signals in LIG spectroscopy. The standard approach[15,16] in studying the dynamics of the transient grating formation is to model the system explicitly using the nonlinear wave equation which couples the electric fields through the

nonlinear susceptibility of the material. This theoretical approach to the FWM scattering efficiency predicts a quadratic dependence on pump power for laser intensities below the saturation intensity, $I < I_s$. Recently this theory was extended to apply to the geometrical situation used here.[17] The system is modeled as an ensemble of two-level atoms, and the fields are assumed to be plane waves. This is only an approximation to the actual case of focused Gaussian beams in a multilevel system, but the results predicted from this model are useful in understanding the spectral and FWM dynamics. This model and the model of Abrams and Lind[15] start with the same assumptions, but the theoretical development of the two models differ.

For a two-level system the polarization can be expressed as

$$P(E_0 + \Delta E) = e^{i\omega t} X(E_0)$$
$$\times \left\{ E_0 + \Delta E - \frac{E_0^2 \Delta E^* + |E_0|(\Delta E)^2}{I_s + |E_0|^2} \right\},$$

(1)

where

$$X(E) = -2(\alpha_0/k)[(i+\delta)/(1+\delta^2+|E/E_s|^2)] \quad (2)$$

δ is the normalized detuning from line center, α_0 is the line-center small-signal attenuation coefficient, E_s is the saturation field, I_s is the saturation intensity, $E_0 = E_a + E_b$, and $\Delta E = E_p + E_s$. E_a and E_b represent the write beams, E_p represents the probe beam, and E_s represents the signal beam. Assuming plane waves for all of the fields and equal intensities for the write beams ($I_a = I_b$), using the slowly varying envelope approximation, and solving the wave equation

$$\nabla^2 E + \frac{\epsilon}{c^2} \frac{\partial^2 E}{\partial t^2} = -\frac{4\pi}{c^2} \frac{\partial^2 P^{NL}}{\partial t^2}, \quad (3)$$

where

$$P^{NL} = X E \quad (4)$$

leads to two coupled equations for the fields. Solving these equations yields an expression for the scattering efficiency given by[17]

$$\eta = \frac{(I/I_s)^2 (1 + 2I/I_s)^2 \exp[2\alpha_0 L/(1+\delta^2)]}{\{[(1+2I/I_s) - 2(I/I_s)^2](\sec\theta - 1)\}^2}$$
$$\times \{\exp(-2\xi_R L) + \exp(-2\xi_R L \sec\theta)$$
$$- 2\exp[-\xi_R(1+\sec\theta)L]\cos[\xi_I(1-\sec\theta)L]\},$$

(5)

where

$$\xi = \xi_R + i\xi_I$$
$$= \alpha_0 \frac{1-i\delta}{1+\delta^2} \frac{[1+2I/I_s - 2(I/I_s)^2]}{[(1+2I/I_s)^2 - 4(I/I_s)^2]^{3/2}}. \quad (6)$$

Equation (5) can be simplified somewhat, if $|\xi L|$ is small and θ is not very large, yielding[17]

$$\eta = \frac{\alpha_0^2/(1+\delta^2)\{(I/I_s)^2(1+2I/I_s)^2L^2\exp(-2\xi_R L)\exp[2\alpha_0 L/(1+\delta^2)]\}}{[(1+2I/I_s)^2-4(I/I_s)^2]^3}[1+\xi_R L(1-\sec\theta)]. \tag{7}$$

For $I \ll I_s$ this equation shows that the FWM scattering efficiency depends quadratically upon the write-beam power. In both equations η decreases with increasing θ.

Figure 1 shows the FWM relative scattering intensity as a function of the laser power in each of the write beams for direct excitation of the $2\overline{A}$ sublevel of the split ^2E state. The LIG was formed by crossing two laser beams from an argon-ion-pumped jet dye laser using DCM [4-(dicyanomethylene)-2-methyl-6-(p-dimethyl-amino-styryl)-4H-pyran] dye tuned to 677.8 nm. Using the measured lifetime, absorption cross section, and absorption wavelength for this transition (2.3 ms, 8.5×10^{-20} cm^2, and 677.8 nm, respectively) the saturation intensity is approximately 1500 W/cm^2. The dashed line in Fig 1 is the best fit to the data using Eq (7) with $I_s = 1500$ W/cm^2. The theoretical curve has a slope of two, while the data has a less-than-quadratic dependence on write-beam power. The solid line in the figure is the best fit to the data using the full scattering efficiency expression, Eq. (5), with the same value for I_s. The theoretical fit to the data is quite good, showing a departure from the quadratic power dependence at high powers.

The difference between the two expressions used to fit the data in Fig. 1 is a result of the simplifying assumption made in deriving Eq. (7) from Eq. (5). The assumption made is that $|\xi L|$ is small. Since the absorption line excited is quite narrow (≈ 1 cm^{-1}) and the laser linewidth is approximately of the same width (0.7 cm^{-1}), it can be assumed that the imaginary part of ξ is zero since the normalized detuning parameter is zero. ξ_R represents the laser-induced change in the absorption coefficient. The results presented above imply that the laser induced change in the absorption coefficient is not negligible for
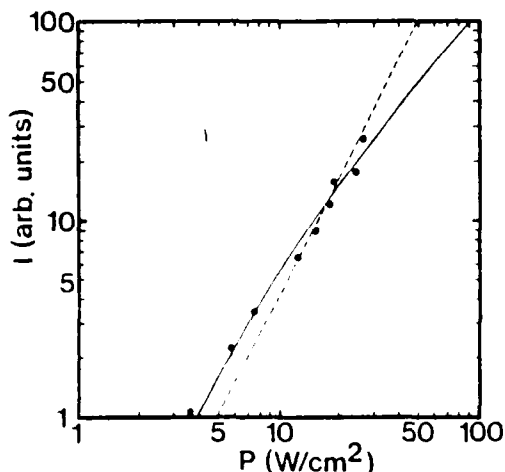
these experimental conditions. This causes additional beam depletion which is evident in the experimental results.

Experimental measurements of the power dependence of the FWM signal pumping into the $^4T_2$ level of the mirror sites have been done previously.[5,8] A slight saturation is evident in the data. This departure from quadratic power dependence is also a result of the laser-induced change in the absorption coefficient and not a purely saturation effect since the power of the write beams was much less than the saturation intensity.

B. Transient LIG signal patterns

Transient FWM signals have many unique features that distinguish them from steady-state FWM signals. Abrams and Lind[15] have studied steady-state FWM processes theoretically, and Silberberg and Bar-Joseph[18] have extended their steady-state solutions to the treatment of the transient FWM response of a saturable absorber. As mentioned earlier, the FWM signal in alexandrite crystals is a result of scattering of the probe beam from a laser-induced grating that is predominantly dispersive. Although the results of Abrams and Lind[15] apply to absorption gratings, dispersion gratings, or a mixed grating, the theoretical treatment of the time evolution of the FWM signal in the presence of all three laser beams has only been applied to pure absorption gratings.[18-20] In this section the theoretical treatment of the time evolution of the FWM signal is extended to the case of a mixed grating, and the results are used to analyze the transient LIG signal from Cr^{3+} population gratings of ions in both types of crystal-field sites in alexandrite.

Assuming a three-level atomic system, where the relaxation between the level directly excited and the metastable level is fast and the lifetime of the metastable level is relatively long, the rate equation for the ground-state population density is

$$\frac{ds_0}{dt} = -(\sigma I/\hbar\omega)s_0+(S-s_0)/\tau. \tag{8}$$

In Eq. (8) σ is the absorption cross section, I is the laser intensity of each write beam of frequency ω, S is the total population of ions, and τ is the lifetime of the metastable level. This model adequately describes the dynamics of Cr^{3+} ions when the $^4T_2$ level is pumped, followed by a fast nonradiative decay to the ^2E level which has a relatively long lifetime (2.3 ms at 12 K). The solution of Eq. (8) assuming a step function for the laser intensity with the initial condition that $I(t=0)=0$ is

$$\frac{s_0(t)}{S} = \frac{1+(I/I_s)\exp[-(t/\tau)(1+I/I_s)]}{1+I/I_s}, \tag{9}$$

where $I_s = (\hbar\omega/\sigma\tau)$ is the saturation intensity. It is important to note that the time development of the system

FIG. 1. FWM relative scattering intensity of Cr^{3+} ions in mirror sites in alexandrite as a function of the laser power of each write beam for direct excitation of the $2\overline{A}$ sublevel of the ^2E state at 50 K. The dashed and solid lines represent the theoretical fits from Eqs. (7) and (5), respectively.

depends upon the saturation intensity and write-beam intensity.

Following the treatment of Abrams and Lind[15] in which the four fields, two write beams, the probe beam, and the signal beam, are assumed to be plane waves, and the interaction between the fields takes place through the complex susceptibility X the interaction is expressed in terms of the wave equation, Eq. (3). The complex susceptibility can be expressed in terms of the complex index of refraction $\tilde{n} = \bar{n} + i(\alpha/2k)$ as

$$X = \bar{n}^2 - 1 - \alpha^2/4k^2 + i(\alpha\bar{n}/k) , \tag{10}$$

where k is the magnitude of the wave vector of the write beams, $\bar{n}$ is the index of refraction, and $\alpha(t) = \sigma s(t)$ is the time-dependent absorption coefficient. Using the nonlinear index of refraction

$$\bar{n}(t) = n + s_2(t)(\Delta n) , \tag{11}$$

where n is the normal index of refraction, and Δn is the change in the index of refraction due to the presence of

an ion in the excited state, it is evident that both the real and imaginary parts of the susceptibility and hence the FWM interaction are time dependent. The expression for the FWM scattering intensity is[15]

$$\eta = |\kappa \sin(\Delta L)|^2 / |\Delta \cos(\Delta L) + \Upsilon_R \sin(\Delta L)|^2 \tag{12}$$

where $\Delta = (|\kappa|^2 - \Upsilon^2)^{1/2}$, L is the length of the sample, Υ_R is the real part of Υ, where

$$\Upsilon(t) = (k/2i)(X + I_s P \, dX/dI) , \tag{13}$$

$$\kappa^*(t) = \tfrac{1}{2} k I_s P \, dX/dI , \tag{14}$$

and $P = 4(I/I_s)\cos^2\theta$. θ is the angle between the two write beams. It is important to note that the FWM process is a result of the term dX/dI, so that if X is independent of I then there is no FWM signal generated. Because only the real part of Υ appears in the expression for η, only the terms Υ_R, κ_R, and κ_I need to be calculated. Using Eqs. (10)–(14) the absorption and coupling coefficients become

$$\Upsilon_R(t) = \frac{1}{2}\left\{ S(\Delta n)n + S[n\sigma + S(\Delta n)\sigma]\frac{1 + P\exp[-t/\tau(1+P)]}{1+P}\right.$$

$$+ SP[n\sigma + S(\Delta n)\sigma]\frac{[1 - t/\tau P(1+P)]\exp[-t/\tau(1+P)] - 1}{(1+P)^2}$$

$$- 2n^2(\Delta n)\frac{\sigma\{1 + P\exp[-t/\tau(1+P)]\}/(1+P)\{1 - t/\tau P(1+P)\exp[-t/\tau(1+P)] - 1\}}{(1+P)^2}$$

$$\left. - n^2(\Delta n)\sigma\frac{\{1 + P\exp[-t/\tau(1+P)]\}^2}{(1+P)^2}\right\} , \tag{15}$$

$$\kappa_R(t) = \tfrac{1}{2} kP\left\{ S[-2S(\Delta n)^2 - 2n(\Delta n)]\frac{[1 - t/\tau P(1+P)]\exp[-t/\tau(1+P)] - 1}{(1+P)^2}\right.$$

$$\left. + S^2[2(\Delta n)^2 - \sigma^2/2k^2]\frac{\{1 + P\exp[-t/\tau(1+P)]\}/(1+P)\{[1 - t/\tau P(1+P)]\exp[-t/\tau(1+P)] - 1\}}{(1+P)^2}\right\} , \tag{16}$$

$$\kappa_I(t) = -\tfrac{1}{2} P\left\{ S[n\sigma + S(\Delta n)\sigma]\frac{[1 - t/\tau P(1+P)]\exp[-t/\tau(1+P)] - 1}{(1+P)^2}\right.$$

$$\left. - 2S^2\sigma(\Delta n)\frac{\{1 + P\exp[-t/\tau(1+P)]\}/(1+P)\{[1 - t/\tau P(1+P)]\exp[-t/\tau(1+P)] - 1\}}{(1+P)^2}\right\} . \tag{17}$$

Equations (15)–(17) have contributions from an absorption grating, a dispersion grating, and a mixed grating.

Previous theoretical work[15–20] has shown that for small write-beam intensities the LIG scattering efficiency increases quadratically with pump intensity, but that it saturates at higher intensities. In the steady state, the maximum LIG signal is obtained for I approximately equal to I_s. However, the transient LIG signal can be much larger than the steady-state LIG signal. When $I < I_s$ the LIG is predicted to increase monotonically to its steady-state value, but when $I \geq I_s$ the transient LIG signal peaks at short times at a value greater than the steady-state LIG signal and then decays to the steady-

state value. The temporal behavior of the transient LIG signal for the case of a mixed or purely dispersive grating is similar to the case of a pure absorption grating.

Alexandrite is an ideal candidate for studying the effects of saturation on the spectral dynamics. The parameter P directly affects the time dependence of the LIG signal, and P is a function of several LIG variables and constants of the material including the lifetime of the excited state. The lifetime of the mirror-site ions ranges from 2.3 ms to 290 μs at temperatures of 12 to 300 K, whereas the lifetime of the inversion sites ranges from 63 to 44 ms over the same temperature range.[11,12] Another method of varying P is by changing the period of the

grating or the angle between the write beams. For these reasons it is possible to vary the saturation intensity, and hence the parameter P which appears in the expressions for the absorption coefficient and coupling constants.

The transient LIG signal for the inversion-site ions shows a transient peak which is dependent on several parameters. Figure 2 shows the normalized transient LIG signal at 30 K for various powers of the write beams. The data was normalized because it is very difficult to determine the absolute scattering efficiency, and the shape of the FWM transient is the only thing needed for the theoretical fits. The solid line is the theoretical fit to the data using Eqs. (12) and (15)–(17) and treating σ and Δn as adjustable parameters. Figure 3 shows the transient FWM signal for several temperatures and write beam crossing angles at constant write beam laser power, along with the theoretical fits. The theoretical fits accurately

model the transient LIG signal as a function of temperature, crossing angle, and laser power. The temperature dependence is a result of the temperature dependence of the excited-state lifetime. The values obtained for σ and Δn from these fits are $0.5\pm0.1\times10^{-20}$ cm^2 and 2.0×10^{-23} cm^3, respectively. Using these values, the saturation intensity is 900 W/cm^2.

This value for the absorption cross section for the inversion site ions at 488 nm is consistent with the upper limit of 1.0×10^{-20} cm^2 obtained from absorption measurements.[11–13] It is difficult to distinguish the inversion-site absorption contribution from the mirror-site absorption since the emission and absorption properties of alexandrite are dominated by the mirror-site ions.[9]

In order to compare the laser-induced change in the index of refraction obtained here with the results of other measurements,[5,8] it is necessary to calculate the steady-state value of Δn, denoted by Δn_{ss}, and given by

$$\Delta n_{ss} = \Delta n [S(I/I_s)/(1+I/I_s)] . \tag{18}$$

For $I = 100$ W/cm^2, Δn_{ss} equals 5.0×10^{-6}. This is an order of magnitude smaller than the value obtained from other measurements[5,8] of Δn_{ss}, but all of the data are consistent with the statement given earlier that the gratings formed are dispersion gratings. It should be noted that the steady-state value of the theoretical signal intensity is smaller than the experimental value at large excitation intensities. This contributes to the discrepancy in the values of Δn.

The same type of measurements were repeated for the mirror-site ions. The $^4T_2$ level of the mirror site ions was pumped by an argon-ion pumped dye laser with Rhodamine 6G as a dye. The results of the measurements are similar to the low-power measurements for the inversion site ions. There is no transient peak formed, and the signal increases monotonically to its steady state value. This can be understood, in contrast to the inversion site results, as a result of two things. First, the laser output from the ring dye laser was less than the maximum power output of the argon-ion laser at 488 nm by a factor of 3. Second, the saturation intensity for the mirror-site ions is greater than the saturation intensity of the inversion-site ions. This is a result of the difference in lifetimes and absorption cross sections. The saturation intensity for the mirror-site ions is estimated to be approximately 1200 W/cm^2 at 12 K and increases with temperature due to the decrease in the lifetime with temperature. Therefore, it is not surprising that no transient peak was observed in the mirror-state LIG signal.

FIG 2. Normalized transient LIG signal for Cr^{2+} ions in inversion sites as a function of time at 30 K for various write-beam powers: (a) 714 W/cm^2, (b) 281 W/cm^2, (c) 45 W/cm^2. The dashed lines represent the data and solid lines represent the theoretical fits using Eq. (12).

III. ENERGY TRANSFER

Laser-induced grating spectroscopy has been used to characterize the properties of long-range energy migration among Cr^{3+} ions in mirror and inversion sites in alexandrite.[5,8] The previous measurements were performed using either an argon-ion laser or argon-ion-pumped ring dye laser with Rhodamine 6G dye for the pump beams. Both of these are resonant with the $^4T_2$ absorption band of the mirror or inversion-site ions. These LIG measurements were extended in the work described
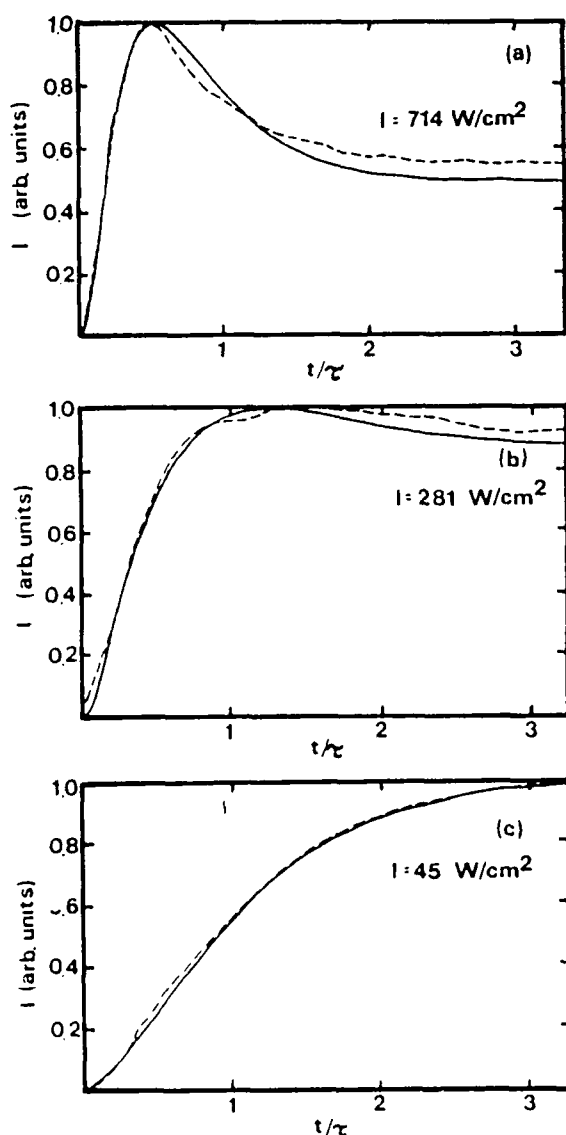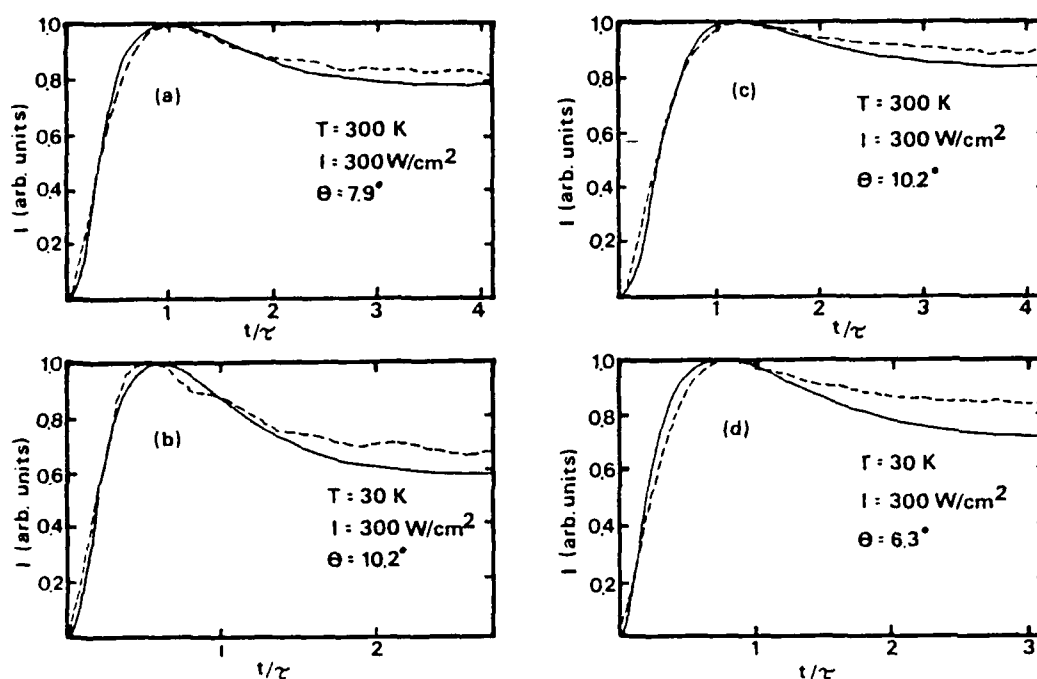
FIG. 3. Normalized transient LIG signal for Cr^{3+} ions in inversion sites for several temperatures and write-beam crossing angles at constant write-beam laser power. (a) $T = 300$ K and $\theta = 7.9°$, (b) $T = 30$ K and $\theta = 10.2°$, (c) $T = 300$ K and $\theta = 10.2°$, and (d) $T = 30$ K and $\theta = 6.3°$. The dashed lines represent the data and the solid lines represent the theoretical fits using Eq. (12).

here to the case of direct excitation into the $2\overline{A}$ sublevel of the ^2E state of the mirror-site ions. The population grating in the ^2E state was established by crossing two laser beams from an argon-ion-pumped jet dye laser using DCM dye tuned to 677.8 nm. In addition experiments were performed using crossed laser beams from both the argon-ion laser and argon-ion-pumped ring dye laser to simultaneously establish gratings in both mirror and inversion site ions in order to determine the effects of the dual gratings on the LIG signals.

It was reported earlier[5] that the FWM signal decay kinetics were nonexponential for excitation into the $^4T_2$ level of the mirror-site ions. The long-time portion of the decay curves was found to approach the decay time expected for an inversion-site grating and was attributed to an inversion-site grating formed as a result of weak inversion-site absorption. In the data presented below for direct excitation of the ^2E level of the mirror-site ions no long-time tail is evident.

In order to use LIG spectroscopy to study energy migration among Cr^{3+} ions the grating decay rate is measured as a function of the grating spacing.[21,22] The grating spacing is related to the total crossing angle of the write beams by

$$\Lambda = \lambda / [2 \sin(\theta / 2)] , \qquad (19)$$

where θ is the total crossing angle between the write beams and λ is the write-beam wavelength. As the grating spacing decreases energy migration from the peak to the valley of the grating becomes more efficient in destroying the LIG. For the initial conditions relevant to this experimental case, the time dependence of the normalized transient-grating signal in the presence of energy

migration processes is given by[23]

$$I_s(t) = \exp(-2t / \tau) \left[J_0(bt)\exp(-\alpha t) \right.$$
$$+ \alpha \int_0^\infty du \exp[-\alpha(t - u)]$$
$$\left. \times J_0(b(t^2 - u^2)^{1/2}) \right]^2 , \qquad (20)$$

where τ is the fluorescence lifetime, α is the exciton scattering rate, J_0 is the Bessel function of order zero, and b is given by

$$b = 4V \sin[(2\pi a / \lambda)\sin(\theta/2)] , \qquad (21)$$

where V is the nearest-neighbor ion-ion interaction rate, a is the average distance between active ions, λ is the excitation wavelength and θ is the crossing angle between the write beams (both in air). The exciton dynamics can be characterized by these parameters in terms of the diffusion coefficient, the mean free path, the diffusion length, the coherence parameter, and the number of sites visited between scattering events given by

$$D = 2V^2 a^2 / \alpha , \qquad (22)$$

$$L_m = \sqrt{2}Va / \alpha , \qquad (23)$$

$$L_d = (2D\tau)^{1/2} , \qquad (24)$$

$$\zeta = b / \alpha , \qquad (25)$$

$$N_s = L_m / a , \qquad (26)$$

respectively.

A. Results for $^4T_2$ excitation

For the grating formed by excitation into the $^4T_2$ level of the mirror-site ions the decay of the signal is nonexponential. The initial part of the decay is consistent with the predicted decay of a mirror-site grating and the long-time part of the decay is consistent with the predicted decay of an inversion site grating. The angular dependence of the grating decay pattern shows that at large crossing angles the long-time decay is very weak or no longer present. This is shown in Fig. 4.

The concentration of inversion-site Cr^{3+} ions in the sample is 2.5×10^{18} cm^{-3}. Assuming a uniformly random distribution of ions, this implies an average separation of 457 nm between inversion-site Cr^{3+} ions. The angles used in the measurements ranged from 2° to approximately 28°. This gives grating spacings ranging from 1.2 to 16 μm. The spatial dependence of the grating is given by

$$n(x,0) \approx [\cos(k_g x) + 1] , \qquad (27)$$

where $k_g = 2\pi/\Lambda$ is the grating k vector, and $n(x,0)$ is the exciton concentration at $t = 0$. The characteristic width of a grating peak is Λ. For a grating spacing of 16 μm this implies a linear density of 35 inversion-site Cr^{3+} ions per grating peak. For a grating spacing of 1.2 μm the linear density of inversion-site Cr^{3+} ions is 2.6 per grating peak. This clearly shows, under the above assumptions, that the number of inversion-site ions per peak of the grating decreases with increasing crossing angle (decreasing grating spacing), and as a result, the inversion-site grating signal decreases in intensity with increasing crossing angle.

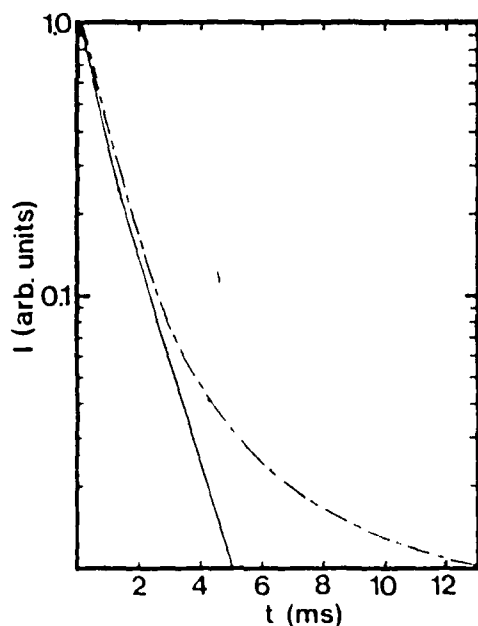In order to conclusively establish that the observed long-time part of the decay patterns is a result of the simultaneous formation of an inversion-site grating along with the mirror site grating, the following experiment was performed. A mirror site grating and an inversion site grating were formed simultaneously in the same region in the sample by using two different sets of pump laser beams as described earlier. A single He-Ne beam was used to probe the dual grating. Because the fringe spacings of the two gratings are not exactly the same due to the different laser frequencies used to write the gratings, it was necessary to keep the crossing angle between the two sets of overlapping write beams very small so that a single probe beam can approximately match the Bragg condition for both gratings simultaneously. The decay kinetics of the resulting dual grating were measured by chopping both sets of pump beams and recording the dual LIG signal. The results are shown in Fig. 5. The decay pattern is similar to the small-angle decay pattern for $^4T_2$ pumping, shown in Fig. 4. This confirms that the long-time part of the decay for $^4T_2$ pumping is due to the presence of an inversion-site grating.

B. Results for ^2E excitation

The FWM signal decay kinetics of the mirror-site grating formed by direct excitation of the ^2E level were also found to be dependent on the grating spacing and temperature. Several approaches[22-24] have been used to theoretically analyze the transient grating kinetics in the presence of energy transfer. Kenkre[23,24] has treated the case for the effects of partially coherent exciton migration, with the initial conditions relevant to the experiments described here. His results are derived from the generalized master equations using the assumption that the initial density matrix for the system is diagonal. This is the situation encountered in systems with localized exciton states or systems containing complete randomness between the phases of the exciton wave functions. The

FIG. 4. The LIG signal decay for excitation of the mirror-site Cr^{2+} ions into the $^4T_2$ level at 30 K at two different write-beam crossing angles. The dashed line is $\theta = 3.5°$; the solid line is $\theta = 23°$.
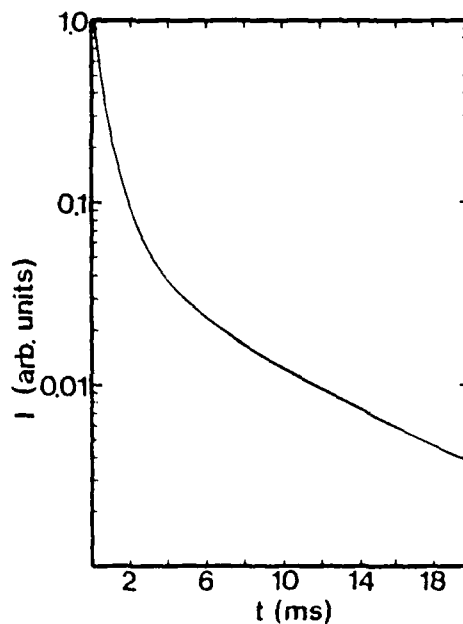

FIG. 5. Dual-grating decay kinetics at 30 K and a write-beam crossing angle of 1.39°.

TABLE I. Energy migration parameters at 25 K.

V (sec^{-1})	1.22×10^6
α (sec^{-1})	0.2×10^6
D (cm^2 sec^{-1})	3.02×10^{-8}
L_m (cm)	3.88×10^{-7}
L_d (cm)	1.18×10^{-5}
N_t	8.63
ζ ($\theta = 5°$)	3.7×10^{-3}

later case is exactly the situation encountered here. At low temperatures the population of excited Cr^{3+} ions is predominantly in the $\bar{E}$ sublevel of the ^2E state, whereas the excitation is into the $2\bar{A}$ sublevel. A correlation exists between different Cr^{3+} sites in the $2\bar{A}$ sublevel immediately after the pump photons are absorbed, since the excitation wavelength spans many Cr^{3+} sites. However, any dephasing mechanism, such as nonradiative processes between the $\bar{E}$ and $2\bar{A}$ sublevels or phonon scattering processes, will result in a loss of this correlation between sites. Therefore, the theory of Kenkre[23] is ideally suited to this system. The dephasing issue will be discussed later in this paper.

For ^2E excitation there is no inversion-site contribution to the LIG signal, and therefore the decay kinetics of the signal can unambiguously be analyzed in terms of energy migration only among mirror site Cr^{3+} ions. Equation (20) was used to fit the slightly nonexponential LIG decay kinetics treating b and α as adjustable parameters. The LIG decay kinetics at each temperature and several different grating spacings were used to characterize the exciton migration at that specific temperature. The pertinent parameters are listed in Table I.

Figure 6 shows the temperature dependence obtained for the scattering rate α. The solid line is the best fit to the data using the expression

$$\alpha = C_1 T^{C_2} \tag{28}$$

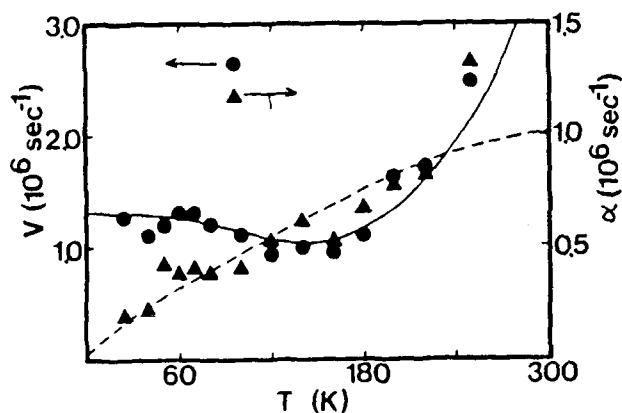with $C_1 = 0.02 \times 10^6$ sec^{-1} and $C_2 = 0.75 \pm 0.08$.

FIG 6. The temperature dependence obtained for the scattering rate and the ion-ion interaction rate for direct excitation of the ^2E level of the Cr^{3+} ions in mirror sites. The solid line is the theoretical fit to the ion-ion interaction rate using Eq. (28), and the dashed line is the theoretical fit to the scattering rate using Eq. (29).

Figure 6 also shows the temperature dependence of the ion-ion interaction rate. For resonant energy migration in the R_1 zero-phonon line originating on ^2E, the ion-ion interaction rate is proportional to the spectral overlap integral of the R_1 absorption and emission transitions, and the intrinsic decay rate of the ^2E level.[25] This can be expressed as

$$V = C_3 \tau^{-1} / \Delta \nu , \tag{29}$$

where $\Delta \nu$ is the FWHM of the zero-phonon line, and it was assumed that the zero-phonon lineshape was Gaussian. The temperature dependencies of τ^{-1} and $\Delta \nu$ have been measured for the R_1 mirror site zero-phonon line in alexandrite.[11] The solid line in Fig. 6 is the best fit to the measured ion-ion interaction rate using Eq. (29) and the measured values of τ^{-1} and $\Delta \nu$.

Using Eq. (22) the diffusion coefficient can be calculated from V and α in terms of a. The magnitude of the diffusion coefficient determined by analyzing the results obtained using $^4T_2$ excitation was calculated in a previous paper[5] assuming completely incoherent migration. Structural measurements have shown that the distribution of Cr^{3+} ions in alexandrite is not uniform.[26] For this reason it is difficult to determine a value for the distance between Cr^{3+} ions, a. The lower limit on a is 0.27 nm, which is the smallest distance between Cr^{3+} ions in mirror sites. For a uniform distribution of Cr^{3+} ions the value of a is 2.99 nm. Assuming a dipole-dipole interaction between Cr^{3+} ions and using the calculated ion-ion interaction rate listed in Table I, the value of a is estimated to be approximately 0.45 nm, which is intermediate between the nearest-neighbor and uniform distribution limits. Using the value of 0.45 nm for a, the magnitudes of D, L_m, and L_d, listed in Table I, are obtained.

It was reported previously[5] that the temperature dependence of D is $T^{-1/2}$ for $T \leq 150$ K. The temperature dependence of α is $T^{0.75}$, and V decreases slightly with temperature up to 180 K (primarily due to a slight increase in $\Delta \nu$ in this temperature range). Using Eq. (22) and these results gives a temperature dependence of approximately $T^{-1/2}$ for D, in agreement with the results obtained with $^4T_2$ excitation. This is shown in Fig. 7.

The scattering rate depends on temperature differently for different mechanisms which limit the exciton mean free path.[27] The exciton scattering mechanism can be due to scattering by defects, optic phonons, or acoustic phonons. All of these processes have different temperature dependences in different limits. Scattering of excitons by acoustic phonons is the dominant scattering mechanism at low temperatures. The most general form of this type of scattering is predicted[27] to have a $T^{3/2}$ temperature dependence. The smaller temperature dependence observed here may be a result of the longer-wavelength phonons not being as effective in scattering localized excitons as the shorter wavelength phonons and the difference in the electron-phonon coupling strengths for the different phonons. Long-wavelength phonons which modulate several neighboring lattice sites together are less effective in scattering excitons localized on a single lattice site than phonons which modulate neighboring sites differently.[28]
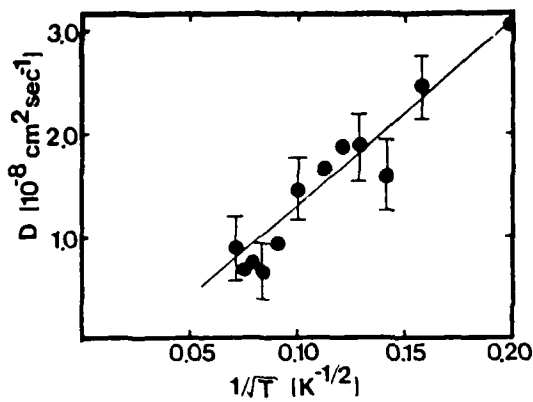
FIG. 7. *Temperature dependence of the exciton diffusion coefficient for* Cr^{3+} *ions in the mirror sites in alexandrite obtained from values of* V *and* α. *The solid line shows a* $T^{-1/2}$ *dependence.*

The results of the measurements of the properties of the exciton migration in alexandrite reported here are the essential characteristics needed to understand the issue of coherence in exciton migration. The term coherence in this case describes the situation in which the exciton behaves like a quasiparticle with a certain momentum. This quasiparticle will move over several lattice spacings, maintaining phase memory, before a scattering event occurs. The phase memory of the exciton does not depend upon the rest of the ensemble of excitons. Transient grating measurements have three different characteristic distances. These are the lattice constant a, the mean free path L_m, and the grating spacing Λ. The transport properties of the exciton are discernible using the LIG technique only if the diffusion length is comparable to half of the grating spacing, and therefore L_d and Λ are on the same length scale. If L_m is less than or equal to a then the exciton motion is completely incoherent and a scattering event occurs on every "hop" of the exciton to another site, leading to a complete loss of phase memory. If $a < L_m \ll \Lambda/2$ then the exciton motion is coherent over a few lattice spacings, but is incoherent on the scale of the experiment. N_s is a measure of the degree of coherence on this length scale. If $L_m \approx \Lambda/2$ then the exciton motion is coherent over many lattice spacings and on a distance scale which is directly discernible from the transient grating signal shapes. ζ is a measure of the degree of coherence on this length scale. Table I shows that the mirror-site Cr^{3+} ions in alexandrite have energy transport characteristics consistent with the second type of coherence mentioned above ($a < L_m \ll \Lambda/2$). The exciton motion is coherent over a few lattice spacings, but is incoherent on the distance scale of the grating, and is thus termed quasicoherent.

The coherence parameter is an important quantity in verifying the assumption mentioned earlier regarding the initial conditions of the experiment. Kenkre[29] has shown that for ζ greater than 2.0 significant differences in the transient grating decay kinetics are possible depending on the initial state of the density matrix. Table I shows that ζ is 3.7×10^{-3}. Therefore even if the initial density ma-

trix were not diagonal, as assumed here, there would be no difference in the transient grating decay kinetics. The LIG signal in this system is insensitive to the initial conditions of the density matrix.

IV. DEPHASING MEASUREMENTS

In a previous paper[5] it was shown that measurements of the FWM signal intensity as a function of the crossing angle between the write beams can be used to determine the dephasing time of the atomic system with respect to the laser beams. The model used to analyze the data was the model discussed in Sec. II describing the interaction between crossed laser beams and a two-level atomic system. The electric fields of the four laser beams interact with each other via the nonlinear polarization induced in the two-level system. Solving the wave equation for this situation leads to a set of coupled differential equations for the complex amplitudes of the fields. Using this approach it was found that the normalized FWM scattering efficiency could accurately be modeled by solving these equations numerically, treating the real and imaginary components of the coupling parameters, D_1^r, D_1^i, D_2^r, and D_2^i, as adjustable parameters. The values of the coupling parameters obtained by these computer fits to the data yielded information on the laser-induced modulation of the real and imaginary parts of the refractive index through the relationships

$$\Delta\alpha_{ss} \approx -2\alpha D_2^i/D_1^i , \tag{30}$$

$$\Delta n_{ss} = (\alpha c/\omega)D_2^r/D_1^i . \tag{31}$$

From these quantities the dephasing time of the atomic system, T_2, can be calculated using

$$T_2 = (2\omega/c)(\Delta n_{ss}/\Delta\alpha_{ss})(\omega - \omega_{21})^{-1} \tag{32}$$

where α is the absorption coefficient at the write-beam wavelength, c is the speed of light, ω is the circular frequency of the write beams, and ω_{21} is the resonant frequency of the atomic transition.

There are several mechanisms that could be responsible for the dephasing of the system. The measured dephasing time is related to population relaxation T_1 and phase disrupting processes among the ions of the ensemble, T_2^{PD}, by the relation[30]

$$T_2^{-1} = \tfrac{1}{2}T_1^{-1} + (T_2^{PD})^{-1} . \tag{33}$$

Population relaxation processes contribute to the total dephasing rate since they are incoherent spontaneous processes. T_2^{PD} can be separated into two parts:

$$(T_2^{PD})^{-1} = (T_2^*)^{-1} + (T_2')^{-1} , \tag{34}$$

where T_2^* is the inhomogeneous dephasing time and T_2' is the homogeneous dephasing time. These dephasing times are related to their respective contribution to the total linewidth through the relations

$$T_2^* = (\pi c \, \Delta\nu^*)^{-1} \tag{35}$$

and

$$T_2' = (\pi c \, \Delta\nu')^{-1} . \tag{36}$$

T_2^* represents the time for the loss of phase coherence between the ions of the ensemble due to small mismatches in the transition energies of the ions. T_2' represents the time for the loss of coherence between the ions of the ensemble due to phonon scattering processes.[22]

A. Results for ^2E excitation

Figure 8 shows the angular dependence of the normalized FWM scattering efficiency for excitation of the $2\overline{A}$ sublevel of the ^2E state at 50 K. The solid line in the figure is the computer fit to the data using the procedure discussed above. The parameters calculated from this fit using Eqs. (30)–(32) are listed in Table II.

For this excitation the total population relaxation is the sum of two processes:

$$T_1^{-1} = T_1^{-1}(2\overline{A}\text{-}\overline{E}) + T_1^{-1}(^2E\text{-}^4A_2) \tag{37}$$

where $T_1^{-1}(2\overline{A}\text{-}\overline{E})$ is the nonradiative decay rate from the upper crystal field sublevel of the ^2E state to the lower sublevel, and $T_1^{-1}(^2E\text{-}^4A_2)$ is the total decay rate from the $2\overline{A}$ and $\overline{E}$ sublevels of ^2E to the ground state, $^4A_2$. $T_1(^2E\text{-}^4A_2)$ is measured[11] to be 2.3 ms at 50 K, and therefore this term in Eq. (37) can be neglected since it is much smaller than the measured dephasing rate of 55 ps. The nonradiative decay time from $2\overline{A}$ to $\overline{E}$, $T_1(2\overline{A}\text{-}\overline{E})$, has been measured by Meltzer et al.[31] at 1.5 K to be 400 ps. This decay time will decrease as temperature is raised, and can be extrapolated to its value at 50 K using the relation

$$T_1^{-1}(50 \text{ K}) = T_1^{-1}(0 \text{ K})(\overline{n} + 1) \tag{38}$$

where n is the phonon occupation number given by

$$\overline{n} = [\exp(\Delta E/k_B T) - 1]^{-1}, \tag{39}$$

k_B is Boltzmann's constant and ΔE is the phonon energy. This gives a value of 260 ps for $T_1(2\overline{A}\text{-}\overline{E})$ at 50 K. This is a factor of 5 slower than the dephasing time measured here. At 50 K the homogeneous linewidth is less than the
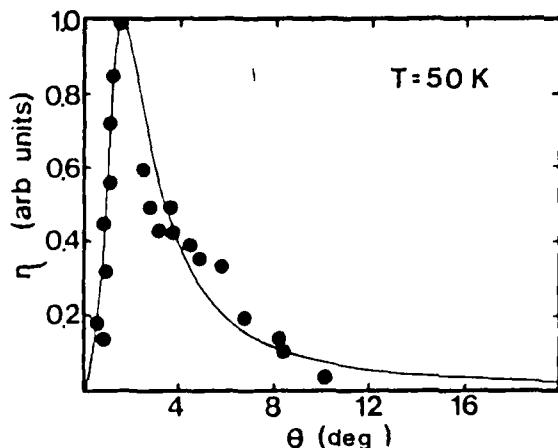

FIG. 8. Normalized FWM scattering efficiency vs the write-beam crossing angle at 50 K for Cr^{3+} ions in the mirror sites directly excited in the $2\overline{A}$ sublevel of the ^2E state. The solid line is the computer-generated fit obtained for a two-level atomic system model for FWM (Refs. 5 and 15).

TABLE II. Dephasing parameters.

λ_{exc} (nm)	677.8
T (K)	50
D_1^r	0.25
D_1^i	0.65
D_2^r	0.35
D_2^i	0.0015
Δn	6.68×10^{-6}
$\Delta\alpha$ (cm^{-1})	4.00×10^{-3}
T_2 (ps)	55.3

inhomogeneous linewidth, which is approximately 2 cm^{-1}.[11] Therefore T_2^* is less than T_2', and the dephasing rate is dominated by the inhomogeneous dephasing. Using Eq. (41) and the measured inhomogeneous linewidth, the inhomogeneous dephasing time is found to be 52 ps. This is in good agreement with the measured result; thus the dephasing mechanism in this case is attributed to dephasing associated with the inhomogeneous linewidth and not population relaxation.

B. Results for $^4T_2$ excitation

For excitation into the $^4T_2$ level, T_2 was found previously[5] to be 80 and 2.2 ps for the inversion sites and mirror sites, respectively and the dephasing time was attributed to the nonradiative decay from the $^4T_2$ level to the ^2E metastable level. These measurements have been extended to temperatures ranging from 30 to 300 K and several different excitation wavelengths. The dephasing time was found to be constant over this temperature range, while the frequency dependence of the dephasing time was found to vary approximately as ω on the high-energy side of the transition peak.

The dynamics of nonradiative decay processes are important in gaining a full understanding of dephasing and the role that phonons play in the dephasing process. In this section a model is presented to describe the second type of dephasing, and it is related to the dephasing results obtained for $^4T_2$ excitation of the mirror-site ions.

Figure 9 shows the model used to analyze the dynamics of the mirror-site Cr^{3+} ions. The ^2E curve actually represents four potential energy curves, and the $^4T_2$ curve represents twelve potential energy curves.[32] This is a result of the splittings of the sublevels of each state. The $^2T_1$ level has been omitted since it does not play a significant role in the nonradiative decay processes.[33–35] Optical absorption occurs from the ground state, $^4A_2$, to an excited vibrational level of the $^4T_2$ level, represented by the vertical line in the figure. The ion is excited into an excited vibrational level of the $^4T_2$ state. Following absorption, the ion relaxes very quickly to the metastable ^2E level. This process can occur in two ways. The first mechanism is one in which the ion remains in the $^4T_2$ level and emits phonons, termed internal conversion (IC), until its energy coincides with the crossing of the two excited-state adiabatic potential-energy curves, the ^2E and $^4T_2$ levels. At this energy, the relaxation process crosses over to the ^2E level, called intersystem crossing (ISC), and the ion continues to emit phonons until the
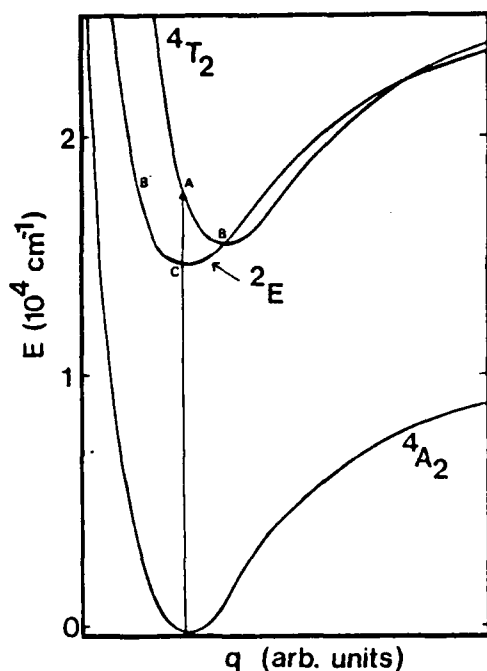
FIG. 9. Model used to analyze the dynamics of the nonradiative decay from the $^4T_2$ level to the ^2E level. The solid vertical line represents optical absorption.

FIG. 10. Coupling scheme for the different energy levels of a Cr^{3+} ion in an octahedral environment.

bottom of the ^2E potential energy curve is reached. This is represented by the path $A-B-C$ in Fig. 9. The second mechanism differs from the first in the point at which the ISC process occurs. In this mechanism the ISC process occurs on the very first step of the relaxation and is followed by the emission of phonons until the bottom of the ^2E potential energy curve is reached. The relaxation predominantly occurs in the ^2E electronic state, and is represented by the $A-B'-C$ path in Fig. 9. These two mechanisms will be designated as IC and ISC, respectively, corresponding to the first steps in the relaxation mechanism.

Nonradiative decay processes occur between nonstationary states of the system.[32] The initial state of the system, as well as the others, is not a pure $^4T_2$ electronic state.[35] It is actually a mixed state of several electronic vibrational states including the $^4T_2$ and ^2E electronic-vibrational states. This is a result of the electron-phonon coupling, the spin-orbit interaction, and the anharmonic potential energy of the excited states of the Cr^{3+} ions. The various electronic states admixed by these interactions are shown in Fig. 10. Englman et al.[36] have shown in the harmonic approximation that the amount of admixture between the ^2E and $^4T_2$ states, which form the initial vibronic eigenstate of the system, can increase significantly as the vibrational quantum number of the upper state increases. Including anharmonic effects can increase the amount of admixture between states even more.

In the model used here to analyze the nonradiative decay pathways from the $^4T_2$ state to the ^2E state, only single-phonon processes are considered. The initial level of the system after optical excitation is an excited vibra-
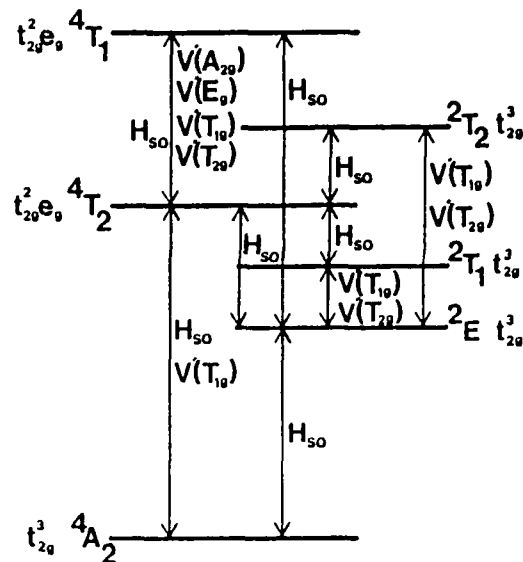
tional level of the $^4T_2$ electronic state. The interactions shown in Fig. 10 admix this state with various intermediate states. From these admixed states relaxation can occur to the vibrational level of the $^4T_2$ state lying just below the initially excited level or to an excited vibrational level of the ^2E state which is at or below the energy of the initial level. The amount of admixture between states which causes the radiationless relaxation processes decreases as the vibrational quantum number of the initial state of the $^4T_2$ electronic state decreases.[36] The first step of the relaxation process is very important in determining the relaxation pathway because the amount of admixture between states which results in a specific relaxation pathway decreases after each step in the nonradiative decay process. Therefore, once the first step occurs, the pathway is determined until points are reached where there is a significant change in the admixture between states, such as at the potential-energy curve crossing points.

The nonradiative decay rate is given by the golden rule:

$$K_{nr} = (2\pi/\hbar) |\langle \Psi_{e'v'} | \Delta H | \Psi_{ev} \rangle|^2 \rho(E_f) , \qquad (40)$$

where e denotes the electronic part and v denotes the vibrational part of the wave function Ψ, primes denote the initial state of the system, ΔH is the perturbation connecting the two levels, and $\rho(E_f)$ is the density of final states. The admixture between states is accounted for in the terms retained in ΔH, where

$$\Delta H = V'q + H_{s.o.} . \qquad (41)$$

Here q is the configuration coordinate representing the symmetry adapted normal mode of the system, V' is the electron-phonon coupling term, and $H_{s.o.}$ is the spin-orbit interaction. Phonons of different symmetry are active in coupling the different levels shown in Fig. 10. These phonon symmetries are given in parentheses after the V'. The first step in the IC mechanism is the transi-

tion from $\Psi(^4T_2,v')$ to $\Psi(^4T_2,v)$ where $v'>v$. First-order perturbation theory is not sufficient to cause this transition, and it will be necessary to use second-order perturbation theory to describe this mechanism. The first step in the ISC mechanism is the transition from $\Psi(^4T_2,v')$ to $\Psi(^2E,v)$. The only operator which can connect these states is the spin-orbit coupling operator. Second-order perturbation theory must also be used to

express the matrix elements in this mechanism.

Assuming that the states involved in the transition are Born-Oppenheimer states,

$$\Psi_{ev}(r,q)=\phi_e(r,q)X_v(q) \tag{42}$$

the nonradiative decay rate for each mechanism can be written as

$$
\begin{aligned}
K_{nr}(\text{ISC})=\frac{2\pi}{\hbar}\Bigg|\sum_v\sum_p\Bigg[\sum_{\Gamma,\gamma,M_s,r}\sum_{\gamma'',M_s''}\langle\phi(^4T_2,\gamma^*,M_s^*)|V'|\phi(\Gamma,\gamma,M_s)\rangle \\
\times\langle\phi(\Gamma,\gamma,M_s)|H_{s.o.}|\phi(^2E,\gamma'',M_s'')\rangle\langle X(^4T_2,v_p')|q_p|X(\Gamma,r_p)\rangle \\
\times\prod_a\langle X(^4T_2,v_a')|X(\Gamma,r_a)\rangle \\
\times\langle X(\Gamma,r_a)|X(^2E,v_a)\rangle/[W(^4T_2)-W(\Gamma)]+\text{c.c.}\Bigg]\Bigg|^2\rho(E_f) \\[2mm]
+\frac{2\pi}{\hbar}\Bigg|\sum_v\sum_p\Bigg[\sum_{\Gamma',\gamma',M_s',r}\sum_{\gamma'',M_s''}\langle\phi(^4T_2,\gamma^*,M_s^*)|H_{s.o.}|\phi(\Gamma',\gamma',M_s')\rangle \\
\times\langle\phi(\Gamma',\gamma',M_s')|V'|\phi(^2E,\gamma'',M_s'')\rangle\langle X(\Gamma',r_p)|q_p|X(^2E,v_p)\rangle \\
\times\prod_a\langle X(^4T_2,v_a')|X(\Gamma',r_a)\rangle \\
\times\langle X(\Gamma',r_a)|X(^2E,v_a)\rangle/[W(^2E)-w(\Gamma')]+\text{c.c.}\Bigg]\Bigg|^2\rho(E_f)
\end{aligned}
\tag{43}
$$

and

$$
\begin{aligned}
K_{nr}(\text{IC})=\frac{2\pi}{\hbar}\Bigg|\sum_v\sum_p\Bigg[\sum_{\Gamma,\gamma,M_s,r}\sum_{\gamma'',M_s''}\langle\phi(^4T_2,\gamma^*,M_s^*)|V'|\phi(\Gamma,\gamma,M_s)\rangle \\
\times\langle\phi(\Gamma,\gamma,M_s)|H_{s.o.}|\phi(^4T_2,\gamma'',M_s'')\rangle\langle X(^4T_2,v_p')|q_p|X(\Gamma,r_p)\rangle \\
\times\prod_a\langle X(^4T_2,v_a')|X(\Gamma,r_a)\rangle \\
\times\langle X(\Gamma,r_a)|X(^2E,v_a)\rangle/[W(^4T_2)-W(\Gamma)]+\text{c.c.}\Bigg]\Bigg|^2\rho(E_f) \\[2mm]
+\frac{2\pi}{\hbar}\Bigg|\sum_v\sum_p\Bigg[\sum_{\Gamma',\gamma',M_s',r}\sum_{\gamma'',M_s''}\langle\phi(^4T_2,\gamma^*M_s^*)|V'|\phi(\Gamma',\gamma',M_s')\rangle \\
\times\langle\phi(\Gamma',\gamma',M_s')|V'|\phi(^4T_2,\gamma'',M_s'')\rangle\langle X(^4T_2,v_p')|q_p|X(\Gamma',r_p)\rangle \\
\times\prod_a\langle X(^4T_2,v_a')|X(\Gamma',r_a)\rangle \\
\times\langle X(\Gamma',r_a)|X(^2E,v_a)\rangle/[W(^4T_2)-W(\Gamma)]+\text{c.c.}\Bigg]\Bigg|^2\rho(E_f),
\end{aligned}
\tag{44}
$$

where γ represents the crystal-field component of the Γ intermediate state, and W is the energy of the state. The vibrational part of the wave function has been separated into promoting and accepting modes, $X(e,v_p)$ and $X(e,v_a)$, respectively. These modes are assumed to be distinct, which is a good approximation for high-symmetry crystal-field sites.[32] Promoting modes represent phonons that mix the initial and final electronic states, and accepting modes represent phonons that absorb the difference in electronic energy. The reason for invoking admixture of intermediate states in the expres-

sion for $K_{nr}(\text{IC})$ is due to the properties of the overlap integrals of the vibrational wave functions. The vibrational wave functions for each particular excited state are orthogonal, and therefore the vibrational overlap integral, commonly called the Franck-Condon factor, vanishes for a transition from one vibrational level to a different vibrational level of the same electronic state. Equations (43) and (44) avoid the "Condon" approximation, which tends to underestimate transition rates by as much as several orders of magnitude.[33,37] These expressions are summed over v and p to include all single-phonon transitions from

v' to all other possible vibrational levels. There is no summation over v' because the system is initially in a specific vibrational level.

The summations in Eqs. (43) and (44) are restricted by symmetry. Figure 10 shows that for $K_{nr}(\text{ISC})$ and an ion in an octahedral environment Γ must belong to the set of states $\{{}^4T_2, {}^4A_2, {}^4T_1\}$ and the corresponding V' must belong to the sets of vibrational symmetries $\{\{A_{1g}, E_g, T_{1g}, T_{2g}\}, \{T_{1g}\}, \{A_{2g}, E_g, T_{1g}, T_{2g}\}\}$. On the other hand Γ' must belong to the set of states $\{{}^2T_1, {}^2E, {}^2T_2\}$ and this requires that V' must belong to the sets of vibrational symmetries $\{\{T_{1g}, T_{2g}\}, \{A_{1g}, A_{2g}, E_g\}, \{T_{1g}, T_{2g}\}\}$. For $K_{nr}(\text{IC})$ Γ and Γ' must belong to the set of states $\{{}^4T_1, {}^4A\}$ and the corresponding V' must belong to the set of vibrational symmetries $\{\{A_{2g}, E_g, T_{1g}, T_{2g}\}, \{T_{1g}\}\}$.

Measurements of the Raman spectra, low-temperature absorption spectra, and Stokes excitation spectra[12] show that phonons of about 240 cm^{-1} are important to the dynamics of the nonradiative relaxation processes from the ${}^4T_{2g}$ to ${}^2E_g$ level. In octahedral symmetry there are three different species of Raman-active active modes: A_{1g}, E_g, and T_{2g}. Symmetry assignments of the different Raman

peaks seen in experiments have been done for the actual symmetry class of the mirror-site ions in alexandrite.[38] These can be correlated with the symmetries of the Raman-active modes in O_h point-group symmetry.[39] O_h symmetry is a good approximation to the actual site symmetry, and tis simplification makes the calculations much easier. These measurements and this correlation show that the 240-cm^{-1} phonons have T_{2g} symmetry. Thus, as a further simplification, it will be assumed that these 240-cm^{-1} phonons of T_{2g} symmetry are the only phonons active in the nonradiative relaxation process. This eliminates many of the terms that would have appeared in Eqs. (43) and (44). The sum over promoting modes and the product over accepting modes are removed, leaving just one term each.

The electronic matrix elements can be reduced to single-electron matrix elements which can then be evaluated by using d-electron wave functions.[40-42] The matrix elements are summed over the final states and the matrix elements squared are then averaged over the initial electronic states. The matrix elements can be expressed using the Wigner-Eckart theorem as[41]

$$\langle (t_{2g}^n)(e_g^m)S\Gamma M\gamma \mid V_\gamma(\Gamma) \mid (t_{2h}^{n'})(e_g^{m'})S'\Gamma'M'\gamma'\rangle$$

$$= \delta(S,S')\delta(M,M')(\bar{\Gamma})^{-1/2}\langle \Gamma\gamma \mid \Gamma'\gamma'\Gamma\gamma\rangle \langle (t_{2g}^n)(e_g^m)S\Gamma\|V(\Gamma)\|(t_{2g}^{n'})(e_g^{m'})S'\Gamma'\rangle \quad (45)$$

where $\bar{\Gamma}$ is the dimension of the Γ representation, $\delta(S,S')$ is the Kronecker delta, $\langle \Gamma\gamma \mid \Gamma'\gamma'\Gamma\gamma\rangle$ is the Clebsch-Gordan coefficient, and

$$\langle (t_{2g}^n)(e_g^m)S\Gamma\|V(\Gamma)\|(t_{2h}^{n'})(e_g^{m'})S'\Gamma'\rangle$$

is the multielectron reduced matrix element. This reduced matrix element can be reexpressed in terms of the single-electron reduced matrix elements, $\langle t_{2g}\|V(\Gamma)\|t_{2g}\rangle$, $\langle e_g\|V(\Gamma)\|e_g\rangle$, and $\langle t_{2g}\|V(\Gamma)\|e_g\rangle$, by using the d wave functions for each representation. These wave functions are denoted $T_{2g}(\xi,\eta,\zeta)$, $T_{1g}(\alpha,\beta,\gamma)$, $E_g(u,v)$, $A_{2g}(e_2)$, and $A_{1g}(e_1)$.[41]

The spin-orbit matrix elements are more complicated. The spin-orbit term in the Hamiltonian can be expressed as[41]

$$H_{s.o.} = (1/\sqrt{2})[-V_{1\alpha}(1T_1) + iV_{1\beta}(1T_1)]$$
$$+ (1/\sqrt{2})[V_{-1\alpha}(1T_1) + iV_{-1\beta}(1T_1)]$$
$$+ V_{0\gamma}(1T_1), \quad (46)$$

where $V_{1\alpha}(1T_1)$ transforms as the α wave function of the T_1 representation with spin quantum number $+1$. Using the Wigner-Eckart theorem, the matrix elements of the spin-orbit interaction can be expressed in terms of the multielectron reduced matrix elements. These multielectron reduced matrix elements can also be expressed in terms of the single-electron reduced matrix element $\langle t_{2g}\|V(1T_1)\|e_g\rangle$ and the results have been tabulated by Tanabe et al.[41] Table III gives the average of the matrix elements squared in terms of the single-electron reduced matrix elements after summing over the different components of the intermediate representations.

Nonradiative decay rates in a diatomic molecule can be affected to a large extent by anharmonic effects.[43] This should also be true in solids.[44] The exact form of the anharmonic potential energy surface for an ion in a solid is not known, but the potential can be approximated by using the well-known Morse potential. This is given by[45]

$$U(q) = D_0\{1 - \exp[-a''(q - q_0)]\}^2, \quad (47)$$

where q is the configuration coordinate, q_0 is the equilibrium position, a'' is the anharmonicity constant, and D_0 is the dissociation energy. The normalized vibrational wave functions for this type of potential are[46-49]

$$X_v = [(a''b_0)(v!)/\Gamma(K - v)]^{1/2}$$
$$\times \exp(-z/2)(z^{b_0/2})L_v^{b_0}(z), \quad (48)$$

where

$$z = k \exp[-a''(q - q_0)], \quad (49)$$

$$K = \nu_e/\nu_e x_e = 4D_0/\nu_e, \quad (50)$$

$$b_0 = K - 2v - 1. \quad (51)$$

$L_v^{b_0}(z)$ is the associated Laguerre polynomial, and Γ is the gamma function. The vibrational energy is given by[45]

$$E_v = \nu_e(v + \tfrac{1}{2}) - \nu_e x_e(v + \tfrac{1}{2})^2. \quad (52)$$

This type of potential can be used to model the ground

TABLE III. Squared matrix elements; $X = \langle t_{2g} \| V' t_{2g} \rangle \| t_{2g} \rangle$, $Z = \langle e_g \| V(1t_1) \| t_{2g} \rangle$.

γ^*	M_s^*	K_{nr} (ISC)
		$\left\| \displaystyle\sum_{\gamma, M_s} \sum_{\gamma'', M_s''} \langle \phi(^4T_2\gamma^* M_s^*) \| V'(T_{2g}) \| \phi(^4T_2\gamma M_s) \rangle \right.$
		$\left. \times \langle \phi(^4T_2\gamma M_s) \| H_{\text{s.o.}} \| \phi(^2E\gamma'' M_s'') \rangle \right\|^2$
ξ	3/2	0
	1/2	$(1/486)(XZ)^2$
	$-1/2$	$(1/486)(XZ)^2$
	$-3/2$	0
η	3/2	$(1/2592)(1 + \sqrt{3})^2(XZ)^2$
	1/2	$(1/3888)(14 + 5\sqrt{3})(XZ)^2$
	$-1/2$	$(1/1296)(2 - \sqrt{3})(XZ)^2$
	$-3/2$	$(1/2592)(1 + \sqrt{3})^2(XZ)^2$
ζ	3/2	$(1/2592)(1 + \sqrt{3})^2(XZ)^2$
	1/2	$(1/7776)(1 + \sqrt{3})^2(XZ)^2$
	$-1/2$	$(1/7776)(1 + \sqrt{3})^2(XZ)^2$
	$-3/2$	$(1/2592)(1 + \sqrt{3})^2(XZ)^2$
		Average $= (1/2916)(4 + \sqrt{3})(XZ)^2$
γ^*	M_s^*	$\left\| \displaystyle\sum_{\gamma, M_s} \sum_{\gamma'', M_s''} \langle \phi(^4T_2, \gamma^*, M_s^*) \| V'(T_{2g}) \| \phi(^4T_1, \gamma, M_s) \rangle \right.$
		$\left. \times \langle \phi(^4T_1, \gamma, M_s) \| H_{\text{s.o.}} \| \phi(^2E, \gamma'', M_s'') \rangle \right\|^2$
ξ	3/2	$(1/384)(XZ)^2$
	1/2	$(1/3456)(XZ)^2$
	$-1/2$	$(1/3456)(XZ)^2$
	$-3/2$	$(1/384)(XZ)^2$
η	3/2	$(1.576)(2 - \sqrt{3})(XZ)^2$
	1/2	$(1/1728)(2 + \sqrt{3})(XZ)^2$
	$-1/2$	$(1/576)(2 + \sqrt{3})(XZ)^2$
	$-3/2$	$(1/576)(2 + \sqrt{3})(XZ)^2$
ζ	3/2	$(1/1152)(XZ)^2$
	1/2	$(1/3456)(7 + 4\sqrt{3})(XZ)^2$
	$-1/2$	$(1/3456)(7 + 4\sqrt{3})(XZ)^2$
	$-3/2$	$(1/1152)(XZ)^2$
		Average $= (1/2592)(5 + \sqrt{3})(XZ)^2$
γ^*	M_s^*	$\left\| \displaystyle\sum_{\gamma', M_s'} \sum_{\gamma'', M_s''} \langle \phi(^4T_2, \gamma^*, M_s^*) \| H_{\text{s.o.}} \| \phi(^2T_1, \gamma', M_s') \rangle \right.$
		$\left. \times \langle \phi(^2T_1, \gamma', M_s') \| V'(T_{2g}) \| \phi(^2E, \gamma'', M_s'') \rangle \right\|^2$
		Vanishes for all γ^*, M_s^*
γ^*	M_s^*	$\left\| \displaystyle\sum_{\gamma', M_s'} \sum_{\gamma'', M_s''} \langle \phi(^4T_2\gamma^*, M_s^*) \| H_{\text{s.o.}} \| \phi(^2T_2\gamma', M_s') \rangle \right.$
		$\left. \times \phi(^2T_2\gamma', M_s') \| V'(T_{2g}) \| \phi(^2E, \gamma'', M_s'') \rangle \right\|^2$
ξ	3/2	0
		$(1/324)(2 + \sqrt{3})(XZ)^2$
	$-1/2$	$(1/324)(2 + \sqrt{3})(XZ)^2$
	$-3/2$	0
η	3/2	$(1/216)(XZ)^2$
	1/2	$(1/216)(XZ)^2$
	$-1/2$	$(1/648)(7 - 4\sqrt{3})(XZ)^2$
	$-3/2$	$(1/216)(XZ)^2$

TABLE III. (Continued).

		K_{nr} (IC)
ζ	3/2	$(1/432)(2 + \sqrt{3})(XZ)^2$
	1/2	$(1/1296)(2 + \sqrt{3})(XZ)^2$
	−1/2	$(1/1296)(2 + \sqrt{3})(XZ)^2$
	−3/2	$(1/432)(2 + \sqrt{3})(XZ)^2$
		Average $= (1/1944)(8 + \sqrt{3})(XZ)^2$
		K_{nr} (IC)
γ^*	M_s^*	$\left| \sum_{\gamma,M_s} \sum_{\gamma'',M_s''} \langle \phi(^4T_2,\gamma^*,M_s^*) | V'(T_{2g}) | \phi(^4T_1,\gamma,M_s) \rangle \right. $
		$\left. \times \langle \phi(^4T_1,\gamma,M_s) \| H_{s.o.} \| \phi(^4T_2,\gamma'',M_s'') \rangle \right\|^2$
ξ	3/2	$(1/384)(XZ)^2$
	1/2	$(1/3456)(XZ)^2$
	−1/2	$(1/3456)(XZ)^2$
	−3/2	$(1/384)(XZ)^2$
η	3/2	$(1/576)(2 - \sqrt{3})(XZ)^2$
	1/2	$(1/1728)(2 + \sqrt{3})(XZ)^2$
	−1/2	$(1/576)(2 + \sqrt{3})(XZ)^2$
	−3/2	$(1/576)(2 + \sqrt{3})(XZ)^2$
ζ	3/2	$(1/1152)(XZ)^2$
	1/2	$(1/3456)(7 + 4\sqrt{3})(XZ)^2$
	−1/2	$(1/3456)(7 + 4\sqrt{3})(XZ)^2$
	−3/2	$(1/1152)(XZ)^2$
		Average $= (1/2592)(5 + \sqrt{3})(XZ)^2$
γ^*	M_s^*	$\left\| \sum_{\gamma',M_s'} \sum_{\gamma'',M_s''} \langle \phi(^4T_2,\gamma^*,M_s^*) \| V'(T_{2g}) \| \phi(^4T_1,\gamma',M_s') \rangle \right.$
		$\left. \times \langle \phi(^4T_1,\gamma',M_s') \| V'(T_{2g}) \| \phi(^4T_2,\gamma'',M_s'') \rangle \right\|^2$
		Vanishes for all γ^*, M_s^*

and excited states of Cr^{3+} ions in alexandrite. Figure 11 shows an approximate Morse potential energy curve for the $^4T_2$ and ^2E excited states. These curves were calculated using the absorption and fluorescence spectra, positions of the zero-phonon lines, and an effective phonon energy of 240 cm^{-1}. The energy difference between the bottom of the $^4T_2$ and ^2E potential energy curves is 800 cm^{-1}. The energy levels of the vibrational levels in each excited state calculated by using Eq. (52) are shown in the figure. Equations (48)–(51) were used to calculate the vibrational wave functions for each vibrational level in both electronic states. These are also shown in the figure.

The vibrational parts of the matrix elements in Eqs. (43) and (44) given by

$$| \langle X(^4T_2v') | X(^2Ev) \rangle |^2 \qquad (53)$$

and

$$| \langle X(^4T_2v') | q_P | X(^2Ev) \rangle |^2 , \qquad (54)$$

etc., can be calculated by using the Morse potential wave functions.[43,47,49–54] The first type of matrix element is the Franck-Condon factor (FCF). The FCF cannot be calculated analytically; therefore, both types of matrix elements in Eqs. (53) and (54) were calculated numerically

The peak in the $^4T_2$ absorption is into the fourth vibrational level of the $^4T_2$ state. Figure 12 shows the calcu-
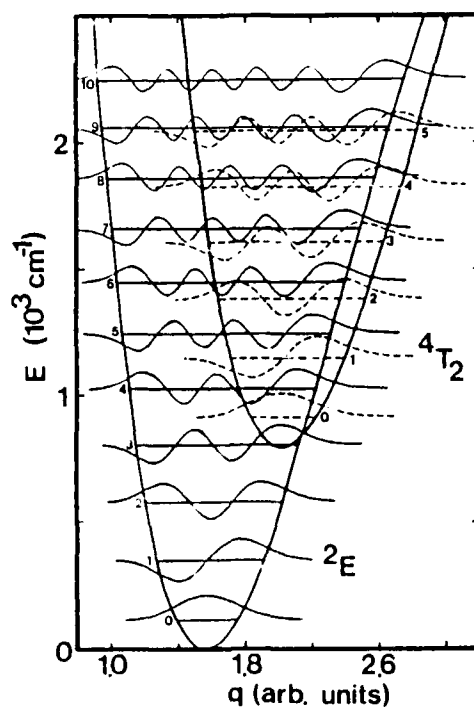

FIG. 11. Morse potentials representing the $^4T_2$ and ^2E levels of Cr^{3+} ions in mirror sites in alexandrite. The horizontal lines represent the vibrational energy levels for 240-cm^{-1} phonons, and the oscillating lines represent the wave functions for each vibrational energy level.
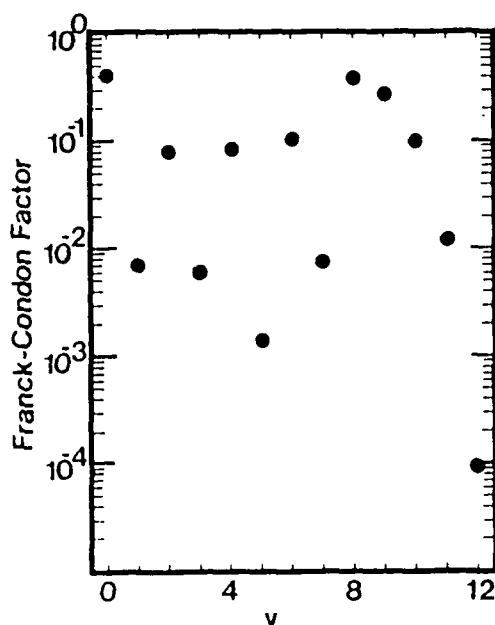
FIG. 12. Franck-Condon factors for a transition from the fourth vibrational level of the $^4T_2$ state to various vibrational levels of the ^2E state designated by vibrational quantum number v.

lated FCF from this level to each of the vibrational levels of the ^2E state. The oscillations are a result of the alternation in sign of the wave functions. The transition from the fourth vibrational level of the $^4T_2$ state to the vibrational level of the ^2E state next lowest in energy $(4 \rightarrow 8)$ has a FCF of approximately 0.14. This FCF is larger than the corresponding FCF in the harmonic approximation because of the shape of the wave functions and the relative positions of the Morse potential-energy curves for large values of q. The potential-energy curves are very close to one another in this region, and the wave functions all have a large positive lobe on this side of the Morse curve. These features are shown in Fig. 11. Therefore, the overlap between vibrational wave functions is predominantly due to the overlap of these positive lobes. The shapes of the wave functions are also indicative of the anharmonicity of the potential-energy curves. The asymmetry of the wave functions is significant even for the second or third vibrational levels. For this reason it is very important to take these anharmonic effects into account.

The vibrational wave functions in a Morse potential are orthonormal. As mentioned previously, this is the reason for resorting to second-order perturbation theory in calculating $K_{nr}(IC)$. The FCF's between the same vibrational sublevels of different electronic states having the same electronic configuration can be set equal to 1 since these potentials are essentially identical. All other FCF's between these levels are small because of orthonormality. The ^2E, $^2T_1$, and $^2T_2$ states originate from the t_{2g}^3 electronic configuration, whereas the $^4T_2$ and $^4T_1$ states originate from the $t_{2g}^2 e_g$ electronic configuration. The vibrational matrix element in Eq. (54) was also calculated numerically. The same types of assumptions mentioned above were used in calculating the various matrix ele-

ments between states.

Equations (43) and (44) can be evaluated by using the results in Table III, the vibrational matrix elements, and spectroscopic data giving the energies of the levels. The reduced matrix elements can be eliminated from the equations by taking the ratio of $K_{nr}(ISC)$ to $K_{nr}(IC)$. This avoids the problems associated with using approximate electronic wave functions to evaluate the single-electron reduced matrix elements which can severely affect the results.[32] Taking the ratio given the relative probability of the two processes. The vibrational matrix elements between a specific vibrational level of an electronic state and another vibrational level of the intermediate electronic state were chosen so that the ion would end up in a level of lower total energy and the calculated rate would have its maximum value. The density of states for the ISC transition was taken from the vibrational level spacing of the ^2E Morse potential curve at the level at which the first step in the nonradiative decay process ends. The density of states for the IC transition was taken from the vibrational level spacing of the $^4T_2$ Morse potential curve at the vibrational level just below the point of optical absorption. This is a result of limiting each step in the nonradiative decay mechanism to single phonon processes. There is an additional factor of $\frac{4}{12}$ that accounts for the difference in the degeneracies in the ratio of the density of final states. The result of this calculation gives

$$\frac{K_{nr}(ISC)}{K_{nr}(IC)} \approx 13 \ . \tag{55}$$

The model for nonradiative decay presented here is different from other models in several respects. The promoting mode interaction is not assumed to be effective only at or near the point where the $^4T_2$ and ^2E potential energy curves cross.[32,55–57] This is one of the reasons that the ISC mechanism can compete with the standard Dexter, Klick, and Russell[56] IC mechanism. The effects of anharmonicities, which are difficult to treat in a solid and have therefore usually been ignored in previous treatments, are included in the estimates of the FCF's and the vibrational matrix elements determined here. The harmonic approximation would lead to FCF's that are much smaller than those obtained here, and this has justified, in the past, the neglect of the ISC channel for nonradiative decay mechanism proposed here. The reason the FCF's are larger when anharmonic effects are included is due to the shape of the wave functions and the shape of the Morse potential-energy curves. The Morse curves shown in Fig. 9 actually have two crossing points, and the curves remain close together in the region between these points. This keeps the vibrational overlap integrals from decreasing to the value that would be obtained in the harmonic approximation. In the harmonic approximation the potential-energy curves cross in only one point, and the curves get farther apart as the vibrational quantum number increases above the crossing point.

Figure 13 shows the dephasing time calculated from the FWM data for Cr^{3+} ions in several different crystal-field environments, alexandrite mirror and inversion sites, emerald, and ruby. The dephasing time is shown as a

function of the energy difference between the peak of the $^4T_2$ absorption and the ^2E absorption. This energy difference is essentially the energy that must be emitted in the nonradiative decay process outlined above. The dephasing mechanism is a result of population relaxation from the $^4T_2$ level. The dependence of the dephasing rate on the energy difference shown in Fig. 13 strongly supports the conclusion reached above that the dominant nonradiative decay channel is the ISC channel. If the nonradiative decay process does not involve the ISC decay channel, then the dephasing rate would not depend on the crystal field strength of the host crystal, and therefore would be independent of the energy difference between the $^4T_2$ and ^2E absorption transitions. If the ISC channel of nonradiative decay is the dominant relaxation pathway, then the well-known exponential dependence of the decay rate on the energy gap should be observed.[35,38] This is observed in the data, confirming the results of the theoretical calculation for the relative branching ratio of the two relaxation pathways. The dominant decay channel in other host crystals with smaller crystal field strengths and therefore a smaller energy difference between $^4T_2$ and ^2E absorption transitions may be different. An increase in the probability of the IC decay channel would decrease the ratio in Eq. (55) leading to the independence of T_2 on the energy difference between the $^4T_2$ and ^2E absorption transitions.

The mechanism for dephasing in this case is consistent with a population relaxation process, namely the $^4T_2$-^2E nonradiative decay. The temperature dependence of the dephasing rate should be the same as that of the multiphoton emission rate. The temperature dependence of the multiphoton emission rate is

$$R \approx (\bar{n} + 1)^{p'} , \qquad (56)$$

where p' is the number of phonons emitted. The energy difference between the peak in the $^4T_2$ and ^2E absorption
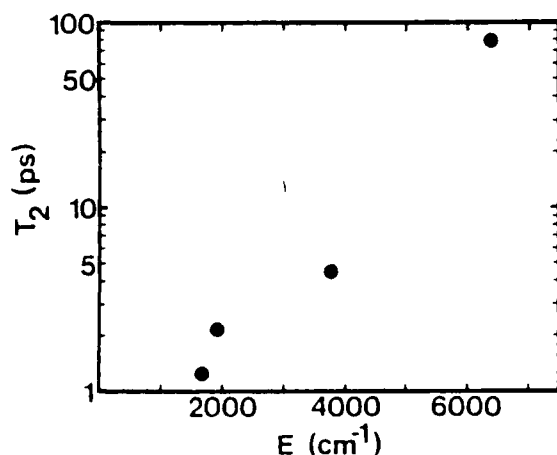

FIG. 13. Dephasing time for Cr^{3+} ions in several different crystal-field environments as a function of the energy difference between the peak in the $^4T_2$ and ^2E absorption transitions. The results were obtained for pumping in the $^4T_2$ level of alexandrite inversion sites, ruby, alexandrite mirror sites, and emerald listed in decreasing order of the energy difference (adapted from data reported in Refs. 5 and 6).

transitions for the mirror site Cr^{3+} ions is 1900 cm^{-1}. Measurements of the vibronic, Raman, and anti-Stokes excitation spectra[12] have shown that the phonons of lowest energy for which the electron-phonon coupling is significant are 240-cm^{-1} phonons. 40-cm^{-1} phonons play an important role in the dynamics of the ^2E state,[31] but should not be as important in the $^4T_2$-^2E nonradiative decay. This leads to a multiphonon emission rate at 300 K that is only slightly higher than the multiphonon emission rate at 30 K. This agrees with the experimental observations within the experimental error.

C. FWM signal intensity

The intensity of the FWM signal for excitation into the ^2E and $^4T_2$ levels was measured under identical conditions: temperature (50 K), grating spacing, power, and polarization. The measured value of the signal intensity was adjusted to account for the difference in the absorption coefficient at the two excitation wavelengths. The results show that the FWM signal formed after direct excitation into the ^2E state is 43 times more intense than the FWM signal formed after excitation into the $^4T_2$ state. In both cases the grating inducing the scattering is a population grating of Cr^{3+} ions in the ^2E level. There are two possible reasons for this. First, it has been shown here than an inversion site grating is formed after excitation into the $^4T_2$ band but not after excitation into the ^2E zero-phonon lines of the mirror-site ions. This can provide a loss mechanism which decreases the FWM signal intensity. Second, the difference in dephasing times, 2.2 and 55 ps, for the $^4T_2$ and ^2E excitations, respectively, may be the reason for this difference. The dephasing time is related to the laser-induced changes in the optical properties of the material[15] which are responsible for the FWM process, and therefore can indirectly affect the FWM scattering efficiency as shown in Eq. (12). Since the first process has been shown to be very weak, the second process should be the dominant cause for the difference in the scattering efficiency at the two excitation wavelengths.

V. DISCUSSION AND CONCLUSIONS

In this paper LIG techniques have been used to extend the previously reported energy transfer and dephasing studies in alexandrite. The temperature dependence of the exciton diffusion constant is the same for excitation into the ^2E level and for excitation into the $^4T_2$ level. Using the theoretical framework developed by Kenkre,[23,24] the temperature dependence of the ion-ion interaction rate and exciton scattering rate have been deduced It should be noted that the formalism of Kenkre is exact only on a perfect lattice, and thus the theory of Kenkre should be considered an approximation to the exciton dynamics of the actual system. In this system there is a broad distribution of distances between Cr^{3+} ions, and hence there is a broad distribution of interaction strengths between Cr^{3+} ions. Therefore, the ion-ion interaction strength in the Kenkre theory should be considered to be an average interaction strength. The temperature depenence of the ion-ion interaction rate is con-

sistent with the Dexter[25] model, dominated by the lifetime and linewidth of the spectral transition. This same analysis was used to analyze the data obtained pumping into the $^4T_2$ level. The ion-ion interaction rate is the same as obtained for the ^2E excitation, but the exciton scattering rate is slightly higher. This may be a result of the additional phonons generated in the nonradiative decay from the $^4T_2$ state to the ^2E state. This also confirms that the grating is formed in the ^2E state. The exciton transport properties imply a nonuniform distribution of Cr^{3+} ions. The intensity of the inversion-site grating contribution to the LIG signal as a function of the grating spacing is consistent with the very low concentration of inversion-site Cr^{3+} ions in this sample. Results of similar measurements[6] have shown that the exciton diffusion coefficient in emerald increases with increasing temperature. For that case the exciton scattering rate was found to increase with temperature similarly to the alexandrite results, but the ion-ion interaction rate exhibited a much stronger increase with temperature. This is due to the smaller crystal-field splitting in emerald which allows the $^4T_2$ level to become thermally populated at much lower temperatures than in alexandrite. The higher oscillator strength for the $^4T_2$-to-$^4A_2$ transition and the greater spectral overlap from the $^4T_2$ emission significantly enhances the energy transfer efficiency.

The transient LIG signal was found to reflect the saturation behavior of the pumping dynamics. The model used to analyze these transients accurately predicts the functional dependence of the pumping dynamics on the lifetime of the excited state, the pump intensity, and the absorption cross section. The absorption cross section for the inversion-site ions at 488 nm and the laser-induced change in the index of refraction were calculated to be 0.5×10^{-20} cm^2 and 5.0×10^{-6}, respectively. The results of similar measurements on ions in the mirror sites are consistent with the higher value of the saturation parameter. The power dependence of the LIG signal shows a quadratic dependence at low pump powers, but at high pump powers a deviation from this dependence is evident. The analysis of the data that this departure from a quadratic dependence is not a result of a normal saturation process in the pumping dynamics, but is a result of beam depletion through the laser-induced change in the absorption coefficient.

Measurements of the FWM scattering efficiency as a function of the grating spacing yield information on the dephasing time of the system. These measurements were done for excitation into the ^2E and $^4T_2$ states and an analysis of the data yielded two different types of dephasing mechanisms. The dephasing time for the direct excitation of the ^2E level is consistent with the linewidth data, implying that the inhomogeneous dephasing time is the dominant dephasing mechanism. It should be noted that this is not a line narrowing experiment and specific subsets of ions are not excited. The dephasing time for excitation into the $^4T_2$ band is consistent with the nonradiative decay time from the $^4T_2$ level to the ^2E level. This is also evidenced in the temperature dependence of the dephasing time. A detailed theoretical analysis of the nonradiative decay process was carried out. The model used for this analysis includes the effects of anharmonicity and the admixing of the different states of the system. The results show the importance of intersystem-crossing in the initially excited vibrational level of the $^4T_2$ state. Calculation of the relative branching ratio shows this pathway for decay to the bottom of the ^2E potential well to be more probable than the pathway leading to the initial relaxation to the bottom of the $^4T_2$ potential well. The dephasing time for alexandrite, emerald and ruby was found to vary approximately exponentially with the energy gap between the peak of the $^4T_2$ absorption and the ^2E absorption, and this is interpreted as evidence for the important role this ISC relaxation pathway plays in the dephasing processes in these materials. Also, the intensities of the FWM signals for excitation into the $^4T_2$ and ^2E levels were found to be significantly different and this is attributed to the difference in the dephasing rates.

ACKNOWLEDGMENT

[*]Permanent address: Institute of Physics, Polish Academy of Sciences, Aleja Lotnikow 32/46, 02-668 Warsaw, Poland.

[1]J. R. Salcedo, A. E. Siegman, D. D. Dlott, and M. D. Fayer, Phys. Rev. Lett. 41, 131 (1978).

[2]H. J. Eichler, J. Eichler, J. Knof, and Ch. Noack, Phys. Status Solidi A 52, 481 (1979).

[3]D. S. Hamilton, D. Heiman, J. Feinberg, and R. W. Hellwarth, Opt. Lett. 4, 124 (1979).

[4]P. F. Liao, L. M. Humphrey, D. M. Bloom, and S. Geschwind, Phys. Rev. B 20, 4145 (1979).

[5]A. Suchocki, G. D. Gilliland, and R. C. Powell, Phys. Rev. B 35, 5830 (1987).

[6]G. J. Quarles, A. Suchocki, R. C. Powell, and S. Lai, Phys. Rev. B (to be published).

[7]A. Suchocki, R. C. Powell, Chem. Phys. accepted for publication.

[8]A. M. Ghazzawi, J. K. Tyminski, R. C. Powell, and J. C. Walling, Phys. Rev. B 30, 7182 (1984).

[9]J. C. Walling, O. G. Peterson, H. P. Jenssen, R. C. Morris, and E. W. O'Dell, IEEE J. Quantum Electron. QE-16, 1302 (1980).

[10]R. E. Newnham, R. Santoro, J. Pearson, and C. Jansen, Am. Mineral. 49, 427 (1964).

[11]R. C. Powell, L. Xi, X. Gang, G. J. Quarles, and J. C. Walling, Phys. Rev. B 32, 2788 (1985).

[12]A. Suchocki, G. D. Gilliland, R. C. Powell, J. M. Bowen, and J. C. Walling, J. Lumin. 37, 29 (1987).

[13]K. K. Shepler, J. Appl. Phys. 56, 1314 (1984).

[14]M. L. Shand, J. C. Walling, and R. C. Morris, J. Appl. Phys. 52, 953 (1981).

[15]R.L. Abrams and R. C. Lind, Opt. Lett. 2, 94 (1978).

[16]A. Yariv and D. M. Pepper, Opt. Lett. 1, 16 (1977).

[17]J. K. Tyminski, R. C. Powell, and W. K. Zwicker, Phys. Rev. B **29**, 6074 (1984).

[18]Y. Silberberg and I. Bar-Joseph, IEEE J. Quantum Electron. **QE-17**, 1967 (1981).

[19]H. Fujiwara and K. Nagawa, J. Opt. Soc. Am. B **4**, 121 (1987).

[20]J. A. Buck and J. R. Rodriguez, J. Opt. Soc. Am. B **4**, 1988 (1987).

[21]C. M. Lawson, R. C. Powell, and W. K. Zwicker, Phys. Rev. Lett. **46**, 1020 (1981).

[22]M. D. Fayer, in *Spectroscopy Excitation Dynamics of Condensed Molecular Systems,* edited by V. M. Agranovich and R. M. Hochstrasser (North-Holland, Amsterdam, 1983), p. 185.

[23]V. M. Kenkre and D. Schmid, Phys. Rev. B **31**, 2430 (1985).

[24]Y. M. Wong and V. M. Kenkre, Phys. Rev. A **22**, 3072 (1980).

[25]D. L. Dexter, J. Chem. Phys. **21**, 836 (1953).

[26]S. C. Stotlar and L. B. Edgett, in Proceedings of the Optical Society of America Annual Meeting, Washington, D.C., 1985 (unpublished).

[27]V. M. Agranovich and M. D. Galanin, *Electronic Excitation Energy Transfer in Condensed Matter* (North-Holland, Amsterdam, 1982).

[28]T. Holstein, S. K. Lyo, and R. Orbach, in *Laser Spectroscopy of Solids,* edited by W. M. Yen and P. M. Selzer (Springer-Verlag, Berlin, 1981), Chap. 2.

[29]V. M. Kenkre and D. Schmid, Chem. Phys. Lett. **140**, 238 (1987).

[30]M. D. Levenson, *Introduction to Nonlinear Laser Spectroscopy* (Academic, New York, 1982).

[31]D. Boye, S. Majetich, J. E. Rives, R. S. Meltzer, and R. M. MacFarlane, J. Lumin. **4**, P74 (1987).

[32]R. H. Bartram, J. C. Charpie, L. J. Andrews, and A. Lempicki, Phys. Rev. B **34**, 2741 (1986).

[33]B. Z. Malkin, Fiz. Tverd. Tela (Leningrad) **4**, 2214 (1962) [Sov. Phys.—Solid State **4**, 1620 (1963)].

[34]R. Englman, B. Champagnon, E. Duval, and A. Monteil, J. Lumin. **28**, 337 (1983).

[35]R. Englman, *Nonradiative Decay of Ions and Molecules in Solids* (North-Holland, Amsterdam, 1979).

[36]R. Englman and B. Barnett, J. Lumin. **3**, 37 (1970); B. Barnett and R. Englman, *ibid.* **3**, 55 (1970).

[37]K. Huang, Sci. Sin. **24**, 27 (1981).

[38]Jia Weiyi, Zheng Qingrong, Shang Yusheng, Wang Yanyun, Yao Zhenyi, He Shouan, Zhou Hetian, and Liu Liling, Kexue Tongbao **30**, 452 (1985).

[39]E. B. Wilson, J. C. Decius, and P. C. Cross, *Molecular Vibrations* (Dover, New York, 1955).

[40]J. S. Griffith, *The Theory of Transition Metal Ions* (Cambridge University Press, Cambridge, England, 1961).

[41]S. Sugano, Y. Tanabe, and H. Kamimura, *Mutiplets of Transition-Metal Ions in Crystals* (Academic, New York, 1970).

[42]A. L. Schawlow, A. H. Piksis, and S. Sugano, Phys. Rev. **122**, 1469 (1961).

[43]B. I. Makshantsev, Opt. Spectrosk. **31**, 355 (1971) [Opt. Spectrosc. (USSR) **31**, 191 (1971)].

[44]M. D. Sturge, Phys. Rev. B **8**, 6 (1973).

[45]P. M. Morse, Phys. Rev. **34**, 57 (1929).

[46]J. A. C. Gallas, Phys. Rev. A **21**, 1829 (1980).

[47]P. A. Fraser and W. R. Jarmain, Proc. Phys. Soc. London Sect. A **66**, 1145 (1953); **66**, 1153 (1953).

[48]V. S. Vasan and R. J. Cross, J. Chem. Phys. **78**, 3869 (1983).

[49]J. A. C. Gallas, H. P. Grieneisen, and B. P. Chakraborty, J. Chem. Phys. **69**, 612 (1978).

[50]T. Y. Chang and M. Karplus, J. Chem. Phys. **52**, 783 (1970).

[51]M. Ramjee, M. L. P. Rao, D. V. K. Rao, and P. T. Rao, J. Chem. Phys. **75**, 1574 (1981).

[52]I. I. Tugov, Opt. Spektrosk. **45**, 660 (1978) [Opt. Spectrosc. (USSR) **45**, 627 (1978)].

[53]V. B. Sovkov and V. S. Ivanov, Opt. Spektrosk. **59**, 1222 (1985) [Opt. Spectrosc. (USSR) **59**, 733 (1985)].

[54]B. I. Makshantsev, Opt Spektrosk. **34**, 872 (1973) [Opt. Spectrosc. (USSR) **34**, 503 (1973)].

[55]A. M. Stoneham and R. H. Bartram, Solid-State Electron. **21**, 1325 (1978).

[56]D. L. Dexter, C. C. Klick, and G. A. Russell, Phys. Rev. **100**, 603 (1955).

[57]R. H. Bartram and A. M. Stoneham, Semicond. Insulators **5**, 297 (1983).

[58]R. Englman and J. Jortner, Mol. Phys. **18**, 145 (1970).

Optical spectroscopy and four-wave mixing in emerald

Gregory J. Quarles,* Andrzej Suchocki,† and Richard C. Powell

Department of Physics, Oklahoma State University, Stillwater, Oklahoma 74078-0444

Shui Lai

Allied Signal, Inc., Morristown, New Jersey 07960

(Received 21 December 1987; revised manuscript received 2 May 1988)

The optical-spectroscopic properties of Cr^{3+} ions in $Be_3Al_2(SiO_3)_6$ crystals were investigated using several techniques. The temperature dependencies of the fluorescence intensity and lifetime were measured between 10 and 300 K and shown to be due to thermal population effects in the $^4T_2$ and ^2E levels. The results of time-resolved site-selection spectroscopy measurements show that the Cr^{3+} ions occupy several different types of sites having nonequivalent crystal fields, and that spectral energy transfer takes place between ions in different types of sites. The results of four-wave mixing measurements show the presence of long-range resonant energy migration among the chromium ions and provide information about the radiationless relaxation rate from the $^4T_2$ level to the ^2E level.

I. INTRODUCTION

The potential use of emerald [$Be_3Al_2(SiO_3)_6$:Cr^{3+}] as a tunable solid-state laser material[1-3] has generated renewed interest in understanding the details of the spectroscopic properties of this crystal. Although the general optical spectroscopic properties of emerald have been characterized,[4-9] there are still important unanswered questions concerning the local crystal-field environment of the Cr^{3+} ions, the characteristics of energy transfer among the Cr^{3+} ions, and the details of radiationless transition in this material. We report here the results of investigating the optical properties of emerald using several different spectroscopic techniques, including time-resolved site-selection spectroscopy (TRSSS) and four-wave mixing (FWM). The results show that the Cr^{3+} ions occupy sites having several different types of local crystal-field environments and that this leads to two different types of energy-transfer processes in this material. The first is a short-range process between ions in sites having nonequivalent crystal-field environments, while the second is a resonant, long-range migration process. These processes are characterized in terms of Frenkel excitons with the mobile excitation energy localized on a Cr^{3+} ion. The radiationless transitions distributing the population of excited ions among the $^4T_2$ and ^2E levels are shown to be responsible for the temperature dependences of the fluorescence intensity and lifetime and for the dephasing time of the four-wave mixing signal.

The sample was used in this work had a rectangular shape of dimensions 7.5 × 13 × 3.8 mm and a dark-green color. It was grown by the hydrothermal method and contained 3 at. % Cr^{3+} ions ($N_0 = 1.77 \times 10^{20}$ cm^{-3}). Emerald has the beryl structure with a space group designated as $P6/mcc$ and two molecules per unit cell.[10] The Cr^{3+} ions substitute for the Al^{3+} ions and "sit" at the center of a slightly distorted octahedral site, as is seen in Fig. 1. The site symmetry of Cr^{3+} in this lattice is[11,12]

D_3. The dominant structure in beryl is the Si_6O_{18} rings which are linked by Be and Al ions. As noted on Fig. 1, the first- and second-nearest-neighbor distances for the Cr^{3+} sites are 4.6 and 5.3 Å, respectively.[10] This is much larger than the 2.65- or 2.7-Å first-nearest-neighbor distances found in similar Cr^{3+}-doped laser materials, ruby[13] and alexandrite,[14] respectively. These larger distances between Cr^{3+} ions allow for high concentrations without appreciable concentration quenching of the fluorescence. However, the tradeoff is that the density of available sites for Cr^{3+} in beryl is 5.9×10^{21} cm^{-3}, which is approximately 12% of that in the corundum lattice of ruby.[9] For emerald doped with 3 at. % Cr^{3+} there is evidence for the presence of exchange coupled pairs of Cr^{3+}

EMERALD
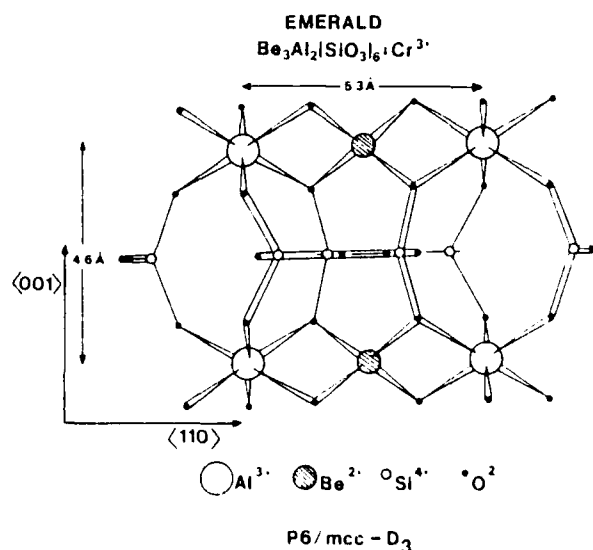$Be_3Al_2[SiO_3]_6$:Cr^{3+}

$P6/mcc - D_3$

FIG. 1. Crystal structure of beryl projected onto a (100) plane. (Taken from Ref. 9.)

ions.[10] Also, at this high level of concentration there is a considerable amount of internal strain in the crystal, causing different local crystal-field environments for the Cr^{3+} ions which results in inhomogeneous broadening of the optical transitions. Both the exchange coupling and microscopic strains can contribute to the spectral structure described in Sec. II.

II. OPTICAL SPECTROSCOPIC PROPERTIES

The absorption and fluorescence spectra of emerald at 70 K are shown in Figs. 2 and 3. The former was obtained using an IBM 9430 UV-Visible Spectrophotometer. The latter was taken using the 488-nm line of an argon laser for the excitation, a 1-m Spex monochromator for spectral dispersion, a RCA-C31034 photomultiplier tube to detect the signal, and a lock-in amplifier to enhance the signal-to-noise ratio. The sample was placed in a cryogenic refrigerator in order to control the temperature. Front-surface excitation of the fluorescence was used to minimize the effects of reabsorption. The peaks in the absorption spectrum are labeled in terms of the octahedral crystal-field designations of the final states of their transitions from the $^4A_2$ ground state. The fluorescence is associated with zero-phonon transitions from the crystal-field-split components of the ^2E level (R lines) and broadband fluorescence, which is a superposition of the vibronic sideband of the R lines and emission from the $^4T_2$ level.

Figure 4 shows the absorption and fluorescence spectra in the region of the R lines at 70 K uncorrected for polarization effects. (The effects of polarization on the spectra are clearly shown in Ref. 3.) Both fluorescence and absorption spectra were taken at temperatures ranging from 10 to 300 K, but the structure in the R_1 and R_2 lines becomes most visible around 70 K. These lines are inhomogeneously broadened with large linewidths, consistent with results reported previously.[15] The fluorescence spectra were obtained with cw excitation at 457.9 nm. Both of the R lines in fluorescence exhibit a structure
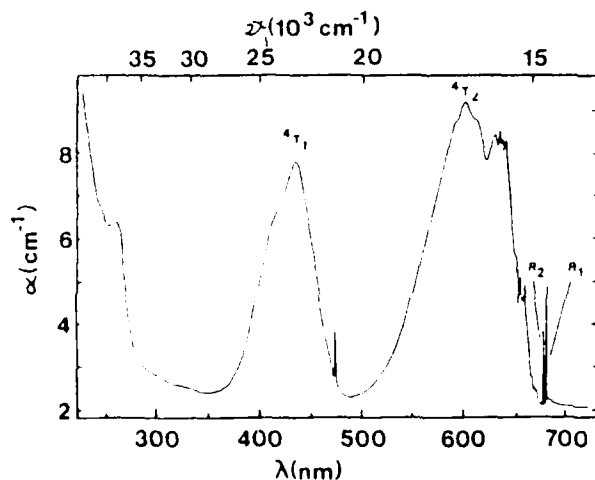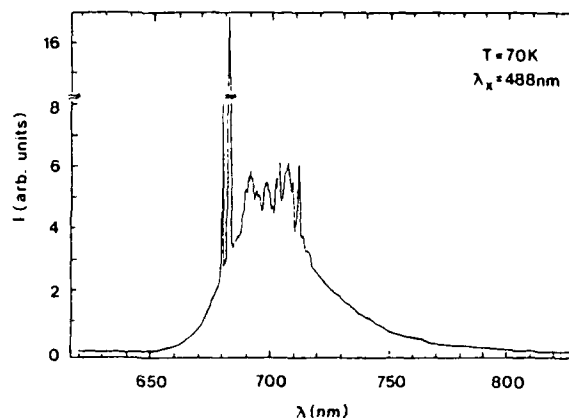

FIG. 3. Fluorescence spectrum of emerald with 3 at. % Cr^{3+} at $T = 70$ K using 488-nm excitation from an argon-ion laser.

consisting of four peaks, and some structure is also observed in absorption. The positions of these components are listed in Table I. Each peak is designated with superscripts, but it is not clear how the peaks in R_1 correlate with those in R_2. Assuming that each of the peaks is associated with a different local crystal-field environment for the Cr^{3+} ion, and assuming the same oscillator strength for the $^4A_{2g} \rightarrow {}^2E_g$ transition for each type of environment, it is possible to estimate the relative concentrations of the Cr^{3+} ions in each of the different environments from the absorption spectra of the R lines. These values are listed in Table I.

The decay kinetics of the fluorescence excitating at 588 nm were monitored using a boxcar integrator. The sig-

FIG. 2. Absorption spectrum of emerald with 3 at. % Cr^{3+} at $T = 70$ K.
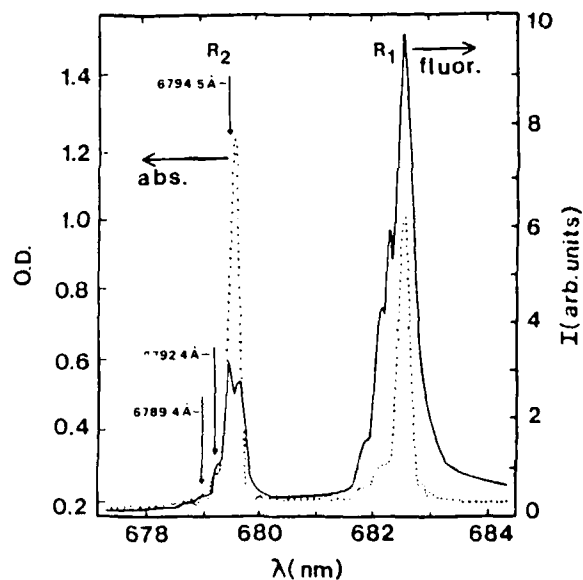

FIG. 4. High-resolution fluorescence and absorption spectra of the R lines in emerald at 70 K. The vertical arrows indicate excitation wavelengths used in site-selection spectroscopy. O.D. is the optical density.

TABLE I. Spectral properties of the R lines of emerald with 3 at. % Cr^{3+} at 20 K.

Parameter	a	b	Site c	d	e
Peak position λ_{R_1} (nm)					
Absorption	681.55	681.80	682.25		682.60
Fluorescence		681.80	682.20	682.30	682.60
Peak position λ_{R_2} (nm)					
Absorption	678.80	678.95	679.24	679.56	
Fluorescence		678.95	679.25	679.50	679.65
Concentration o ions					
N_i ($\times 10^{18}$ cm^{-3})	1.72	3.68		171.60[a]	
Fluorescence decay time τ (ms)					
$\lambda_{ex}=678.94$ nm		1.112			1.436
		0.317			
$\lambda_{ex}=679.24$ nm		1.859	1.079		1.610
		0.707	0.351		
$\lambda_{ex}=679.45$ nm			1.540		1.575
Fluorescence rise time t, (μs)					
$\lambda_{ex}=678.94$ nm		83.89			218.7
$\lambda_{ex}=679.24$ nm		95.86	112.0		213.2
$\lambda_{ex}=679.45$ nm			149.8		364.2

[a]This represents the sum of the concentrations of ions in sites c and d since their transitions are not well resolved; the transition from ions in site e is too small to determine an accurate concentration.

nals were found to be single-exponential decays over two decades between 12 and 200 K. The decay time of the fluorescence was 1.7 ms at temperatures below 60 K. This is slightly longer than the low-temperature lifetimes reported by Kisliuk and Moore[16] and by Hassan et al.[9] In both of these cases it was suggested that traces of Fe^{2+} ions quenched the Cr^{3+} fluorescence. Above 60 K the

lifetime decreases with increasing temperature due to thermal population of the $^4T_2$ level. The temperature dependence of the fluorescence lifetime is shown in Fig. 5. A theoretical prediction for the temperature dependence of the fluorescence lifetime can be obtained from the expression

$$\tau^{-1}=\tau_E^{-1}+\tau_T^{-1}\exp(-\Delta E/k_B T) . \qquad (1)$$

Here it has been assumed that the ^2E and $^4T_2$ levels are separated by an energy ΔE and their populations are in thermal equilibrium. τ_E and τ_T are the intrinsic lifetimes of these levels and it is assumed that the intermediate $^2T_1$
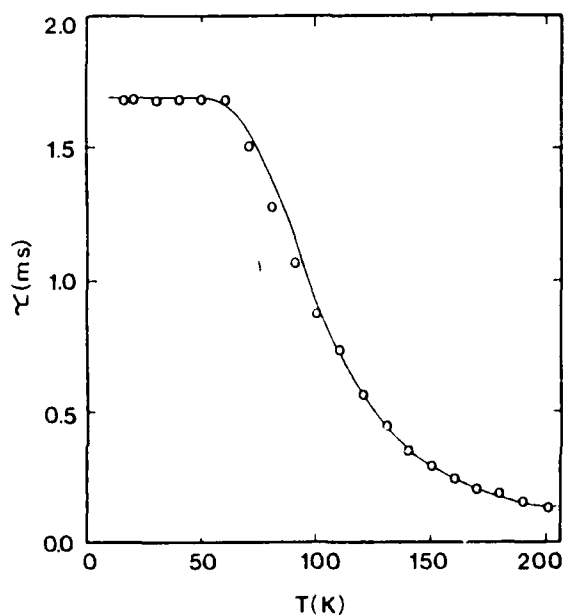

FIG. 5 Temperature dependence of the fluorescence lifetime of emerald.

TABLE II. Spectral energy transfer parameters for emerald with 3 at. % Cr^{3+} at 20 K.

From fitting the temperature dependence of the fluorescence lifetime	
ΔE	381 cm^{-1}
τ_T	14 μs
τ_E	1.7 ms
From time-resolved site-selection spectroscopy results	
$I_a(0)/I_s(0)$	0.085
Ω	15.59 $s^{-1/2}$
R_0	7.42 Å
From fitting the fluorescence-decay kinetics	
a''	4.67×10^{-41} cm^6/s
D_n	6.51×10^{-13} cm^2/s
a'	15.98 Å
R_0	6.11 Å
Theoretical prediction	
D_n	4.6×10^{-13} cm^2/s

levels do not play a significant role in the spectral dynamics.[16] Using Eq. (1) with the intrinsic lifetimes and the energy gap treated as adjustable parameters, the best fit to the data is shown as a solid line in Fig. 5. The value of the energy gap between the ^2E and the $^4T_2$ levels is found to be equal to 381 cm^{-1}, which is in good agreement with previous reported values.[16,17] The intrinsic decay time of the $^4T_2$ level was found to be 14 μs, which is close to the values found from previous investigations.[9,16] The intrinsic lifetime of the ^2E level was found to be 1.7 ms. The parameters used in obtaining this fit are listed in Table II.

III. TIME-RESOLVED SITE-SELECTION SPECTROSCOPY

Time-resolved site-selection spectroscopy (TRSSS) measurements were used to characterize the properties of short-range spectral energy transfer between Cr^{3+} ions with different crystal-field environments in emerald. A nitrogen-laser-pumped dye laser, using Oxazine 720 dye with a narrow linewidth (< 0.6 Å) was used to selectively excite the Cr^{3+} ions having a specific type of crystal-field environment. Excitation in the R_2 line typically yields three emission peaks in the R_1 line, and the energy transfer is predominantly from ions in crystal-field environments, resulting in higher-energy transitions to those in environments having lower-energy transitions. Using the labeling scheme from Table I, the ions with environments giving transitions a and b act as sensitizers and those with the environment giving transition d act as activators. It was not possible to resolve the c or e transitions using nanosecond pulse excitation into the R_2 line, and thus ions with environments giving rise to these transitions are also counted as activators. By taking spectral scans of the fluorescence emission at different times after the laser-excitation pulse, it was possible to characterize the time evolution of the energy transfer between Cr^{3+} ions having different crystal-field environments.

The experimental apparatus for the TRSSS measurements has been described previously.[18] The emerald sample was excited using three different laser wavelengths, 6789.4, 6792.4, and 6794.5 Å, which are shown as vertical arrows in the R_2 absorption line in Fig. 4. The fluorescence spectra of the R_1 lines were then spectrally resolved through a 1-m monochromator and directed onto a RCA-C31034 photomultiplier tube. The input and output slits were maintained at 100 μm to ensure a resolution of ≤ 0.4 Å.

Figure 6 shows the typical fluorescence spectrum of the R_1 lines at 20 K and at 1.00 ms after excitation at 6789.4 Å. It was possible to resolve three separate peaks in the fluorescence as shown in the figure. To study the spectral energy transfer, it is necessary to know the area associated with each peak and how it evolves with time. To get a good estimate for the area, the data were deconvoluted with a curve-fitting routine that fitted three overlapping Gaussian peaks to the fluorescence spectra. The separate Gaussians are denoted by the dashed lines in Fig. 6, with the overall fit shown by the solid line. The Gaussian profile fits the data quite well. From the curve-fitting routine it was possible to obtain the total area, the peak
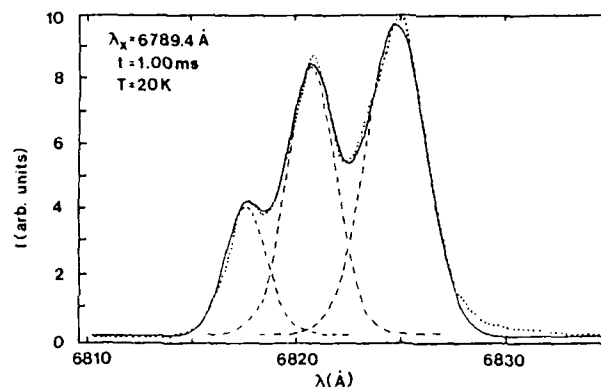

FIG. 6. Fluorescence spectra of the R_1 lines in emerald at 1.0 ms after the pulse after selectively exciting the R_2 line at 6789.4 Å at 20 K. The dots represent experimental data points and the dashed and solid lines represent the fitting with three overlapping Gaussian curves.

wavelength and intensity, and the full width at half maximum for each Gaussian component.

The fluorescence risetimes and lifetimes of each of the three peaks were monitored for each excitation wavelength and temperature, and their values at 20 K are listed in Table I. The two highest-energy peaks are both double-exponential decays with fast risetimes, while the lowest-energy peak is single exponential over two decades with a much longer risetime. The accuracy of the lifetimes and risetimes is approximately ±5%. To characterize the properties of energy transfer between ions with different types of crystal-field environments, the two highest-energy peaks are designated as being from sensitizer ions and the lowest-energy peak as being from activator ions, as discussed above. Figure 7 shows the fluorescence spectra of the R_1 lines for four different temperatures at 100 μs after the three different excitation wavelengths. As the excitation wavelength is shifted to lower energy, the number of distinct peaks decreases until there is only one fluorescence peak remaining, that being associated with the emission from the activator ions excited by the lowest-energy excitation wavelength. There is also very slight backtransfer from activator to sensitizer sites, noticeable mostly at higher temperatures. Figure 8 shows the fluorescence spectra at 20 K, for the three excitation wavelengths, at five different times after the pulse. The two highest-energy peaks (transitions from sites a and b) evolve at approximately the same rate, while the lowest-energy peak (transitions from sites c, d, and e) evolves more slowly and becomes the dominant peak at the longer times after the pulse.

The time evolution of the R_1 lines is demonstrated in Fig. 9, which shows the changes in the ratios of the integrated fluorescence intensities of the activator transition to that of the sensitizer transition. These areas are taken from the fits of the experimental data with Gaussian curves. There is an initial buildup of the ratios of the relative area of the transitions and, at longer times after

the pulse, an equilibrium condition is approached.

The time evolution of the ratios can be modeled using a phenomenological rate-parameter model.[18] The sensitizer ions are those preferentially excited by the laser at a rate W_s, whereas the activator ions receive the energy through energy transfer as well as a small amount of direct pumping at a rate W_a. n_a and n_s are the concentrations of the ions in the excited states, W_{sa} is the rate of energy transfer from sensitizer to activator, and β_a and β_s are the fluorescence decay rates associated with each

type of ion. As noted above, the time-resolved spectral data show that backtransfer from activator ions to sensitizer ions is negligible at low temperatures and weak at high temperatures. Therefore this process is neglected in the analysis. The reason that there is no strong backtransfer in this case is that the concentration of ions in activator sites is much higher than the concentration of ions in sensitizer sites and strong energy transfer occurs among activator ions. This is discussed in detail in the next section. With these assumptions, the rate equations
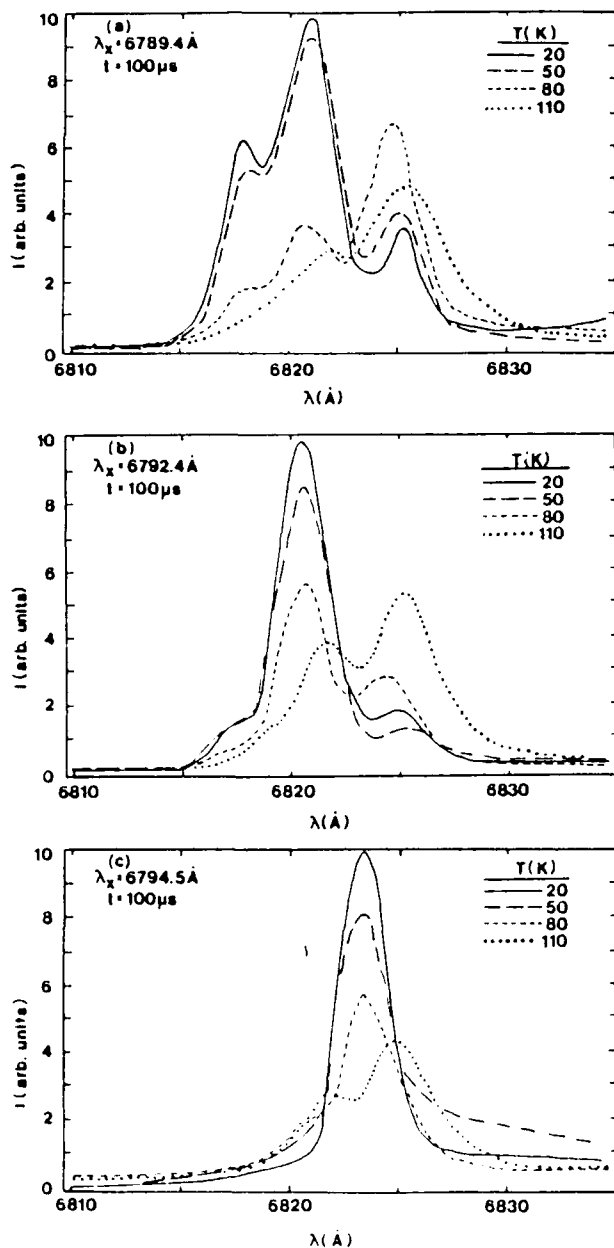

FIG. 7 Fluorescence spectra of the R_1 lines in emerald for different temperatures at 100 μs after the pulse after selectively exciting the R_2 line at (a) 6789.4 Å, (b) 6792.4 Å, and (c) 6794.5 Å
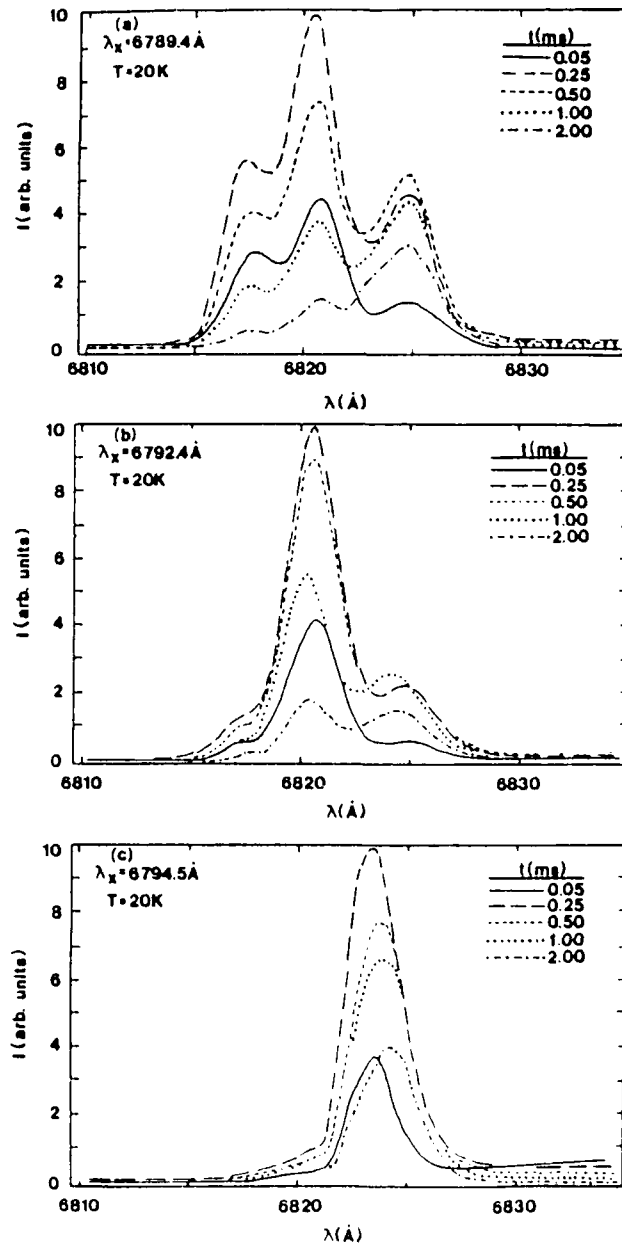
FIG. 8. Fluorescence spectra of the R_1 lines in emerald at 20 K at five different times after the pulse after selectively exciting the R_2 lines at (a) 6789.4 Å, (b) 6792.4 Å, and (c) 6794.5 Å.

describing the time evolution of the populations of the excited state are

$$\frac{dn_s}{dt} = W_s - \beta_s n_s - W_{sa} n_s , \tag{2}$$

$$\frac{dn_a}{dt} = W_a - \beta_s n_a + W_{sa} n_s . \tag{3}$$

These equations can be solved assuming a δ-function excitation pulse and an explicit time dependence for the energy-transfer rate. The solutions were obtained using various types of time dependencies for W_{sa} associated with different types of energy-transfer mechanisms. It was found that the best fit to the data was obtained with a time dependence for the energy-transfer rate of $t^{-1/2}$. The physical meaning of this time dependence is discussed below. The solutions of Eqs. (2) and (3) in this case are given by

$$n_s(t) = n_s(0)\exp(-\beta_s t - 2\Omega t^{1/2}) , \tag{4}$$

$$n_a(t) = n_s(0)[\exp(-\beta_s t) - \exp(-\beta_s t - 2\Omega t^{1/2})]$$

$$+ n_a(0)\exp(-\beta_a t) , \tag{5}$$

where the time dependence of the energy-transfer rate is written explicitly as $W_{sa} = \Omega t^{-1/2}$. The ratio of the integrated fluorescence intensities is proportional to the ratios of the excited-state populations,

FIG. 9. Time dependence of the ratios of the integrated fluorescence intensities of the R_1 lines from Cr^{3+} ions in sensitizer and activator sites for four different temperatures. The solid and dashed lines represent the theoretical fits to the experimental data using a rate-equation model.

$$I_a/I_s = (\beta'_a/\beta'_s)(\{[I_a(0)h\nu_s/I_s(0)h\nu_a](\beta'_s/\beta'_a) + 1\}\exp(2\Omega t^{1/2}) - 1) , \tag{6}$$

where β'_a and β'_s are the radiative decay rates associated with the activator and sensitizer ions, respectively. The solid and dashed lines in Fig. 9 represent the best fits of Eq. (6) to the experimental data, treating $I_a(0)/I_s(0)$ and Ω as adjustable parameters. The values for these parameters at 20 K are listed in Table II.

The $t^{-1/2}$ variation of the energy-transfer rate is characteristic of a single-step electric-dipole–dipole interaction between randomly distributed sensitizers and activators. This time dependence may still be observed when additional energy migration among the sensitizer ions is present. In order to determine the importance of sensitizer energy migration compared to single-step transfer, the change in the fluorescence intensity was monitored as a function of time. This decay can be fitted with an expression for the time evolution of the f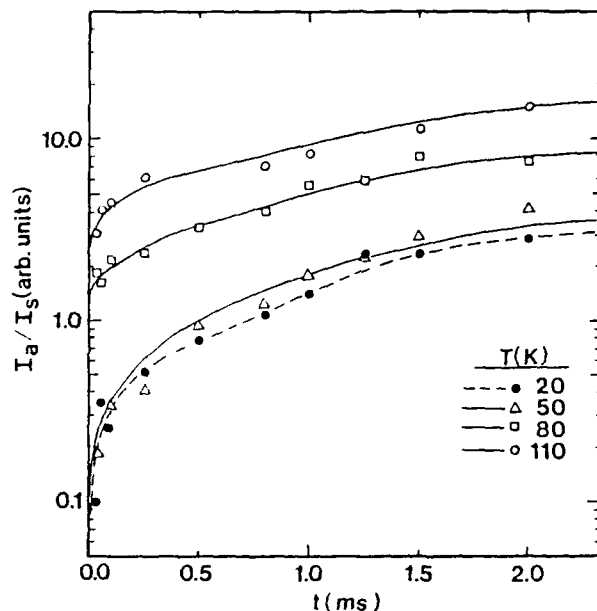luorescence with the energy-transfer rate expressed by an appropriate energy-transfer theory. In each of these theories the excitation energy is treated as a mobile Frenkel exciton localized on a specific ion and able to migrate on a lattice of sensitizer ions. Analysis of the data was attempted using several models and it was found that the best analytical model for describing the transfer kinetics in emerald is that of Chow and Powell.[19] This theory assumes that an exciton is created on the sensitizer site and migrates among the sensitizers, and at each step in the random walk the exciton has a possibility of transferring its energy to any activator in the lattice. It is also assumed for this model that the ion-ion interaction is of electric-dipole–dipole type and that the sensitizer-sensitizer interaction is large compared to that of the sensitizer-activator interaction. Thus, the energy-transfer rate is given by[19]

$$W_{sa} = 4\pi N_a D_n a'[1 + a'(\pi D_n t)^{-1/2}] + 4\pi N_a \alpha''/3a'^3$$

$$+ 2\pi N_a a'^2 \int_{a'}^{\infty} dr(\alpha''/r^6)\{erfc[(r - a')/(4D_n t)^{1/2}]\}^2$$

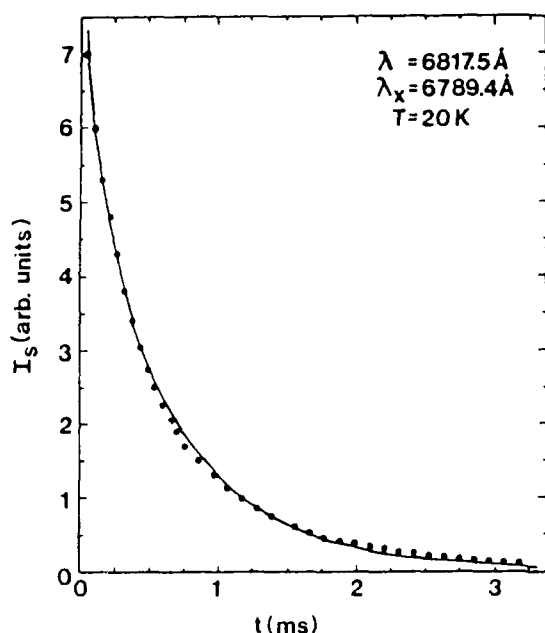$$- 8\pi N_a a' \int_{a'}^{\infty} dr(\alpha''/r^5)\{erfc[(r - a')/(4D_n t)^{1/2}]\} , \tag{7}$$

FIG. 10. Time dependence of the fluorescence emission intensity of one sensitizer site of Cr^{3+} in emerald at 20 K. The solid line represents the theoretical fit to the data using the Chow-Powell model for energy transfer.

where N_a is the total number of activators $(1.716 \times 10^{20}$ cm^{-3} as listed in Table I), $\alpha'' = R_0^6 \beta_s$ is the parameter describing the single-step transfer between a sensitizer and an activator defined in terms of the critical interaction distance R_0 and the sensitizer intrinsic decay rate β_s, D_n is the diffusion coefficient for the random walk among the sensitizer ions, and a' is the trapping radius of an activator ion.

Figure 10 shows the typical results of fitting this equation to one of the experimental decay curves. The agreement between theory and experiment is excellent. The validity of this theory is determined by the criterion that $\pi D_n a'^4 \alpha''^{-1} > 1$. For 20 K the values obtained from the fitting procedure are $D_n = 6.51 \times 10^{-13}$ cm^2/s, $a' = 15$ Å, and $\alpha'' = 4.66 \times 10^{-41}$ cm^6/s, and these give a typical value of 22.1 for the validity inequality. Thus the criterion is met and we assume that this model accurately describes the spectral energy transfer in emerald. This is in good agreement with the results of previous studies that predicted a dipole-dipole-interaction mechanism for emerald from the analysis of fluorescence-line-narrowing results.[9] Using the analysis of the data described above, the values of D_n were determined at several temperatures and found to be essentially independent of temperature below 100 K. Above this temperature it was difficult to obtain an accurate analysis of the data because of thermal line broadening.

IV. FOUR-WAVE MIXING RESULTS

Four-wave mixing (FWM) measurements were used to characterize the properties of long-range spatial energy migration in emerald. The details of the experimental

setup used in this work were described previously in Ref. 20. Crossed laser beams from a ring dye laser were tuned to 588 nm, in order to resonantly pump the $^4T_2$ band. This establishes a population grating of excited Cr^{3+} ions in the sample. The total laser power used in this work was about 300 mW. A He-Ne laser was used as the probe beam and the signal beam was processed by a Princeton Applied Research-EG&G signal averager. By chopping the write beams on and off, the kinetics of the laser-induced grating could be monitored. These are influenced by the fluorescence decay and the spatial migration of Cr^{3+} excitation energy from the peak-to-valley regions of the grating. The primary measurements involved in this work are the variations of the FWM signal efficiency and decay rate with the crossing angle of the write beams. The former provides information about radiationless decay and excited-state-absorption processes, while the latter provides information about the properties of energy migration among the Cr^{3+} ions. Characterizing the energy migration is the main focus of this work.

For a simple sine-wave grating, the scattering efficiency at the Bragg angle is given by[21]

$$\eta = \exp(-2\alpha L)[\sin^2(d\pi \Delta n/2\lambda) + \sinh^2(d \Delta\alpha/4)] ,$$

(8)

where α and L are the absorption coefficient and thickness of the sample, and d is the thickness of the grating. Making the assumption that there is little or no beam depletion, and that the product of the grating thickness and the modulation depth is small, Eq. (8) simplifies to

$$\eta \approx (\pi/2\lambda)^2(d^2\Delta n^2) + (\tfrac{1}{4})^2(d^2\Delta\alpha^2) .$$

(9)

For the type of population grating of interest here, it is possible to estimate the value of $\Delta\alpha$ from the a standard rate-equation analysis of the populations of the energy levels and the transitions between them,[22,23]

$$\Delta\alpha = N_0 I_0 \sigma_1(\sigma_1 - \sigma_2)/(2I_0\sigma_1 + h\nu/\tau) ,$$

(10)

where N_0 is the concentration of active ions, I_0 is the intensity of the write beams, τ is the fluorescence lifetime, and σ_1 and σ_2 are the ground- and excited-state absorption cross sections, respectively. A similar expression can be derived for the change in Δn using an oscillator model for the transitions.[23] However, the results involve a sum over oscillator strengths for all possible transitions and this is difficult to calculate accurately.

One method for determining the contributions to the FWM signal due to Δn and $\Delta\alpha$ is to measure the variation of the signal intensity with the crossing angle of the write beams, θ.[20] The angle at which the peak scattering efficiency occurs is sensitive to the relative magnitudes of the complex coupling constants which describe the interaction among the four laser beams in the crystal, D_1 and D_2. The real and imaginary parts of D_1 and D_2 were determined by using a Runge-Kutta technique to solve the four simultaneous differential equations describing the coupled waves in the crystal. The results were fitted to the data using a computer fitting routine and treating D_1', D_1'', D_2', and D_2'' as adjustable parameters. The details

of this procedure are described fully in Ref. 20 and the values obtained for the coupling parameters are listed in Table III.

The relationships between the coupling parameters and the physical quantities of interest have been derived by analyzing the interaction of the laser beams with the ensemble of atoms.[24,25] The values of $\Delta\alpha$, Δn, and T_2 are given by

$$\Delta\alpha = -2\alpha D_2' / D_1' , \qquad (11)$$

$$\Delta n = (\alpha c / \omega)(D_2^r / D_1') , \qquad (12)$$

$$T_2 = (2\omega/c)(\Delta n / \Delta\alpha)(\omega - \omega_{21})^{-1} , \qquad (13)$$

where α is the absorption coefficient for the write-beam wavelength ($\alpha = 5.57$ cm^{-1} at 588 nm), c is the speed of light, ω is the circular frequency of the write beams, and ω_{21} is the resonant frequency of the atomic transitions. The dephasing time can be separated into two contributions,

$$T_2^{-1} = (2T_1)^{-1} + \gamma , \qquad (14)$$

where γ is the pure dephasing rate due to phonon scattering and T_1^{-1} represents the dephasing due to population relaxation. The values obtained for these parameters are listed in Table III. Using the value obtained for $\Delta\alpha$ in Eq. (10). A value for the excited-state absorption cross section can be obtained. The magnitude of σ_2 obtained in this way agrees with the value of 2.79×10^{-20} cm^2 reported from direct excited-state absorption measurements.[26]

The FWM signal-decay kinetics were found to be nonexponential and dependent on the crossing angle of the write beams for all temperatures for which a signal was visible. Above 160 K no FWM signal was observed,

TABLE III. Results of the four-wave mixing measurements in emerald with 3 at. % Cr^{3+} at 12 K.

Results from scattering-efficiency measurements	
D_2'	2.0×10^{-6}
D_2'	8.0×10^{-9}
D_1^r	5.0×10^{-7}
D_1'	4.0×10^{-7}
$\Delta\alpha$	0.22 cm^{-1}
Δn	1.3×10^{-4}
T_2	1.2×10^{-12} s
η (absolute value for $\theta = 5.3°$)	4.0×10^{-3}
σ_2	2.8×10^{-20} cm^2
Results from grating-decay-kinetics measurements	
V	1.91×10^5 s^{-1}
α'	2.55×10^3 s^{-1}
D_r	2.79×10^{-7} cm^2/s
L_m	1.05×10^{-5} cm
L_D	3.06×10^{-5} cm
N_s	106

and this can be attributed to the small value of the fluorescence lifetime at these temperatures.[27] The signal kinetics are consistent with the predictions of the theory of Kenkre,[28] which describes the decay of a laser-induced grating in the presence of long-mean-free-path exciton migration. Again, it should be emphasized that the term exciton in this case refers to a Frenkel exciton in which the excitation energy is localized on an individual Cr^{3+} ion and can migrate on a lattice of Cr^{3+} ions. In the Kenkre model, the time dependence of the normalized FWM signal is given by

$$I_s(t) = e^{-2t/\tau} \left| J_0(bt)e^{-\alpha't} + \alpha' \int_0^\infty du \, e^{-\alpha'(t-u)} J_0(b(t^2 - u^2)^{1/2}) \right|^2 , \qquad (15)$$

where τ is the fluorescence lifetime, α' is the exciton scattering rate, and b is given by

$$b = \pi^2 a n V\theta / 45\lambda . \qquad (16)$$

Here, V is the ion-ion–interaction rate, n is the index of refraction of the crystal, θ is the crossing angle of the write beams, and λ is the wavelength of the write beams. The average distance between uniformly distributed chromium ions in this sample is estimated to be $a = 9.87$ Å.

The FWM signal-decay kinetics were fitted using Eq. (15), treating α' and b as adjustable parameters. In order to emphasize the effects of energy migration, both the experimental data and the theoretical expression were divided by exp($-2t/\tau$), which eliminates the fluorescence-decay contribution to the signal kinetics. A typical theoretical fit to the data is shown in Fig. 11. The excellent fit to the nonexponential shape of the curve indicates the presence of long-mean-free-path exciton migration. The values of α' and V obtained in this way can be used

to calculate the parameters for characterizing the dynamics of the excitation migration. These include the resonant diffusion coefficient, the mean free path, the diffusion length, and the number of sites visited between scattering events,

$$D_r = 2V^2 a^2 / \alpha' , \qquad (17)$$

$$L_m = 1.414 V_a / \alpha' , \qquad (18)$$

$$L_D = (2D_r \tau)^{1/2} , \qquad (19)$$

$$N_s = L_m / a . \qquad (20)$$

The values of α', V, D_r, L_m, L_D, and N_s were calculated for each temperature and the values obtained at low temperature are listed in Table III. It should be pointed out that the expressions in Eqs. (17)–(20) are for migration on a uniform lattice and thus should be considered as approximate values for the random lattice associated with the case of interest here.

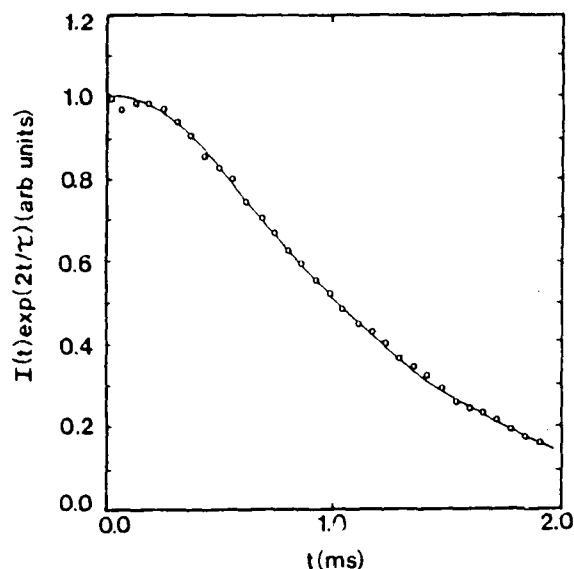Figure 12 shows the temperature dependences of the

FIG. 11. Four-wave mixing decay kinetics (points) and theoretical fit to the data using Eq. (15) (solid line) after dividing by the fluorescence-decay factor. $T = 16$ K and the crossing angle of the write beams is $\theta = 20°$.
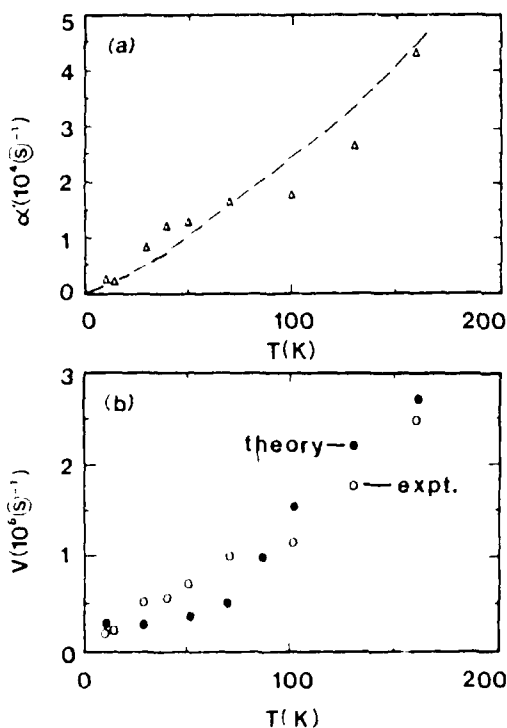

FIG. 12. Temperature dependence of (a) the ion-ion-interaction rate V and, (b) the exciton scattering rate α' obtained from FWM data. The dashed line in (a) and the solid points in (b) represent theoretical predictions.

ion-ion-interaction rate and the scattering rate. Both α' and V increase with temperature in this range. The increase in the former can be attributed to increased scattering by acoustic phonons. The theoretical treatment of Frenkel exciton scattering by acoustic phonons has been developed by Agranovich and co-workers.[29] The results of their work show that the scattering rate should increase as $T^{3/2}$ and the dashed line in Fig. 12(a) shows this type of variation. This provides a reasonable explanation for the experimentally observed temperature dependence of α'.

The temperature dependence of V can be attributed to the relative increase in the vibronic sideband emission compared to the R-line emission as temperature is raised. This causes an increase in the overlap between the emission and absorption spectra and an increase in the total emission rate. Both of these factors cause the ion-ion-interaction rate to increase. This can be approximated by

$$V(T) = C\tau^{-1}(I_{vib}/I_R) , \qquad (21)$$

where the I's represent the intensities of the two components of the fluorescence spectrum and C is a proportionality constant. Using the values of the relative intensities and the fluorescence lifetime measured experimentally in Eq. (21) gives the theoretical points shown in Fig. 12(b), which are in good agreement with the experimentally determined temperature dependence for V.

Using Eq. (17), the diffusion coefficient for long-range resonant exciton migration can be determined. Figure 13 shows the results obtained using the experimental points for V and α'. The solid line in the figure is obtained using the theoretical curves given in Figs. 12(a) and 12(b). There is a good agreement between the two results.
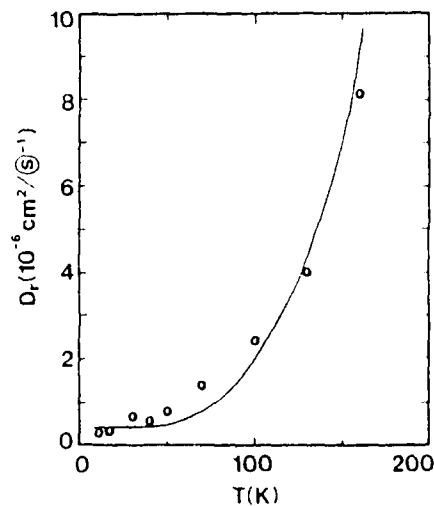

FIG. 13. Temperature dependence of the exciton diffusion coefficient obtained from FWM data. The solid line represents the theoretical prediction for D_r.

V. SUMMARY AND CONCLUSIONS

Laser site-selection spectroscopy shows that the Cr^{3+} ions in emerald have different types of local crystal-field environments. The origin of these different environments cannot be determined from available spectroscopic information. The beryl host structure does not have distinctly different lattice sites for the Al^{3+} ions for which the Cr^{3+} ions substitute. However, this type of spectral structure has been observed for many types of optically active ions in crystals and is generally attributed to two possible sources. The first is microscopic strains associated with neighboring lattice imperfections (either point defects or dislocations). The second is exchange interaction between pairs of Cr^{3+} ions. The identification of the origin of the spectral structure in emerald requires further work with a variety of samples having different concentrations of defects and of Cr^{3+} ions. However, it is not necessary to know the exact nature of the inequivalent environments to analyze the general dynamics of the energy-transfer processes in the material, which is the central interest of this work.

The results described here indicate that there are two different types of energy-transfer processes taking place in emerald. The first is short-range spectral migration among Cr^{3+} ions having different types of local crystal-field environments, while the second is long-range spatial migration among Cr^{3+} ions having resonant transition energies. The former evolves from ions having local environments leading to high-energy transitions in the spectral profile to ions having local environments leading to low-energy transitions. The relative concentration of the latter type of ions is about 2 orders of magnitude greater than the former. In this case the spectral transfer is consistent with an electric-dipole–dipole interaction mechanism and is independent of temperature at low temperature. The latter type of spatial transfer involves a stronger interaction mechanism between ions in the more concentrated type of environment, and the transfer rate increases with increasing temperature due to the increasing importance of vibronic emission.

For both types of energy transfer observed in this work, the multistep migration of energy is modeled as a mobile Frenkel exciton with excitation energy localized on an individual Cr^{3+} ion. Theoretical estimates can be made for the diffusion coefficient describing this type of process. For incoherent hopping migration via dipole-dipole interaction, the diffusion can be expressed as[30,31]

$$D_n = (4\pi N_i R_0^6 / 6\tau_i) \int_a^\infty R^{-2} \exp(-4\pi N_i R^3 / 3) dR .$$

$$(22)$$

Here, N_i is the concentration of ions in the type of site transferring the energy and τ_i is the fluorescence decay time of these ions. R_0 is the critical interaction distance which can be determined from the overlap of the emission and absorption spectra of the ions between which transfer is occurring. The lower limit of the integral is taken to be the nearest-neighbor distance of 4.6 Å. The value of D_n calculated from this expression using measured spectral data is listed in Table II. The result is the same order of magnitude as that determined from the ex-

perimental results described above. This is also consistent with the values obtained for the diffusion coefficient in other materials measured under similar conditions.

The order of magnitude of the diffusion coefficient describing long-range resonant energy migration is significantly larger than the spectral diffusion coefficient. If Eq. (22) is solved using the greater concentration of ions in sites c, d, and e, a value is predicted for the diffusion coefficient of the order of 4×10^{10} cm^2 s^{-1}, which is still much smaller than the diffusion coefficient determined by FWM results. The only way the higher values of the diffusion coefficient to be predicted theoretically is to assume a stronger mechanism of the ion-ion interaction. If the energy transfer takes place by exchange interaction, Eq. (22) is replaced by[32]

$$D_{ex} = (2\pi N_i P_o / 3) \int_0^\infty R^4 \exp[-(2R/L + 4\pi N_i R^3 / 3)] ,$$

$$(23)$$

where L is the average Bohr radius of the electron wave functions and P_o is a constant that depends on the spatial overlap of the wave functions and the spectral overlap integral. These parameters have not been determined specifically for emerald, and thus an exact value for D_{ex} cannot be obtained for this system. However, for Cr^{3+} ions in Al_2O_3 (ruby) these parameters have been found to be[11,33] $L = 0.97$ Å and $P_o = 4.3 \times 10^{14}$ s^{-1}. Using these values in Eq. (23) gives $D_{ex} \approx 10^{-7}$ cm^2 s^{-1}, which is in good agreement with the value of D_r obtained from FWM measurements. The value of L will always be close to 1 Å, but P_o can vary appreciably from host to host. The nearest-neighbor spacings between Cr^{3+} ions in the ruby lattice are smaller than in emerald, but the concentration of Cr^{3+} ions present in our emerald sample is much greater than in most ruby samples.[11,33] Thus the predicted value of D_{ex} obtained from Eq. (23) must be taken as only a rough estimate for emerald. However, the point of this analysis is to show that a strong, short-range interaction mechanism such as exchange can lead to a diffusion coefficient of the order of magnitude of that obtained from FWM measurements.

It should be emphasized that there is no discrepancy between the results of TRSSS and FWM measurements. The former probes the properties of energy transfer from ions in a specific type environment to ions in other types of environments. These results are strongly affected by the fact that the concentration of ions in activator environments is significantly greater than the concentration of ions in sensitizer environments. This leads to a dipole-dipole interaction with negligible backtransfer. On the other hand, the FWM measurements are only sensitive to energy migration of distances of the order of a grating spacing. Thus the energy transfer measured by this method takes place among the ions in the highest-concentration environment through a strong interaction mechanism such as exchange. Both types of measurements are necessary to obtain a complete picture of the different types of energy-transfer processes taking place in the sample.

The value obtained for D_r is similar to that obtained

for alexandrite.[20] However, the temperature dependence of D_r is quite different in alexandrite and emerald. In both materials the scattering rate limiting the mean free path of the excitons was found to increase with temperature. However, at low temperatures the ion-ion-interaction rate in alexandrite is independent of temperature, whereas in emerald it increases with temperature. This is because the vibronic emission transitions begin to become important at much lower temperatures in emerald than in alexandrite, as can be seen from their fluorescence spectra. This is associated with the weaker crystal field at the site of the Cr^{3+} ion in the emerald host compared to alexandrite.

The dephasing time found for emerald is less than the values found from ruby and alexandrite.[20] This follows a trend of decreasing T_2 with decreasing crystal-field strength. Assuming the dephasing is dominated by the radiationless relaxation to the bottom of the ^2E potential well, the dependence on crystal-field strength implies

direct relaxation in the ^2E level instead of initial relaxation in the $^4T_2$ level. Since the two states are mixed, the branching ratio for radiationless relaxation will be determined by the relative densities of states at the terminal point of the absorption transition. For the materials investigated thus far, the branching ratio in the ^2E level will be much greater than that in the $^4T_2$ level. For hosts with smaller crystal-field strengths the relative magnitudes of these branching ratios will be quite different. Therefore, making similar measurements on low-crystal-field-strength materials is an important test of this model for interpreting the T_2 results.

*Present address: Naval Research Laboratories, Code 6551, Washington, D.C. 20375-5000.

†Permanent address: Institute of Physics, Polish Academy of Sciences, Aleja Lotnikow 32/46, 02-668, Warsaw, Poland.

[1]M. L. Shand, in *Proceedings of the International Conference on Lasers '82*, edited by R. C. Powell (SPS Press, McLean, VA, 1982), p. 799.

[2]J. Buchert, A. Katz, and R. R. Alfano, in *Proceedings of the International Conference on Lasers '82*, Ref. 1, p. 791.

[3]S. Lai, J. Opt. Soc. Am. B **4**, 1286 (1987).

[4]D. L. Wood, J. Chem. Phys. **42**, 3404 (1965).

[5]S. V. Brum-Grzhimailo and G. V. Klimusheva, Opt. Spektrosk. **8**, 3421 (1960) [Opt. Spectrosc. (USSR) **8**, 179 (1960)].

[6]B. Morosin, Acta Cryrstallogr. Sect. B **28**, 1899 (1972).

[7]B. Halperin, D. Nicollin, and J. A. Koningstein, Chem. Phys. **42**, 277 (1979).

[8]T. F. Veremeichik, Phys. Status Solidi B **124**, 719 (1984).

[9]Z. Hasan, S. T. Keany, and N. B. Manson, J. Phys. C **19**, 6381 (1986).

[10]A. Edgar and D. R. Hutton, J. Phys. C **11**, 5051 (1978).

[11]W. L. Bragg and J. West, Proc. R. Soc. London, Ser. A **111**, 691 (1926).

[12]R. J. Birgeneau, J. Chem. Phys. **50**, 4282 (1969).

[13]R. G. Wyckoff, *Crystal Structure* (Interscience, New York, 1948), Vol. II, p. 7.

[14]E. F. Farrell, J. H. Fang, and R. E. Newnham, Amer. Mineral **48**, 805 (1963).

[15]D. L. Wood, J. Ferguson, K. Knox, and J. F. Dillon, Jr., J. Chem. Phys **37**, 890 (1963).

[16]P. Kisliuk and C. A. Moore, Phys. Rev. **160**, 307 (1967).

[17]W. H. Fonger and C. W. Struck, Phys. Rev. B **11**, 3251 (1975).

[18]D. Sardar and R. C. Powell, J. Lumin. **22**, 349 (1981).

[19]H. C. Chow and R. C. Powell, Phys. Rev. B **21**, 3785 (1980).

[20]A. Suchocki, G. D. Gilliland, and R. C. Powell, Phys. Rev. B **35**, 5830 (1987).

[21]H. Kogelnik, Bell Syst. Tech. J. **48**, 2909 (1969).

[22]K. O. Hill, Appl. Opt. **10**, 1695 (1971).

[23]A. M. Ghazzawi, J. K. Tyminski, R. C. Powell, and J. C. Walling, Phys. Rev. B **30**, 7182 (1984).

[24]A. Yariv and D. M. Pepper, Opt. Lett. **1**, 16 (1977).

[25]R. L. Abrams and R. C. Lind, Opt. Lett. **2**, 94 (1978); **3**, 205 (1978).

[26]W. M. Fairbank, Jr., G. K. Klauminzer, and A. L. Schawlow, Phys. Rev. B **11**, 60 (1976).

[27]A. Suchocki, J. D. Allen, R. C. Powell, and G. M. Loiacono, Phys. Rev. B **36**, 6729 (1987).

[28]Y. M. Wong and V. M. Kenkre, Phys. Rev. B **22**, 3072 (1980); V. M. Kenkre and D. Schmid, *ibid.* **31**, 2430 (1985).

[29]V. M. Agranovich and M. D. Galanin, *Electronic Excitation Energy Transfer in Condensed Matter* (North-Holland, Amsterdam, 1982); V. M. Agranovich and Yu. V. Konobeev, Opt. Spektrosk. **6**, 642 (1959); **6**, 648 (1959) [Opt. Spectrosc. (USSR) **6**, 155 (1959); **6**, 421 (1959)]; Phys. Status Solidi **27**, 435 (1968).

[30]S. Chandrasklar, Rev. Mod. Phys. **15**, 1 (1943).

[31]T. Forster, Ann. Phys. (Leipzig) **2**, 55 (1948); Z. Naturforsch. **49**, 321 (1949).

[32]D. L. Dexter, J. Chem. Phys. **22**, 836 (1953).

[33]G. F. Imbusch, Phys. Rev. **153**, 326 (1967).

Four-wave-mixing spectroscopy of a Cr³⁺-doped transparent glass ceramic

Frederic M. Durville[*] and Richard C. Powell

Department of Physics, Oklahoma State University, Stillwater, Oklahoma 74078-0444

Georges Boulon and Bernard Champagnon

Université Lyon I, Villeurbanne, France

(Received 29 June 1987)

Four-wave-mixing (FWM) experiments were performed on a Cr³⁺-doped transparent ceramic material with the composition of cordierite. Whereas no FWM signal could be observed in a normal glass of this type, a strong signal was observed after devitrification. The signal strength increases as temperature is lowered, even though the fluorescence lifetime is constant. The variation of the signal strength and decay rate with crossing angle of the write beams shows that there is no long-range energy migration, and the dephasing time due to radiationless processes in the excited state is very fast compared to Cr³⁺-doped crystals. The increase of the signal intensity with laser power shows the effects of saturation and excited-state absorption.

I. INTRODUCTION

Glass ceramics are highly attractive materials for many optical technology applications because they combine the properties of crystals with the advantages of glasses.[1,2] Several different authors have suggested the application of Cr³⁺-doped transparent glass ceramics as lasers and other luminescent devices.[3-7] In earlier publications[3-10] we reported a technique for synthesizing a transparent glass ceramic similar to cordierite without any nucleating agent other than Cr³⁺. This particular technique results in a high concentration of Cr³⁺ ions, with most of them being in the crystalline phase. The fluorescence properties of this material were also reported.[8-10] The luminescence consists mainly of a broad line centered around 693 nm, with a width of approximately 250 cm⁻¹ at room temperature. This fluorescence comes from the ^2E-$^4A_2$ transitions of the Cr ions in the MgAl₂O₄ crystalline phase. The significant inhomogeneous broadening was attributed to a cation disorder in this phase.

In this paper, we report the results of further investigations of the spectroscopic properties of this material using four-wave mixing (FWM) spectroscopy. This technique has been shown to be a powerful tool in characterizing the spectral dynamics of rare-earth and transition-metal ions in crystalline hosts.[11,12] The results obtained in this work show that devitrification allows FWM signals to be observed in glass ceramics whereas no signal could be observed in the normal glass. The properties of the variation of the signal with laser power, write-beam-crossing angle, and temperature provide information about the pumping, decay, and energy-transfer characteristics of the Cr³⁺ ions in this type of host material.

II. EXPERIMENT

The base glass used to obtain the glass ceramic has the following composition (in mol %): 56.9 SiO₂, 22.36

Al₂O₃, 20.39 MgO, and 0.35 Cr₂O₃. This is close to the mineral cordierite and contains 1.77×10^{20} Cr atoms per cm³. The glass ceramic is obtained by heating the glass to 950°C. The final sample is about 68% crystallized. The crystalline regions are about 350 Å in diameter and their composition is Mg $(Al_{1-x}Cr_x)_2O_4$. Since x is much less than 1, the particles are similar to chromium-doped spinel crystals.[8]

The experimental setup used for the FWM measurements is shown in Fig. 1. The 514.5-nm line of a Spectra Physics argon laser was used to excite the high-energy side of the $^4A_2$-$^4T_2$ absorption band of the Cr³⁺ ions. An argon-laser-pumped jet dye laser with rhodamine 6G tuned to 571.5 nm was used to excite the low-energy side of the same absorption band. The total power was varied using a variable neutral-density filter. The laser output was split into two beams which were slightly focused and crossed inside the sample to form an interference pattern in the shape of a sine wave. The difference
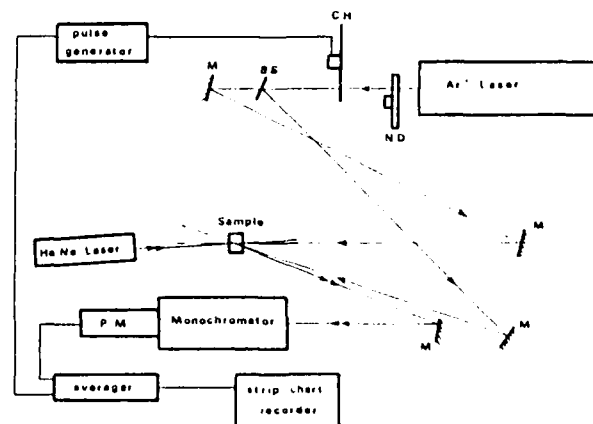

FIG. 1. Experimental setup for FWM measurements. CH chopper; ND, variable neutral-density filter; M, mirror; BS, beam splitter; and PM, photomultiplier tube.

in the optical path lengths of these two write beams was less than the coherence length of the laser.

The interference pattern of the crossed laser beams induces a change in the complex refractive index of the sample with the same spatial pattern. This appears as a refractive-index grating which can be probed by scattering a read beam produced by a 10-mW He-Ne laser at 632 8 nm. The maximum signal intensity is obtained for the Bragg scattering condition. For this situation, the read beam is slightly misaligned from being counterpropagating with one of the write beams and the signal beam is slightly off counterpropagating with the other write beam. A mirror was used to pick off the signal beam and send it through a 0.25-m monochromator to eliminate sample fluorescence. The signal was detected by a Hamamatsu R1547 photomultiplier tube, processed by an EG&G/PAR signal averager, and read out on a strip-chart recorder. For transient measurements, a mechanical chopper was used to turn the write beams off and on. To determine the temperature dependence of the FWM signal, the sample was mounted on the cold finger of a cryogenic refrigerator with a temperature controller capable of temperature variation between about 15 and 300 K.

III. DESCRIPTION OF RESULTS

FWM experiments were attempted on the normal glass sample, but no signal could be observed at any temperatures. On the other hand, for the glass ceramic a strong FWM signal was observed for both the 514.5- and 571.5-nm excitation lines. The scattering efficiency was measured to be approximately 0.01 with the 514.5-nm excitation at a write-beam intensity at 1.3×10^4 W cm^{-2}. When exciting with the 571.5-nm line at a write-beam intensity of 3.8×10^3 W cm^{-2}, the scattering efficiency was found to be approximately 0.002. In addition, a thermal lensing effect was also observed with the 514.5-nm excitation line, becoming significantly important at intensities greater than 4.0×10^3 W cm^{-2}, and leading to the destruction of the FWM signal above 1.3×10^4 W cm^{-2}. For this study, we restricted the laser power to below 5.0×10^3 W cm^{-2}.

When the write beams were chopped off, the decay rate of the FWM signal was measured to be equal to twice the measured $^2E^{-4}A_2$ luminescence decay rate for all crossing angles of the write beams. The same result was obtained for both excitation wavelengths at all temperatures. This is the normal behavior for a population grating without the presence of any long-range energy migration.

The scattering efficiency was measured for different write-beam crossing angles using the 514.5 nm laser line. At room temperature and relatively high power ($3 8 \times 10^3$ W cm^{-2}), the angular dependence of the FWM signal is shown in Fig. 2(a). The observed behavior with a rather flat angular dependence is quite unusual. When the power is decreased to 6.4×10^2 W cm^{-2}, the angular dependence changes drastically, as shown in Fig. 2(b). A change in the shape of the angular dependence is also observed when the temperature is lowered to 120 K [Fig. 2(c)].
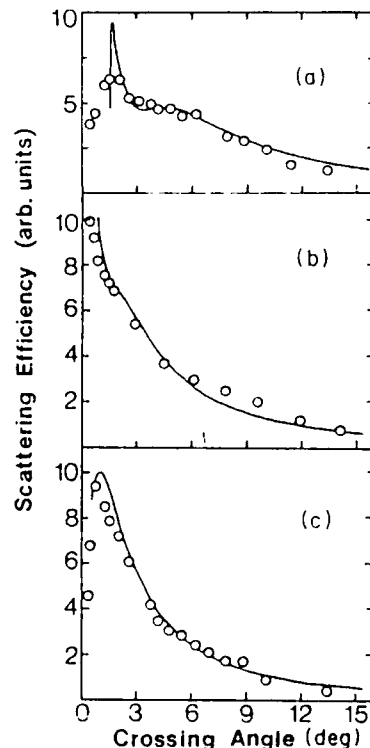

FIG. 2. FWM scattering efficiency vs crossing angle of the write beams in the sample for an excitation wavelength of 514.5 nm. (a) $T = 300$ K, $P = 3.8 \times 10^1$ W cm^{-1}. (b) $T = 300$ K, $P = 6.4 \times 10^2$ W cm^{-2}. (c) $T = 120$ K, $P = 3.8 \times 10^1$ W cm^{-2}. (See text for explanation of theoretical lines.)

The intensity of the FWM signal was monitored as a function of temperature and found to increase as the temperature was lowered. Typical results are shown in Fig. 3. The same type of temperature dependence of the FWM signal was observed for both excitation wavelengths. The temperature dependence of the luminescence decay rate was also measured for this sample and no change was observed in this temperature range. The temperature dependence of the FWM signal intensity from a population grating is generally proportional to
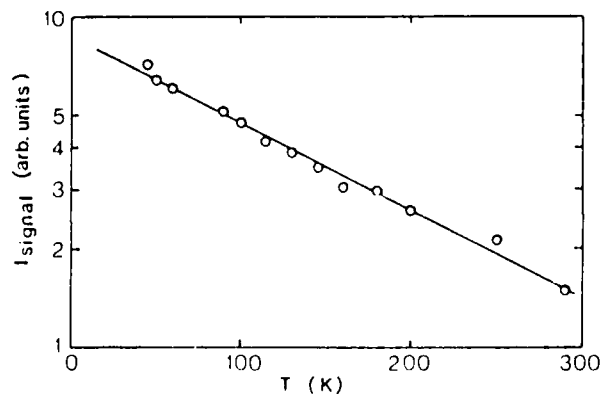

FIG. 3. Temperature dependence of the FWM scattering efficiency for an excitation wavelength of 514.5 nm.

the temperature dependence of the fluorescence lifetime. Since this is not the case for the glass ceramic studied here, other temperature-dependent processes must be affecting the FWM signal.

The FWM scattering efficiency was also recorded as a function of total laser power in the write beams and the results are presented in Fig. 4. With the 514.5-nm excitation line [Fig. 4(a)], the signal intensity follows approximately a quadratic dependence on the writing-beam intensity $[I_e = (I_1 I_2)^{1/2}]$ at low powers. Above 4.0×10^3 W cm⁻² the signal tends toward a saturation level. With the 571.5-nm excitation line [Fig. 4(b)] the signal follows a fourth-law dependence on laser power with no observed saturation.

IV. DISCUSSION

For the type of sample investigated here, the FWM signal is associated with the scattering of the write beam from a laser-induced population grating. The grating arises from the modulation of the complex refractive index of the material due to the difference in the polarizability of the Cr³⁺ ions in the ground state and excited state.[13] The absence of a FWM signal in the base glass is not surprising due to the very low quantum yield of Cr³⁺ ions in this host even at low temperatures.[3,14] This is associated with strong nonradiative relaxation for Cr³⁺ ions in weak crystal field sites.

For a holographic grating, the FWM scattering efficiency is expressed in terms of the contributions from the modulated absorption and dispersion parts of the refractive index as[15]

$$\eta = \exp(-2\alpha_0 \Gamma)[\sinh^2(\Delta\alpha\Gamma/2) + \sin^2(\pi\Gamma\Delta n/\lambda)] . \quad (1)$$

Here $\Gamma = d/\cos(2\theta)$ where d is the grating thickness and θ is the crossing angle of the write beams in the sample. As a first approximation, the contribution from the ab-

sorption part can be neglected and the sine function expanded. This predicts that the signal intensity I_s will be proportional to the square of the modulation of the refractive index, Δn,

$$I_s \propto |\Delta n|^2 . \quad (2)$$

In the absence of any long-range energy migration, Δn will decay with the decay of the excited-state population, and therefore

$$I_s(t) = I_0 \exp(-2t/\tau_f) \quad (3)$$

where τ_f is the fluorescence lifetime. In this glass ceramic sample, the ²E fluorescence decay is highly nonexponential due to the wide distribution of crystal field sites and the presence of strong ion-ion interactions.[10] In this case, we define the lifetime as the $1/e$ time of the decay of the fluorescence intensity. The FWM signal exhibits the same degree of nonexponentiality, and thus the $1/e$ definition is again used for the signal decay time. Typical fluorescence and FWM signal decays are shown in Fig. 5. Equation (3) predicts that the FWM signal will decay with a decay time equal to half that of the fluorescence decay. This corresponds exactly to what we observe and holds for all times of the nonexponential decays for our glass ceramic sample. Thus we attribute the FWM signal to scattering from a population grating of Cr³⁺ ions in the ²E excited state without any long-range energy migration, at all temperatures in the range 20–300 K. The sample consists of microcrystals of about 400 Å diameter embedded in a glass matrix, and the grating spacing is of the order of 10 000 Å. Since the FWM signal is only sensitive to energy migration over distances of the order of the grating, it is not surprising that no long-range energy transfer is ob-
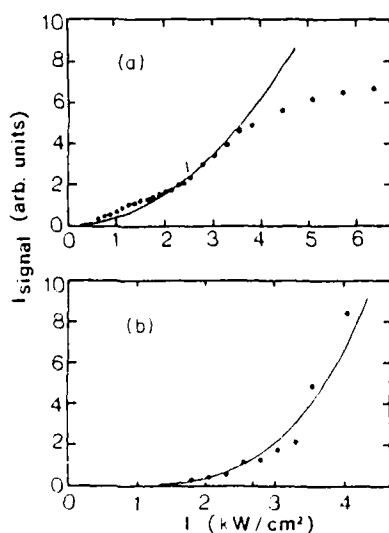

FIG. 4. FWM scattering efficiency vs total write-beam power for (a) 514.5 excitation and (b) 571.5-nm excitation. (See text for explanation of the theoretical lines.)
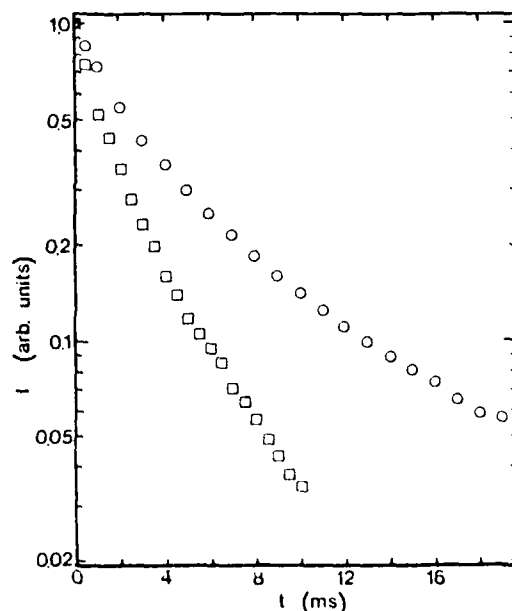

FIG. 5. Decay curves at 120 K of the fluorescence (circles) and FWM signal for $\theta = 2.6°$ (squares).

served. We expect some energy diffusion within each microcrystal, but not between different microcrystals. This is similar to what has been observed in semiconductor-doped glasses.[16]

Assuming a simple two-level model for the atomic system, equations describing the FWM scattering efficiency versus crossing angle have been derived,[11] but no analytic solution has been obtained for these equations. To analyze the experimental results, the two coupled, complex differential equations needed to describe the FWM signal are solved numerically using a fourth-order Runge-Kutta method. The numerical values of the coupling coefficients obtained by fitting this model to experimental results can then be used to determine the laser-induced modulation of the absorption $\Delta\alpha$ and dispersion Δn parts of the refractive index.[11] Theoretical fits to the data are shown as solid lines in Fig. 2 and the values of the fitting parameters are listed in Table I. Using these results, the dephasing time of the atomic system T_2 can then be calculated from the expression[11]

$$T_2 = (2\omega/c)(\Delta n/\Delta\alpha)(\omega - \omega_{12})^{-1} , \qquad (4)$$

where ω_{12} is the center frequency of the transition. The values of T_2 obtained from this analysis are reported in Table I. Depending on the temperature and excitation power, the dephasing time varies from 10.2 to 53.4 fs.

In previous work of this type on Cr^{3+} crystals,[11] the magnitude of the dephasing time has been related to the energy gap between the $^4T_2$ and ^2E levels. The smaller this gap the smaller T_2. However, for the glass ceramic the average energy gap is greater than 1400 cm^{-1}, which is consistent with the observation of a constant fluorescence decay time between 10 and 300 K. Extrapolating the crystal results to this value of ΔE predicts a dephasing time of the order of several picoseconds. However, the glass ceramic has a much greater degree of inhomogeneous broadening not present in the crystalline hosts.[10] The broad distribution of crystal field strengths for the Cr^{3+} sites results in some of them having the relaxed $^4T_2$ level below the ^2E level. This is shown by the observation of weak luminescence from the $^4T_2$ level along with the strong luminescence from the ^2E level.[10] The observed nonlinear polarization responsible for the FWM properties is due to a combination of the individual nonlinear polarizabilities of each of the Cr^{3+} ions. In addition, strong interactions between the Cr^{3+} ions and electron-phonon interactions are present. This is

demonstrated by the strongly nonexponential luminescence decay curves. The dephasing is mainly governed by the fastest relaxation mechanism, even if this involves only a small part of the total Cr^{3+} ions.

The results listed in Table I indicate that the FWM signal arises mainly from a dispersion grating. At low temperatures, the contribution from the absorption grating is more important. The values of Δn and $\Delta\alpha$ listed in Table I were obtained by fitting the experimental data of the relative signal intensity versus the crossing angle of the write beams. However, the value obtained this way for Δn is consistent with that calculated from the absolute value of the scattering efficiency at room temperature, assuming negligible contribution from an absorption grating.

A theoretical expression for the modulation of the absorption part of the refractive index can be derived from the rate equations describing the atomic system.[17] For the simplest case, the absorption is given by

$$\alpha_0 = \sigma_1 N_1 + \sigma_2 N_2 , \qquad (5)$$

where N_1 and N_2 are the populations of the ground and excited states, respectively, and $N = N_1 + N_2$ represents the total number of Cr^{3+} ions per unit volume. σ_1 and σ_2 are the absorption cross sections in the ground and excited states, respectively. Under cw pumping, the solutions of the rate equations give

$$(N_2 - N_1) = N[(\sigma_1 I - h\nu/\tau_f)/(\sigma_1 I + h\nu/\tau_f)] . \qquad (6)$$

The intensity of the laser interference pattern inside the sample varies sinusoidally as $I = I_0[1 + \sin(\mathbf{k}\cdot\mathbf{r})]$. The amplitude of the laser-induced modulation of the absorption coefficient is[17]

$$\Delta\alpha = N_{2p}(\sigma_2 - \sigma_1)/2 , \qquad (7)$$

where N_{2p} is the excited-state population in the peak region of the grating, given by

$$N_{2p} = 2NI_0\sigma_1/[2I_0\sigma_1 + h\nu\tau_f^{-1}] . \qquad (8)$$

Using the same model, the modulation of the dispersion part of the refractive index can be found by treating the atoms as damped harmonic oscillators.[18] In this case the dispersion part of the refractive index is given by

$$n^2 - 1 = \sum_i [N_i f_i(\omega_i^2 - \omega^2)]/[(\omega_i^2 - \omega^2)^2 + (\omega\gamma_i)^2] , \qquad (9)$$

where i refers to all different possible transitions with os-

TABLE I. Parameters obtained from FWM measurements.

Parameter	$T = 300$ K		$T = 120$ K
	$P = 6.4 \times 10^2$ W cm^{-2}	$P = 3.8 \times 10^3$ W cm^{-2}	$P = 3.8 \times 10^3$ W cm^{-2}
$\Delta\alpha$ (cm^{-1})	0.24	0.13	0.97
Δn	1.36×10^{-5}	5.33×10^{-6}	1.07×10^{-5}
T_2 (sec)	5.34×10^{-14}	3.79×10^{-14}	1.02×10^{-14}
$\eta(\Delta\alpha)$	1.17×10^{-4}	1.27×10^{-4}	7.12×10^{-3}
$\eta(\Delta n)$	2.05×10^{-2}	3.17×10^{-3}	1.98×10^{-2}
η_{theor}	2.09×10^{-2}	3.30×10^{-3}	1.98×10^{-2}
η_{expt}	1.60×10^{-4}	2.50×10^{-3}	2.30×10^{-2}

cillator strengths f_i at frequencies ω_i, and widths γ_i. If the laser frequency is near resonance with only one ground-state and one excited-state transition, the other terms in the sum can be neglected and combining Eqs. (6), (8), and (9) gives an expression for the modulation of the dispersion part of the refractive index,

$$\Delta n = (N_{2p}/2n_p)$$

$$\times \{ f_2(\omega_2^2 - \omega^2)[(\omega_2^2 - \omega^2)^2 + \gamma_2^2 \omega^2]^{-1}$$

$$- f_1(\omega_1^2 - \omega^2)[(\omega_1^2 - \omega^2)^2 + \gamma_1^2 \omega^2]^{-1}| \; , \qquad (10)$$

where n_0 is the refractive index of the unperturbed sample.

Equation (1) along with Eqs. (5)–(10) can be used to interpret the observed temperature and power dependences of the FWM signal. The data in Fig. 3 indicate that the temperature dependence of the scattering efficiency can be described by

$$\eta(T) = \eta(0) \exp(-T/T_c) \; , \qquad (11)$$

where $T_c = 165.5$ K. For th · glass ceramic in the range of temperatures investigated here, the absorption coefficient (and thus the ground-state absorption cross section) and the fluorescence decay time are both constant with temperature. Thus Eqs. (7)–(11) imply that the observed temperature dependence of the FWM signal is associated with the spectroscopic characteristics of the excited state. The increase in the FWM signal intensity as temperature is lowered would be consistent with an excited-state absorption transition whose width decreases or whose oscillator strength increases at low temperatures. Although these are normal spectral temperature dependences, at the present time, no specific data are available on the excited-state absorption characteristics of this sample.

The same simple two-level system model predicts that the power dependence of the scattering efficiency is governed by the excited-state population N_{2p}, which is proportional to the incident laser intensity, and thus

$$\eta \propto |I_e|^2 \; . \qquad (12)$$

This theoretical prediction is consistent with the data shown in Fig. 4(a) for 514.5-nm excitation at lower powers. Above about 4.0×10^3 W cm^{-2} a deviation from the quadratic dependence is observed.

Several phenomena can contribute to the deviation from a quadratic power dependence. First, saturation of the excited-state population can occur.[19,20] The "saturation intensity" of a two-level atomic system is given by[19]

$$I_s = (\epsilon_0 c / 2)(\hbar^2 / \mu \tau_f T_2) \; , \qquad (13)$$

where μ is the electric dipole moment, $\mu^2 = 2\hbar\alpha_0\epsilon_0 / NkT_2$. The calculated value for the laser power needed to saturate the population of the ^2E level in this sample is 9.0×10^6 W cm^{-2}. This calculation does not take into account the effects of inhomogeneous broadening. Second, thermal lensing becomes important above 3.8×10^3 W cm^{-2}. This can contribute to the destruction of the grating through thermal effects and, in addition, produce a self-focusing effect that increases the

power density of the write beams inside the sample. The latter effect would make it possible to reach saturation of the ^2E population at a lower laser power than that predicted theoretically.

The power dependence of the scattering efficiency for 571.5-nm excitation can be described by a fourth-power dependence on the total laser intensity. This implies that the nonlinear interaction between the excitation beams and the ions occurs through the fifth-order susceptibility, $\chi^{(5)}$. The most important contribution to $\chi^{(5)}$ usually arises from the population of an intermediate state.[21,22] This can occur through either two-photon absorption or excited-state absorption processes. Excited-state absorption is known to be important in other types of Cr^{3+}-doped samples.[23,24] For example, an excited-state absorption band is located around 18 000 cm^{-1} in ruby.[24] The strength of the crystal field at the site of the Cr^{3+} ions in our sample is similar to that of ruby, and thus we can expect a similar excited-state absorption band to be present. The 517.5-nm (17 500-cm^{-1}) excitation is close to the maximum of this excited-state absorption transition, whereas the 514.5-nm (19 440-cm^{-1}) excitation is on the edge of the band. This could explain the observation of excited-state absorption effects with the former excitation wavelength and not the latter. However, as noted above, no information on excited-state absorption is currently available for the type of sample investigated here.

The observed power dependence suggests that high scattering efficiency can be achieved with 571.5-nm excitation. For example, considering the measured value of 0.002 for an intensity of 3.8×10^3 W cm^{-2}, extrapolation to higher power densities of the order of 1.0×10^4 W cm^{-2} should produce a scattering efficiency of approximately 0.094. Such high scattering efficiencies are associated with the contribution from $\chi^{(5)}$, which may be related to the high Cr^{3+} concentration and the long excited-state lifetime of about 6 ms.

V. CONCLUSIONS

This work represents the first investigation of four-wave mixing properties of a transparent glass ceramic material. Since no FWM signal can be observed in the normal glass whereas a strong signal was observed in the ceramic sample, these results demonstrate that devitrification drastically enhances the strength of FWM. The observed characteristics of the FWM signal provide information about the spectral dynamics of Cr^{3+} ions in this type of material. The properties of the FWM signal are consistent with scattering from a laser-induced population grating of Cr^{3+} ions in the ^2E level. The variation of the signal with temperature and laser power indicate that the properties of the FWM signal are governed by the spectroscopic characteristics of the excited state. No long-range energy migration takes place in this sample, probably due to the separation of the microcrystals. The inhomogeneous broadening due to random disorder in the crystal field sites along with ion-ion interaction leads to a fast dephasing time of the atomic system. The maximum signal strength is limited

by thermal lensing and saturation effects. However, scattering efficiencies as high as a few percent were observed, indicating that this type of transparent glass ceramic may be an attractive new material for FWM applications such as optical switching and phase conjugation. A final important aspect of this work is showing the usefulness of FWM techniques in studying the optical properties of ions in crystals. Somewhat different applications of this technique used on other types of materials have been published since this manuscript was originally prepared.[25]

*Permanent address: Universite Lyon I, Villeurbanne, France.

[1]J. Zarzycki, Les Verres et L'etat Vitreux (Masson, Paris, 1982).

[2]P. W. McMillan, Glass Ceramics (Academic, New York, 1979).

[3]L. J. Andrews, G. M. Beall, and A. Lempicki, J. Lumin. 36, 65 (1986).

[4]M. Bouderbala, G. Boulon, A. M. Lejus, A. Kisilev, R. Reisfeld, A. Buchj, and M. Ish-Shalom, Chem. Phys. Lett. 130, 438 (1986).

[5]V. Poncon, M. Bouderbala, G. Boulon, A. M. Lejus, A. Kisilev, R. Reisfeld, A. Buch, and M. Ish-Shalom, Chem. Phys. Lett. 130, 438 (1986).

[6]G. Boulon, Mater. Chem. Phys. 16, 301 (1987).

[7]R. Reisfeld, A. Kisilev, E. Greenberg, A. Buch, and M. Ish-Shalom, Chem. Phys. Lett. 104, 153 (1984); 105, 405 (1984).

[8]F. Durville, B. Champagnon, E. Duval, G. Boulon, F. Gaume, A. Wright, and A. Fitch, Phys. Chem. Glasses 25, 126 (1984).

[9]B. Champagnon, F. Durville, E. Duval, and G. Boulon, J. Lumin. 31/32, 345 (1984).

[10]F. Durville, B. Champagnon, E. Duval, and G. Boulon, J. Phys. Chem. Solids 46, 701 (1985).

[11]A. Suchocki, G. D. Gilliland, and R. C. Powell, Phys. Rev. B 35, 5830 (1987); A. M. Ghazzawi, J. K. Tyminski, R. C. Powell, and J. C. Walling, ibid. 30, 7182 (1984).

[12]R. C. Powell, J. K. Tyminski, A. M. Ghazzawi, and C. M. Lawson, IEEE J. Quantum Electron. QE-22, 1355 (1986); J. K. Tyminski, R. C. Powell, and W, K. Zwicker, Phys. Rev. B 29, 6074 (1984); C. M. Lawson, R. C. Powell, and W. K. Zwicker, ibid. 26, 4836 (1982); Phys. Rev. Lett. 46, 1029 (1982).

[13]J. Feinberg, in Optical Phase Conjugation, edited by R. A. Fisher (Academic, New York, 1983), p. 417.

[14]L. J. Andrews, A. Lempicki, and B. C. McCollum, J. Chem. Phys. 74, 5526 (1981); Chem. Phys. Lett. 74, 404 (1980).

[15]H. Kogelnik, Bell System Tech. J. 48, 2909 (1969).

[16]R. K. Jain and R. C. Lind, J. Opt. Soc. Am. 73, 647 (1983).

[17]K. O. Hill, Appl. Opt. 10, 1695 (1971).

[18]K. A. Nelson, R. Casselegno, R. J. D. Miller, and M. D. Fayer, J. Chem. Phys. 77, 1144 (1982).

[19]R. L. Abrams and R. C. Lind, Opt. Lett. 2, 94 (1978); 3, 205 (1978).

[20]P. F. Liao and D. M. Bloom, Opt. Lett. 3, 4 (1978).

[21]R. C. Lind, D. G. Steel, and G. J. Dunning, Opt. Eng. 21, 190 (1982).

[22]R. K. Jain, Opt. Eng. 21, 199 (1982).

[23]L. J. Andrews, S. M. Mitelman, M. Kokta, and D. Gabbe, J. Chem. Phys. 84, 5229 (1986).

[24]W. M. Fairbank, G. K. Klauminzer, and A. L. Schawlow, Phys. Rev. B 11, 60 (1975).

[25]S. C. Rand, J. F. Lam, R. S. Turley, R. A. McFarlane, and O. M. Stafsudd, Phys. Rev. Lett. 59, 579 (1987).

LASER-INDUCED GRATING SPECTROSCOPY
OF Cr3+-DOPED Gd3Ga5O12 AND Gd3Sc2Ga3O12 CRYSTALS

Andrzej SUCHOCKI [1] and Richard C. POWELL

Department of Physics, Oklahoma State University, Stillwater, OK 74078-0444, USA

The absorption and fluorescence spectra and fluorescence lifetimes of Cr^{3+} ions in two garnet hosts, $Gd_3Ga_5O_{12}$ and $Gd_3Sc_2Ga_3O_{12}$, were measured as a function of temperature. In addition, laser-induced grating measurements were made as a function of laser power and write beam crossing angle for various temperatures between 10 and 300 K. For short writing times, Cr^{3+} population gratings are produced and the observed signal dynamics were used to determine the properties of exciton migration in these materials. The exciton diffusion coefficient for $Gd_3Ga_5O_{12}:Cr^{3+}$ was found to decrease as temperature is raised while in $Gd_3Sc_2Ga_3O_{12}:Cr^{3+}$ the diffusion coefficient increases. Contributions to the laser-induced gratings from absorption and dispersion changes were determined and this was used to provide information on radiationless decay and excited state absorption processes. The differences in the results obtained on these two materials are attributed to the spectral effects produced by the different crystal field splittings of the Cr^{3+} energy levels. For long writing times, long-lived changes in the refractive index were also observed and attributed to optically induced color centers.

1. Introduction

Garnet crystals such as $Gd_3Ga_5O_{12}$ (GGG) and $Gd_3Sc_2Ga_3O_{12}$ (GSGG) have been used as host materials for lasers with Cr^{3+} and Nd^{3+} as the active ions. The fundamental optical spectroscopic properties of these materials have been measured [1-14] but many of the details of the optical properties have not yet been studied. It is especially important to understand the process of energy transfer among the chromium ions since this can effect the lasing characteristics of Cr^{3+} lasers and the efficiency of sensitizing Nd^{3+} ions in double-doped laser crystals. We report here the results of a study of Cr^{3+}-doped GGG and GSGG crystals using both standard spectroscopy techniques and the technique of four-wave mixing (FWM) to produce laser-induced gratings (LIGs). The results obtained on energy migration among the Cr^{3+} ions are significantly different for the two garnet hosts. This is attributed to the different magnitudes of the crystal field splitting of the Cr^{3+} energy levels. The effects of optically induced color centers

are also observed with LIG spectroscopy.

The GGG:Cr^{3+} sample used for these experiments was 1.5 mm thick. The average concentration of Cr^{3+} ions was 0.5 at%, but color gradients in the crystal indicate a nonuniform distribution of chromium. The majority of the measurements reported here were performed on the dark green part of the crystal, where the Cr^{3+} concentration was highest. The GSGG:Cr^{3+} was 0.55 cm thick with 0.5 at% Cr^{3+} and no obvious color gradients. The Cr^{3+} ions substitute for the Ga^{3+} ions in GGG and for the Sc^{3+} ions in GSGG. This results in a local crystal field site with an octahedral coordination of oxygen ions in the garnet lattice [7,15]. The presence of different types of crystal field sites for Cr^{3+} in GGG has been recognized previously [7] and attributed to the statistical occupancy of the next nearest neighbor sites with Gd^{3+} instead of Ga^{3+}.

The sample was mounted on the cold finger of a cryogenic refrigerator with a temperature controller which allowed the sample temperature to be maintained to about ± 0.5 K between 10 and 300 K. The absorption spectra were taken on an IBM 9430 UV–visible spectrophotometer. The fluorescence spectra were recorded with the use of a 1 m Spex mono-

---

[1] Permanent address: Institute of Physics, Polish Academy of Sciences, Al. Lotnikow 32/46, 02-668 Warsaw, Poland.

chromator and an RCA C31034 photomultiplier tube. Excitation was provided by either a Spectra Physics cw argon ion laser or by a pulsed Molectron nitrogen laser-pumped dye laser using a solution of oxazine 720 and rhodamine B in ethanol and DMSO [16]. For chopped cw excitation an EG&G/PAR model 128 lock-in amplififer was used to enhance the signal-to-noise ratio, while for pulsed excitation an EG&G/PAR model 165 boxcar averager was used.

Four-wave mixing was used to establish and probe laser-induced gratings. The LIG measurements were performed using either the 488.0 or 514.5 nm line of the argon laser for the "write beams" and a helium-neon laser for the "read beam". The write beams were chopped to measure the transient behavior of the LIG signal beam. The signal was recorded by an EG&G 4202 signal averager and processed by an IBM XT computer. The LIG scattering efficiency was measured with the use of a lock-in amplifier. More complete details of the LIG experimental setup have been published previously [17].

2. Spectroscopic properties of Cr^{3+} ions in GGG and GSGG

The absorption spectra of Cr^{3+} in GGG and GSGG at 12 K are shown in fig. 1. The two broad bands are characteristic of the transitions from the $^4A_2$ ground state of the $3d^3$ electron configuration of Cr^{3+} ions in an octahedral environment to the $^4T_1$ and $^4T_2$ levels, respectively. The third band in the GGG crystal peaked near 350 nm is attributed to transitions terminating on the $^4T_1(b)$ level. Sharp lines appear in three regions of the spectra. The two lines near 695 nm are the R lines due to transition terminating on the components of the ^2E level split by spin–orbit interaction and lower-order crystal field perturbations. The nearby lines at higher energy are a mixture of vibronic transitions and zero-phonon lines associated with transitions terminating on the $^2T_1$ and $^4T_2$ levels. The structure on the low-energy side of the $^4T_1$ band may be due to vibronic transitions or zero-phonon lines associated with transitions terminating on the $^2T_2$ or $^4T_1$ levels. The sharp lines around 310 nm are due to transitions of the Gd^{3+} ions which are split into several Stark components as shown in the insert.
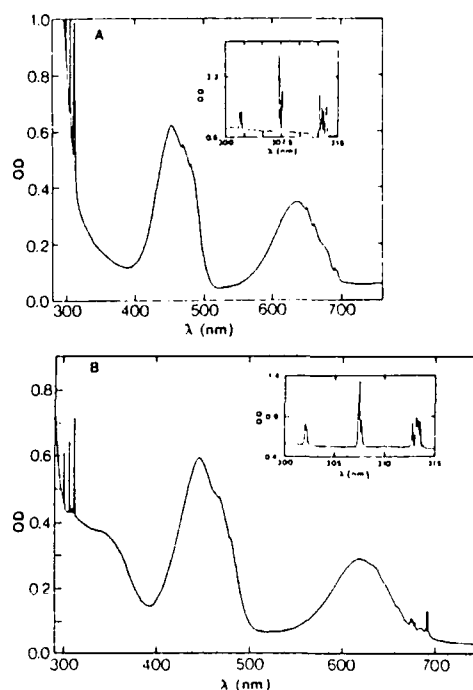

Fig. 1. Absorption spectra of GSGG:Cr^{3+} (A) and GGG:Cr^{3+} (B) at 12 K. The inserts show expanded views of the gadolinium transitions. (See text for sample thicknesses and Cr^{3+} concentrations.)

The portions of the fluorescence spectra associated with the vibronic transitions from the ^2E level at 12 K are shown in fig. 2. The vibronic peaks extend to lower energy from the R lines with some specific phonon peaks identifiable. However, it is difficult to identify many phonon progressions in the complex structure due to the overlapping of the different vibronic transitions associated with the large number of phonon modes in the garnet crystal structure.

The absorption and fluorescence spectra at low temperature in the region of the R lines are shown in fig. 3. For GGG:Cr^{3+} the R lines exhibit a significant amount of structure and there is a prominent secondary peak on the low-energy side of the R_1 line near 694.5 nm. It is not possible to resolve any similar structure in the spectra of GSGG:Cr^{3+} due to the greater overlap with the $^4T_2$ emission band. The spectral positions of the zero-phonon lines and the splittings of the energy levels are listed in table 1.

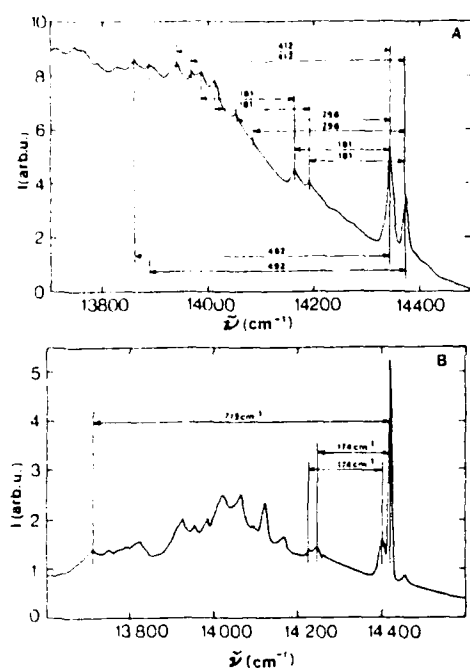The structure observed in the R lines in GGG:Cr^{3+}

Fig. 2 Fluorescence spectra at 12 K for (A) GSGG:Cr^{3+} and (B) GGG:Cr^{3+}

Fig. 3. Absorption and fluorescence spectra in the region of the R lines for (A) GSGG:Cr^{3+} at 12 K and (B) GGG:Cr^{3+} at 30 K.

was investigated in greater detail using site-selection spectroscopy techniques. Fig. 4 shows higher-resolution spectra of the R_1 and R_2 lines at 20 K for this sample. The R_2 spectrum was again recorded after broadband excitation. The upper and lower traces of the R_1 spectrum were obtained using narrow line excitation from the nitrogen laser-pumped dye laser set on wavelengths of 691.53 and 692.25 nm, respectively, while the middle trace was taken after excitation with the 488.0 nm argon ion laser line which is equivalent to broadband excitation. In the latter case, the cw laser excitation was chopped at a frequency of 500 Hz which tends to suppress the stronger but slower component of the R_1 line. The two wavelengths of the dye laser excitation are absorbed at different positions in the R_2 line and the spectra were recorded at 200 μs after the excitation pulse. The general shape of the spectral peak near 694.5 nm does not vary with time after the excitation pulse but peak position of the stronger component of the R_1 line moves to longer wavelengths as time increases. The exact shapes of the R lines at very short times after the excitation pulse were impossible to determine due
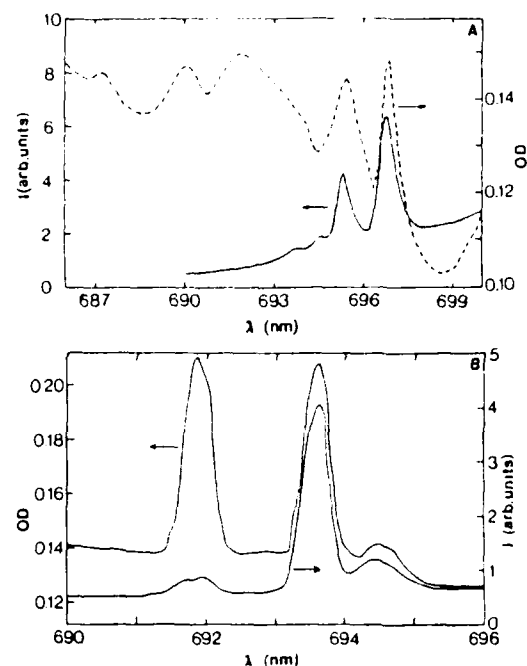
to strong, broadband superfluorescence from the dye laser.

The data described above are consistent with having at least four nonequivalent crystal field sites for the Cr^{3+} ions in GGG crystals. The positions of the R_1 lines for ions in each type of center can be determined from the site-selection measurements and are listed in table 1. The emission transitions associated with ions in the a and b sites are strongly overlapped and those associated with the c and d sites are strongly overlapped. For the R_2 lines, all four of the transitions are overlapped to the extent that it is impossible to accurately determine their exact peak positions. The strong overlap only allows for measurement of the fluorescence lifetimes of the ^2E levels for ions in the two sets of sites with strongly overlapped transitions, and their values at 12 K are also listed in table 1. The time-resolved spectroscopy results indicate that the only type of spectral energy transfer taking place at low temperatures is between ions in the sites labeled a and those in the sites labeled b. However, the strong overlap of the transitions of ions in these two

Table 1
Spectroscopic properties of Cr³⁺ ions in GSGG and GGG crystals

Parameter	GSGG	GGG
R position (nm)	696.8	693.5 (a)
		693.8 (b)
		694.5 (c)
		694.8 (d)
ΔE_a (cm⁻¹)	29	30
ΔE (cm⁻¹)	50	298
τ (ms)	0.232	1.5 (a and b)
		1.0 (c and d)
τ_r (ms)	0.242	1.6
τ_2 (µs)		40
λ_n	9.9×10^{-6}	$(3.7-9.9) \times 10^{-5}$
Δa (cm⁻¹)	0.082	2.8-3.2
J_x (fs)⁻¹	33	8-33
D (cm² s⁻¹)	3.9×10^{-7}	1.1×10^{-8}
D'	0.30	0.20-0.45
D	0.30	0.09-0.20
D''	0.31	0.27-0.31
D'''	0.01	0.01-0.05

° Measured at 12 K
ᵇ From I dependence.
ᶜ For pumping into the ⁴T₂ band.
ᵈ Measured at 300 K for GSGG and at 18 K for GGG.

Fig. 4. Fluorescence spectra of the R lines of GGG:Cr³⁺ at 30 K. (A) R₂ excited by 488.0 nm light chopped at 500 Hz. (B) Top curve: R₁ excited by a 10 ns pulse at 691.53 nm. Middle curve: R₁ excited by 488.0 nm light chopped at 500 Hz. Bottom curve: R₁ excited by a 10 ns pulse at 692.25 nm.

types of sites makes it difficult to obtain an accurate quantitative measurement of the transfer properties.

The fluorescence decay kinetics of the two major R₁ lines of GGG:Cr³⁺ at 12 K are both single exponential with a decay time of 1.5 ms. The secondary peak has a single-exponential decay with a fluorescence lifetime of 1.0 ms at the same temperature. The fluorescence of Cr³⁺ in GSGG at low temperature is also single exponential with a decay time of 232 µs at all emission wavelengths. The variation of the fluorescence lifetimes with temperature are shown in fig. 5. The data were obtained after pulsed dye laser excitation into the ⁴T₂ absorption band and the fluorescence was monitored in the vibronic emission band. The emission from GSGG:Cr³⁺ was found to be single exponential at all temperatures, whereas the observed decay kinetics for GGG:Cr³⁺ were nonexponential between 12 and 200 K and were single exponential at higher temperatures. At low temperatures the decay curves for GGG:Cr³⁺ can be approximated as the sum of two exponentials, and the open and filled circles in the figure represent the 1/e decay times of the long and short components of the double-exponential curves. The stronger compo-
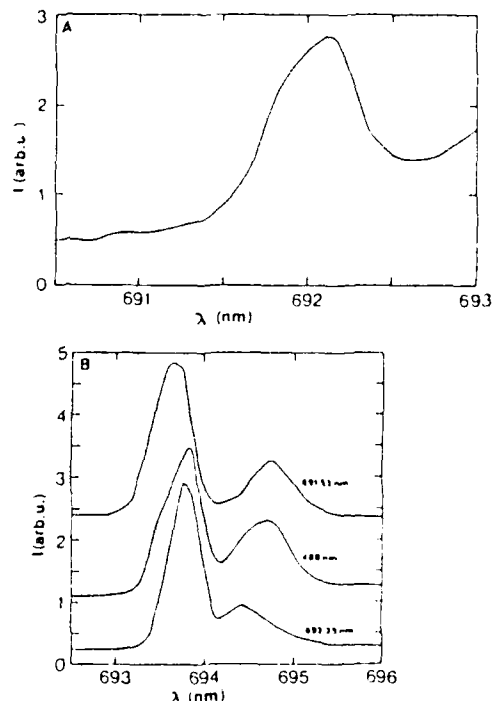
nent with the longer decay time is associated with emission from ions in the a and b sites while the short component is associated with emission from ions in the c and d sites. For both samples, the lifetimes decrease as temperature is raised with the magnitude of decrease being significantly greater for GGG:Cr³⁺ than for GSGG:Cr³⁺.

The fluorescence emission occurs from both the ²E and ⁴T₂ levels which are in thermal equilibrium and have a total quantum efficiency close to unity at room temperature and below. This results in a single lifetime which is a weighted combination of the intrinsic lifetimes of the two levels. The temperature dependence of the fluorescence lifetime can be associated with two possible physical processes, a change in the relative population of the two levels, or a change in the intrinsic lifetime of one of the two levels. For the first type of process, assuming a Boltzmann popula-
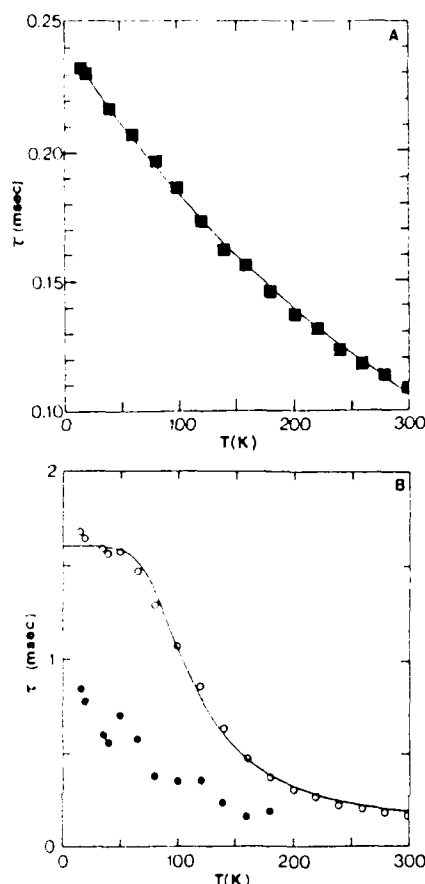
Fig. 5. Temperature dependence of the fluorescence decay times of (A) GSGG:Cr³⁺ and (B) GGG:Cr³⁺ where the open and full circles represent the long and short components of the double exponential decays, respectively. (See text for explanation of the theoretical lines.)

tion distribution, the measured fluorescence lifetime is given by [6]

$$\tau^{-1} = \frac{\tau_E^{-1} + \tau_T^{-1} \exp(-\Delta E/kT)}{1 + \exp(-\Delta E/kT)}. \qquad (1)$$

Here the intrinsic lifetimes of the ^2E and $^4T_2$ levels are τ_E and τ_T, respectively, k is the Boltzmann constant and ΔE is the energy separation of the two levels. This process provides a good explanation for the temperature variation of the longer component of the fluorescence lifetime of GGG:Cr³⁺. The best fit of eq. (1) to the data is shown as a solid line in fig. 5.

This was obtained with $\tau_E = 1.6$ ms, $\tau_T = 40$ μs, and $\Delta E = 298$ cm⁻¹. These are listed in table 1. The value obtained for ΔE is very close to the splitting between the R₁ line and the sharp line in the absorption spectrum at 697 nm. This is consistent with assigning the line at 697 nm to the zero-phonon transition to the lowest component of the $^4T_2$ level and with having the crossing point of the ^2E and $^4T_2$ potential coordinates occur at the bottom of the $^4T_2$ potential well.

No attempt was made to obtain a similar theoretical fit to the temperature dependence of the short-lifetime component of GGG:Cr³⁺ since the accuracy of these data was much poorer. This is because the magnitudes of the short lifetimes were determined after subtracting the extrapolated curve associated with the long-lifetime component. This procedure provides a rough estimate of the short-lifetime values but cannot be considered to be extremely accurate.

It was not possible to obtain a good fit to the GSGG:Cr³⁺ data using eq. (1). In this case the origin of the temperature dependence of the fluorescence lifetime appears to be associated with the increase in vibronic emission probability. For low-energy vibronic emission involving effective phonons with energy $\hbar\omega$, this can be expressed as

$$\tau^{-1} = \tau^{-1}(0) \exp(kT/\hbar\omega), \qquad (2)$$

where $\tau(0)$ is the lifetime of the purely electronic transition. The solid line in fig. 5 shows the best fit of eq. (2) to the GSGG:Cr³⁺ data obtained by treating $\tau(0)$ and $\hbar\omega$ as adjustable parameters. The good fit was obtained with $\tau(0) = 242$ μs and $\hbar\omega = 253$ cm⁻¹.

3. Results of laser-induced grating measurements

Four-wave mixing is an important technique for establishing and probing laser-induced gratings in solids. These LIGs are useful in studying the dynamics of exciton migration in doped crystals [17–21] as well as providing information on thermal, nonlinear optical, radiationless relaxation, and excited state absorption properties. In spectroscopic application of FWM, the crossed write beams are used to create a refractive index grating and the probe beam scatters off this grating. The scattered signal beam carries information about the physical properties of the mate-

rial associated with the laser-induced grating. For characterizing the properties of ions in solids, FWM is used to form population gratings. In this case the write beams are tuned to resonance with an absorption transition of the dopant ions thus creating a sine wave spatial distribution of ions in the excited state. If the ions have a different polarizability in the excited state than in the ground state, this excited state population distribution acts as a refractive index grating. The dynamics of the transient signal decay are especially helpful in understanding the properties of energy migration processes which contribute to the destruction of the grating. The variation in the LIG signal magnitude with write beam crossing angle is useful in determining the induced changes in the complex refractive index, and from this information the dephasing time and excited state absorption cross section can be obtained. Laser-induced grating measurements were performed on Cr^{3+} ions in GGG and GSGG crystals at temperatures ranging from about 15 to 300 K and the results are described below.

3.1. Transient LIG decay dynamics

Transient population gratings were established and probed for Cr^{3+} ions in GGG and GSGG using short enough writing times to prevent optical damage to the materials. The 488.0 nm line of the argon laser beam was for the write beams to excite the $^4T_1$ absorption band, the excited state population was built up in the $^4T_2$ and ^2E levels after radiationless relaxation. The decay dynamics of the scattered probe beam were monitored as a function of crossing angle of the write beams and temperature.

For the GGG:Cr^{3+} sample, the decay curves of the LIG signal were found to be double exponentials for temperatures less than 200 K, in agreement with the double-exponential behavior of the fluorescence decay kinetics in this temperature range. The long components of the decay curves are dependent on the crossing angle of the write beams θ and on temperature. Examples of the results are shown in fig. 6. The insert shows the double-exponential curve at 18 K for $\theta = 7.06°$ and the decay rate of the longer component of the signal K is plotted as a function of the crossing in the major part of the figure. At small values of θ the signal decay rate tends toward a value close to twice the measured value of the fluorescence decay
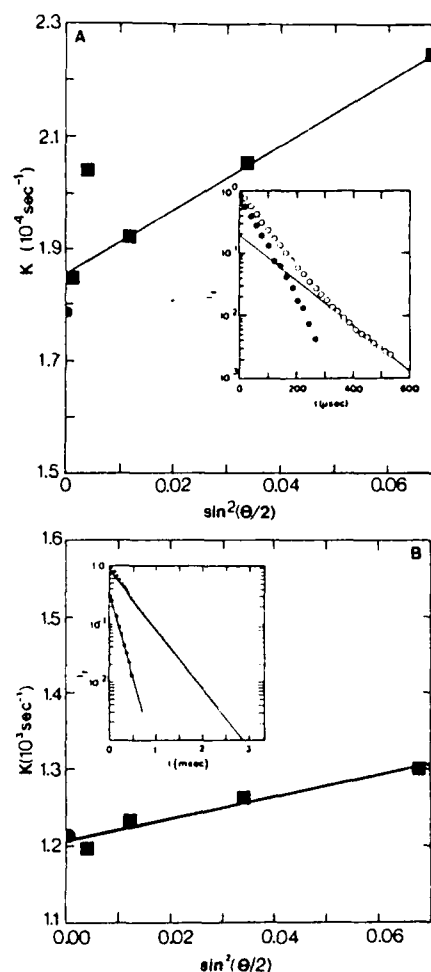

Fig. 6. Examples of the dependence of the transient LIG signal decay rates on the crossing angle of the write beams. (A) Short component of the signal obtained on GSGG:Cr^{3+} at 250 K. The insert shows the time evolution of the LIG signal at this temperature for $\theta = 3.51°$. The full points are the result of subtraction of the long-decay component extrapolated to short times. (B) Long component of the signal obtained on GGG:Cr^{3+} at 18 K. The insert shows the time evolution of the LIG signal at this temperature for $\theta = 7.06°$. The open points are the results of subtraction of the long-decay component from the total signal.

rate of the Cr^{3+} ions in type a and b sites as indicated by the filled circle in the figure. This is consistent with creating a populating grating of Cr^{3+} ions, mainly in type a and b sites. This component accounts for more than 80% of the LIG signal at all temperatures, which is consistent with the fluorescence data.

The second contribution to the transient LIG signal in GGG:Cr³⁺ was found to be independent of the first one and is attributed to a population grating of Cr³⁺ ions in the c and d types of sites. This grating is responsible for the short component of the LIG signal decay and the decay rate is approximately equal to twice the short component of the fluorescence decay rate. This component of the LIG decay rate is independent of the crossing angle θ.

The decay kinetics of the LIG signals for GSGG:Cr³⁺ were found to be single exponential at temperatures less than 200 K. The decay rates were independent of the crossing angle of the write beams and equal to twice the measured decay rate of the fluorescence in this temperature range. Above 200 K the decay kinetics became dependent on the write beam crossing angle θ and above 240 K the signal decays became double exponentials. The longer-decay components were still found to be independent of θ but their decay rates were the same as those of the fluorescence emission. The long-time part of the decay kinetics was extrapolated to short times and subtracted from the total signal to determine the decay rate of the short-time part of the decay kinetics. An example of this procedure is shown in the insert in fig. 6. Although this introduces some degree of uncertainty in the exact values determined for the decay rate of the short component of the signal decay, it is clear from the example results shown in fig. 6 that there is a distinct dependence of this decay rate on the write beam crossing angle. The circle at $\theta=0°$ represents twice the fluorescence decay rate measured under the same experimental conditions.

The decay rate of a laser-induced grating in the presence of exciton migration by an incoherent hopping motion can be expressed as [21]

$$K = 2/\tau + 32(\pi/\lambda)^2 \sin^2(\theta/2) D,\qquad(3)$$

where the first term described the destruction of the grating due to the fluorescence decay of the ions in the excited state with a decay time τ and the second term describes the destruction of the grating due to the migration of the excitation energy from the ions in the peak to ions in the valley region of the grating. The latter term depends on the diffusion coefficient of the energy migration D, and the grating spacing $\Lambda = \lambda/2 \sin(\theta/2)$, where λ and θ are the wavelength and crossing angle of the write beams in the crystal.

Applying this theory to the experimental results described above for GGG:Cr³⁺ indicates that long-range energy migration occurs among ions in the type a and b sites but not among ions in the type c and d sites. The solid line in fig. 6 represents the best fit to the experimental data using eq. (3). The theory predicts a linear dependence of K on $\sin^2(\theta/2)$ and, at zero crossing angle, a value of $2/\tau$ which is in agreement with the experimental data. The values of the diffusion coefficient obtained from this type of analysis of the data are plotted versus temperature in fig. 7. The small values of D result in large error bars in the results, but it is obvious that the energy migration decreases with increasing temperature and is negligible above 150 K.

Between 200 K and room temperature, the LIG signal decay for GGG:Cr³⁺ is a single exponential and independent of θ. The decay times are measured to be approximately half those of the fluorescence de-
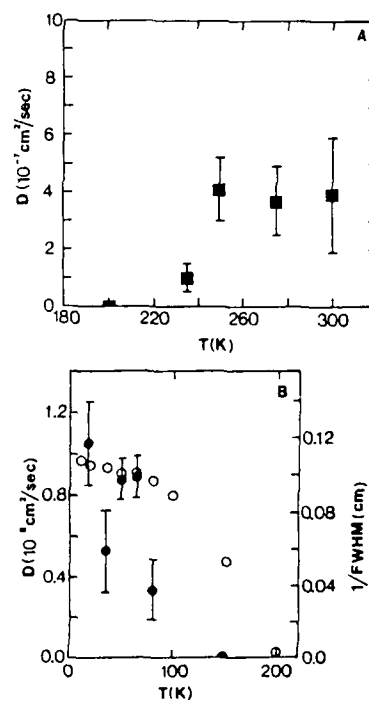

Fig. 7. Temperature dependence of the exciton diffusion coefficient for (A) GSGG:Cr³⁺ and (B) GGG:Cr³⁺. In (B), D is represented by full circles and the reciprocal of the full width at half maximum of the R₁ + R₂ lines is represented by open circles.

cay. Thermal broadening of the spectral transitions makes it impossible to distinguish between transitions associated with ions in different types of site. These results show that no long-range spatial migration of energy is taking place in this temperature range.

For GSGG:Cr³⁺, the lack of dependence of the short-time compenent of the LIG signal decay on the write beam crossing angle below 200 K indicates a lack of long-range energy migration among Cr³⁺ ions at low temperatures. Above 200 K energy migration does occur and estimates for the diffusion coefficient can be obtained by using eq. (3) to fit the data obtained on the dependence of K on θ. An example of this is shown as a solid line in fig. 6 and the results of this type of analysis provides information on the temperature dependence of the diffusion coefficient as shown in fig. 7. The weak dependence of K on θ results in large error bars in the estimates of D. However, there is a definite increase in D between 200 K and room temperature.

3.2. LIG scattering efficiency characteristics

The depencence of the transient LIG signal efficiencies on the power of the write beams for 488.0 nm excitation are shown in fig. 8 for two temperatures for both samples. The observed power dependences are different at low and high temperatures and neither are quadratic as expected from a simple two-level model for the atomic system [22,23]. This indicates the importance of the presence of multiple levels and transitions but is difficult to interpret quantitatively with presently available data.

The variation of the LIG scattering efficiency with the crossing angle of the write beams at 488.0 nm is shown in fig. 9 for both samples. The solid lines represent the best fits to the data using the model developed in detail in ref. [17]. In this model, the equations representing the four coupled waves in the crystal are solved numerically on the computer treating the coupling parameters as adjustable parameters. Using a two-level system model to describe the interaction of the laser beams with the crystal shows the complex coupling parameters to be determined by the laser-induced changes in the absorption and dispersion parts of the complex refractive index [22, 23].
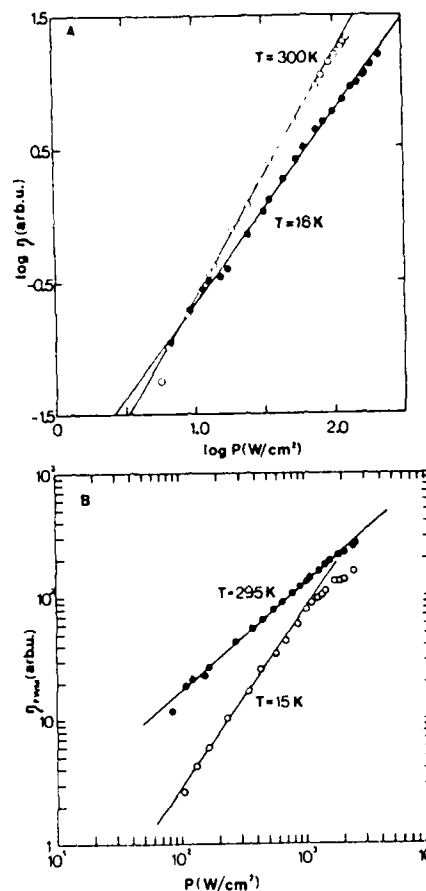
Fig. 8. Variation of the LIG scattering efficiency with the power of the write beams at two temperatures for $\theta = 3.5°$ for (A) GSGG:Cr³⁺ and (B) GGG:Cr³⁺.

$$\Delta\alpha = -2D_2'/D_1' ,\qquad(4)$$

$$\Delta n = (\alpha c/\omega)D_2'/D_1' .\qquad(5)$$

Here the real and imaginary parts of the jth coupling coefficient are represented by D_j' and D_j', respectively, and ω is the frequency of the write beams. The values of the coupling coeffients found from fitting the data can be used in eqs. (4) and (5) to determine $\Delta\alpha$ and Δn. The ratio of these contributions to the laser-induced grating can be used to obtain the dephasing time of the atomic system,

$$T_2 = (2\omega/c)(\Delta n/\Delta\alpha)/(\omega - \omega_{21}) ,\qquad(6)$$

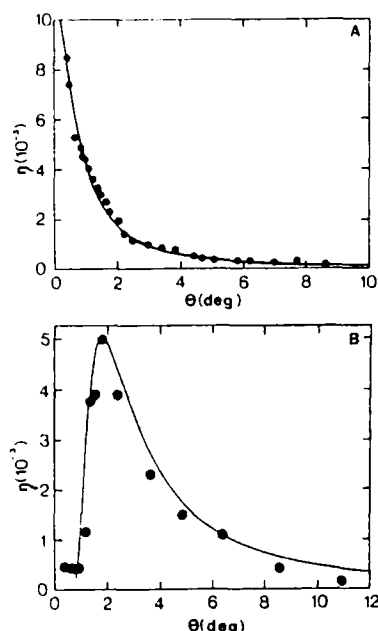where ω_{21} is the peak frequency of the atomic tran-

Fig. 9. Variations of the LIG scattering efficiencies with the crossing angle of the write beams at 40 K for (A) GSGG:Cr^{3+} and (B) GGG:Cr^{3+}. (See text for explanation of the theoretical lines.)

sition. The dephasing time can be written as

$$\Gamma_2^{-1} = 2T_1^{-1} + \gamma , \tag{7}$$

where γ is the pure dephasing rate due to phonon scattering processes and T_1 represents lifetime dephasing due to decay processes. The values of Δn, $\Delta \alpha$, and T_2 obtained in this way are listed in table 1 along with the relevant component of the coupling coefficients.

3.3. Long-lived refractive index changes

After long writing times, the LIG signal decay becomes a double exponential at all temperatures for both samples. Both components of the decay rates under this condition are independent of θ but the long component has a decay rate approximately equal to the fluorescence decay rate while the short-component decay rate is approximately twice that of the fluorescence. These results can be interpreted in terms of the presence of two types of laser-induced grating. The first is due to the excited state population of Cr^{3+}

ions and gives rise to the shorter signal decay. The second is associated with a very long-lived laser-induced refractive index grating. Since the probe beam simultaneously interacts with both types of grating, the signal decay kinetics is described by the square of the sum of the changes in the refractive index associated with the two gratings,

$$\eta = |A \exp(-t/\tau_1) + B \exp(-t/\tau_2)|^2$$
$$= A^2 \exp(-2t/\tau_1) + 2AB \exp(-t/\tau_1 - t/\tau_2)$$
$$+ B^2 \exp(-2t/\tau_2) , \tag{8}$$

where A and B are the magnitudes of the relative contributions due to the transient and long-lived gratings, respectively, and $\tau_1/2$ and $\tau_2/2$ are their decay times. The ratio B/A is very small for this sample (a few percent) and the decay time of the transient grating is much shorter than the decay time of the long-lived one. Thus eq. (8) reduces to approximately

$$\eta = A^2 \exp(-2t/\tau_1) + 2AB \exp(-t/\tau_1) . \tag{9}$$

Fig. 10 shows typical signal decays after long write times. The contribution of the long-lived grating becomes greater for longer writing times than those used to characterize the properties of the transient grating. For a given writing time and laser power, the signal associated with the long-lived grating was also found to increase with increasing temperature between 12 and 300 K. The strength of the long-lived grating is dependent on the writing time in a complicated manner. There is a critical writing time, of the order of a few minutes, when the LIG signal efficiency from the long-lived grating reaches a maximum and begins to decrease. For the results shown in fig. 10, both write beams were turned off after one minute causing a rapid decay of the transient grating followed by a slow, oscillatory decay associated with the long-lived grating. At longer times one of the write beams was turned on to erase the remaining long-lived grating. The kinetics of the long-lived grating signal are essentially independent of the crossing angle of the write beams, but the oscillatory decay of the signal does not permit an accurate estimate of the decay times.

Exciting with the 514.5 nm line of the argon ion laser which falls between the $^4T_{1g}$ and the $^4T_{2g}$ absorption bands enhances the relative contribution of the long-lived grating. Fig. 11 shows the dependence of both components of the LIG signal on the power

Fig. 11. Dependences of the transient and long-lived contributions to the LIG scattering efficiency on the power of the write beams for GGG:Cr^{3+} at 40 K for 514.5 nm excitation.
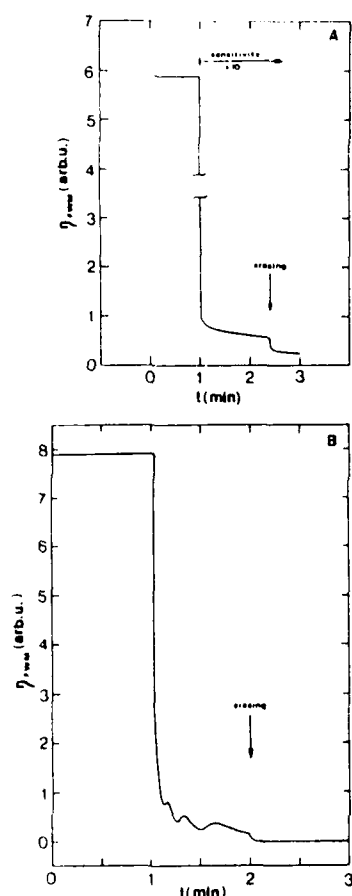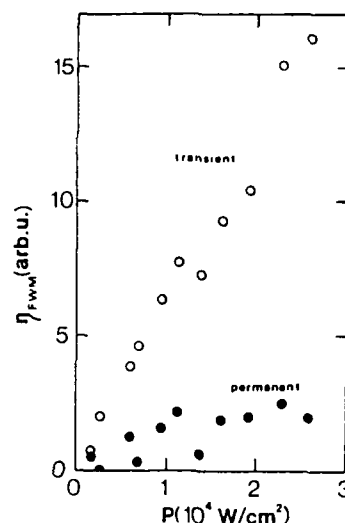
Fig. 10. LIG signal decays at 300 K showing the decays of the long-lived contributions to the signals and the effects of erasing by a single laser beam for (A) GSGG:Cre^{3+} and (B) GGG:Cr^{3+}.

of the write beams after writing for 2 min at 40 K for GGG:Cr^{3+}. The scattering efficiency was measured just before and about 12 s after both write beams were turned off. The scattering efficiency of the transient grating exhibits a linear dependence on the laser power whereas the scattering efficiency associated with the long-lived grating has a much weaker power dependence and saturates at relatively low power levels. Similar results were observed for GSGG:Cr^{3+}.

4. Discussion and conclusions

Despite the similarity of the two garnet host crystals, there are some significant differences in the op-

tical properties of Cr^{3+} ions in GGG and GSGG. One important difference between these two materials is the magnitude of the crystal field splitting of the ^2E and $^4T_2$ levels. The value of ΔE is 298 cm^{-1} for GGG. For GSGG this splitting is 50 ± 5 cm^{-1} which is consistent with reported values that range from close to 0 cm^{-1} up to 50 cm^{-1}. One major effect this has is to change the mechanism causing the temperature dependence of the fluorescence lifetime. For the wide energy gap in GGG:Cr^{3+}, the thermal effects on the population distribution between the two levels dominate the temperature dependence of τ. For a small energy gap material such as GSGG:Cr^{3+} these population distributions do not change with temperature. Instead the increase in the vibronic emission probability with increasing temperature dominates the temperature dependence of τ.

The energy migration observed in these samples can be described as a random walk of an exciton caused by ion–ion interaction [24,25]. The mechanism of ion–ion interaction is difficult to establish because of the presence of concentration gradients of the Cr^{3+} ions and the different types of crystal field site. By assuming electric dipole–dipole interaction among a statistically random distribution of ions, a theoreti-

cal estimate for the diffusion coefficient can be obtained from the expression

$$D = \frac{4\pi nR_0^6}{6\tau_s} \int_a^\infty r^{-2} \exp(-4\pi Nr^3/3)\, dr , \qquad (10)$$

where τ_s is the decay time of the sensitizer fluorescence and R_0 is the critical interaction distance. In the Forster–Dexter theory [24,26] the critical interaction distance is proportional to the overlap integral between the emission spectrum of the sensitizer ions and the absorption spectrum of the activator ions. For energy transfer which occurs due to ions in the ^2E excited state of Cr^{3+}, the overlap integral is approximately inversely proportional to the linewidth (fwhm) of the R lines.

To understand the observed energy transfer in GGG:Cr^{3+}, the average value of the concentration of Cr^{3+} ions $N = 1.4 \times 10^{20}$ cm^{-3} and the value of R_0 estimated by using the width of the R lines at 12 K to determine the overlap intergral, 29 Å, eq. (10) gives the value of $D = 2.3 \times 10^{-9}$ cm^2/s. This value is about an order of magnitude smaller than the experimentally determined value of the diffusion coefficient at $T = 12$ K. This estimate gives a lower limit for D. A higher value can be obtained for regions of high concentration due to a nonuniform distribution of Cr^{3+} ions. Also, energy transfer may take place through exchange interaction which is more difficult to estimate theoretically but will lead to a larger value of the ion–ion interaction rate.

The temperature dependence of D and the inverse of the fwhm of $R_1^0 + R_2^0$ for GGG:Cr^{3+} are compared in fig. 7. Both decrease with temperature with the diffusion coefficient decreasing somewhat faster than the inverse of the linewidths. This gives a reasonable explanation for the observed temperature dependence of the exciton diffusion coefficient. It should be noted that the assumption of energy migration mostly within the ^2E level is valid only for a wide ΔE material such as GGG:Cr^{3+}. It was also found that the magnitude of the exciton diffusion coefficient for GGG:Cr^{3+} at 18 K decreased to 6.9×10^{-9} cm^2/s when the light green region of the sample was excited. This indicates a concentration dependence associated with D as expected. The exact quantitative dependence requires a knowledge of the microscopic concentration gradient of the Cr^{3+} ions.

For GSGG:Cr^{3+} the small value of ΔE means that energy migrations will occur in both the ^2E and $^4T_2$ levels. Thus the spectral overlap integral must be calculated from the absorption and emission spectra instead of approximating it by the width of the R lines. This was calculated to be about 9.3 Å at low temperatures. Using this in eq. (10) again predicts a value for D which is significantly smaller than the measured value. As with GGG:Cr^{3+}, this is probably due to a nonuniform distribution of Cr^{3+} ions or stronger ion–ion interaction mechanisms such as superexchange. As temperature is raised the increase in vibronic emission causes an increase in the spectral overlap which results in an increase in D with temperature. This is qualitatively consistent with results for GSGG:Cr^{3+} shown in fig. 7. Thus the difference in ΔE is responsible for the significant difference in energy migration properties in GSGG:Cr^{3+} and GGG:Cr^{3+}.

The values of the dephasing time T_2 found from the LIG scattering efficiency results are significantly faster than those reported for other Cr^{3+}-doped crystals [17]. However, previous measurements were made by pumping into the $^4T_2$ band instead of the $^4T_1$ band as was done in this work. If the dephasing is dominated by radiationless relaxation processes, these results indicate the presence of faster decay processes in the higher level. To develop a complete understanding of dephasing processes requires comparing results obtained by pumping different transitions in a series of samples of different Cr^{3+}-doped crystals with different crystal field splittings. This systematic study is currently in progress.

The value of $\Delta\alpha$ for GSGG:Cr^{3+} determined from LIG measurements can be used to determine the excited state absorption cross section at the wavelength of the laser write beams. A simple rate equation analysis of the optical dynamics of a two-level atomic system can be used to obtain an estimate for the difference in the absorption coefficient in the peak and valley regions of the grating,

$$\Delta\alpha = I_0 N\sigma_1(\sigma_2 - \sigma_1)/(2I_0\sigma_1 - h\nu/\tau) , \qquad (11)$$

where I_0 is the energy density of the laser pump beams with photon energy $h\nu$, N is the concentration of active ions, τ is the fluorescence decay time of the excited state, and σ_1 and σ_2 are the ground and excited state absorption cross sections, respectively. This

equation can be solved for σ_2 and the measured values of the parameters used to calculate the excited state absorption cross section. Doing this gives a value of 2.1×10^{-20} cm^2, which is consistent with the value found [27] from excited state absorption measurements on GSGG:Cr^{3+}. No direct measurements of the excited state absorption spectrum of GGG:Cr^{3+} have been reported, and thus a similar comparison cannot be made with the LIG results obtained on this sample.

There is additional evidence for the effects of excited state absorption in the results obtained for the *power dependence of the LIG scattering efficiency.* The deviation from a simple quadratic dependence can be attributed to the fact that at the two laser wavelengths used, the excited state absorption cross sections are greater than the ground state cross sections. A quantitative description of the results would require a four-wave mixing analysis based on a three-level atomic system which is extremely complicated. A qualitative comparison of these results with those obtained on other Cr^{3+}-doped laser crystals such as ruby and alexandrite indicates that excited state absorption effects are significantly more important in these garnets than in the other hosts.

The long-lived grating is most probably associated with the creation of transient color centers in the host crystal. The creation of color centers in garnet crystals due to exposure to high-intensity light (especially in the ultraviolet region of the spectrum) is a well-known phenomenon [28]. The tendency to produce color centers has been attributed to oxygen deficiency in the garnet lattice [29]. In GSGG crystals the production of color centers was found to be accompanied by the valence change [14,30] Cr^{3+}–Cr^{2+}. This type of charge transfer process can also produce space charge electric fields in a crystal. The oscillatory decay kinetics observed for the long-lived grating may be due to the creation of space charge fields in GGG. Similar oscillatory kinetics have been reported in writing and erasing holographic gratings due to charge relocation in photorefractive crystals [31,32]. The dark decay times of the long-lived gratings in these crystals are of the order of several hours which indicates that this type of optically induced refractive index change can be an important loss mechanism for laser operation based on this material.

The results reported here demonstrate the usefull-

ness of LIG spectrocopy in characterizing the properties of solid state laser materials. This technique provides information about the properties of energy migration, radiationless decay processes, excited state absorption, and optically induced color centers. However, the results are quite complicated and there are still a number of details concerning these processes which require further study. It is especially important to compare the results of LIG measurements with those obtained by other techniques to verify some of the proposed interpretations. Also a systematic study of different types of Cr^{3+}-doped materials is needed.

References

[1] E.V. Zharikov, N.N. Il'ichev, V.V. Laptev, A.A. Malyutin, V.G. Ostroumov, P.P. Pashinin and I.A. Shcherbakov, Soviet J. Quantum Electron. 12 (1982) 338.

[2] E.V. Zharikov, V.V. Laptev, E.I. Sidorova, Yu.P. Timofeev and I.A. Shcherbakov, Soviet J. Quantum Electron. 12 (1982) 1124.

[3] G. Huber and K. Petermann, in: Tunable solid state lasers, Vol. 47, eds. P. Hammerling, A.B. Budgore and A. Pinto (Springer, Berlin, 1985) p. 11.

[4] E.V. Zharikov, V.V. Osiko, A.M. Prokhorov and I.A. Shcherbakov, Izv. Akad. Nauk SSSR Ser. Fiz. 48 (1984) 1330.

[5] M. Pardavi-Horvath, I. Foldvari, I. Fellegvari, L. Gosztonyi and J. Paitz, Phys. Stat. Sol. (a) 84 (1984) 547.

[6] E.V. Zharikov, S.V. Lavrishchev, V.V. Laptev, V.G. Ostroumov, Z.S. Saidov, V.A. Smirnov and I.A. Shcherbakov, Soviet J. Quantum Electron. 14 (1984) 332.

[7] B. Struve and G. Huber, Appl. Phys. B 36 (1985) 195; 30 (1983) 117; 28 (1982) 235.

[8] A.L. Denisov, V.G. Ostroumov, Z.S. Saidov, V.A. Smirnov and I.A. Shcherbakov, J. Opt. Soc. Am. 83 (1986) 95.

[9] G. Boulon, C. Garapon and A. Monteil, in: Advances in laser science II, eds. M. Lapp, W.C. Stwalley and G.A. Kenney-Wallace (A.I.P., New York, 1987) p. 87.

[10] E.V. Zhariko., N.N. Il'ichev, V.V. Laptev, A.A. Malyutin, V.G. Ostroumov, P.P. Pashinin, A.S. Pimenov, V.A. Smirnov and I.A. Shcherbakov, Soviet J. Quantum Electron. 13 (1983) 82.

[11] A.M. Prokhorov, Soviet Phys. Usp. 29 (1986) 3.

[12] W.F. Krupke, M.D. Shinn, J.E. Marion, J.A. Caird and S.E. Stokowski, J. Opt. Am. B 3 (1986) 102, and references therein.

[13] M.K. Ashurov, E.M. Zharikov, V.V. Laptev, I.N. Nasyrov, V.V. Osiko, A.M. Prokhorov, P.K. Khabibullaev and I.A. Shcherbakov, Izv. Akad. Nauk SSSR Ser. Fiz. 48 (1984) 95.

[14] E.V. Zharikov, N.N. Il'ichev, S.P. Kalitin, V.V. Laptev, A.A. Malyutin, V.V. Osiko, Y.G. Osvroymov, P.P. Pashinin, A.M. Prokhorov, V.A. Smirnov, A.F. Umyskov and I.A. Shcherbakov, Izv. Akad. Nauk SSSR Ser. Fiz. 48 (1984) 1354.

[15] S. Geller, Z. Krist. 125 (1967) 1.

[16] B.M. Pierce and R.R. Birge, IEEE J. Quantum Electron. QE-18 (1982) 1164.

[17] A. Suchocki, G.D. Gilliland and R.C. Powell, Phys. Rev. B 35 (1987) 5830.

[18] V.M. Kenkre and D. Schmid, Phys. Rev. B 31 (1985) 2430.

[19] R.F. Loring and S. Mukamel, J. Chem. Phys. 83 (1985) 4353.

[20] D.K. Garrity and J.L. Skinner, J. Chem. Phys. 82 (1985) 260.

[21] J.R. Salcedo, A.E. Siegman, D.D. Dlott and M.D. Fayer, Phys. Rev. Letters 41 (1978) 131.

[22] A. Yariv and D.M. Pepper, Opt. Letters 1 (1977) 16.

[23] R.L. Abrams and R.C. Lind, Opt. Letters 2 (1978) 94; 3 (1978) 205.

[24] D.L. Dexter, J. Chem. Phys. 21 (1953) 836.

[25] Z.G. Soos and R.C. Powell, Phys. Rev. B 6 (1972) 4035.

[26] T. Forster, Ann. Phys. 2 (1948) 55.

[27] L.J. Andrews, S.M. Hitelman, M. Kokta and D. Gabbe, J. Chem. Phys. 84 (1986) 5229.

[28] R. Metselaar, J.P.M. Damen, P.K. Larsen and M.A.H. Huyberts, Phys. Stat. Sol. (a) 34 (1976) 665.

[29] J.V. Meier, N.P. Barnes, D.K. Remelius and M.R. Kokta, IEEE J. Quantum Electron. QE-22 (1986) 2058.

[30] M.K. Ashurov, E.V. Zharikov, V.V. Laptev, I.N. Nasyrov, V.V. Osiko, A.M. Prokhorov, P.K. Khabibullaev and I.A. Shcherbakov, Izv. Akad. Nauk SSSR Ser. Fiz. 48 (1984) 1343.

[31] P. Gunter, Phys. Rept. 93 (1982) 199.

[32] J.P. Herriau and J.P. Huignard, Appl. Phys. Letters 49 (1986) 1140.

Four-wave-mixing spectroscopy of Cr-doped garnet crystals

Faqir M. Hashmi, Keith W. Ver Steeg, Frederic Durville, and Richard C. Powell

Center for Laser Research, Oklahoma State University, Stillwater, Oklahoma 74078-0444

G. Boulon

Universite Claude Bernard Lyon I, F-69622 Villeurbanne CEDEX, France
(Received 5 March 1990)

The characteristics of the four-wave-mixing signal of Cr^{3+} ions were measured for host crystals of $Gd_3Sc_2Ga_3O_{12}$, $Gd_3Ga_5O_{12}$, $(Gd,Ca)_3(Ga,Mg,Zr)_2Ga_3O_{12}$, and $La_3Lu_2Ga_3O_{12}$. Signal strengths and decay times were measured as functions of laser-beam crossing angles and temperature. The results are used to determine the properties of radiationless decay and energy-transfer processes in these samples. By comparing the characteristics of the $^4T_2$-^2E radiationless relaxation process among these and previously investigated Cr^{3+}-doped laser crystals, it is shown that the ratio of the intersystem-crossing relaxation rate to the internal conversion relaxation rate decreases as the strength of the crystal field of the host material decreases. The properties of energy migration among the Cr^{3+} ions in the different host materials is found to depend on the average separation of the Cr^{3+} ions, the strength of the crystal field, and the electron-phonon interactions.

I. INTRODUCTION

The use of garnet crystals such as $Gd_3Ga_5O_{12}$ (GGG) and $Gd_3Sc_2Ga_3O_{12}$ (GSGG) doped with Cr^{3+} and/or Nd^{3+} as laser materials has stimulated an interest in the study of the physical properties of these and similar garnets. A good deal of research has been directed towards the study of material characteristics essential to lasing.[1-9] These characteristics can be altered by changing the material's composition. This can be accomplished by studying other garnets such as $La_2Lu_3Ga_3O_{12}$ (LLGG) or by additional doping of optically inert ions. One attempt at the latter approach is substituting Ca^{2+}, Mg^{2+}, and Zr^{3+} ions for some of the Gd^{3+}, and Ga^{3+} ions in GGG to give a mixed garnet structure designated GGGM.[8,10] An understanding of how the crystal structure affects the dephasing and energy-transfer characteristics of the optically active ions is therefore essential. To this end, four-wave-mixing (FWM) spectroscopy is a useful tool. Previous studies of the spectroscopic properties as well as preliminary FWM results on GGG, GSGG, and GGGM have been reported.[9,11] This paper extends the previous work by using FWM to study energy migration and optical dephasing of Cr^{3+} ions by pumping into the $^4T_2$ band in GGGM, GGG, and GSGG, and by pumping into the $^4T_1$ band in LLGG. The results are compared to those obtained previously on Cr^{3+} ions in other laser crystals.

As reported in Ref. 10, the substitution of Zr^{3+}, Ca^{2+}, and Mg^{2+} ions for Ga^{3+} and Gd^{3+} ions in GGG results in a relatively high segregation coefficient of 2.8 and a larger lattice constant of 12.4942 Å. This produces a lower crystal field at the site of the dopant ion which is intermediate between the crystal-field values for GGG and GSGG. In addition, there are several nonequivalent sites for the Cr^{3+} ions which causes spectral structure

and significant inhomogeneous broadening of the optical transitions. The sample used in this study, provided by the Chrismatec company in France, was $4 \times 4 \times 5$ mm^3 with a concentration of 5.4×10^{19} Cr^{3+} ions/cm^3. The GSGG and GGG samples were 5.5- and 1.5-mm thick with Cr^{3+} concentrations of 1.4×10^{20} and 1×10^{20} cm^{-3}, respectively. The LLGG sample was approximately $20 \times 10 \times 4$ mm^3, with the large flat surfaces perpendicular to the [111] direction, and a concentration of 5.0×10^{19} Cr^{3+} ions/cm^3.

Figures 1 and 2 show the room-temperature absorption and emission spectra of the GGGM and LLGG samples. The absorption spectra, taken by an IBM 9430 uv-visible spectrometer, are dominated by two strong absorption bands, centered at 460 and 640 nm in GGGM and 485 and 685 nm in LLGG. In both samples, the higher-energy band is due to the $^4A_2$-$^4T_1$ absorption transition
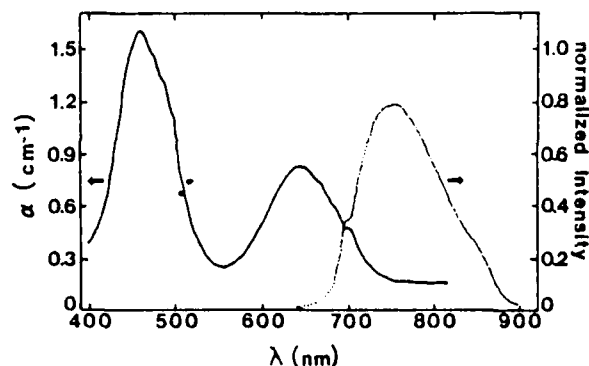

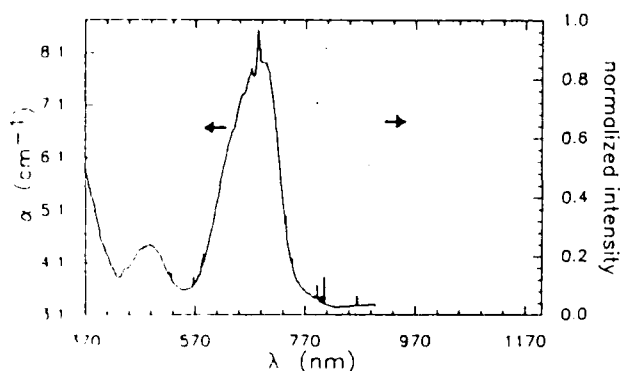FIG. 1. Room-temperature absorption (solid line) and emission spectrum (dotted line) of Cr^{3+}-doped GGGM.

FIG. 2. Absorption (solid line) and emission spectrum (dotted line) of Cr³⁺-doped LLGG at 12 K.

and the lower-energy band results from the $^4A_2$-$^4T_2$ transition. The sharp, relatively weak, spin forbidden transitions from the $^4A_2$ ground state to the ^2E, $^2T_1$, and $^2T_2$ states are overlapped by the broad bands. The transition matrix elements interfere destructively on one side of the sharp transition resonance and constructively on the other. This results in the absorption spectra having a characteristic antiresonant line shape, or Fano resonance, in the vicinity of the overlap. For GGGM, the dips in the lineshape on the low-energy side of the $^4T_1$ and $^4T_2$ bands are due to overlap with the sharp $^2T_2$ and $^2T_1$ transitions. The zero phonon line due to the $^4A_2$-^2E absorption is located at 695 nm. For LLGG, the lower crystal-field results in the $^4T_1$ and $^4T_2$ bands shifting towards lower energy. The antiresonances due to $^2T_1$ and $^2T_2$ therefore appear on the high-energy side of the two broad absorption bands. The prominent antiresonance near the peak of the $^4T_2$ band is due to the $^4A_2$-^2E transition. The other sharp lines in the spectrum correspond to the transitions of Nd³⁺, which is an unwanted impurity.

The emission spectrum was excited by a nitrogen laser-pumped dye laser, analyzed with a 1-m spectrometer, and detected by an RCA C31034 photomultiplier tube for the GGGM and an RCA 7102 for the LLGG. The fluorescence for both samples is characterized by a very broad, Stokes shifted emission which is the result of the low crystal field causing the $^4T_2$ energy level to be lowered; in the case of LLGG, $^4T_2$ is 1000 cm⁻¹ lower than ^2E as measured from minima to minima on the configuration coordinate diagram. For GGGM, the $^4T_2$-$^4A_2$ emission is centered at 750 nm with the ^2E-$^4A_2$ transition manifesting itself as a shoulder at 695 nm. For LLGG, the fluorescence is centered at 820 nm with the sharp dips and peaks due to Nd³⁺ impurities. For excitation at both 490 and 685 nm, the fluorescence decay of LLGG was single exponential, with the corresponding lifetime ranging from 120 μs at 11 K to 70 μs at room temperature. This is consistent with the fluorescence being dominated by emission from the $^4T_2$ level rather than the long-lived metastable ^2E level. Although the absorption at the peak of the $^4T_2$ band is about twice that at the

peak of the $^4T_1$ band, the fluorescence intensity resulting from excitation at 685 nm is slightly less than the fluorescence from 490 nm excitation. This implies that some sort of fluoresence quenching occurs for excitation into the $^4T_2$ band. It is conceivable that a center other than the Cr³⁺ is being excited. However, analysis of the $^4T_2$ fluoresence shows an emission peak and lifetime consistent with excitation of Cr³⁺ which implies that the additional center must be nonfluorescing. We are unable to conclusively explain these results at the present time, although it appears that fluoresence quenching of the $^4T_2$ band may be the reason why no laser-induced grating is observed when exciting into this level, as discussed in the following.

II. RESULTS FOR FOUR-WAVE-MIXING SPECTROSCOPY

FWM is an effective method for studying long-range energy migration and optical dephasing phenomenon among dopant ions in solids.[12-14] Earlier papers[9,12,14] describe in detail the procedure for using FWM techniques as a spectroscopic tool. Figure 3 shows the experimental setup used in these experiments. Emission from a Spectra Physics argon ion laser or argon ion laser-pumped ring dye laser was passed through a chopper (CH) and divided into two beams of equal intensities using a 50:50 beam splitter (BS). These two noncollinear laser beams (called the write beams) are then focused onto the sample using the appropriate mirrors M_1, M_2, and M_3. The path length is adjusted so that the two write beams cross inside the sample creating a sinusoidal interference pattern. Since the energy of the laser photons is resonant with the energy of an electronic transition of the Cr³⁺ ions, an excited-state population grating is created having the same spatial pattern. This population grating produces a sinusoidal variation in the refractive index due to the difference in the polarizability of Cr³⁺ ions in the excited state versus the ground state. A very low power He-Ne laser beam nearly counterpro-
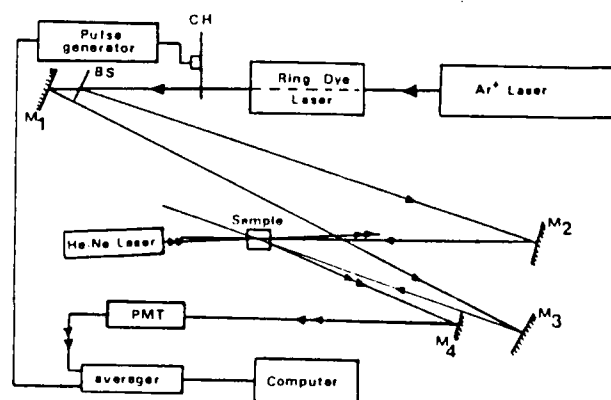

FIG. 3. Experimental setup for four wave mixing. CH — chopper BS — beam splitter and M — mirror. For excitation into the $^4T_1$ band, the ring dye laser is removed from the setup.

pagating to one of the write beams is scattered off this grating. When the Bragg condition is satisfied, the diffracted beam is nearly counterpropagating to the second write beam. This laser-induced grating (LIG) signal is then directed to an RCA C31034 photomultiplier tube (PMT) using mirror M_4. The output of the PMT is taken into an EG&G Princeton Applied Research model 4202 signal averager (averager) and then to an IBM XT personal computer where the digital data is stored. The trigger to the averager was provided by the chopper and pulse generator assembly. The sample was kept in a cryostat and the temperature was controlled using a CTI Cryogenics closed-cycle helium refrigerator and a Lake Shore Cryotronics model 805 temperature controller. The temperature measurements were accurate to better than 0.5 K.

The LIG signal carries all of the information about the physical processes influencing the population grating. Gratings were created by laser pumping into the $^4T_1$ band using an argon ion laser and pumping the $^4T_2$ band using an argon ion laser pumped dye laser. In both cases the population grating is observed after radiationless relaxation processes establish an equilibrium population in the ^2E and $^4T_2$ levels.

Figure 4 shows the intensity of the signal beam at room temperature for GGGM with 514.5 nm pumping. When both write beams are turned off at $t=0$, the signal decreases by a significant amount with a decay time of the order of the Cr^{3+} fluorescence lifetime indicating that the major contribution to the signal is associated with the Cr^{3+} population grating. The presence of a small residual signal indicates the presence of a long-lived grating, which is due to other physical processes such as charge relocation or the creation of color centers. To erase this long-lived grating, a single "erase beam" was turned on at $t=4$ min. Similar long-lived components to the LIG
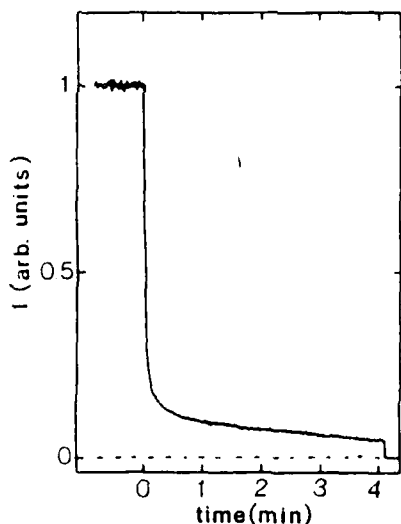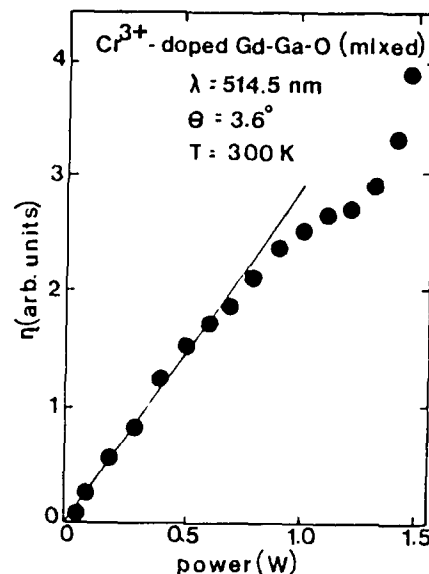

FIG. 5. Scattering efficiency as a function of laser beam power for excitation into the $^4T_1$ band of Cr^{3+}-doped GGGM.

signals were observed in the GGG and GSGG samples[9] but no long-lived grating component was observed for the LLGG sample. The characteristics of the signal beam associated with the population grating are discussed in the following.

The scattering efficiency for GGGM is plotted as a function of write beam power in Fig. 5. It was found to vary quadratically for low values of power, saturate for intermediate powers and then rise again for higher powers. The saturation occurs at power levels where the rate of pumping ions into the metastable state is equal to the fluorescence decay rate of the metastable state. The quadratic dependence and saturation level are consistent with the predicted behavior for this type of population grating.[14] The behavior at higher laser power indicates the onset of additional nonlinear optical processes. In order to ensure the validity of the results in the following sections, the write beam powers were kept low enough that the system was well below saturation.

A. Energy transfer

The decays of the LIG signal in GGGM were recorded at temperatures between 18 K and room temperature for both 514.5 and 581 nm excitation at various crossing angles of the write beams. The decay of the transient signal is shortened by energy migration from the peak to the valley region of the grating. As the crossing angle of the write beams is increased, the grating spacing is decreased and the effects of energy transfer are enhanced. The grating spacing Λ is given by

$$\Lambda = \lambda/[2\sin(\theta/2)], \tag{1}$$

FIG. 4 LIG signal decay after the write beams are turned off at $t=0$ min, and after an erase beam is turned on at $t=4$ min.

where θ is the write beam crossing angle. The crossing angles used here ranged from about 2° to about 22° giving
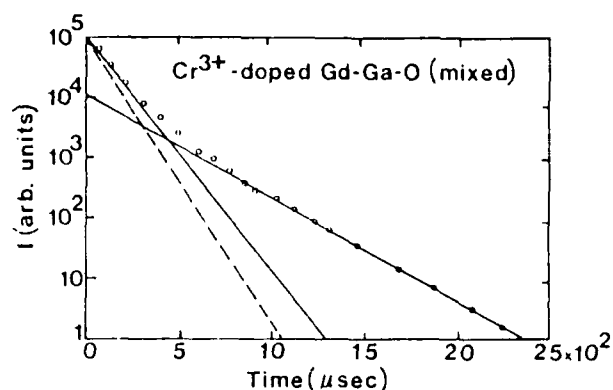
FIG. 6. Transient LIG signal decay at 18 K for Cr^{3+}-doped GGGM using 514.5 nm excitation. Total signal is shown to be comprised of two single exponentials.

a grating spacing ranging from about 1.4 μm to about 16 μm for the two wavelengths used.

Figure 6 shows an example of the decay of the transient LIG signal in GGGM. The decay is a double exponential which is consistent with the presence of two crystal-field sites for Cr^{3+} ions in the sample.[10] The decay times of the two components were found to have the same temperature and crossing angle dependences, therefore we show the analysis only for the short component.

Figure 7 shows an example of the signal decay rate in GGGM as a function of $\sin^2(\theta/2)$ for a given temperature. From the slope of the curve, we can calculate the exciton diffusion coefficient D for that temperature as described in the following. The temperature was varied from 18 to 300 K but no energy migration was observed for temperatures exceeding 150 K.

To obtain detailed information about the ion-ion interaction rate and exciton-phonon scattering rate, we have used the theory developed by Kenkre et al.[13] The
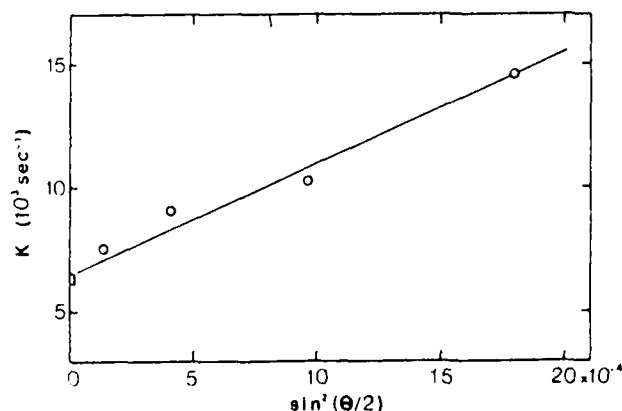
basic assumptions used in the development of this model are consistent with the conditions of our experiments. According to this theory, exponential decays of the normalized transient grating signal in the presence of exciton migration can be described by

$$I_r(t) = \exp\{-2t\{[(1/\tau_f + \alpha)^2 + b^2]^{1/2} - \alpha\}\} . \quad (2)$$

Here τ_f is the fluorescence lifetime, α is the exciton scattering rate, and b is defined as,

$$b = 4V \sin[(2\pi a/\lambda)\sin(\theta/2)] , \quad (3)$$

where V is the nearest-neighbor ion-ion interaction rate, and a is the average distance between active ions. The exciton dynamics can be characterized by these parameters in terms of the diffusion coefficient D, the diffusion length L_d, the mean free path L_m, and the number of sites visited between successive scattering events N_s. These parameters are given by

$$D = 2V^2 a^2/\alpha , \quad (4)$$

$$L_d = (2D\tau_f)^{1/2} , \quad (5)$$

$$L_m = \sqrt{2}Va/\alpha . \quad (6)$$

$$N_s = L_m/a , \quad (7)$$

respectively. Table I shows the energy migration parameters for Cr^{3+} in GGGM determined in these experiments.

In Fig. 8, the exciton diffusion coefficient D is plotted as a function of temperature. The data can be fit by an expression of the form

$$D = A + (B/\sqrt{T}) , \quad (8)$$

which is consistent with phonon scattering limiting the mean free path of the exciton migration.[15]

Figure 9 shows the temperature dependences of the ion-ion interaction rate and the exciton-phonon scattering rate for GGGM. The ion-ion interaction rate is independent of the temperature while the exciton-phonon scattering rate increases linearly with temperature. This

FIG. 7. FWM signal decay rate as a function of $\sin^2(\theta/2)$ for Cr^{3+}-doped GGGM. The point at $\theta = 0$ is twice the measured fluorescence decay rate.
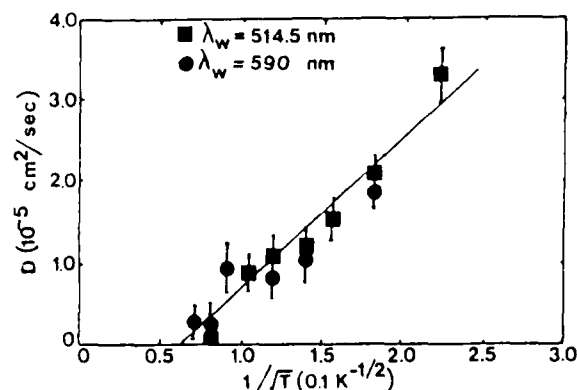

FIG. 8. Variation of the exciton diffusion coefficient D with respect to the temperature for Cr^{3+}-doped GGGM.

TABLE I. Energy migration parameters for Cr^{3+}-doped GGGM.

$T(K)$	$a(10^4 \ sec^{-1})$	$V(10^6 \ sec^{-1})$	$D(10^{-5} \ cm^2/sec)$	$L_m(\mu m)$	$L_d(\mu m)$
18	1.160	4.186	6.41	0.74	15.81
30	1.303	4.206	5.76	0.65	15.18
40	1.968	3.760	3.05	0.39	11.05
50	3.493	4.190	2.14	0.25	9.25
70	5.024	3.830	1.24	0.15	6.86
90	7.159	4.085	0.99	0.12	6.29
110	10.350	3.980	0.65	0.08	4.84
150	11.210	4.060	0.31	0.07	3.34

increase is associated with the additional phonons available at higher temperatures.

Similar studies on LLGG revealed that when exciting the $^4T_1$ band at 488 nm, the transient grating decay rate was independent of the angle between the write beams at all sample temperatures between 25 and 220 K. This is consistent with no long-range energy migration occurring in this material. No FWM signal could be observed when exciting the $^4T_2$ band at 660 nm.

B. Optical dephasing measurements

The laser beams in a FWM experiment drive the system of ions coherently and the time it takes the system of ions to lose phase coherence affects the strength of the FWM signal. Dephasing can occur when the ions interact with the phonons of the system or with other ions in the ensemble or when decay to another energy level occurs. The model used to describe the effect of dephasing on the FWM signal was developed in Refs. 16, 17, and 18 and extended for our experimental conditions in Refs. 12 and 14. The main assumption of this model is the approximation of the ensemble of ions as a two-level system.

The model describes an ensemble of two-level systems and their interaction with the four laser beams through four coupled differential equations. These equations have been solved numerically treating the real and imaginary parts of the coupling parameters D_1 and D_2 as adjustable parameters defined below:

$$D_1 = D_1' + iD_1' = 2\pi\mu L(\kappa - \xi) , \qquad (9)$$

$$D_2 = D_2' + iD_2' = \pi\mu\Delta\kappa L , \qquad (10)$$

where μ is the permeability of the material, ξ is an effective susceptibility, L is the distance of the overlap region, κ is a parameter related to the complex index of refraction, and $\Delta\kappa$ is the laser induced modulation of κ. This can be separated into a modulation Δn of the refractive index and Δa of the absorption coefficient. These parameters are related to the adjustable coupling parameters D_1', D_1', D_2', and D_2' as follows:

$$\Delta a = -2\bar{a}D_2'/D_1' , \qquad (11)$$

$$\Delta n = (\bar{a}c/\omega)D_2'/D_1' , \qquad (12)$$

where ω is the frequency of the laser line, $\bar{a}$ is the average absorption coefficient at the write beam wavelength and c is the speed of light. The dephasing time, T_2 is given by

$$T_2 = (2\omega/c)(\Delta n/\Delta a)(\omega - \omega_{21})^{-1} , \qquad (13)$$

where ω_{21} is the resonant transition frequency.

The set of coupled differential equations can be solved for special cases.[12] To see the effect of the crossing angle on the scattering efficiency, we consider one special case where,

$$(D_2')^2 + (D_2')^2 - (D_1' + D_2')^2 > 0 \qquad (14)$$

and

$$D_1' - D_2' \neq \begin{cases} 0 \\ [(D_2')^2 + (D_2')^2 - (D_1' - D_2')^2]^{1/2} . \end{cases} \qquad (15)$$

The scattering efficiency is then given by

$$\eta(\theta) = 2[(D_2')^2 + (D_2')^2][(D_2')^2 + (D_2')^2 - (D_1' + D_2')^2]^{-1}$$
$$\times \sin^2 \{k[(D_2')^2 + (D_2')^2 - (D_1' + D_2')^2]^{1/2}$$
$$\times \ln[\tan(\theta/4)]\} . \qquad (16)$$

FIG. 9 Variation of the exciton-phonon scattering rate a and ion-ion interaction rate V as functions of temperature for Cr^{3+}-doped GGGM.

The crossing angle θ in the preceding expression is directly connected with the overlap of the laser beams which in turn determines the modulation of the complex index of
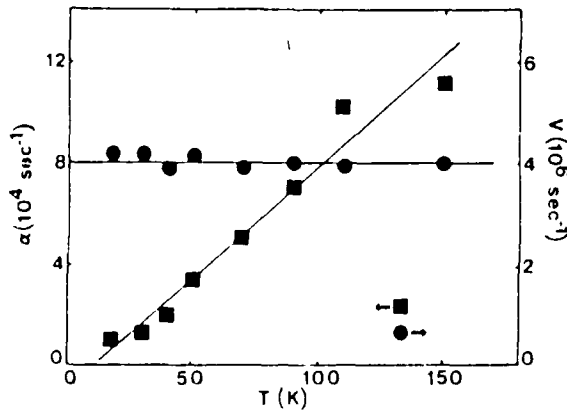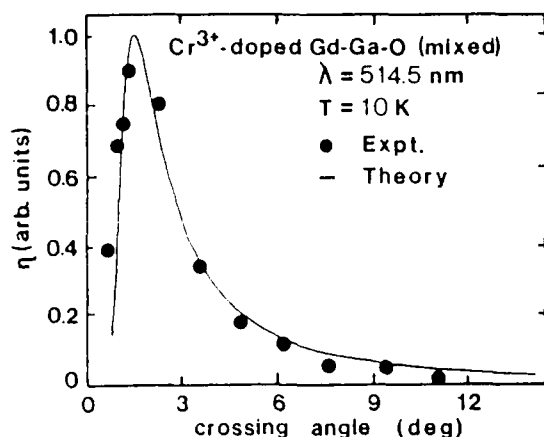
FIG. 10. LIG scattering efficiency as a function of crossing angle of the write beams for excitation into the $^4T_1$ band of Cr^{3+}-doped GGGM.
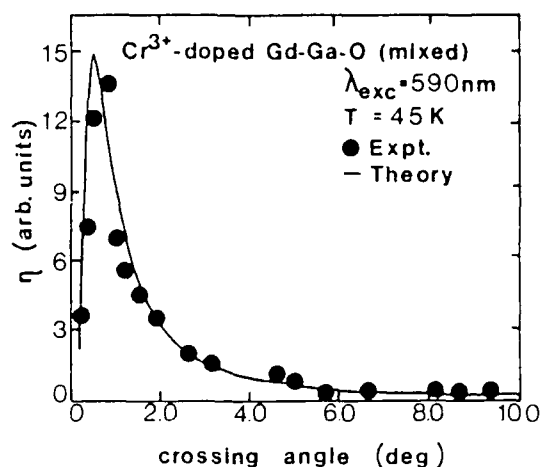

FIG. 11. LIG scattering efficiency as a function of crossing angle of the write beams for excitation into the $^4T_2$ band of Cr^{3+}-doped GGGM.

refraction and the absorption coefficient. The coefficients in the expression for η are found numerically.

In Fig. 10 the scattering efficiency is plotted as a function of the crossing angle for excitation into the $^4T_1$ band

of GGGM. Solid circles represent the experimental data points whereas the solid line denotes the theoretical fit. The good agreement between theory and experiment shows that for write beam powers well below saturation,

TABLE II. Parameters for the best fit to the scattering efficiency vs crossing angle plot and the dephasing time T_2 for Cr^{3+}-doped laser materials. NA indicates that the data is not available.

| Material and transition	D_1^c	D_1^i	D_2^c	D_2^i	T_2 (ps)
Alexandrite (Ref. 12) (inversion) $^4T_2$	0.006	0.015	0.135	0.00002	80±5
Ruby (Ref. 12) $^4T_2$	NA	NA	NA	NA	4.5±3
Alexandrite (Ref. 12) (mirror) $^4T_2$	NA	NA	NA	NA	2.2±4
Alexandrite (Ref. 14) (mirror) ^2E	0.250	0.650	0.350	0.0015	55.3
Emerald (Ref. 29) $^4T_2$	5.0×10^{-7}	4.0×10^{-7}	2.0×10^{-6}	8.0×10^{-9}	1.2
GGG $^4T_2$	0.205	0.20	0.230	0.0007	1.35±0.5
GGG (Ref. 9) $^4T_1$	0.2−0.45	0.09−0.2	0.27−0.31	0.01−0.05	0.008−0.033
GSGG $^4T_2$	0.210	0.18	0.240	0.001	0.77±0.5
GSGG (Ref. 9) $^4T_1$	0.30	0.30	0.31	0.01	0.033
GGGM $^4T_1$	0.92	0.01	0.100	0.05	0.0028±0.0005
GGGM $^4T_2$	0.200	0.22	0.235	0.001	0.92±0.5
LLGG $^4T_1$	0.400	0.280	0.303	0.015	0.74±0.5
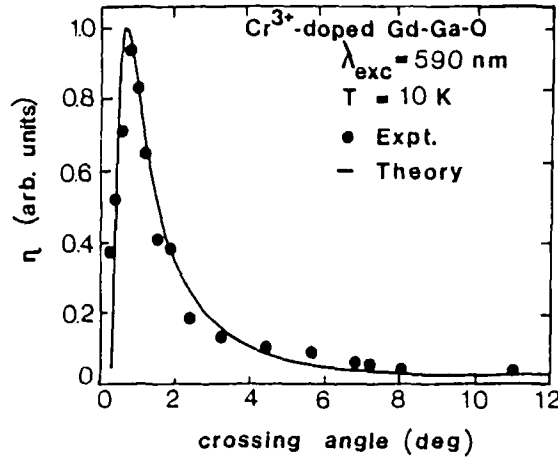
FIG. 12. Scattering efficiency as a function of crossing angle for the excitation into $^4T_2$ band of Cr^{3+} ions in Cr^{3+}-doped GGG.
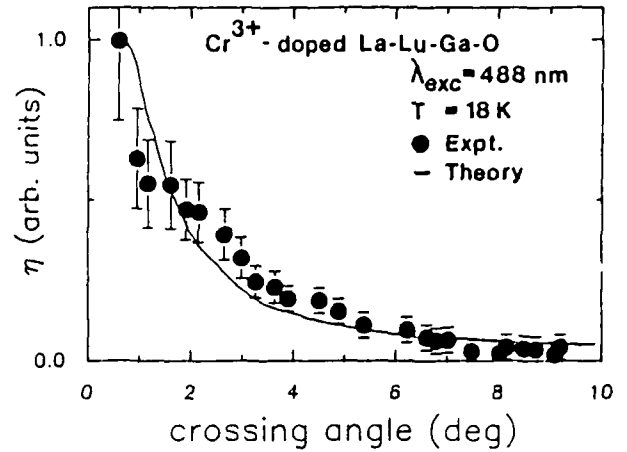

FIG. 14. LIG scattering efficiency as a function of crossing angle of the write beams for excitation into the $^4T_1$ band of Cr^{3+}-doped LLGG.

the two-level system gives a reasonable description of the results. The values of the parameters used to obtain the best fit along with the calculated dephasing times for different materials used in this survey are given in Table II.

Figures 11–14 give the experimental data and theoretical fits for the scattering efficiencies as a function of the write beam crossing angle for the excitation into the $^4T_2$ band of GGGM, GGG, GSGG, and the $^4T_1$ band of LLGG, respectively. The values of the parameters used to obtain the best fit and the corresponding dephasing time are given in Table II.

The expression for the dephasing time T_2 is given by[18]

$$1/T_2 = 1/T_1 + 1/T_2^{PD} ,\qquad (17)$$

where T_1 is the relaxation time of the excited level and T_2^{PD} is the time associated with the scattering mechanisms.

For excitation into the $^4T_2$ band, the dephasing is dominated by the time an ion takes to relax to the metastable ^2E level. This relaxation can follow two possible paths as described by the model proposed by Gilliland et al.[14] Figure 15 (adopted from Ref. 14) shows the energy-level parabolas for Cr^{3+} ions. The laser excites an ion into an excited vibrational level of the $^4T_2$ band at point A. It
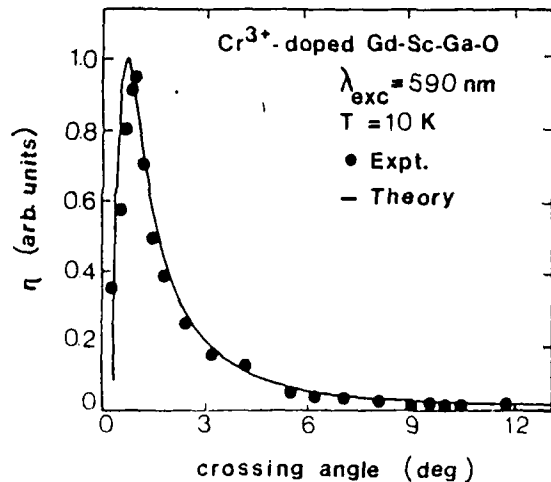

FIG. 13. LIG scattering efficiency as a function of crossing angle of the write beams for excitation into the $^4T_2$ band of Cr^{3+}-doped GSGG.
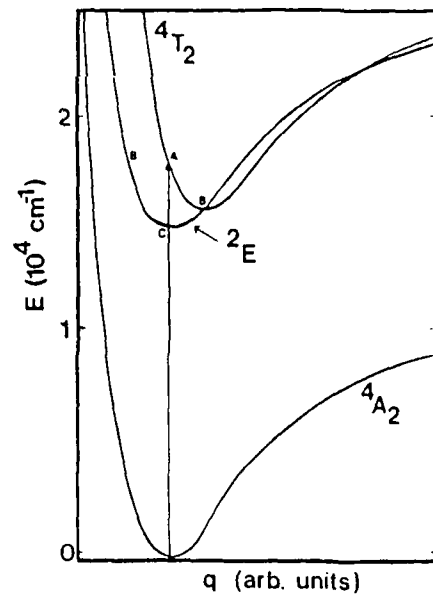

FIG. 15. Model used to analyze the dynamics of the nonradiative decay from the $^4T_2$ level to the ^2E level of Cr^{3+} ions in Alexandrite. The solid vertical line represents optical absorption (adopted from Ref. 14).
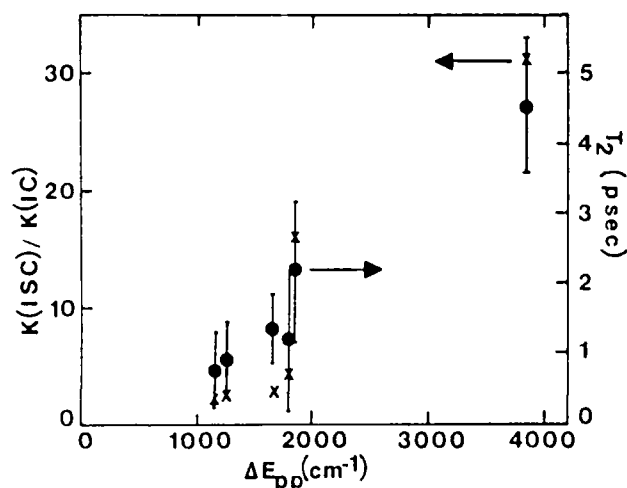
FIG. 16. T_2-dephasing time and the ratio K_{nr} (ISC)/K_{nr}(IC) as a function of ΔE_{pp} (the energy difference between the peak of the ^4T, band and the peak of the ^2E band in the absorption spectrum of Cr^{3+}-doped laser materials).

FIG. 17. Dephasing time (T_2) as a function of the ratio K(ISC)/K(IC).

can then relax within the $^4T_2$ band following the path through point B (where the two parabolas cross). The excitation then crosses over to the ^2E state and emits phonons until it reaches the bottom of the ^2E potential well. This process is called internal conversion (IC) and the corresponding nonradiative rate is denoted by K_{nr} (IC). Alternatively, the excited ion can relax by immediately crossing over to the ^2E band at point B' and then emitting phonons to reach the bottom of the potential well. This process is called intersystem crossing (ISC) and the corresponding nonradiative rate is denoted by K_{nr} (ISC). As noted in Ref. 14, after the first step is taken, the entire path for the dephasing is determined. The dephasing time T_2 is directly affected by whether IC or ISC path is the preferred channel for the nonradiative relaxation. Since the details of this process are described in Ref. 14, we will only mention the important points.

The nonradiative decay rates are calculated using standard perturbation theory techniques.[19] The vibrational

matrix elements are calculated using a single effective phonon frequency and Morse potential wave functions to account for anharmonicity.[20-27] The multielectron reduced matrix elements involved here are expressed in terms of the single-electron reduced matrix elements which have already been tabulated by Sugano et al.[28] Due to the difficulties involved in calculating the exact electronic wave functions needed for the evaluation of the single-electron matrix elements, only the ratio of the two rates K_{nr}(ISC)/K_{nr}(IC) is considered.

Calculations were performed for the Cr-doped laser materials ruby, alexandrite, emerald, GGG, GGGM, and GSGG, which have been investigated by FWM spectroscopy. The results can be used to determine the relationship between the dephasing process and the energy

TABLE III. Results of dephasing time measurements on Cr^{3+}-doped laser materials for pumping into the $^4T_2$ band.

Material	ΔE_{pp} (cm^{-1})	K_{nr}(ISC)/K_{nr}(IC)	$\Delta\alpha$ (cm^{-1})	Δn (10^{-5})
Alexandrite (Ref. 12) (Inversion)	5500		0.001 1	2.52
Ruby (Ref. 12)	3850	31	0.001 06	8.16
Alexandrite (Ref. 12) (Mirror)	1950	13	0.001 9	1.83
Emerald (Ref. 29)	1800	4.0	0.22	13
GGG	1650	2.6	0.009 3	1.44
GGGM	1250	2.3	0.003 5	0.38
GSGG	1150	2.2	0.003 1	0.35

difference between the peak of the $^4T_2$ band and the peak of the ^2E band in the absorption spectrum denoted by ΔE_{pp}. Nonradiative decay rates were calculated for the two possible dephasing paths and results of the calculations are given in Table III.

It is interesting to note that for all the materials considered, the ratio $K_{nr}(\text{ISC})/K_{nr}(\text{IC})$ is greater than 1. This generalizes the conclusion drawn in Ref. 14 that in Cr-doped laser materials, after pumping into the $^4T_2$ level, the dominant relaxation path for the excitation is ISC and not IC.

In Fig. 16 the ratio $K_{nr}(\text{ISC})/K_{nr}(\text{IC})$ and the dephasing time are plotted as a function of the energy splitting ΔE_{pp}. The two quantities have the same dependence on ΔE_{pp}. To further demonstrate this relationship, the dephasing time T_2 is plotted as a function of the ratio $K_{nr}(\text{ISC})/K_{nr}(\text{IC})$ in Fig. 17 and the result is a straight line.

III. DISCUSSION AND CONCLUSIONS

Investigations of long-range energy migration have been carried out on several different Cr^{3+}-doped laser crystals. No long-range energy migration was observed in ruby, the inversion site ions in alexandrite, or LLGG.

Detailed information on ion-ion interaction rates and exciton-phonon scattering rates was not available from the previous results reported for GGG and GSGG. Table IV summarizes the results for GGG, GSGG, GGGM, LLGG, emerald, ruby, and inversion and mirror site ions in alexandrite. The characteristics of energy transfer vary significantly from host to host depending on parameters such as the distance between the Cr^{3+} ions, the lifetime of the metastable state, the spectral overlap between absorption and emission, and the electron-phonon interactions. The variation of each of these parameters from host to host makes it difficult to establish a simple trend for energy transfer in Cr^{3+}-doped crystals.

One critical parameter in a diffusion or random walk picture of energy migration is the spacing between the sites of the lattice on which the random walk is occurring, designated as a. In this case a is the average separation between Cr^{3+} ions. This appears explicitly in the expression for both the ion-ion interaction rate V and the diffusion coefficient D. This separation is affected by the Cr^{3+} concentration in the sample, the host lattice spacings, and the distribution properties of the Cr^{3+} ions in the host. For mirror sites in alexandrite crystals, it is well known that the Cr^{3+} ions are not distributed randomly and the value of a used in Table IV was estimated from previous measurements on this sample.[12,14] For the

TABLE IV. Energy migration parameters for Cr^{3+}-doped laser crystals. NA indicates that the data is not available.

Material and transition	Dq (cm^{-1})	ΔE (cm^{-1})	D (10^{-8} cm^2/sec)	V (10^5 sec^{-1})	α (10^3 sec^{-1})	T (K)	a (Å)	N (10^{18} cm^{-3})	l_d (10^{-6} m)
Alexandrite (inversion) $^4T_2$ (Refs. 12,14,31)	2200	6400	0	NA	NA	ALL	41	2.5	NA
Ruby ^2E (Ref. 35)	1820	2300	0	NA	NA	ALL	59−108	79−490	3
Alexandrite (mirror) ^2E (Refs. 14,31)	1680	800	3	12	200	25	27	8.9	12
Emerald $^4T_2$ (Refs. 29,34,35)	1620	400	28	1.9	2.6	12	10	177	31
GGG $^4T_1$ (Refs. 4,9)	1597	298	1	NA	NA	18	NA	140	NA
GGGM (Ref. 10)	1567	100	6410	42	12	18	15	54	16
GSGG $^4T_1$ (Refs. 4,9)	1565	50	10	NA	NA	230	NA	NA	NA
LLGG $^4T_1$	1480	−1000	0	NA	NA	ALL	15	50	NA

other samples, the values listed for a are the average Cr^{3+} separations assuming a uniform distribution of ions. This of course is a rough approximation to the true situation of randomly distributed impurity ions. Note that for the two high crystal-field cases of ruby and alexandrite inversion sites, the values of a are extremely large. This results in a very small value for V and thus explains the lack of long-range energy migration in these cases.

The samples in Table IV are listed in order of decreasing crystal field. As the crystal field decreases, the population distribution of the excited state of the Cr^{3+} ions changes from being primarily in the ^2E level to being primarily in the $^4T_2$ level. The latter level has a shorter lifetime and larger Stokes shift compared to the former level. The lifetime decrease results in an increase in V while the increased Stokes shift decreases the spectral overlap integral thus decreasing the number density of ions, N and V. The value of the ion-ion interaction rate decreases by an order of magnitude between alexandrite (M) and emerald and then increases by an order of magnitude between emerald and GGG. The fluorescence lifetime is not significantly different for alexandrite (M) and emerald samples so the observed decrease in V is associated with the decreased spectral overlap. The increase in the case of GGGM may, however, be associated with the smaller fluorescence lifetime in this sample. The increased values of D for these three samples is associated with the decreased values of α as well as changes in the number density of ions, N. The value of V was found to be essentially independent of temperature at low temperatures for alexandrite mirror sites and the GGGM sample indicating that α and N do not vary with T in this range. However, in emerald V was found to increase with temperature because N increases.[29] The temperature dependence of V was not determined for the other samples.

The values of the scattering rate α which limits the mean free path of the migrating energy varies from alexandrite (M) to GGGM and is found to increase with temperature. Since the details of the exciton-phonon coupling are not known, it is not possible to predict the sample-to-sample variation in α.

From the discussion above, it is possible to understand the observed differences in the energy diffusion coefficient D from sample to sample. The values of D increase with increasing ion-ion interaction rate and decrease with increasing excitation scattering rate. The diffusion coefficient increases with temperature in emerald where V is phonon assisted but decreases with temperature for alexandrite mirror sites and GGGM where V is constant and α increases with temperature. Recently Kaplyanskii has combined the techniques of site-electron spectroscopy and Stark shifting of spectral lines to distinguish between resonant and nonresonant energy transfer between Cr^{3+} ions at low temperature.[30] He observed "anomalously fast and effective" resonant energy transfer among the Cr^{3+} ions in mirror sites in alexandrite crystals but not in ruby crystals. His results are consistent with the results of FWM studies of energy migration in these samples.

Comparing the results obtained on the dependence of the FWM signal magnitude of the crossing angle of the write beams with the model proposed by Gilliland et al.[14] for the dephasing mechanism in Cr-doped materials, we conclude that internal conversion is the dominant relaxation path when the chromium ions are excited to the $^4T_1$ level. This is due to the fast relaxation of the excitation to the bottom of the $^4T_1$ configuration potential well. The information on optical dephasing obtained from FWM measurements pumping into the $^4T_2$ level shows that radiationless relaxation to the ^2E level through intersystem crossing is the dominant dephasing process in these Cr^{3+}-doped laser crystals. The relative importance of dephasing through internal conversion within the $^4T_2$ level becomes more important as the crystal field of the host decreases.

The analysis for determining the dephasing time, change in refractive index (Δn), and the change in absorption coefficient ($\Delta\alpha$) assumes an effective two-level system model. The use of this model, despite its simplicity, has been justified on the basis of its ability to predict values of $\Delta\alpha$ which are consistent with values determined independently by ground and excited-state absorption measurements. Such checks have been done when values of the excited-state absorption cross section σ_f are available, such as for alexandrite,[31] ruby,[32] GSGG,[33] and emerald.[34,35]

Recently, the results of FWM measurements on Nd^{3+}-doped materials has been analyzed using a model based on an effective four-level system.[36] In this model, the laser beams interact with ions both in the ground state and metastable state. The transitions from the ground and metastable states to higher-energy states is accounted for by combining the upper states into two effective states. A density matrix formalism yields the change in the real and imaginary parts of the nonlinear susceptibility between ions in the peak and valley of a population grating. By measuring the absolute magnitude of the FWM signal in a variety of samples, it was concluded that the dominant contribution to the signal comes from the real part of the nonlinear susceptibility associated with the off resonant, allowed transitions to the levels of different configuration in the ultraviolet spectral region. The relative values of Δn and $\Delta\alpha$ obtained in this work are consistent with the proposed model. In this case the weak contribution to the signal associated with the imaginary part of the nonlinear susceptibility comes from the resonant interaction with the pump transition. Recognizing the contributions due to these two different types of transitions, the expressions for Δn and $\Delta\alpha$ will be the same for the two-level and four-level modes.

It is important to note that the procedure for using the two-level system fit to the crossing angle dependence of the FWM scattering efficiency to find the dephasing time should be approached with caution. This approach has been justified on the basis that values found for $\Delta\alpha$ are in good agreement with those values found independently from excited-state absorption measurements. Equation (11) shows how $\Delta\alpha$ depends on the fitting parameter D'_2; however, the computer fit to the crossing angle dependence of the FWM scattering efficiency can be relatively insensitive to the parameter D'_2. This may result in large

error bars for $\Delta\alpha$ and thus a large error in the value determined for T_2 which is dependent on $\Delta\alpha$, as shown in Eq. (13).

Accurate confirmation of the values of T_2 determined by these FWM measurements must come from a direct measurement of the dephasing time. Photon echo measurements are currently being made on these Cr^{3+}-doped materials to determine T_2.

[1]B. Struve, G. Huber, V. V. Laptev, I. A. Scherbakov, and Y. V. Zharikov, Appl. Phys. B 28, 235 (1982).

[2]B. Struve and G. Huber, J. Appl. Phys. 57, 45 (1985).

[3]E. V. Zharikov, N. N. Il'ichev, V. V. Laptev, A. A. Malyutin, V. G. Ostroumov, P. P. Pashinin, and I. A. Shcherbakov, Sov. J. Quantum. Electron. QE-12, 338 (1982).

[4]B. Struve, G. Huber, Appl. Phys. B 36, 195 (1985).

[5]E. V. Zharikov, V. V. Laptev, E. I. Sidorova, Yu. P. Timofeev, and I. A. Shcherbakov, Sov. J. Quantum Electron. QE-12, 1124 (1982).

[6]G. Huber and K. Petermann, in Tunable Solid State Lasers, edited by P. Hammerling, A. B. Budgore, and A. Pinto (Springer, Berlin, 1985), Vol. 47, p. 11.

[7]E. V. Zharikov, V. V. Osiko, A. M. Prokhorov, and I. A. Shcherbakov, Izv. Adad. Nauk SSSR Ser. Fiz. 48, 1330 (1984).

[8]G. Boulon, C. Garapon, and A. Monteil, in Advances in Laser Sciences II, edited by M. Lapp, W. C. Stwalley, and G. A. Kenney-Wallace (AIP, New York, 1987), p. 87.

[9]Andrzej Suchocki and Richard C. Powell, Chem. Phys. 128, 59 (1988).

[10]A. Monteil, C. Garapon, and G. Boulon, J. Lumin. 39, 167 (1988).

[11]F. Durville, R. C. Powell, and G. Boulon, J. Phys. (Paris) Colloq. 48, C7-517 (1987).

[12]A. Suchocki, G. D. Gilliland, and R. C. Powell, Phys. Rev. B 35, 5830 (1987).

[13]V. M. Kenkre and D. Schmid, Phys. Rev. B 31, 2430 (1985).

[14]Guy D. Gilliland, Andrzej Suchocki, Keith W. Ver Steeg, Richard C. Powell, and Donald F. Heller, Phys. Rev. B 38, 6227 (1988).

[15]V. M. Agranovich and M. D. Galanin, Electronic Excitation Energy Transfer in Condensed Matter (North-Holland, Amsterdam, 1982).

[16]R. L. Abrams and R. C. Lind, Opt. Lett. 2, 94 (1978).

[17]A. Yariv and D. M. Pepper, Opt. Lett. 1, 16 (1977).

[18]M. D. Levenson, Introduction to Nonlinear Laser Spectroscopy (Academic, New York, 1982).

[19]Eugen Merzbacher, Quantum Mechanics (Wiley, New York, 1970).

[20]P. M. Morse, Phys. Rev. 34, 57 (1929).

[21]B. I. Makshantsev, Opt. Spektrosk. 31, 355 (1971) [Opt. Spectrosc. (USSR) 31, 191 (1971)].

[22]M. D. Sturge, Phys. Rev. B 8, 6 (1973).

[23]J. A. C. Gallas, Phys. Rev. A 21, 1829 (1983).

[24]P. A. Fraser and W. R. Jarmain, Proc. Phys. Soc. London Sec. A 66, 1145 (1953).

[25]J. A. C. Gallas, H. P. Grieneisen, and B. P. Chakarborty, J. Chem. Phys. 69, 612 (1978).

[26]V. S. Vasan and R. J. Cross, J. Chem. Phys. 78, 3869 (1983).

[27]R. Englman and B. Barnett, J. Lumin. 3, 37 (1970).

[28]S. Sugano, Y. Tanabe, and H. Kamimura, Multiplets of Transition Metal Ions in Crystals (Academic, New York, 1970).

[29]Gregory J. Quarles, Andrzej Suchocki, and Richard C. Powell, Phys. Rev. B 38, 9996 (1988).

[30]S. A. Basun, A. A. Kaplyanskii, V. N. Matrosov, S. P. Feofilov, A. A. Chernyshev, and A. P. Shkadarevich, Opt. Spektrosk. 66, 1067 (1989) [Opt. Spectrosc. (USSR) 66, 624 (1989)].

[31]M. L. Shand, J. C. Walling, and R. C. Morris, J. Appl. Phys. 52, 953 (1981).

[32]W. M. Fairbank, Jr., G. K. Klauminzer, and A. L. Schawlow, Phys. Rev. B 11, 60 (1975).

[33]L. J. Andrews, S. M. Hitelman, M. Kokta, and D. Gabbe, J Chem. Phys. 84, 5229 (1986).

[34]R. C. Powell, A. Suchocki, G. D. Gilliland, and G. J. Quarles, J. Lumin. 38, 250 (1987).

[35]T. F. Veremeichik, Phys. Status Solidi B 124, 719 (1984).

[36]R. C. Powell, S. A. Payne, L. L. Chase, and G. D. Wilke, Phys. Rev. B 41, 8593 (1990).

IV. NONLINEAR OPTICAL PROPERTIES OF CRYSTALS AND GLASSES

The six manuscripts in this section describe the results of investigations of two classes of nonlinear optical materials, rare earth-doped glasses and displacive ferroelectrics. The first five papers focus on a new method for producing laser-induced holographic gratings in glasses. This type of laser-induced refractive index change forms the basis of devices for optical technology applications such as demultiplexers, filters, beam deflectors, and optical limiters. This method developed involves generating a significant number of local vibrational modes by radiationless relaxation of the resonantly pumped rare earth ion. These local vibrational modes provide enough energy to cause a structural change in the glass host surrounding the rare earth ion and this changes the refractive *index*. The gratings are stable at room temperature and can be erased thermally. The important new results of this investigation include characterizing the effects of both alkali and alkaline earth modifier ions on the efficiency of grating formation, demonstrating the difference between Pr^{3+} and Eu^{3+} ions in the dynamics of grating formation, developing a two-level system model to describe the local structural modification, developing a polarizability change model to explain the origin of the refractive index change, and demonstrating the device capabilities of these materials for holographic information storage, demultiplexing, and amplitude modulation of light signals. The fifth manuscript describes the radiative and radiationless relaxation processes that take place in Eu^{3+}-doped

fluoride and oxide glasses under high-power, picosecond-pulse excitation. A comparison of these spectral properties originating from excitation into highly excited states of the rare earth ion is useful in determining the best host glasses for producing holographic gratings.

The final manuscript describes a comprehensive investigation of the nonlinear optical properties of $KNbO_3$. This is a displacive ferroelectric crystal that can be used for frequency doubling, photorefractive phase conjugation, and other applications related to its electro-optic properties. Using continuous wave four-wave mixing and two-beam energy transfer techniques the properties of charge relocation dynamics resulting in a photorefractive effect on a millisecond time scale were determined. The effects of different types of doping ions on these photorefractive properties were measured. In addition, the nonlinear optical response of the material to picosecond pulse excitation was investigated. The results of these experiments revealed laser-induced absorptive changes on time scales of a nanosecond and an ultrafast, picosecond response. The latter can be affected by contributions from several physical sources. However, one important physical processes that was identified is stimulated scattering from niobium hopping modes.

Properties of laser-induced gratings in Eu-doped glasses

Edward G. Behrens, Frederic M. Durville,* and Richard C. Powell

Department of Physics, Oklahoma State University, Stillwater, Oklahoma 74078-0444

Douglas H. Blackburn

National Institute of Standards and Technology, Gaithersburg, Maryland 20894
(Received 25 August 1988; revised manuscript received 20 October 1988)

The properties of permanent, laser-induced gratings were studied in Eu^{3+}-doped glasses. These gratings are associated with a structural modification of the glass host in the local environment of the Eu^{3+} ions, and we have investigated the effects produced by altering the Eu^{3+} concentration and by changing the composition of the glass host. A two-level-system model is developed to explain the results.

I. INTRODUCTION

We have previously reported the observation of permanent, laser-induced refractive-index gratings in Eu^{3+}-doped glasses using four-wave-mixing (FWM) techniques.[1-3] These gratings were established using crossed write beams in resonance with the $^7F_0$-$^5D_2$ absorption transition of the Eu^{3+} ion and displayed buildup times of the order of 15 min. The grating is stable at room temperature but can be erased thermally by heating the sample to temperatures above room temperature or it can be erased optically with a single beam tuned in resonance with the $^7F_0$-$^5D_2$ transition of the Eu^{3+} ion. No grating formation or erasure occurs if the laser beams are not in resonance with the $^7F_0$-$^5D_2$ absorption transition of the Eu^{3+} ion.

A model was proposed to explain these gratings in which the network former and network modifier ions of the glass host can arrange themselves into two different configurations in the local environment of the Eu^{3+} ion. This leads to double-minimum potential wells for the Eu^{3+} electronic energy levels. It is assumed that the material possesses a different index of refraction depending on which configuration is present. When the Eu^{3+} ion relaxes nonradiatively from the $^5D_2$ level to the $^5D_0$ level several high-energy "phonons" are created. The local heating produced by the vibrational modes can produce a change in the structure of the local environment of the Eu^{3+} ion by causing the ions to move from one equilibrium configuration to the other.

In this paper we extend our previous work by looking at different hosts, altering the Eu^{3+} concentration, and varying the network modifier ion in a series of silicate glasses. Finally, the details of the two-level-system model are developed to provide a quantitative explanation of the data.

II. EXPERIMENTAL RESULTS OF SCATTERING EFFICIENCY MEASUREMENTS

A. Effects of Eu^{3+} concentration

To study the effect of the Eu^{3+}-ion concentration on the permanent, laser-induced grating, samples were obtained whose compositions varied only in the Eu^{3+} concentration. The first samples investigated were two Eu^{3+}-doped metaphosphate samples, one with a composition of 90 mol % $La(PO_3)_3$ and 10 mol % $Eu(PO_3)_3$, and the other with 50 mol % $La(PO_3)_3$ and 50 mol % $Eu(PO_3)_3$. These are labeled MP10 and MP50, respectively.

Permanent, laser-induced gratings were written in each sample at room temperature and the scattering efficiency of these gratings was measured using a HeNe laser for the read beam. The experimental configuration and procedures used were the same as those reported previously.[1] It was found that the laser-induced grating signal intensity of the MP50 sample was eight times stronger than that of the MP10 sample. This is consistent with the double-minimum potential-well model discussed below.

One other set of samples was investigated along this line, a lithium borate glass, LB15, with a composition of 75 mol % B_2O_3, 10 mol % Li_2O, and 15 mol % Eu_2O_3. It was possible to establish a permanent, laser-induced grating in this sample whereas in a previously investigated lithium borate sample, LB1, with only 1 mol % Eu_2O_3 no grating was created.

B. Effects of modifier ions

To study the effect of the network modifier ions of the host glass on the ability to produce gratings with high scattering efficiencies, five silicate glasses were obtained which had identical compositions except for one modifier ion. This modifier ion was changed through the series of alkali-metal ions Li, Na, K, Rb, and Cs. The exact compositions of these glasses are listed in Table I.

Permanent, laser-induced gratings were written in each of the five samples at room temperature and measurements were made of the scattering efficiencies using a HeNe laser for the read beam. The effective scattering efficiency, which is defined below, was found to decrease as the modifier ion was changed as Li→Na→K →Rb→Cs and the results are shown in Fig. 1 where the experimental values of the effective scattering efficiency are plotted versus the mass of the alkali-metal modifier ion. The solid line represents the best fit to the data using the theoretical treatment discussed in Sec. III.

TABLE I. Composition of silicate glass samples investigated. (Notation discussed in text.)

Sample	Sample composition (mol %)		
	Network former	Network modifier	Eu content
LS5	70 SiO$_2$	15 Li$_2$O	5 Eu$_2$O$_3$
		5 BaO	
		5 ZnO	
NS5	70 SiO$_2$	15 Na$_2$O	5 Eu$_2$O$_3$
		5 BaO	
		5 ZnO	
KS5	70 SiO$_2$	15 K$_2$O	5 Eu$_2$O$_3$
		5 BaO	
		5 ZnO	
RS5	70 SiO$_2$	15 Rb$_2$O	5 Eu$_2$O$_3$
		5 BaO	
		5 ZnO	
CS5	70 SiO$_2$	15 Cs$_2$O	5 Eu$_2$O$_3$
		5 BaO	
		5 ZnO	

C. Fluoride glasses

Along with the other samples investigated a new fluoride glass was acquired, CLAP5, with a composition of 36.1 mol % PbF$_2$, 26.1 mol % CdF$_2$, 27.1 mol % AlF$_3$, 4.7 mol % LiF, and 5.0 mol % EuF$_3$. No permanent grating was observed in this sample. This is the same result as obtained previously with other fluoride glasses.[1,3]

The lack of permanent grating formation in fluoride-glass hosts is consistent with the fact that Eu^{3+}-doped fluoride glasses have been shown[3] to exhibit a significant amount of radiative emission from the ^5D_J levels above $^5D_0$. This results in fewer ions relaxing nonradiatively from the $^5D_2$ and $^5D_1$ levels to the $^5D_0$ metastable state

leading to a smaller number of high-energy "phonons" being available. Since it is these high-energy local mode vibrations which are responsible for the formation of a permanent, laser-induced grating, no grating will be produced in these glasses.

In contrast, it was found that in a fluorophosphate glass, (FP, Schott FK-54), with 5 mol % EuF$_3$, it was possible to produce a permanent, laser-induced grating. This implies that the fluorophosphate glass contains enough of the characteristics of the phosphate glasses to allow formation of the permanent grating.

D. Temperature dependence of scattering efficiency

The temperature dependence of the laser-induced grating signal intensity in an EP sample was measured at temperatures above room temperature and the results were reported previously.[1] This section reports the results of measurements of the laser-induced grating signal intensity at temperatures below room temperature. To obtain the data the sample was mounted in a cryogenic refrigerator and the temperature was lowered to the desired level. Then a permanent grating was written and the scattering efficiency measured. This procedure was repeated at each temperature of interest. The laser-induced grating signal intensity is plotted versus temperature in Fig. 2.

As can be seen from the results, the trend toward higher laser-induced grating signal intensities continues at lower temperatures. However, there is a change in the slope between high and low temperatures. The solid lines in Fig. 2 describe an exponential temperature variation of the form

$$I = I_0 \exp\left[\frac{\Delta}{k_B T}\right], \tag{1}$$

where Δ is the activation energy. The values obtained for
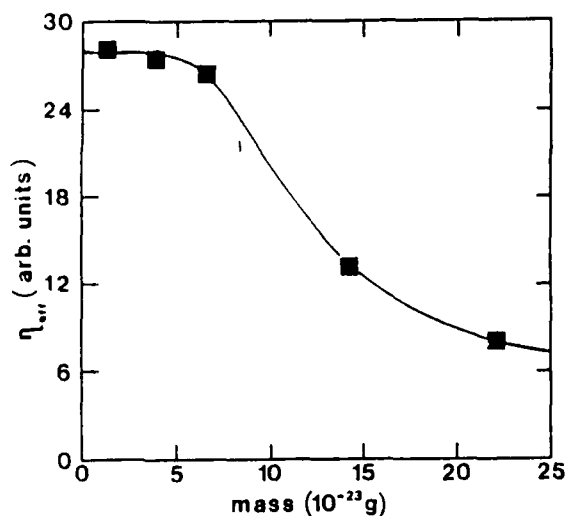

FIG. 1. Scattering efficiency of the samples listed in Table I as a function of the mass of the alkali-metal ion. ■, experimental points; ——, theoretical points.
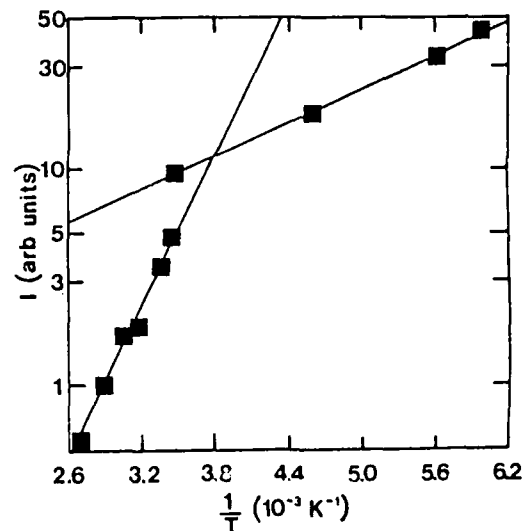

FIG. 2. Intensity of signal beam of the EP sample as a function of temperature.

Δ in the high-temperature and low-temperature regions are 2219 and 189.6 cm^{-1}, respectively.

III. THEORETICAL MODEL

In the double-minimum potential-well model the network former and network modifier ions of the glass host can arrange themselves in two possible configurations in the local environment of the Eu^{3+} ion. Thus these ions or groups of these ions have available to them two mutually accessible equilibrium positions and move in a potential of the form shown in Fig. 3. In this model it is assumed that the index of refraction depends on which configuration is present. Thus the total index of refraction of the material will be of the form

$$n = n_1 N_I + n_{II} N_{II} , \tag{2}$$

where $N_{I (II)}$ is the population of well I (II) and $n_{I (II)}$ is the index of refraction per ion populating the well. When the laser beam is turned on the population of the wells will display a time dependence of the form

$$\frac{dN_I(t)}{dt} = -p_I N_I(t) + p_{II} N_{II}(t) , \tag{3}$$

$$\frac{dN_{II}(t)}{dt} = p_I N_I(t) - p_{II} N_{II}(t) , \tag{4}$$

where $p_{I (II)}$ is the jump frequency and is the probability per unit time that the ion will have enough energy to jump from well I (II) to well II (I). In these experiments the system is allowed to reach equilibrium before measurements are taken. Thus the population of each well can be taken as constant and Eqs. (3) and (4) give the ratio of the populations of the two wells as

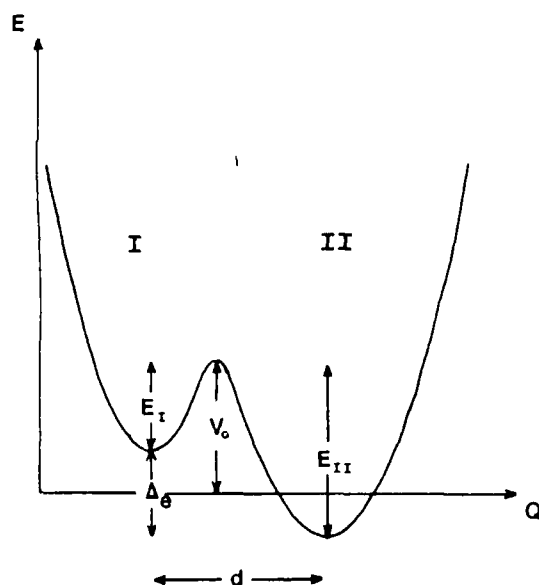$$\frac{N_I(\infty)}{N_{II}(\infty)} = \frac{p_{II}}{p_I} , \tag{5}$$

FIG. 3. Model two-level system.

where $p_{I,II}$ is given by[4]

$$p_{I,II} = v_{I,II} \exp\left[-\frac{E_{I,II}}{k_B T}\right] . \tag{6}$$

k_B is Boltzmann's constant and $v_{I,II}$ is the attack frequency which is the number of attempts the ion makes at surmounting the barrier of height $E_{I,II}$. Equations (5) and (6) lead to the thermal equilibrium condition

$$\frac{N_I(\infty)}{N_{II}(\infty)} = \frac{v_{II}}{v_I} \exp\left[-\frac{\Delta_e}{k_B T}\right] , \tag{7}$$

where $\Delta_e = E_{II} - E_I$. The equations derived so far are completely general and are valid for single-beam or crossed-beam experiments.

For crossed beams the intensity of the laser-induced grating signal is given by[5]

$$I \propto |n_p - n_v|^2 , \tag{8}$$

where n_p and n_v refer to the index of refraction of the peak and valley regions of the laser-induced grating with

$$n_p = n_I N_{Ip}(\infty) + n_{II} N_{IIp}(\infty) , \tag{9}$$

$$n_v = n_I N_{Iv}(\infty) . \tag{10}$$

The p and v subscripts refer to the peak and valley regions of the laser-induced grating whereas the I and II subscripts refer to the potential well occupied. In arriving at Eq. (10) it is assumed that the ions in the valley region of the grating remain in well I for all times. These equations lead to the following expression for the laser-induced grating signal intensity:

$$I \propto |N_{IIp}(\infty)\Delta n_{II-I}|^2 , \tag{11}$$

where $\Delta n_{II-I} \equiv n_{II} - n_I$. By using the thermal equilibrium condition and the fact that the total population of the wells must remain constant, the laser-induced grating signal intensity can be written as

$$I \propto \frac{N_I^2(0)|\Delta n_{II-I}|^2}{\left[1 + \frac{v_{II}}{v_I} \exp\left[\frac{-\Delta_e}{k_B T}\right]\right]^2} , \tag{12}$$

where $N_I(0)$ is defined as $N_{Ip}(0) = N_{Iv}(0) \equiv N_I(0)$.

This model can be used to interpret the observed changes in laser-induced grating signal intensities. For the MP50 sample and the MP10 sample the only difference will be in the initial population of configuration I. The ratio of the laser-induced grating signal intensities will be given by

$$\frac{I_{50}}{I_{10}} \propto \left[\frac{N_I(0)_{50}}{N_I(0)_{10}}\right]^2 . \tag{13}$$

This ratio of the squares of the initial populations was calculated using the Eu^{3+} concentration and the size of the peak region of the grating and was found to be 56.33. This number is larger than the measured ratio of eight, however, taking into consideration the simplicity of the model which does not include any saturation effects

which have been seen in power dependence measurements,[1] the model does a fairly good job in predicting the relative change in laser-induced grating signal intensities with a change in Eu^{3+} concentration.

This model can also be used to explain the results shown in Fig. 1. Since the only component of these glasses which has changed is the alkali-metal ion and it is seen that the effective scattering efficiency varies as the mass of this alkali-metal ion, this alkali-metal ion can be taken as the ion that is moving to provide the double-equilibrium configuration surrounding the Eu^{3+} ion. In Eq. (12), $N_I(0)$, which is the initial population of well I, will depend on the size of the peak or valley regions of the laser-induced grating. Therefore, the effective scattering efficiency is defined as

$$\eta_{\text{eff}} = \frac{I}{N_I^2(0)} \propto \frac{|\Delta n_{II-I}|^2}{\left[1 + \frac{\nu_{II}}{\nu_I} \exp\left[\frac{-\Delta_e}{k_B T}\right]\right]^2} . \tag{14}$$

The attack frequency $\nu_{I,II}$ is proportional to the mass of the ion in the well and can be expressed as

$$\nu_{I,II} = \left[\frac{k_{I,II}}{m}\right]^{1/2} , \tag{15}$$

where $k_{I,II}$ is the force constant of well I,II, respectively, and m is the mass of the ion populating the well. Δn_{II-I} is the change in refractive index per ion and is treated as an adjustable parameter. The term Δ_e which is the difference in the minima of the potential wells can be expressed more specifically using the mathematical formalism developed to describe a double-minimum potential well.[6]

Basis states $|\phi_1\rangle$ and $|\phi_2\rangle$ are chosen which are ground states for the appropriate single-well potentials. These basis states are eigenstates of the Hamiltonian of the unperturbed system H_0 with eigenvalues E_1 and E_2,

$$H_0|\phi_1\rangle = E_1|\phi_1\rangle , \tag{16}$$

$$H_0|\phi_2\rangle = E_2|\phi_2\rangle . \tag{17}$$

Upon applying a perturbation W which couples $|\phi_1\rangle$ and $|\phi_2\rangle$ the Hamiltonian matrix will become

$$(H) = \begin{bmatrix} E_1 + \langle\phi_1|W|\phi_1\rangle & \langle\phi_1|H|\phi_2\rangle \\ \langle\phi_2|H|\phi_1\rangle & E_2 + \langle\phi_2|W|\phi_2\rangle \end{bmatrix} . \tag{18}$$

To a good approximation $\langle\phi_i|W|\phi_i\rangle \ll E_i$. Defining the zero of energy to be midway between E_1 and E_2 the Hamiltonian matrix will become

$$(H) = \frac{1}{2} \begin{bmatrix} \Delta_e & \Delta_0 \\ \Delta_0 & -\Delta_e \end{bmatrix} , \tag{19}$$

where Δ_0 is defined as

$$\Delta_0 = 2\langle\phi_1|H|\phi_2\rangle . \tag{20}$$

$\Delta_0/2$ is the coupling energy and is the difference between the two lowest symmetric states. The solution for the coupling energy is derived in a number of quantum mechanics text books and is given by[7]

$$\Delta_0 = \hbar\omega_0 \exp\left[-d\left[\frac{2mV_0}{\hbar^2}\right]^{1/2}\right] , \tag{21}$$

where $\hbar\omega_0$ is an energy roughly equal to the zero-point energy and will vary as $1/\sqrt{m}$. For this reason we can write

$$\Delta_0 = \hbar\left[\frac{k}{m}\right]^{1/2} \exp\left[-d\left[\frac{2mV_0}{\hbar^2}\right]^{1/2}\right] , \tag{22}$$

where k is the force constant for the initial configuration.

The coupling energy can be related to the asymmetry by[8]

$$\tan\theta = \frac{\Delta_0}{\Delta_e} , \tag{23}$$

where θ is a measure of the mixing of the original eigenstates due to the perturbation. Combining Eqs. (22) and (23) gives

$$\Delta_e = \frac{\hbar}{\tan\theta}\left[\frac{k}{m}\right]^{1/2} \exp\left[-d\left[\frac{2mV_0}{\hbar^2}\right]^{1/2}\right] . \tag{24}$$

Inserting this into Eq. (14), the effective scattering efficiency becomes

$$\eta_{\text{eff}} \propto \frac{|\Delta n_{II-I}|^2}{\left[1 + \frac{\nu_{II}}{\nu_I} \exp\left[\frac{-\hbar}{k_B T \tan\theta}\left[\frac{k}{m}\right]^{1/2} \exp\left[-d\left[\frac{2mV_0}{\hbar^2}\right]^{1/2}\right]\right]\right]^2} . \tag{25}$$

Equation (25) was fitted to the experimental values of the effective scattering efficiency with $|\Delta n_{II-I}|^2$, ν_{II}/ν_I, $\hbar\sqrt{k}/k_B T \tan\theta$, and $d(2V_0/\hbar^2)^{1/2}$ treated as adjustable parameters. The best fit to the data is the solid line plotted in Fig. 1 where the following values were found for the adjustable parameters:

$$|\Delta n_{II-I}|^2 = 2.787 \times 10^{-37} ,$$

$$\frac{v_{II}}{v_I} = 1.329 ,$$

$$\frac{\hbar\sqrt{k}}{k_B T \tan\theta} = 2.25 \times 10^{10} g^{1/2} ,$$

$$d\left[\frac{2V_0}{\hbar^2}\right]^{1/2} = 2.39 \times 10^{11} g^{-1/2} .$$

It is seen that as an ion moves from one potential well to the other the index of refraction changes by 5.279×10^{-19}. The number of ions that accumulate in well II is of the order of 1×10^{15}. This gives a total change in the index of refraction of 5.279×10^{-3}. This number is of a similar order of magnitude to that found in other experiments.[9]

From the ratio of the attack frequencies the relationship between the force constants of the individual well can be found. From Eq. (15) it is seen that

$$\frac{v_{II}}{v_I} = \left[\frac{k_{II}}{k_I}\right]^{1/2} . \tag{26}$$

It is seen that the force constant for well II; k_{II}, is 1.329 times larger than that for well I, k_I.

It is also possible to approximate the distance between the two wells, d, using the last parameter. From Fig. 3 it is seen that V_0 must be as large as $\Delta_e/2$. Taking V_0 to range from 3000 cm^{-1} for LS5 to 45 cm^{-1} for CS5 leads to values of d from 0.023 to 0.189 Å, respectively. It should be remembered that this model has considered only the alkali-metal ion to be the source of the double-minimum potential well. There are realistically many ions involved and the small values for d suggest that even though individual ions may move over large distances, the net effect on the configuration coordinate is minimal in moving between equilibrium configurations.

From the final two adjustable parameters it is possible to calculate Δ_e for each sample using Eq. (24). These values are listed in Table II. It is observed that as the mass of the network modifier ion increases there is a dramatic change in the asymmetry. As this ion becomes heavier the difference in the minima of the two wells becomes less, implying that the change in the local environment of the Eu^{3+} ion becomes less pronounced as you go as Li$\rightarrow$Na$\rightarrow$K$\rightarrow$Rb$\rightarrow$Cs. It has been reported that in binary alkali silicate glasses the glass becomes more ordered as the radius of the alkali-metal ion increases.[10]

This same trend would be expected to continue in these glasses and as the glass becomes more ordered there would be less opportunity for multiple configurations leading to a smaller asymmetry between the two potential wells.

From Eq. (7) and the fact that the initial population of well I must equal the final population of well I and well II, it is possible to find the final populations of the two wells for each sample. These populations along with the ratio of the final population of well II to the initial population of well I are given in Table II. This ratio can be interpreted as the relative effectiveness of moving an ion initially in well I to well II. It is observed that in LS5, NS5, and KS5 almost 100% of the ions are driven into well II. In RS5 and CS5 a majority will end up in well II, however, it is a much smaller number than in the first three. In the heavier alkali-metal glasses it is harder to trap the ions in well II, implying the change in local environment of the Eu^{3+} ions is less than in the lighter alkali-metal glasses.

The inability to produce a laser-induced grating in fluoride glasses is also consistent with the double-minimum potential-well model which requires the presence of high-energy "phonons" to enable the ions to surmount the barrier and hop from well I to well II. With the absence of the high-energy local mode vibrations produced by radiationless relaxation of the Eu^{3+} ions the ions remain trapped in well I and no grating will be produced.

Finally, the temperature variation of the laser-induced grating signal intensity can be explained using the same model. Solving Eq. (7) for $N_{IIp}(\infty)$ and substituting directly into Eq. (11) leads to the following equation for the laser-induced grating signal intensity:

$$I \propto N_I^2(\infty) \Delta n_{II-I}^2 \left[\frac{v_I}{v_{II}}\right]^2 \exp\left[\frac{2\Delta_e}{k_B T}\right] . \tag{27}$$

Thus the measured activation energy is half the asymmetry. From Sec. II D the activation energy was measured to be 2219 cm^{-1} leading to an asymmetry of 1109.5 cm^{-1} for the high-temperature case. Even though this glass is different than the silicate glasses discussed above it is seen that the asymmetry is of the same order. The low-temperature activation energy was found to be 189.6 cm^{-1}, giving an asymmetry of 94.8 cm^{-1}. This suggests that as the temperature is lowered the minima of the two wells approach each other implying that the difference in energy of the ions in each well at low temperature is not

TABLE II. Summary of parameters.

Sample	Δ_e (cm^{-1})	$N_I(0)$	$N_I(\infty)$	$N_{II}(\infty)$	$\dfrac{N_{II}(\infty)}{N_I(0)}$
LS5	6068.38	1.041×10^{16}	0	1.041×10^{16}	1.00
NS5	1714.43	1.809×10^{16}	1.0×10^{13}	1.808×10^{16}	0.999
KS5	838.61	0.815×10^{16}	1.81×10^{14}	7.969×10^{15}	0.978
RS5	225.84	0.718×10^{16}	2.21×10^{15}	4.972×10^{15}	0.692
CS5	89.69	0.442×10^{16}	2.04×10^{15}	2.376×10^{15}	0.538

as great as at high temperature. This leads to the conclusion that at low temperature the local structure around each Eu^{3+} ion is close to the same in each configuration. This seems to be reasonable since at low temperature you would expect the structure to resist changes to a new configuration whereas at high temperatures the changes are more likely.

IV. DISCUSSION AND CONCLUSIONS

The double-minimum potential-well model used to describe the formation of the permanent, laser-induced grating agrees well with experimental results. It also provides some insight into the physical processes involved in the formation and erasure of these gratings. However, caution must be used in the interpretation of the physical parameters since a simple model is being used to describe a complex and poorly understood physical system.

The Eu^{3+} ions play a major role by providing the high-energy local mode phonons required to produce a structural modification of the glass host. The strength of the grating which can be produced is proportional to the concentration of Eu^{3+} ions, however, at high Eu^{3+} concentrations saturation effects occur.

The structure of the glass host in the local environment of the Eu^{3+} ions is also important to the formation of the grating. By changing one of the network modifier ions, variations in the laser-induced grating signal intensity can be produced.

As a simple model consider the glass to consist of point masses connected by springs. These point masses have available to them two equilibrium configurations which result from a change in position or a change in the force constants of the springs to which they are attached. Independent measurements have shown the elastic constants of the glasses to decrease from LS5 to CS5.[11] This implies that the two equilibrium configurations will be more stable in the lighter alkali-metal glasses than in the heavier ones. This will result in a larger value of $N_{11}(\infty)/N_1(0)$ in the lighter alkali-metal glasses than in the heavier alkali-metal glasses and is what is observed in Table II.

Stronger elastic constants also suggest there will be less displacement of the ions in the lighter alkali-metal glasses. This is exactly what was calculated in Sec. III where it was found that d ranged from 0.023 Å for LS5 to 0.189 Å for CS5. Also in Sec. III it was discovered that the ratio of k_{11} to k_1 was 1.329. Since k_1 decreases from LS5 to CS5, $\Delta k = k_{11} - k_1$ will also decrease from the lighter to the heavier alkali-metal-ion glasses. This suggests that Δ_e should be largest in LS5 and decrease to its smallest value in CS5. However, the actual physical displacement of the ions increases from LS5 to CS5 and suggests Δ_e should increase from LS5 to CS5. In order to form a permanent, laser-induced grating whose signal intensity decreases for LS5 to CS5 as seen in Fig. 1, Δ_e must decrease from LS5 to CS5. Therefore, the change in force constants must dominate over the change in position.

Measurements of the temperature dependence of the laser-induced grating signal intensity provides a direct means of obtaining the asymmetry and verifying the two-level-system model. For the glasses investigated in this paper the asymmetries, as found by the two methods, were of the same order of magnitude. Lowering the sample temperature results in a decrease in the asymmetry suggesting that as the temperature decreases the glasses begin to resist changes to their structure.

All of the above results are important when considering these glasses for potential optical devices. Even though much more is understood concerning the formation of the grating, the exact structure of the glass host is still unclear. Knowledge of this structure will lead to a better understanding of the processes involved.

*Permanent address: S.A. Laser Application Industrielle et Commerciale, Recherches et Systems, Z.I. Sainte Elisabeth, Montceau 71300, France.

[1] F. M. Durville, E. G. Behrens, and R. C. Powell, Phys. Rev. B 34, 4213 (1986); E. G. Behrens, F. M. Durville, and R. C. Powell, Opt. Lett. 11, 653 (1986).

[2] R. C. Powell, F. M. Durville, E. G. Behrens, and G. S. Dixon, J. Lumin. 40-41, 68 (1988).

[3] F. M. Durville, E. G. Behrens, and R. C. Powell, Phys. Rev. B 35, 4109 (1987).

[4] C. Kittel, in Introduction to Solid State Physics (Wiley, New York, 1976).

[5] H. Kogelnik, Bell Syst. Tech. J. 48, 2909 (1969).

[6] W. A. Phillips, in Amorphous Solids. Low Temperature Properties, Vol. 24 of Topics in Current Physics, edited by W. A. Phillips (Springer-Verlag, Berlin, 1981), p. 1.

[7] D. Park, in Introduction to the Quantum Theory (McGraw-Hill, New York, 1964), p. 100.

[8] W. A. Phillips, J. Low-Temp. Phys. 4, 351 (1972).

[9] F. M. Durville and R. C. Powell, J. Opt. Soc. Am. Ser. B 7, 1934 (1987).

[10] S. A. Brawer and W. B. White, J. Chem. Phys. 63, 2421 (1975); S. Brawer, Phys. Rev. B 11, 3173 (1975).

[11] J. P. Wicksted and G. W. Gangwere (private communication).

Characteristics of laser-induced gratings in Pr^{3+}- and Eu^{3+}-doped silicate glasses

Edward G. Behrens and Richard C. Powell

Center for Laser Research, Oklahoma State University, Stillwater, Oklahoma 74078

Douglas H. Blackburn

National Institute of Standards and Technology, Gaithersburg, Maryland 20899

Four-wave mixing techniques are used to produce laser-induced gratings in Pr^{3+}-doped silicate glasses for the first time to our knowledge. The characteristics of the laser-induced grating are investigated and compared with those found in Eu^{3+}-doped silicate glasses. An attempt to form a laser-induced grating in an Er^{3+}-doped silicate glass was made. Under excitation conditions similar to those in previous experiments, no laser-induced grating could be produced. Differences between the samples are discussed in terms of high-energy phonons, which are emitted when the rare-earth ion relaxes nonradiatively. Temperature dependences of the laser-induced grating signal intensity are investigated in Eu^{3+}-doped silicate glasses, and the results are compared with theoretical predictions.

1. INTRODUCTION

Recently we employed four-wave mixing techniques to produce superimposed permanent and transient laser-induced gratings (LIG's) in a variety of Eu^{3+}-doped glasses.[1] Laser-induced holographic gratings of this type are of significant interest to technologies such as optical data processing, medical imaging, and fiber-optic communication, for which holographic information storage and retrieval are important. The glasses used to write LIG's in these experiments are common silicate and phosphate glasses. So far we have attempted to write LIG's in Eu^{3+}- and Nd^{3+}-doped glasses, with success being achieved only in Eu^{3+}-doped samples.

In this paper we report the results obtained from attempts to write LIG's in Pr^{3+}- and Er^{3+}-doped silicate glasses and extend our previous research on Eu^{3+}-doped silicate glasses to include measurements of the energies of grating formation. Grating formation was accomplished in the Pr^{3+} silicate glass, and various properties of the LIG in this sample are presented. No permanent gratings were observed in the Er^{3+}-doped sample.

The experimental configuration used to produce LIG's and measure their properties was described previously.[2] The output from a Spectra-Physics cw argon-ion laser is tuned to resonance with a preselected absorption transition of the rare-earth ion. The values of the argon-ion laser wavelengths used in these experiments are 488.0 nm for the Pr^{3+}- and Er^{3+}-doped samples and 465.8 nm for the Eu^{3+}-doped sample. This laser beam is split into two write beams, which are focused to a 500-μm beam waist and crossed inside the sample. The path lengths of the two write beams are maintained equal to within the coherence length of the laser. In the region in which the write beams overlap, a sinusoidal interference pattern is created. The interference pattern from the crossed write beams

creates a change in the optical properties of the sample with the same shape. This is the LIG whose wavelength, Λ, depends on the write-beam wavelength, λ_w, and on the write-beam crossing angle, 2θ, through the condition

$$\Lambda = n\lambda_w/2 \sin 2\theta. \tag{1}$$

The LIG is probed by a third beam with wavelength λ_p, which scatters off the grating. In these experiments a He–Ne laser is used as a probe beam. The maximum scattered signal beam is obtained at the Bragg condition for the incident probe beam:

$$n\lambda_p = 2\Lambda \sin \Phi, \tag{2}$$

where Φ is the Bragg angle. A mirror is used to pick off the signal beam and direct it through a cut-off filter to eliminate sample fluorescence. A photomultiplier tube is then used to detect the signal and the output processed by a PAR-EG&G boxcar averager, and a hard copy is recorded. To separate the permanent and the transient portions of the LIG a chopper is inserted between the write beams and the sample. When the write beams are chopped off, the permanent portion of the LIG is the only signal visible. When the write beams are on, the visible signal consists of a superposition of the permanent and transient portions of the LIG signal. Thus the permanent and transient portions of the LIG signal can be separated and measured. For measurements of the erase time of the permanent LIG a single beam, tuned to the same absorption transition as used to write the grating, illuminates the grating region. Owing to the length of the erase time the output from the photomultiplier tube is sent directly to a strip-chart recorder. To measure the temperature dependence of the permanent LIG the sample is mounted in a resistance-heated furnace that can control the temperature between 300 and 775 K.

2. EXPERIMENTAL RESULTS

Permanent changes in the refractive index of a material can be induced by lasers as a result of several physical processes. However, most of these processes are not consistent with the experimental observations reported previously. For example, the photoionization of defects can cause a change in the refractive index.[3-5] However, the energy-level scheme for Eu^{3+} in these glass hosts is not compatible with an ionization transition at the laser wavelength and powers used in these experiments. Also, no spectral evidence was observed for the presence of Eu ions in valence states other than trivalent. In addition, the fact that optical erasure occurs only when Eu^{3+} ions are resonantly excited is not consistent with the photoionization mechanism.
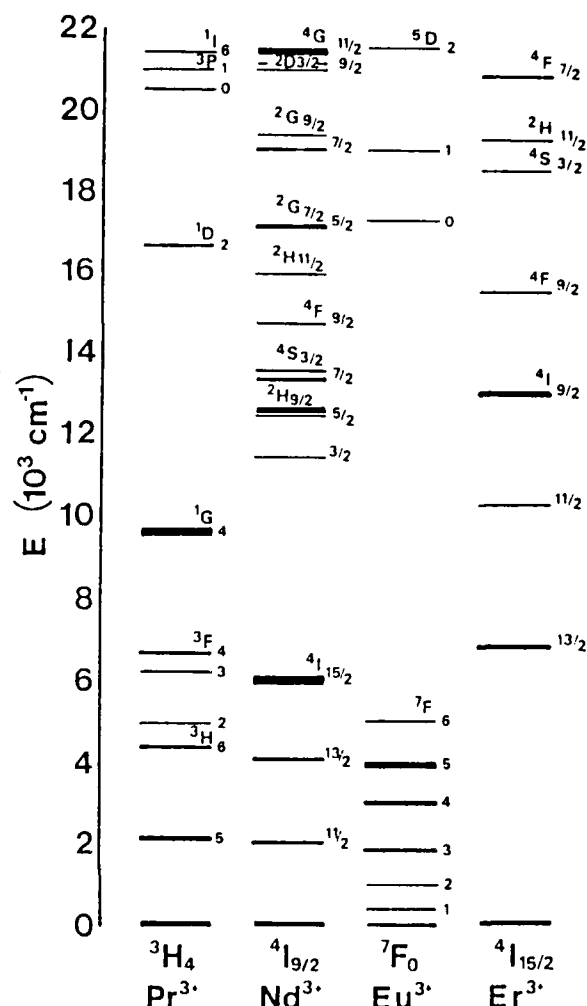
Thermal processes can directly produce refractive-index changes and laser-induced stress-optic changes. Among these changes are permanent effects that have been seen in rare-earth-doped glasses.[6,7] However, these effects occur at higher laser powers than those used in our experiments. For the laser powers used in these experiments, the thermal properties of the glass hosts produce a rise in the temperature of the sample of only a few degrees, which is too small to give a measurable effect.

The mechanism that is consistent with the observed results is a change in the local structure of the glass caused by the vibrational energy released during the radiationless relaxation of the rare-earth ions. The radiationless relaxation transitions of rare-earth ions in glasses have been shown to be multiphonon emission processes, each of which generates several high-energy phonons of the order of 1000 cm^{-1}.[8] Here the term "phonon" is used to refer to any vibrational mode of the host material. Figure 1 displays the relevant energy levels of several trivalent rare-earth ions. Since these phonons are generated by the rare-earth ions and the thermal diffusion in glasses is slow, they remain localized, thus creating a high level of nonthermalized vibrational energy around each ion. This can produce a local effective temperature that is extremely high, depending on the energy gap that is being crossed in the relaxation process. For the excitation conditions in the Eu^{3+}-doped-glass experiments, effective local temperatures of several thousand kelvins can be produced. This is easily hot enough to permit ionic motion over short ranges and thus produce a local structural modification of the host glass. The energy associated with this local temperature rise[1] is consistent with the measured activation energies for the formation and erasure of permanent gratings. In addition, the time scale of several minutes for grating formation and erasure is consistent with the time scale for producing structural changes.

The rare-earth ion plays a key role in the formation and erasure of permanent LIG's in these glasses since the ions are the source of the high-energy phonons. To study this role we conducted experiments on silicate-glass samples doped with Pr^{3+}, Er^{3+}, and Eu^{3+}.

A. LIG Characteristics in Pr^{3+}-Doped Glass

The characteristics of the LIG in the Pr^{3+} silicate glass (70 SiO_2, 15 Na_2O, 5 ZnO, 5 BaO, and 5 Pr_2O_3 in units of mol. %) were investigated as functions of the laser power and write-beam crossing angle. The same qualitative be-

Fig. 1. Partial energy-level diagram for several trivalent rare-earth ions.

havior was observed in the Pr^{3+}-doped sample as was seen in the Eu^{3+}-doped glasses.[1,2] When the Pr^{3+}-doped sample was illuminated by the crossed write beams tuned to resonance with the $^3H_4-^3P_0$ absorption transition, a small signal was observed immediately. This was followed by a gradual buildup of signal intensity. The time required to reach the maximum LIG signal intensity is of the order of tens of seconds, with the exact time depending on the laser power. If the laser write beams are not tuned in resonance with the $^3H_4-^3P_0$ absorption transition, no signal is observed. When the write beams are blocked, the LIG signal intensity rapidly decreases. However, it decreases not back to the baseline but rather to a value of approximately 90% of the maximum LIG signal, where it remains indefinitely. The remaining portion is referred to as the permanent signal and can be erased by illuminating the grating with a single laser beam tuned to resonance with the same Pr^{3+} absorption transition used to write the grating. It should be noted that no erasure occurs if the single beam is not tuned to the $^3H_4-^3P_0$ absorption transition. The erase time is of the order of tens of seconds, with the exact time depending on laser power.

This permanent signal can also be erased thermally. The important thing to note is that the build-up and erase times in the Pr^{3+}-doped glass are all of the order of seconds, whereas in the Eu^{3+}-doped glass these time scales were of the order of tens of minutes.

The lifetime of the transient part of the LIG was measured to be 200 μsec, which is approximately the same as the fluorescence lifetime of the $^1D_2$ level of the Pr^{3+} ion, which was measured to be 194 μsec. For a population grating the signal intensity is proportional to the square of the modulation of the index of refraction,[9] Δn:

$$I_S = |n|^2. \tag{3}$$

Δn will decay with the decay of the excited-state population, leading to a time dependence of the signal intensity of

$$I_S(t) = I_0 \exp(-2t/\tau_f), \tag{4}$$

where τ_f is the fluorescence lifetime. Thus the grating decays with a lifetime of half of the fluorescence lifetime. However, in these samples there is an interference effect between the permanent and transient LIG's that leads to a signal intensity given by[1,2]

$$I_S = |\Delta n_T|^2 \exp - (2t/\tau) + 2|\Delta n_T||\Delta n_P| \exp - (t/\tau)$$
$$+ |\Delta n_P|^2, \tag{5}$$

where Δn_T and Δn_P are the changes in the index of refraction due to the transient and permanent gratings, respectively, and $1/\tau$ is the fluorescence decay rate. The first term is much smaller than the last two and can be neglected. Thus the lifetime of the transient grating will be equal to the fluorescence lifetime of the excited state responsible for the population grating. Therefore the transient grating is associated with an excited-state population grating that is due to the difference in susceptibility of the ions in the $^3H_4$ ground state and the $^1D_2$ metastable state.

Figure 2 displays the normalized intensities of the permanent and transient LIG signals as a function of the total write-beam crossing angle, 2θ. It is seen that both the transient and permanent signals have the strongest intensity at the smallest write-beam crossing angle, which corresponds to the largest value of grating spacing. As the write-beam crossing angle is increased, and the grating spacing decreases, the intensities of both the permanent and the transient signals decrease. This is typical behavior for FWM signals, with the exact form depending on the coupling mechanism for the beams.[10]

The LIG signal intensity, build-up times, and erase times were also measured for different values of the total power of the laser write beams. The absolute value of the scattering efficiency, which is defined as

$$\eta = P_S/P_P, \tag{6}$$

where P_S is the power of the signal beam and P_P is the power of the probe beam, was measured to be 1.33×10^{-4}. This is of similar magnitude to values consistently found in Eu^{3+}-doped samples.

Figure 3 shows the normalized intensity of the permanent and transient signals as a function of the laser power. As in the case of the Eu^{3+}-doped samples the transient
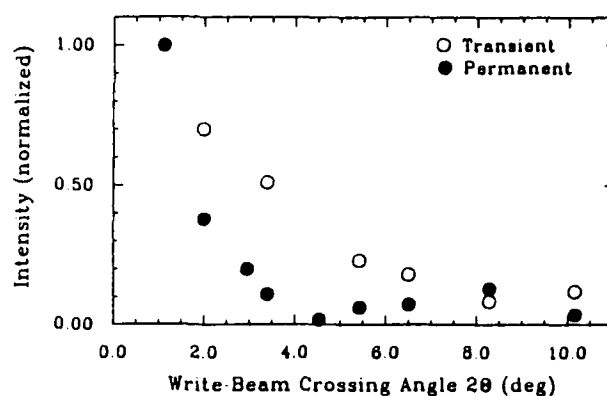

Fig. 2. LIG signal intensity as a function of write-beam crossing angle 2θ in the Pr^{3+} sample.
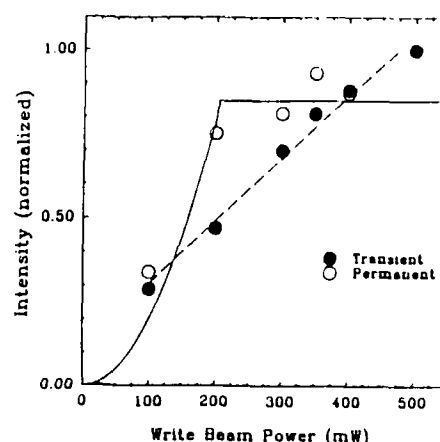

Fig. 3. LIG signal intensity as a function of the total laser write-beam power in the Pr^{3+} sample. The solid and dashed lines are discussed in the text.

signal intensity varies linearly with laser power throughout the range of write-beam powers available in these experiments. The permanent signal displays nonlinear behavior up to approximately 200 mW, where saturation occurs. Equation (5) predicts the power dependence of the LIG signal intensity. Since Δn_T and Δn_P depend on the difference in population between the ground and excited states, they will vary linearly with laser power. The permanent part of the LIG signal intensity, which is proportional to $|\Delta n_P|^2$, is predicted to display a quadratic power dependence. This is demonstrated by the solid curve in Fig. 3, where the expression ax^2 was fitted to the data below 200 mW. Above 200 mW saturation of the LIG occurs, which is represented by the solid horizontal line. Since $\Delta n_T \ll \Delta n_P$, Δn_T can be neglected in the middle term of Eq. (5), leaving a transient LIG signal intensity proportional to Δn_P and displaying a linear type behavior as observed. The dashed line represents a linear-regression fit to the transient grating values.

The measurements of the transient and permanent signal intensities took place after the permanent signal had reached its maximum value. Thus the variation of the

transient grating signal intensity is measured in the presence of a strong permanent grating. The observed saturation in the permanent signal shows that there is a limit to the structural modification of the glass.

The build-up and erase times of the permanent grating as a function of laser write-beam power are displayed in Fig. 4. It is seen that as the laser power is increased both the erase time and the build-up time decrease. The erase time decreases linearly as the laser power is increased, but the build-up time decreases almost exponentially with increasing laser power. The general trend in both cases of decreasing times with increasing power is consistent with the model proposed previously and is discussed further below.

The final measurement performed on the Pr^{3+} sample was of the effect of temperature on the formation of the permanent LIG. The sample was placed in a resistance-heated furnace and the temperature increased to the desired level. A LIG was then written and the scattering intensity of the permanent portion measured. This procedure was repeated as the temperature was increased from 300 to approximately 600 K. Figure 5 shows the results of these measurements. These results display a behavior that is nonexponential. There seems to be an inflection at approximately 415 K. Fitting the regions above and below 415 K separately with single exponential equations leads to the solid lines displayed in Fig. 5. The activation energies measured for the high- and low-temperature regions are 2.825×10^3 and 9.28×10^2 cm^{-1}, respectively. This behavior is also seen in the Eu^{3+}-doped glasses and is discussed in more detail below.

B. Fluorescence Characteristics of Pr^{3+}- and Er^{3+}-Doped Glasses

To characterize the relaxation process of the Pr^{3+} and Er^{3+} ions, which is important to the formation or lack of formation of the LIG, fluorescence spectra were measured. To form the permanent LIG in the Pr^{3+}-doped glass sample the Pr^{3+} ion is excited from the $^3H_4$ ground state to the $^3P_0$ excited state. Figure 6 shows the room-temperature fluorescence of the Pr^{3+}-doped glass. The fluorescence spectrum displays peaks at 540, 620, 645, 715, and 735 nm, which correspond to radiative transitions from the $^3P_0$ state to the $^3H_5$, $^3H_6$, $^3F_2$, $^3F_3$, and $^3F_4$ states, respec-

Fig. 5. Temperature dependence of LIG scattering intensity for Pr^{3+}-doped silicate glass. The solid lines are discussed in the text.
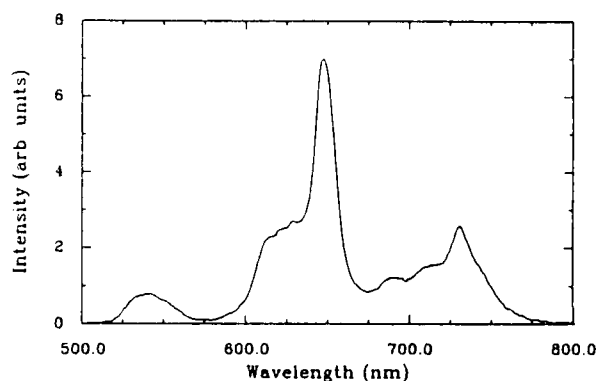
Fig. 6. Room-temperature fluorescence of the Pr^{3+}-doped glass sample after excitation into the $^3P_0$ excited state.

tively. These levels then relax nonradiatively to the ground state. There is also a peak at 690 nm, which corresponds to the $^1D_2-^3H_5$ transition. A transition from $^1D_2$ to $^3H_4$ should also be present at 605 nm; however, in this case it is buried in the shoulder of the $^3P_0-^3H_6$ transition. The nonradiative relaxation occurring in this sample produces phonons with energies of the order of 1000 cm^{-1} and will produce the structural modification needed to form the permanent LIG. The same type of relaxation behavior is observed in Eu^{3+}-doped glasses, which produce permanent LIG's.

In the case of a Nd^{3+}-doped glass sample (NdP_5O_{14}) the Nd^{3+} ion is excited from the $^4I_{9/2}$ ground state to the $^4G_{9/2}$ excited state. Relaxation occurs through the emission of phonons: however, in the Nd^{3+} ion the energy levels are much closer than in the Eu^{3+} or Pr^{3+} ions. Thus, when the Nd^{3+} ion relaxes, the phonons emitted are of much lower energy than those from Eu^{3+} or Pr^{3+}, and as a result no permanent LIG is formed.

The silicate glass doped with Er^{3+} (70 SiO_2, 15 Na_2O, 5 ZnO, 5 BaO, and 5 Er_2O_3 in units of mol. %) is an interesting case. From Fig. 1 it is seen that overall the spacing between the energy levels is much greater than in Nd^{3+}
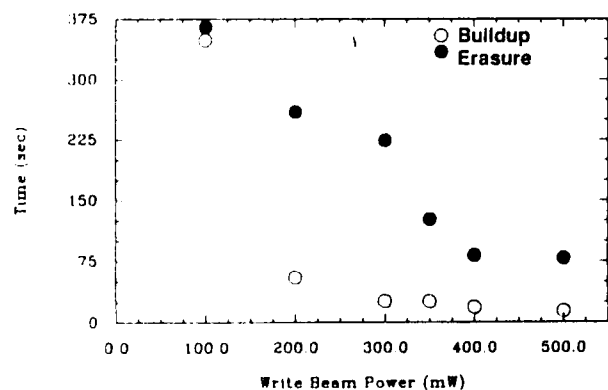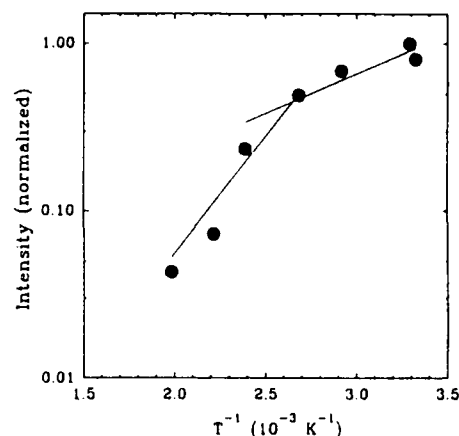

Fig. 4. Build-up time and erase time of the permanent LIG as a function of the total laser write-beam power in the Pr^{3+} sample.

but not quite so large as in Eu^{3+} or Pr^{3+}. Write-beam wavelengths of 4880 and 5145 Å, which correspond to absorption transitions of the Er^{3+} ion from the $^4I_{15/2}$ ground state to the $^4F_{7/2}$ and $^2H_{11/2}$ excited states, respectively, were utilized in an attempt to create a permanent LIG in this sample. Under both excitation conditions no grating was observed. The explanation for this is found in the fluorescence spectrum of the Er^{3+} sample obtained with the 4880-Å wavelength as the excitation source and is displayed in Fig. 7. A large peak is observed near 540 nm, which corresponds to a radiative transition from the $^4S_{3/2}$ excited state to the $^4I_{15/2}$ ground state. This shows that the Er^{3+} ion relaxes nonradiatively from the $^4F_{7/2}$ level down to the $^4S_{3/2}$ level by the emission of phonons before relaxing radiatively to the ground state. These phonons have small energies, comparable with those in the Nd^{3+} sample, which are insufficient to create the changes necessary to produce a permanent LIG. Notice that there is a broad peak at 630 nm, which corresponds to a radiative transition from the $^4F_{9/2}$ excited state to the ground state. For the Er^{3+} ions to relax nonradiatively from the $^4S_{3/2}$ level to the $^4F_{9/2}$ level they must cross an energy gap comparable with those seen in the Eu^{3+} and Pr^{3+} samples, suggesting the existence of high-energy phonons. However, from the size of the fluorescence peak it appears that only a few of these phonons are available for the formation of the permanent LIG. No transient grating is observed in the Er^{3+}-doped sample. Since no permanent grating is present, only the first term in Eq. (5) survives. If a transient grating occurs it will have an intensity proportional to $|\Delta n_T|^2$. In the Eu^{3+}- and Pr^{3+}-doped samples no gratings associated with this term are observed. Therefore it is not surprising that no transient grating is seen in the Er^{3+}-doped sample.

These results confirm the previous conclusion that, to create the type of permanent LIG described here, it is necessary to have a high concentration of rare-earth ions that have a relatively large energy gap between excited electronic energy levels and that this gap should be crossed by radiationless relaxation.

C. Activation Energies for LIGs in Eu^{3+}-Doped Glasses

Previously a model was developed to describe the effect of the network modifier ions on the permanent LIG signal intensity in Eu^{3+}-doped alkali-metal silicate glasses.[11] The compositions of these glasses are listed in Table 1. One parameter predicted by this model was the activation energy for grating formation. To verify the predicted value, the temperature dependence of the scattering intensity was measured and is displayed in Fig. 8. The same procedure as reported for the Pr^{3+}-doped glass was used here. For the samples with the heavier modifier ions, KS5, RS5, and CS5, the intensity varies exponentially with temperature. This leads to the straight lines in Fig. 8(a) with a single slope on the semilog plot. However, as the mass of the modifier ion of the sample decreases, to NS5 and LS5, the intensity no longer displays single exponential behavior but rather has two regions with differing slopes. These are displayed, by the solid and dashed lines in Fig. 8(b). The intersection of the lines occurs at approximately 455 K for both samples. An identical type of behavior was observed in a Eu^{3+}-doped phosphate glass,
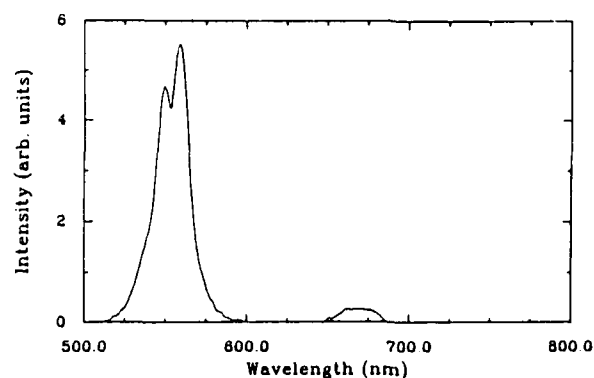

Fig. 7. Room-temperature fluorescence of the Er^{3+}-doped glass sample after excitation into the $^4F_{7/2}$ excited state.

Table 1. Composition of Eu^{3+}-Doped Alkali-Metal Glasses

Sample	Network Former	Network Modifier	Eu^{3+} Content
LS5	70.0 SiO_2	15.0 Li_2O 5.0 BaO 5.0 ZnO	5.0 Eu_2O_3
NS5	70.0 SiO_2	15.0 Na_2O 5.0 BaO 5.0 ZnO	5.0 Eu_2O_3
KS5	70.0 SiO_2	15.0 K_2O 5.0 BaO 5.0 ZnO	5.0 Eu_2O_3
RS5	70.0 SiO_2	15.0 Rb_2O 5.0 BaO 5.0 ZnO	5.0 Eu_2O_3
CS5	70.0 SiO_2	15.0 Cs_2O 5.0 BaO 5.0 ZnO	5.0 Eu_2O_3

where the temperature at the intersection of the slopes was 263 K.[11]

That a structural modification of the host is responsible for the permanent LIG suggests that there are two processes responsible for this modification in the rare-earth-doped glasses. Remember that this behavior was also seen in the Pr^{3+} sample. One process dominates at low temperature, and the other at high temperature. In the high-temperature region the temperature dependence of the intensity is controlled by the network-modifier ion of the host. This is displayed in Fig. 8 by the variation of the slopes in this region. In the low-temperature region the temperature dependence of the intensity must be controlled by a common element among the different rare-earth-doped samples, such as other network-former or network-modifier ions, in order to produce roughly the same activation energy for each sample. It would also appear that the temperature at which crossover occurs depends on the host glass.

Table 2 lists the measured activation energies, where ΔE_L and ΔE_H refer to these low- and high-temperature regions. Since the two-level system model was concerned only with the effect of the alkali-metal network modifier
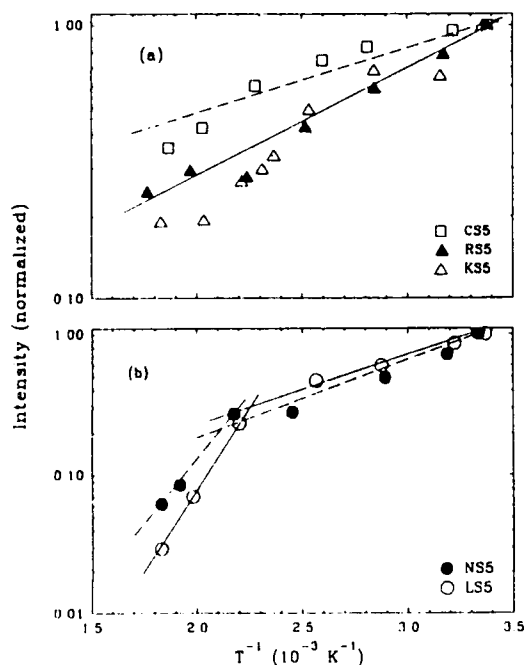
Fig. 8. Temperature dependence of LIG scattering intensity for Eu³⁺-doped samples: (a) dashed line, CS5; solid line, RS5; dotted line, KS5; (b) solid line, NS5; dashed line, LS5.

ion, only the high-temperature region will be discussed. More investigations need to be undertaken to determine the source of the low-temperature activation energy.

3. DISCUSSION AND CONCLUSIONS

The results obtained on the Pr^{3+}-doped silicate glass are consistent with the double-minima potential well model proposed previously.[1,2,11] In this model the possibility of two different structures of the glass host in the local environment of the rare-earth ion leads to double-minima potential wells for the rare-earth-ion electronic energy levels. It is assumed that the index of refraction is different for each well and that the total index of refraction of the material is $n = n_1 N_1 + n_2 N_2$, where n_1 and n_2 are the indices of refraction of the different wells and N_1 and N_2 are the populations of these wells. The ions move from well I to well II when they receive energy from the nonradiative relaxation of the rare-earth ion.

In Subsection 2.C measurements of the activation energy for grating formation, ΔE, were presented for Eu^{3+}-

doped alkali-metal glasses. These values can be compared with those predicted from the two-level system model proposed previously. In the two-level system model the LIG signal intensity is given by[11]

$$I = |N_{IIP}(\infty) \Delta n_{II-I}|^2, \qquad (7)$$

where $N_{IIP}(\infty)$ is the population of well II in the peak of the grating at long times and Δn_{II-I} is the difference in index of refraction between wells I and II. $N_{IIP}(\infty)$ can be expressed as

$$N_{IIP}(\infty) = N_{IP}(\infty) (\nu_I/\nu_{II}) \exp(\Delta_e/kT), \qquad (8)$$

where $N_{IP}(\infty)$ is the population of well I at long times, ν_I and ν_{II} are the attack frequencies of wells I and II, respectively, Δ_e is the asymmetry of the two-level system, k is Boltzmann's constant, and T is the temperature. This gives the temperature-dependent LIG signal intensity as

$$I = N_I^2(\infty) \Delta n^2_{II-I}(\nu_I/\nu_{II})^2 \exp(2\Delta_e/kT). \qquad (9)$$

For the measurements here the prefactors are[11] $\Delta n^2_{II-I} = 2.8 \times 10^{-37}$ and $(\nu_I/\nu_{II})^2 = 1.77$. $N^2_I(\infty)$ depends on the host and varies from 0 to 2.04×10^{15}. The values for the parameters of Eq. (9) were obtained previously by fitting the equation describing the effective scattering efficiency,

$$\eta_{eff} = |\Delta n_{II-I}|^2 (1 + (\nu_{II}/\nu_I) \exp\{[-\hbar(k/m)^{1/2}(k_B T \tan \theta)^{-1}]$$
$$\times \exp[-d(2mV_0/\hbar^2)^{1/2}]\})^{-2}, \quad (10)$$

to the experimental values of the effective scattering efficiency as a function of the network modifier ion mass. $|\Delta n_{II-I}|$, ν_{II}/ν_I, $\hbar k^{1/2}/k_B T \tan \theta$, and $d(2V_0/\hbar^2)$ were treated as adjustable parameters. Δ_e is related to the adjustable parameters through the equation

$$\Delta_e = (\hbar k^{1/2}/\tan \theta \ m^{1/2}) \exp[-d(2mV_0/\hbar^2)^{1/2}]. \quad (11)$$

However, the main concern is with the exponential term in Eq. (9). In order to relate this term to the experimental data we compared it with an Arrhenius-type behavior, $I = I_0 \exp(\Delta E/kT)$. From this it is seen that the measured value of the activation energy ΔE is equal to twice the asymmetry of the two-level system model Δ_e.

The values obtained for Δ_e for all the samples along with the measured activation energies found in Subsection 2.C are presented in Table 3. It is seen that the agreement among the values is quite good considering the simplicity of the model; all values are within an order of magnitude of one another. It should also be pointed out that the equation derived for the permanent LIG signal intensity is applicable to any rare-earth ion and depends only on the

Table 2. Activation Energies of Eu³⁺-Doped Alkali-Metal Glasses

Sample	ΔE_H ($\times 10^3$ cm⁻¹)	ΔE_L ($\times 10^2$ cm⁻¹)
LS5	3.87	8.16
NS5	3.02	7.93
KS5	0.89	0.89
RS5	0.62	0.62
CS5	0.47	0.47

Table 3. Activation Energies and Asymmetries of Eu³⁺-Doped Alkali-Metal Glasses

Sample	ΔE_H ($\times 10^3$ cm⁻¹)	$2\Delta_e$ ($\times 10^3$ cm⁻¹)
LS5	3.87	12.14
NS5	3.02	3.43
KS5	0.89	1.68
RS5	0.62	0.45
CS5	0.47	0.18

glass host. Therefore the activation energy from the Pr^{3+}-doped silicate glass should be the same as that in the NS5 sample. This activation energy for the Pr^{3+} sample was found to be 2.825×10^3 cm^{-1}, compared with 3.428×10^3 cm^{-1} for the NS5 sample, in excellent agreement with the two-level system model.

It is found that in the Pr^{3+}-doped glass the LIG build-up and erase times are faster than those found previously for Eu^{3+}-doped glasses. To compare the ability to form LIG's in the Pr^{3+}- and Eu^{3+}-doped glasses, a quantum efficiency for grating formation is defined as the fractional amount of refractive-index change created per phonon emitted. A theoretical expression for this is derived below.

The wavelengths used to write the LIG's are different in each sample. In the Pr^{3+}-doped sample an excitation wavelength of 488.0 nm was used, which had a power density of 62.5 W/cm^2 when focused inside the sample. The Eu^{3+}-doped sample was excited with a wavelength of 465.8 nm and a power density of 20 W/cm^2. The absorption coefficients were 5.4 cm^{-1} for the Pr^{3+}-doped sample and 3.78 cm^{-1} for the Eu^{3+}-doped sample. The number of photons absorbed per unit time can then be calculated for each sample. These are 1.53×10^{17} sec^{-1} for the Eu^{3+}-doped sample and 1.08×10^{18} sec^{-1} for the Pr^{3+}-doped sample. These values are far below those needed to produce a saturation of the absorption of the rare-earth ions in the interaction region.

To calculate the number of phonons produced for each rare-earth ion that is excited, several assumptions need to be made. First, it has been reported that in these types of silicate glass the highest-energy phonons available have energies of approximately 1000 cm^{-1}.[12] Thus the assumption is made that the nonradiative energy emitted when the rare-earth ion relaxes will be in the form of 1000 cm^{-1} phonons. The second assumption concerns the relaxation channel followed by the rare-earth ion. In the case of the Eu^{3+} ion, measurements have shown that no radiative relaxation occurs from the $^5D_2$ or $^5D_1$ levels.[12] Thus the Eu^{3+} ion, which is excited into the $^5D_2$ level, is assumed to relax nonradiatively to the $^5D_0$ metastable state. From this level the Eu^{3+} ion relaxes radiatively to the $^7F_1$ level. The final step occurs nonradiatively with the relaxation from the $^7F_1$ state to the $^7F_0$ ground state. The nonradiative relaxation mentioned in the above process generates approximately 4000 cm^{-1} of energy, which is emitted in the form of four high-energy phonons.

For the Pr^{3+} ion, which is excited into the $^3P_0$ state, fluorescence measurements show that the majority of the fluorescence occurs from the $^3P_0$–$^3F_2$ transition. Relaxation then occurs by nonradiative relaxation from the $^3F_2$ state to the $^3H_4$ ground state. Thus it is assumed that on average every ion produces an amount of nonradiative energy equivalent to the energy gap between these two states. The energy of this gap is approximately 5000 cm^{-1}, so that five high-energy phonons are produced for each Pr^{3+} ion excited.

Using the above assumptions, we found that there are 6.12×10^{17} phonons/sec produced in the Eu^{3+}-doped sample and 5.40×10^{18} phonons/sec produced in the Pr^{3+}-doped sample at these power levels.

The scattering efficiency for the two samples is 2.53×10^{-5} and 1.33×10^{-4} for the Eu^{3+}-doped sample and the Pr^{3+}-doped sample, respectively. The build-up time for

the Eu^{3+}-doped sample is 900 sec and for the Pr^{3+}-doped sample 60 sec. This gives a change in scattering efficiency per unit time of 2.81×10^{-8} sec^{-1} for the Eu^{3+}-doped sample and 2.22×10^{-6} sec^{-1} for the Pr^{3+}-doped sample. Defining a quantum efficiency for grating formation as the change is scattering efficiency per phonon,

$$\eta_{QE} = \Delta\eta/\Phi, \qquad (12)$$

where $\Delta\eta$ is the change is scattering efficiency per unit time and Φ is the number of phonons emitted per unit time, we find that η_{QE} for the Eu^{3+}-doped sample is 4.59×10^{-26} and for the Pr^{3+}-doped sample 4.10×10^{-25}. Thus in the Pr^{3+}-doped sample the change in LIG scattering efficiency per phonon is 10 times stronger than in the Eu^{3+}-doped sample.

This difference in ability to form the LIG was unexpected in terms of the two-level system model. One parameter that affects grating formation is the asymmetry, given in Eq. (11), which is a measure of the difference in energy between the two wells. The asymmetry was predicted to be the same for the two samples, and measurements confirmed this prediction. Therefore the difference in grating-forming ability does not seem to be attributable to the asymmetry. Another parameter involved in grating formation is the barrier height between the two wells. The barrier height, V_0 in Eq. (11), is part of an adjustable parameter, which also contains d, the configuration coordinate distance. However, it seems that both of these parameters, like the asymmetry, should be related to the glass host and not to the rare-earth ion. The final possibility is that the origin of the refractive-index change in the two potential wells is associated with differences in the polarizabilities of the rare-earth ions in different local environments. In this case the Pr^{3+} and Eu^{3+} ions would need to experience different changes in polarizabilities when they move between the two wells. This would create a difference in grating-forming ability. The variation of the polarizability of Nd^{3+} ions from host to host was recently investigated by four-wave mixing.[13] The observed change in polarizability that is due to optical pumping is significantly greater than the well-to-well change observed here. Thus it appears that this difference in polarizability might be the origin of the refractive-index difference of the two potential wells observed in these experiments. This possibility will be investigated in future experiments.

In conclusion, we have presented results on the formation of laser-induced holographic gratings in Pr^{3+}- and Eu^{3+}-doped glasses. Characteristics of the LIG in Pr^{3+}-doped silicate glass were discussed and found to be similar to those seen in Eu^{3+}-doped glasses. Explanations have been presented for the lack of grating formation in Er^{3+}- and Nd^{3+}-doped glasses based on the absence of high-energy phonons. Comparisons between experimental values of the activation energy for grating formation and those predicted by the two-level system model were conducted, and it was found that the two-level system model is quite accurate in predicting these values.

ACKNOWLEDGMENT

REFERENCES

1. E. G. Behrens, F. M. Durville, and R. C. Powell, Opt. Lett. **11**, 653 (1986).
2. F. M. Durville, E. G. Behrens, and R. C. Powell, Phys. Rev. B **34**, 4213 (1986).
3. P. Gunter, Phys. Rep. **93**, 199 (1982).
4. A. Winnacker, R. M. Shelby, and R. M. Macfarlane, Opt. Lett. **10**, 350 (1985).
5. R. M. Macfarlane and R. M. Shelby, in *Coherence and Energy Transfer in Glasses*, P. A. Fluery and G. Golding, eds. (Plenum, New York, 1984).
6. L. G. DeShazer, Solidlite, Suite 224, 16150 NE 85th Street, Redmond, Washington 98052-3529 (personal communication).
7. C. L. Sauer, PhD dissertation (University of Southern California, Los Angeles, Calif., 1980).
8. C. Layne, W. H. Lowdermilk, and M. J. Weber, Phys. Rev. B **16**, 10 (1977).
9. H. Kogelnik, Bell Syst. Tech. J. **48**, 2909 (1969)
10. J. Feinberg, in *Optical Phase Conjugation*, R. A. Fisher, ed. (Academic, New York, 1983), p. 417.
11. E. G. Behrens, F. M. Durville, R. C. Powell, and D. H. Blackburn, Phys. Rev. B. **39**, 6076 (1989).
12. F. M. Durville, E. G. Behrens, and R. C. Powell, Phys. Rev. B **35**, 4109 (1987).
13. R. C. Powell, S. A. Payne, L. L. Chase, and G. D. Wilke, "Four-wave mixing of Nd^{3+}-doped crystals and glasses," Phys. Rev. B (to be published).

Optical applications of laser-induced gratings in Eu doped glasses

Edward G. Behrens, Richard C. Powell, and Douglas H. Blackburn

Laser-induced changes in the refractive index are used to create superimposed transient population gratings and permanent structural gratings in Eu^{3+} doped silicate and phosphate glasses. Potential uses for these laser-induced gratings (LIGs) are investigated. First, the structural gratings are shown to be permanent at room temperature and their use as a holographic storage medium is discussed. Second, a permanent LIG of this type is used to demultiplex multifrequency laser beams, demonstrating its use as a tunable line filter. Third, the transient LIG is used to modulate the amplitude of a laser beam which is passed through the sample and scatters off the permanent LIG. This results in information being transferred from one beam to another beam. It was found that thermal lensing plays an important role in the formation of this type of permanent LIG and a procedure for determining the tilt angle of the fringes of the LIG is discussed.

I. Introduction

In the past decade there has been a dramatic increase in interest in optical devices resulting from the emerging applications of optical technology. These devices rely on the interaction of light with matter and some of them are created by optical interference methods. Examples of the this type include photooptical switches,[1] narrowband waveguide reflection filters,[2] and opto-optical deflectors.[3] We have studied the interaction of laser light with Eu^{3+} doped glasses and reported the formation of superimposed permanent and transient laser-induced refractive index gratings (LIGs).[4-7] We suggest several uses for these types of grating in glasses.

In Sec. II the experimental configuration used to write the LIGs is discussed. The formation of the LIGs is the same regardless of the planned application. Section III discusses three of the possible applications of LIGs in these glasses. The characteristics of these LIGs relevant to their use for holographic information storage, frequency selective filtering, and beam-to-beam information transfer through amplitude modulation are described.

II. Experimental Configuration

The experimental configuration used to form the LIGs has been reported previously.[4,5] The output of a cw Ar-ion laser tuned to 4658 Å is split into two write beams and crossed inside the sample at an angle 2θ. In the region in which the beams overlap a sinusoidal interference pattern of the light intensity is created. This produces a modulation of the optical properties of the sample which will have the same sinusoidal pattern as that of the light intensity. This region is then probed with a third beam which sees the variation in the optical properties as a refractive index grating. A mirror mounted on a translational base which can move parallel to the sample is placed between the probe laser and the sample. This facilitates proper alignment of the probe beam and allows the angle between the probe beam and the perpendicular to the sample to be monitored. The probe beam, with a wavelength in the sample λ_p, is reflected off this mirror and onto the sample at an angle Φ, from the perpendicular to the sample. When this probe beam is properly aligned, a fourth beam, the signal beam, will be diffracted from the LIG. This signal beam carries information regarding the LIG and is monitored with a photomultiplier tube and recorded on a strip-chart recorder.

The samples used in these experiments are ordinary phosphate and silicate glasses which have been doped with Eu^{3+} ions. In the information storage and demultiplexing experiments a phosphate glass with composition 10 $Eu(PO_3)_3$ and 90 $La(PO_3)_3$ was used. In the signal modulation experiment the sample was a

silicate glass with composition 70 SiO_2, 15 Li_2O, 5 ZnO, 5 BaO, and 5 Eu_2O_3. All compositions are in mol %. For convenience these samples will be referred to as EP and LS, respectively. Both samples display the same LIG characteristics so either one could have been used for any of the experiments. The laser wavelength used for writing the gratings is in resonance with the $^7F_0$—$^5D_2$ absorption transition of the Eu^{3+} ions.

III. Results

A. Holographic Information Storage

The time evolution of a LIG is reflected in the intensity of the signal beam and for the type of gratings of interest here this time dependence is displayed in Fig. 1. When the write beams are turned off the grating decays with a rate equal to the decay rate of the $^5D_0$ excited state of the Eu^{3+} ion.[4,5] However, the signal does not return to zero but rather to approximately 60% of its original value due to the formation of a permanent grating. The permanent grating can then be erased thermally by heating the sample to temperatures above room temperature or it can be erased optically by illuminating the grating with a single beam tuned in resonance with the $^7F_0$—$^5D_2$ absorption transition of the Eu^{3+} ion. No grating formation or erasure occurs if the beams are not in resonance with the $^7F_0$—$^5D_2$ absorption transition.

A model was proposed to explain these gratings in which the network former and network modifier ions of the glass host can arrange themselves into two different configurations in the local environment of the Eu^{3+} ion.[8] This leads to a double-minima potential well for the Eu^{3+} electronic energy levels. It is assumed that the material possesses a different index of refraction depending on which configuration is present. When the Eu^{3+} ion relaxes nonradiatively from the $^5D_2$ level to the $^5D_0$ level several high energy phonons are created. The local heating produced by the vibrational modes can produce a change in the structure of the local environment of the Eu^{3+} ion by causing the ions to move from one equilibrium configuration to the other.

The results demonstrate that permanent holographic images can be written in rare earth doped phosphate and silicate glasses using this technique. Since the mechanism responsible for the formation of the permanent LIG involves structural changes which are stable at room temperature, these images have an infinite fading time. These holograms have many applications in areas such as optical information processing and medical imaging where long-time information storage is important. Even though the response time of the material is too slow for real time processing the room temperature stability makes it important for read only applications. This is a significant advantage over many photorefractive crystals which are currently being used in these applications.

To contrast the advantages and disadvantages of these rare earth doped glasses over photorefractive
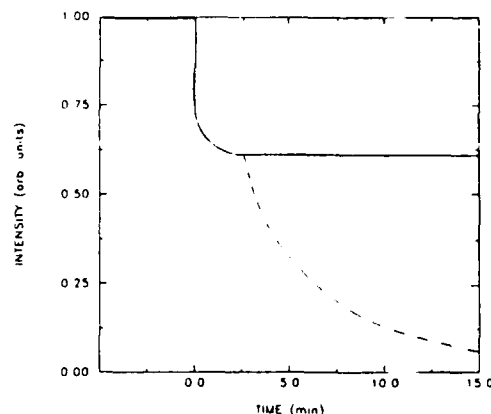

Fig. 1. Time evolution of LIG signal intensity in the EP glass sample.

crystals consider the required properties of photorefractive crystals for holographic applications as proposed by Gunter and Huignard.[9] The properties are:
1. sensitivity,
2. dynamic range,
3. recording and erasure time,
4. laser wavelength for inducing refractive index change,
5. resolution, and
6. room temperature operation.

There are two figures of merit used to determine the photorefractive sensitivity. In the first case the photorefractive sensitivity is given by

$$S_{n1} = \frac{dn_i}{dw},$$ (1)

which is defined as the change in refractive index per absorbed energy and volume. Values between roughly 5×10^3 J/cm^3 and 20×10^3 J/cm^3 have been found for S_{n1}^{-1} in photorefractive crystals. Although the refractive index change in rare earth doped glasses using low power laser beams is of the order of 10^{-3} to 10^{-5}, which is roughly the same as in $LiNbO_3$, the long time needed to produce this change drastically reduces the sensitivity. Rough calculations give S_{n1}^{-1} for rare earth doped glasses to be 9600×10^3 J/cm^3, which is 3 orders of magnitude larger than in photorefractive crystals. However, the second definition, which is more practical in characterizing the holographic recording potential, defines the photorefractive sensitivity as[9]

$$S_{n1} = \frac{d(\eta^{1/2})}{dw} \times \frac{1}{d},$$ (2)

where η is the diffraction efficiency and d is the sample thickness. This equation states that the sensitivity is the change in diffraction efficiency per unit absorbed energy and volume. Since diffraction efficiencies as high as 25% have been observed in these glasses[4,5] a value of 19.2 mJ/cm^2 is calculated for S_{n1}^{-1} as compared to values which range from 2.5–1000 mJ/cm^2 for photorefractive crystals. In this case the rare earth doped glasses compare favorably to photorefractive crystals.

As mentioned in the above paragraph the maximum change in the refractive index in the rare earth doped glasses has been measured to range from 10^{-3} to 10^{-5}. This is identical to the results reported for $LiNbO_3$ and is in the range of values reported for numerous other photorefractive crystals.[9]

Perhaps the main differences between photorefractive crystals and rare earth doped glasses occur in the recording and erasure time of the grating. In photorefractive crystals, the refractive index changes are due to electrooptic effects driven by space charge fields and the time to record a grating depends in the efficiency of the charge generation and transport process. However, in the rare earth doped glass the refractive index change is due to a rearrangement of the structure in the local environment of the rare earth ion. This requires a large amount of vibrational energy and a long time is needed for the grating buildup. Thus, the time required to produce the refractive index change mentioned above is several orders of magnitude larger in rare earth doped glasses than in photorefractive crystals. The same time scales are also observed for grating erasure.

In most cases the laser wavelengths required to produce the refractive index changes range from the near UV to the near infrared for photorefractive crystals. For the rare earth doped glasses investigated up to this time, the required laser wavelengths are in the visible region of the spectrum and have been accessible using a common Ar-ion laser. A unique wavelength is required for the rare earth doped glasses, whereas a range of wavelengths can generally be used for photorefractive crystals.

Finally, the most important difference between these materials occurs in their room temperature operation. Photorefractive crystals possess a volatile memory at room temperature and must undergo fixing methods to avoid dark erasure at room temperature. On the other hand, the memory in rare earth doped glasses is permanent at room temperature because of the structural phase change responsible for the refractive index change. Also, as long as the probe beam is not in resonance with a rare earth absorption transition no erasure will occur during read out of holograms.

From the above comparisons it can be seen that the rare earth doped glasses have certain advantages over photorefractive crystals in applications that require long time storage, room temperature operation, and multiple readings of holographic gratings. For applications that require a relatively fast response time, the photorefractive crystals possess the advantage. As will be mentioned below, the response time of rare earth doped glasses depends on the decay kinetics of the rare earth ion. Finding a rare earth ion that displays faster decay parameters will increase the response time and may become comparable to those in photorefractive crystals.

B. Demultiplexing Results

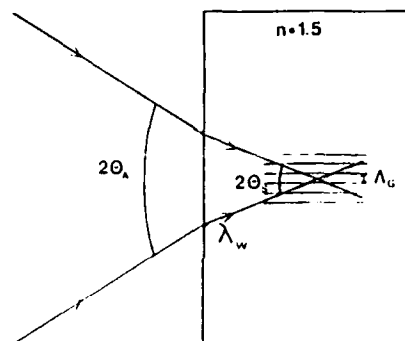To investigate the demultiplexing properties of the LIG in these types of glasses a permanent grating was

Fig. 2. Definition of parameters in the grating formation process: λ_w is the write beam wavelength in the sample; $2\theta_A$ is the write beam crossing angle in air; n is the index of refraction of the LS sample; $2\theta_S$ is the write beam crossing angle inside the sample; and Λ_G is the laser-induced grating wavelength.
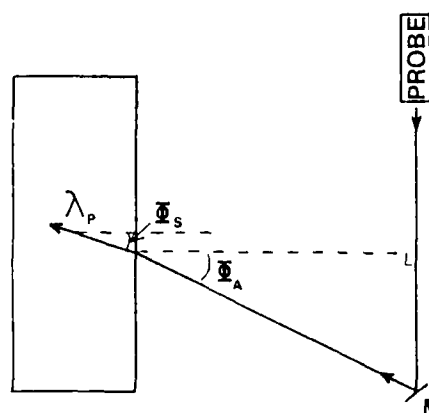

Fig. 3. Definition of parameters in the probe portion of the experiment. λ_P is the probe beam wavelength in the sample, Φ_A and Φ_S are the angles between the probe beam and the perpendicular to the sample in air and in the sample, respectively.

written in the EP glass sample. The angle between the write beams, $2\theta_A$ was measured to be 2.22° in air or, with an index of refraction of 1.5 for the glass, 1.48° inside the sample, which is defined as $2\theta_S$. The grating spacing, which is the distance between the fringes of the LIG, is designated as Λ_G. The definition of these parameters is displayed in Fig. 2.

The LIG was probed with both a He–Ne laser and several different lines of an Ar-ion laser. The strength of the probe beam was kept under 15 mW and out of resonance with the $^7F_0$—$^5D_2$ Eu^{3+} absorption transition to insure no erasure of the LIG. The geometry of the probe portion of the experiment is presented in Fig. 3. The alignment of the probe beam for maximum scattering efficiency is determined by the probe beam wavelength and the wavelength of the LIG.

To determine the spatial displacement of the probe beam, its intensity was measured as a function of its angle of incidence Φ_A. This measurement was performed with probe beam wavelengths in air of 632.8, 514.5, 501.7, 496.5, 488.0, and 476.5 nm. Figure 4 displays the results where Φ_A has been converted to Φ_S
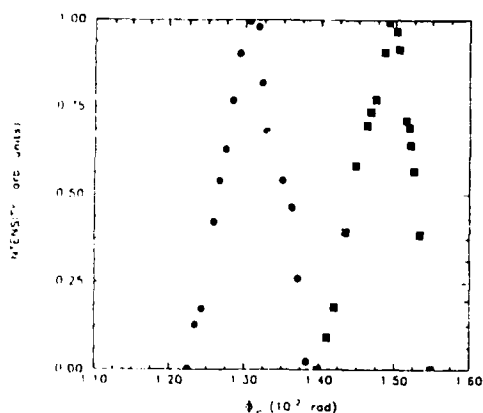
Fig. 1 Intensity of laser-induced grating signal as a function of the angle between the probe beam and the perpendicular to the sample. The symbols correspond to: ■, 632.8 nm; ●, 488.0 nm.

Fig. 5. Angle in the sample at which maximum scattering intensity occurs vs probe beam wavelength in the sample.

and, for clarity only, the results from probe beam wavelengths of 632.8 and 514.5 nm are displayed. It should be pointed out that the same type of behavior was observed for all probe beam wavelengths with a shift in the angle for maximum scattering. It is seen that as Φ_S is varied, the signal intensity increases from zero to a maximum then decreases back to zero as would be expected for Bragg scattering.

Figure 5 displays the probe beam wavelength in the sample, λ_p vs the angle Φ_S at which maximum signal intensity occurs. As the probe beam wavelength decreases, the angle at which maximum signal intensity occurs also decreases. This is described by the Bragg scattering equation[10]

$$n\lambda_p = 2\Lambda_G \sin\Phi_0, \tag{3}$$

where λ_p is the probe beam wavelength, Λ_G is the wavelength of the LIG grating, and Φ_0 is the Bragg angle. For the experiments performed here, the values of Φ_S plotted in Fig. 5 may not represent the Bragg angle Φ_0. If the fringes of the LIG are not perpendicular to the sample surface, Φ_S will not be equal to Φ_0. If the fringes of the LIG make an angle Φ' to the perpendicular to the sample surface, the Bragg angle will be $\Phi_0 = \Phi_S - \Phi'$ as is displayed in Fig. 6.

To correct for this the Bragg angle Φ_0 must be replaced with $\Phi_S - \Phi'$. It is unlikely that Φ' will be known accurately, thus consider the case of two probe beams λ_{p1} and λ_{p2} which have two separate Bragg angles Φ_{01} and Φ_{02}. Since only Φ_S is changing, Φ' will remain the same for both beams so that

$$\lambda_{p1} = 2\Lambda_G \sin(\Phi_{S1} - \Phi') \tag{4}$$

$$\lambda_{p2} = 2\Lambda_G \sin(\Phi_{S2} - \Phi'). \tag{5}$$

For small angles $\sin(\Phi_S - \Phi') = (\Phi_S - \Phi')$. Taking the difference between these two equations gives

$$\Delta\lambda_p = 2\Lambda_G \Delta\Phi_S. \tag{6}$$
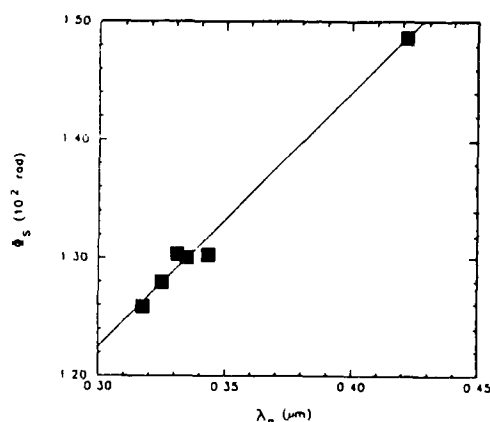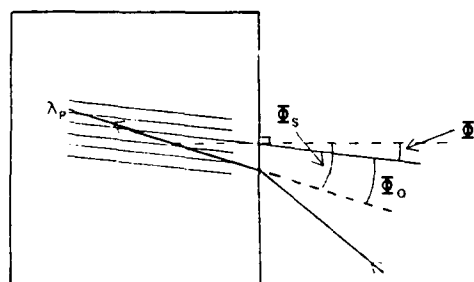
Thus, the grating spacing is given by

Fig. 6. Definition of Bragg angle and other angles involved in the grating spacing calculation.

$$\Lambda_G = \frac{\Delta\lambda_p}{2\Delta\Phi_S}. \tag{7}$$

The solid line in Fig. 5 represents the best fit to the data and the slope of the line gives

$$m = \frac{\Delta\Phi_S}{\Delta\lambda_p} \tag{8}$$

so that the wavelength of the permanent grating is

$$\Lambda_G = \frac{1}{2m}. \tag{9}$$

The slope of the solid line in Fig. 5 was found to be 0.0214 μm corresponding to a grating spacing of 23.364 μm. To check this value the grating spacing of the sinusoidal light interference pattern was calculated. This is also given by Bragg's law and will exhibit a wavelength of

$$\Lambda_L = \frac{\lambda_W}{\Theta_S}. \tag{10}$$

where λ_W is the write beam wavelength. For a write beam wavelength of 0.3105 μm and crossing angle of 0.0258 radians the wavelength of the sinusoidal interference pattern should be 12.022 μm. It is seen that the LIG apparently displays a wavelength approximately twice that of the sinusoidal laser interference pattern.

It has been shown that the Eu^{3+}-doped phosphate glasses exhibit thermal lensing.[11] When illuminated with a single beam tuned in resonance with the $^7F_0$—$^5D_2$ Eu^{3+} absorption transition, a permanent change is produced in the refractive index of these glasses. The change in the refractive index is proportional to the change in the temperature of the glass. This temperature profile can be approximated by a parabola, producing an effective thin lens with a positive focal length. In the crossed beam configuration, each beam will produce its own thermal lens. This will result in a new crossing angle $2\Theta_S'$ as shown in Fig. 7 and produce a change in the wavelength of the laser interference pattern.

We can predict the change in the crossing angle of the write beams by considering the thermal lens to act as an effective positive focal length lens placed in the path of each beam. The focal length can be calculated by using a method similar to that used in Durville's experiments.

In the long time limit the focal length of the effective lens is given by[11]

$$f = \frac{\pi k w^2 \frac{\partial n}{\partial T}}{0.553PA} , \qquad (11)$$

where k = thermal conductivity
$\quad w$ = beam waist
$\quad P$ = beam power
$\quad A$ = absorbance of sample, and
$\quad \dfrac{\partial n}{\partial T}$ = change in refractive index per change in temperature.

Here k, A and $(\partial n)/(\partial T)$ are properties of the sample and will be the same in both experiments. This leads to a focal length of

$$f_B = \frac{f_D P_D w_B^2}{P_B w_D^2} , \qquad (12)$$

where the D subscripts refer to the values quoted in[11] and the B subscripts refer to the values in this experiment. With w_B = 0.5 mm and P_B = 0.07 W, a focal length of 38.563 mm is found. From this, the change in Θ_S can be calculated and a new value for the wavelength of the laser interference pattern of 24.109 μm is calculated. This is in good agreement with the wavelength of the LIG found from Eq. (7).

It is also possible to calculate the tilt angle Φ' shown in Fig. 6. From

$$\lambda_P = 2\Lambda_G \sin(\Phi_S - \Phi') \qquad (13)$$

and with the small angle approximation, the tilt angle will be given by

$$\Phi' = \Phi_S - \frac{\lambda_P}{2\Lambda_G} . \qquad (14)$$

For this experiment a tilt angle of 5.860×10^{-3} rad is found. Notice that if Φ_S is measured from a reference other than the perpendicular to the sample, this will give the angle between the fringes and the reference.
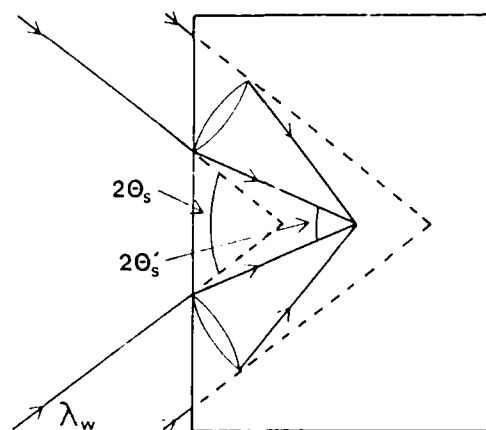

Fig. 7. Definition of angles involved in thermal lensing process: $2\Theta_S$ is the write beam crossing angle in the sample without thermal lensing; $2\Theta_S'$ is writed beam angle with thermal lensing.

The demultiplexing of the various frequencies of laser beams by the LIG demonstrates the ability of using these holographic gratings as frequency selective notch filters. The filter can be tuned to different frequencies by rotating the sample to different angles. By stacking different holographic gratings in the same material, several laser beams of different frequencies can be filtered simultaneously at the same angle of incidence. The limiting factor to the resolution of such a device is the fringe spacing of the LIG and gratings can be formed with spacings more than an order of mangitude smaller than that of the grating used in these experiments.

C. Signal Modulation

The final experiment performed was to demonstrate amplitude modulation of the LIG signal. After writing the LIG as described in Sec. II, the write beams were turned on and off randomly. The result was an amplitude modulation of the signal beam as shown in Fig. 8. The top portion of the figure displays the time dependence of the write beams. The time scale of the experiment was approximately two minutes. The middle section depicts the intensity of the probe beam. As can be seen, the probe beam is stable at a constant amplitude before interacting with the LIG. The bottom section of Fig. 8 displays the time dependence of the intensity of the signal beam, which is an amplitude modulation of a constant beam.

The time dependence of the intensity has been discussed previously and is given by[1]

$$I(t) = I_1(t) + I_2, \qquad (15)$$

where I_1 and I_2 represent the transient and permanent contributions to the intensity. Thus, when the write beams are on a total signal intensity of $I = I_1 + I_2$ will be measured; however, when the write beams are turned off the transient signal will decay leaving a total intensity of $I = I_2$. The decay will be exponential with the decay time of the transient grating.
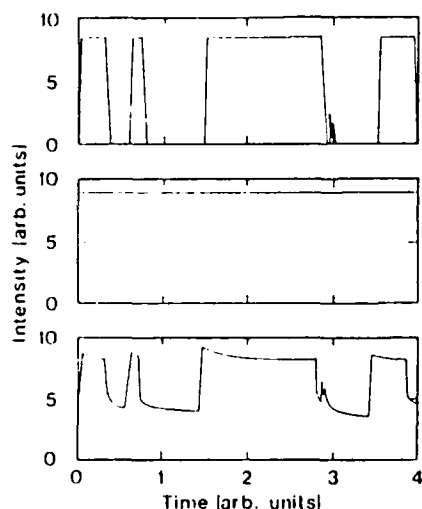
Fig. 8 From top to bottom: write, probe, and signal beam intensities in the modulation experiment.

The rate at which the signal amplitude can be modulated is limited by the decay time of the transient component of the signal intensity. The decay time of the transient component has been associated with a population grating of the Eu^{3+} ions in the $^5D_0$ metastable state.[1] This limits the amplitude modulation by a decay time of 2.7 ms in this sample.[12]

These results establish that the superimposition of transient and permanent LIGs generated by the mechanism described here can be utilized to allow one light beam to modulate the intensity of another light beam. This provides a means of transferring information from one beam to the other. The speed at which information can be transferred will depend on the modulation rate, which is limited by the lifetime of the metastable state of the rare earth ion and can vary between a kilohertz and a megahertz for different rare earth transitions.

IV. Conclusions

Three potential uses of LIGs have been demonstrated in Eu^{3+} doped glasses which have the ability to produce superimposed permanent and transient gratings. These include holographic storage, demultiplexing multifrequency laser beams, and beam-to-beam information transfer. The LIGs can be written at room temperature with low laser power, have exhibited scattering efficiencies as high as 25%, and remain stable at room temperature indefinitely.

These same type of LIGs have been formed in a Pr^{3+} doped silicate glass with composition 70 SiO_2, 15 Na_2O, 5 ZnO, 5 BaO, and 5 Pr_2O_3 mol %.[13] The transient component of the signal in this glass is associated with

the relaxation of the $^1D_2$ metastable state which has a lifetime of the order of microseconds. This will produce an increase of 3 orders of magnitude in the response time of the transient grating compared with the Eu^{3+} doped glasses. This will allow for a faster amplitude modulation rate of light beams passing through the sample. However, the response time of the permanent holographic grating is still very slow in Pr^{3+} doped glasses.

The above results are important when considering these glasses for potential optical devices. The type of glasses used in this work include common silicate glasses which can be made into fibers, and thus these LIG devices can be used in fiber optic systems. A better knowledge of the microscopic structural change associated with the permanent LIG in these glasses will allow for optimization of these materials for specific use.

References

1. K. Tanaka and A. Odajima, "Photo-Optical Switching Devices by Amorphous As_2S_4 Waveguides," Appl. Phys. Lett. 38, 481 (1981).
2. B. S. Kawasaki, K. O. Hill, D. C. Johnson, and Y. Fujii, "Narrow-Band Bragg Reflectors in Optical Fibers," Opt. Lett. 3, 66 (1978).
3. G. T. Sincerbox and G. Roosen, "Opto-Optical Light Deflection," Appl. Opt. 22, 690–697 (1983).
4. F. M. Durville, E. G. Behrens, and R. C. Powell, "Laser-Induced Refractive-Index Gratings in Eu-doped Glasses," Phys. Rev. B 34, 4213 (1986).
5. E. G. Behrens, F. M. Durville, and R. C. Powell, "Observation of Erasable Holographic Gratings at Room Temperature in Eu^{3+} Doped Glasses," Opt. Lett. 11, 653 (1986).
6. R. C. Powell, F. M. Durville, E. G. Behrens, and G. S. Dixon, "Four-Wave Mixing and Fluorescence Linenarrowing Studies of Eu^{3+} Ions in Glasses," J. Lumin. 40, 68 (1988).
7. F. M. Durville, E. G. Behrens, and R. C. Powell, "Relationship Between Laser-Induced Gratings and Vibrational Properties of Eu-Doped Glasses," Phys. Rev. B 35, 4109 (1987).
8. E. G. Behrens, F. M. Durville, R. C. Powell, and D. H. Blackburn, "Properties of Laser-Induced Gratings in Eu-Doped Glasses," Phys. Rev. B 39, 6076 (1989).
9. P. Gunter and J.-P. Huignard, in Photorefractive Materials and Their Applications I: Topics in Applied Physics, P. Gunter and J.-P. Huignard Eds. (Springer-Verlag, Berlin, 1988).
10. H. Kogelnik, "Coupled Wave Theory for Thick Hologram Gratings," Bell Syst. Tech. J. 48, 2909 (1969).
11. F. M. Durville and R. C. Powell, "Thermal Lensing and Permanent Refractive Index Changes in Rare-Earth-Doped Glasses," J. Opt. Soc. Am. 4, 1934–1942 (1987).
12. X. Gang and R. C. Powell, "Site-Selection Spectroscopy and Energy Transfer Studies of Eu^{3+} Ions in Glass Hosts," J. Appl. Phys. 57, 1299 (1985).
13. E. G. Behrens, R. C. Powell, and D. H. Blackburn, Phys. Rev. B, to be published.

Refractive index gratings in rare-earth-doped alkaline earth glasses

Valentina A. French and Richard C. Powell

Center for Laser Research, Oklahoma State University, Stillwater, Oklahoma 74078-0444

Douglas H. Blackburn and David C. Cranmer

National Institute of Standards and Technology, Gaithersburg, Maryland 20894

Four-wave-mixing techniques were used to produce permanent laser-induced refractive index gratings in Eu^{3+}-doped silicate glasses. These gratings are associated with a thermally induced change in the local glass structure at the site of the Eu^{3+} ions, leading to a double-minimum potential well for the electronic energy levels of the Eu^{3+} ions. The effects on the characteristics of the permanent laser-induced gratings produced by changing the divalent modifier ions of the glass host are reported and a theoretical model is presented to explain the physical origin of the change in the refractive index of the material.

I. INTRODUCTION

The observation of permanent laser-induced gratings in Eu^{3+}-doped glasses using four-wave-mixing (FWM) techniques was reported previously.[1] These gratings were produced by resonant excitation of the Eu^{3+} ions into the $^5D_2$ level. A model was proposed[1,2] to explain the formation of these gratings based on a thermally induced change in the local glass structure at the site of the Eu^{3+} ions. This results in the description of each electronic level of the Eu^{3+} ions in terms of a *double-minimum potential well*. The model assumes that the index of refraction of the material changes, depending on which potential well is occupied by the Eu^{3+} ions.

Laser-induced refractive index gratings in Eu^{3+}-doped glasses are important when considering such glasses for optical devices. Several potential uses of these types of gratings have been demonstrated[1] including holographic storage, demultiplexing multifrequency laser beams, and beam-to-beam information transfer. In addition, silicate glasses can be made into fibers and thus devices based on laser-induced gratings in Eu^{3+}-doped silicate glasses can be used in fiber optics systems.

In the work reported here we extend the previous investigations[1,2] by describing the variation of the FWM signal intensity of a series of Eu^{3+}-doped silicate glasses with different divalent alkaline network modifier ions. The temperature dependence of the signal from one of the samples was measured and a theoretical explanation for the change in the refractive index associated with the double-minimum potential well model is developed.

II. EXPERIMENTAL RESULTS

The effect of different divalent network modifier ions on the characteristics of permanent laser-induced gratings was studied in five Eu^{3+}-doped silicate glasses with identical compositions except for one modifier ion which was changed through a series of divalent alkaline elements: Mg, Ca, Zn, Sr, and Ba. The compositions of these glasses are listed in Table I.

Permanent laser-induced gratings were written in each sample at room temperature using crossed write beams from a c.w. argon-ion laser tuned to the 465.8 nm line in order to resonantly excite the $^5D_2$ level of the Eu^{3+} ions. The two write beams, each having a power of 30 mW, were focused to beam waists of 400 μm and superimposed inside the sample at a crossing angle of about 3°. The scattering efficiency of these gratings was measured using a He-Ne laser at 632.8 nm as the probe beam, which was focused to a waist of 200 μm and had a power of 5 mW. The experimental setup was the same as reported previously.[1] The writing time of the grating was about 15 min.

It was found that the scattering efficiency of the laser-induced gratings decreased as the mass of the modifier ion increased. Figure 1 displays a plot of the experimental values of the scattering efficiency versus the reduced mass of the modifier and the rare earth ion. The solid line represents the theoretical fit to the experimental data as explained in Sec. III.

The temperature dependence of the laser-induced signal intensity in the Mg glass sample was measured at temperatures below and above room temperature. For low temperature measurements the sample was mounted in a cryostat and the temperature was controlled using a CTI-Cryogenics

TABLE I. Composition of glass samples investigated

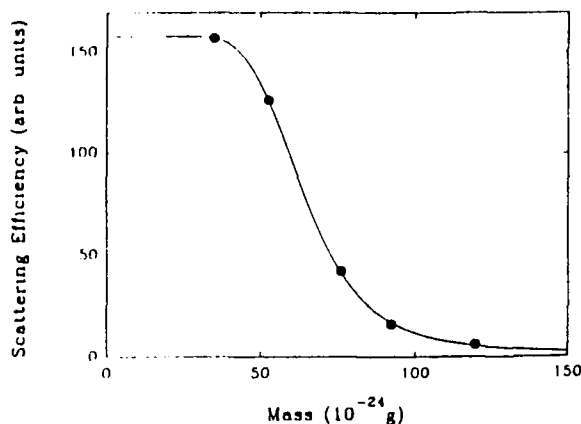|	Sample composition (mol %)		
Sample	Network former	Network modifiers	Eu content
Mg glass	65 SiO₂	15 Na₂O 15 MgO	5 Eu₂O₃
Ca glass	65 SiO₂	15 Na₂O 15 CaO	5 Eu₂O₃
Zn glass	65 SiO₂	15 Na₂O 15 ZnO	5 Eu₂O₃
Sr glass	65 SiO₂	15 Na₂O 15 SrO	5 Eu₂O₃
Ba glass	65 SiO₂	15 Na₂O 15 BaO	5 Eu₂O₃

FIG. 1 Scattering efficiency of the laser-induced permanent gratings as a function of the reduced mass of the alkaline earth modifier ion and rare-earth ion. ● experimental points; , theoretical prediction.

closed cycle helium refrigerator and a Lake Shore Cryotronics model 805 temperature controller. For high temperature measurements the sample was mounted in a resistance heated furnace with a Cromel-Alumel thermocouple. The laser-induced signal intensity is plotted versus temperature in Fig. 2. As can be seen from the graph, the signal intensity increases as the temperature decreases. There is a change in slope between high and low temperature regions. The solid lines in Fig. 2 correspond to an exponential variation of the signal intensity given by[2]

$$I = I_0 \exp(\Delta / k_B T), \tag{1}$$

where Δ is an activation energy. The experimental values obtained for Δ are 2.72×10^3 cm^{-1} for the high temperature region and about 0.25×10^3 cm^{-1} for the low temperature region.

III. INTERPRETATION OF RESULTS

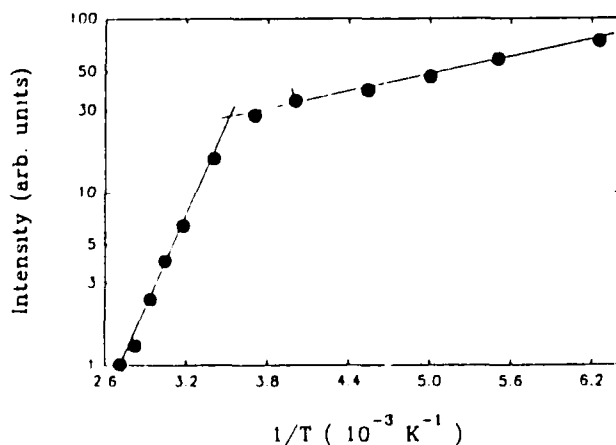The model proposed previously to explain laser-induced permanent gratings is based on thermally induced changes

FIG. 2 Intensity of the laser-induced signal in the Mg glass sample as a function of temperature

in the local glass structure at the site of the Eu^{++} ions.[2] This model assumes that the network forming and modifier ions can arrange themselves in two possible configurations leading to different local environments surrounding the Eu^{++} ions. Each structural arrangement has a different refractive index. This results in double-minima potential wells for the electronic energy levels of the Eu^{++} ions. It is also assumed that the heat generated through radiationless decay of the excited Eu^{++} ions is responsible for the laser-induced change in the local structure of the glass host.[1] This can be pictured as the Eu^{++} ions moving from one potential well minimum to the other.

Using the double-minimum potential well model to explain permanent laser-induced gratings in the Eu^{++}-doped glasses investigated here, the effective scattering efficiency of these gratings is given by[2]

$$\eta \propto (|\Delta n_{\text{II,I}}|^2) \Big/ \left(1 + (\nu_{\text{II}}/\nu_{\text{I}}) \exp\left\{\frac{-\hbar(k/m)^{1/2}}{k_B T \tan \Theta}\right.\right.$$

$$\left.\left. \times \exp[-d(2mV_0/\hbar^2)^{1/2}]\right\}\right)^2 \tag{2}$$

where $\Delta n_{\text{II,I}}$ is the change in refractive index per ion, ν_{II} is the attack frequency (the number of attempts an ion in well I(II) makes to surmount the potential height of that well), $\tan \Theta = \Delta_0/\Delta_c$, Δ_0 being the coupling energy[2] and Δ_c the asymmetry (the difference in the minima of the two potential wells), k is the force constant of the initial configuration, m the mass of the ion populating the well, d is the distance between the minima of well I and well II and V_0 the potential barrier between the two wells.[2] The value used for m in Eq. (2) was the reduced mass of the divalent modifier ion and rare earth ion for each of the samples investigated. Although, realistically there are many ions moving and thus contributing to the formation of the two equilibrium configurations, we consider in this model that the main source of the double-minimum potential well is the change in position of the divalent modifier ion and the rare-earth ion. The change in position of all other ions is considered to be very small, so that their contribution to the double-minimum potential well is negligible. Equation (2) was fit to the experimental values of the scattering efficiency treating $|\Delta n_{\text{II,I}}|^2$, $\nu_{\text{II}}/\nu_{\text{I}}$, $\hbar k^{1/2}/(k_B T \tan \Theta)$, and $d(2V_0/\hbar^2)^{1/2}$ as adjustable parameters. The solid line in Fig. 1 represents the best fit to the experimental data where the values found for the adjustable parameters are:

$$|\Delta n_{\text{II,I}}|^2 = (1.58 \pm 0.05) \times 10^{-44},$$

$$\nu_{\text{II}}/\nu_{\text{I}} = 15.6 \pm 0.5,$$

$$\hbar k^{1/2}/(k_B T \tan \Theta) = (2.25 \pm 0.10) \times 10^{10} \text{ g}^{1/2},$$

$$d(2V_0/\hbar^2)^{1/2} = (2.55 \pm 0.10) \times 10^{11} \text{ g}^{-1/2}.$$

The sensitivity of the fit to these values of the adjustable parameters is expressed by the $\pm$ error bars given above.

The constant of proportionality in Eq. (2) was calculated using the fact that the scattering efficiency of the FWM signal is given, to a first approximation, by[4]

$$\eta = \exp(-2\alpha_0 \Gamma) \pi^2 \Gamma^2 (\Delta n_{\text{total}})^2/\lambda^2 \tag{3}$$

here $\Gamma = D/\cos 2\theta$, where D = grating thickness, 2θ = angle between the write beams in the sample, λ = wavelength

TABLE II. Summary of parameters.

Sample	Δ_e ($\times 10^3$ cm^{-1})	$N_I(0)$ ($\times 10^{19}$)	$N_I(\infty)$ ($\times 10^{19}$)	$N_{II}(\infty)$ ($\times 10^{19}$)	$N_{II}(\infty)/N_I(0)$	d (Å)
Mg glass	1.72	6.84	0.02	6.82	0.99	0.04
Ca glass	0.99	4.59	0.49	4.10	0.89	0.06
Zn glass	0.57	5.25	2.55	2.70	0.51	0.08
Sr glass	0.41	7.59	5.11	2.48	0.33	0.09
Ba glass	0.26	5.52	4.50	1.02	0.18	0.12

of the write beams, Δn_{total} = modulation of the refractive index of the sample, α_0 = absorption coefficient of the sample at the write beam frequency.

The values of the adjustable parameters were used in Eqs. (7) and (24) from Ref. 2 to calculate the difference in the minima of the two wells, Δ_e, the population of well I before excitation, $N_I(0)$ (initially all ions are assumed[2] to be in well I), and the population of each well after the system has reached equilibrium, $N_{I,II}(\infty)$, for each of the samples investigated in this work. The values of these parameters are listed in Table II. It is observed that the asymmetry decreases as the mass of the divalent modifier ion increases. This same trend was reported[2] in a series of silicate glasses with different monovalent modifier ions and was attributed to the fact that the glass becomes more ordered as the radius of the modifier ion increases and therefore the possibility for multiple configurations decreases.

The decrease in the difference between the two potential minima in the samples with heavier modifier ions is an indication of the fact that there is less thermally induced change in the local glass structure. Because of this, it is more difficult to trap ions in well II in these samples. This is shown in Table II by the decrease in the ratio $N_{II}(\infty)/N_I(0)$ as the mass of the modifier ion increases.

Using the value obtained for the last adjustable parameter, it is possible to approximate[2] the distance, d, between the two potential minima, which is a measure of the average distance the ions move. This distance varies from 0.04 Å for the Mg glass sample to 0.12 Å for the Ba glass sample, as listed in Table II. These small values for d indicate that, as individual ions or groups of ions move between the two possible equilibrium configurations, I and II, the effect on the average configuration coordinate is very small.

The change in refractive index per ion is 1.26×10^{-22}, and considering the number of ions that accumulate in well II, which is of the order of 1×10^{19}, the total change in the refractive index of the material is 1.26×10^{-3}. This is consistent with the results obtained for silicate glasses with monovalent modifier ions in an earlier paper,[2] where the values for $|\Delta n_{II}|^2$ and $\hbar k^{1/2}/(k_B T \tan \Theta)$ were found to be 1.69×10^{-11} and 2.25×10^{-10} g$^{1/2}$, respectively. (These values were reported incorrectly in the earlier paper.)

From Sec. II the activation energy for the Mg glass sample for the high temperature region was found to be 2.72×10^3 cm^{-1} and since the activation energy is twice the asymmetry,[2] this would give an asymmetry of 1.36×10^3 cm^{-1}. This value is slightly lower than the calculated value

for Δ_e listed in Table II. However, considering the simplicity of the model used here to describe a complex physical system, the experimental and calculated values for Δ_e are close enough. Similar results were obtained for the glasses with monovalent modifier ions.[2] In that work it was demonstrated that the measured activation energy decreased with increasing mass of the modifier ion in the same way as the asymmetry factor. Since this dependence is already established, we did not repeat temperature dependence measurements on all of the samples with divalent modifier ions but only used one sample to again demonstrate the equivalence of ΔE_H and $2\Delta_e$ in this set of samples.

IV. THEORETICAL MODEL

One important assumption made in the double-minimum potential well model is that the refractive index of the material is different for the two possible local configurations, that is n depends on which potential minimum is occupied by the Eu^{3+} ions.[1,2] This change in the refractive index needs to be theoretically explained and evaluated.

Starting from the Clausius–Mossotti equation, the change in refractive index, Δn_{total}, between the two configurations can be related to the change in the polarizability, $\Delta \alpha_p$, of the Eu^{3+} ions in configuration II as compared to configuration I by

$$\Delta n_{total} = (2\pi/n) f_I^2 N_{cx} \Delta \alpha_p, \qquad (4)$$

where $f_I = (n^2 + 2)/3$ is the Lorentz field correction and N_{cx} is the number density of the Eu^{3+} ions in configuration II. Using the numerical values calculated from our experimental data for the change in refractive index per ion, Δn_{II}, the number of ions that have moved to well II, $N_{II}(\infty)$, and the volume of interaction of the laser beams inside the sample, the change in polarizability, $\Delta \alpha_p$, is calculated to be 0.0134 Å^3.

For a theoretical evaluation of the change in polarizability we used the model developed by Powell et al.[] to calculate the change in polarizability of the $^4F_{3/2}$ excited state of Nd^{3+} compared to that of the $^4I_{9/2}$ ground state for a variety of host materials. They considered that the Nd^{3+} ion was a multilevel system and that the laser beams could interact with all possible transitions between those levels. Having recognized that the $4f$-$4f$ transitions "borrow" intensity from the $4f$-$5d$ and $4f$-ng transitions, they estimated that the main contribution to the change in the polarizability of the Nd^{3+} ion was due to the $4f$-$5d$ interactions.

Here we consider that the change in polarizability of the

Eu^{3+} ions in configuration II as compared to configuration I is mainly due to the 4f-5d transitions which are far from resonance and given by[ ]

$$\Delta\alpha_{\parallel} \quad |(3v_{0}^{5d}-\alpha_{LS})/(7\pi)|\{|(v_{0}^{5d}-v_{LS})^{2}-v^{2}|^{-1}$$

$$|(v_{0}^{5d})^{2}-v^{2}|^{-1}\}(4f|r|5d)|^{2}, \qquad (5)$$

where v_{0}^{5d} is the average energy of the $4f^{6}5d$ states, v is the energy of the laser photons, v_{LS} is the energy difference between the two equilibrium configurations I and II, and α_{LS} is the fine structure constant.

Figure 3 shows the relevant energy levels of the Eu^{3+} ions with the two possible local configurations of the glass host, I and II. The numerical values used in Eq. (5) were the free-ion values[ ] The lowest $4f^{6}5d$ level of the Eu^{3+} free ion is known[ ] to be at 85,500 cm^{-1} and, due to the 20,000 cm^{-1} splitting of the 5d level, the median energy of the $4f^{6}5d$ manifold is at about 95,500 cm^{-1}. The value of the radial integral $(4f|r|5d)$ for the Eu^{3+} free ion is[ ] 0.41 Å and α_{LS} 1/137. Using the value of $\Delta\alpha_{\parallel}$ calculated from the experimental results and Eq. (4) in Eq. (5), the energy difference between the two configurations is found to be v_{LS} 3.14 × 10^{4} cm^{-1}.

Since the difference between the ground state energy of the Eu^{3+} ion in configuration II as compared to configuration I was calculated to be 1.72 × 10^{4} cm^{-1} for the Mg glass sample, as listed in Table II, the remaining energy difference between the two configurations is accounted for by a shift of 1.42 × 10^{4} cm^{-1} in the 5d levels of configuration II as compared to configuration I. From Table II, it is seen that the shift in the ground state energy becomes smaller as the mass of the modifier ion increases. This would lead to increasing shifts in the 5d levels, from 1.42 × 10^{4} cm^{-1} for the Mg glass sample to 2.88 × 10^{4} cm^{-1} for the Ba glass sample.

The energy difference between the two equilibrium configurations was calculated based on the free-ion value of the radial integral $(4f|r|5d)$. The value of this integral will be

Configurational
coordinate

FIG. 3 Configurational coordinate diagram showing the relevant energy levels of the Eu ion with the two possible local configurations of the glass host, I and II.

smaller[ ] for the Eu^{3+} ions incorporated into a host environment. This, in turn, would mean that the energy shifts from one configuration to the other may be somewhat larger than those calculated using the free-ion value for the radial integral. Even then, the results predicted by this model are reasonable, since site-selective spectroscopy has shown[ ] energy shifts in the 5d level of about 6,000 cm^{-1} from one site of the impurity ion to another in a glass host. However, it is also true that the value of the radial integral can change significantly due to a change in local environment.[ ] It is impossible to tell from these results whether the change in the radial integral or the change in the position of the 5d level makes the dominant contribution to the change in the polarizability. Both types of changes will contribute to the observed results.

V. CONCLUSIONS

Using the double-minimum potential well model to explain permanent laser-induced gratings in Eu^{3+}-doped glasses, a theoretical explanation was developed for the change in the refractive index for different local structural configurations of the material. The change in the refractive index was related to the change in the polarizability of the Eu^{3+} ions in the two types of configuration, which in turn, was calculated from the experimental data to be $\Delta\alpha_{\parallel} = 0.0134$ Å^{3}. The change in refractive index per ion was obtained as an adjustable parameter from fitting Eq. (2) to the experimental data and therefore has the same value for all glass samples investigated here. The total change in refractive index varies from host to host due to the fact that the number of ions moving from configuration I to configuration II is host dependent as shown in Table II. However, the actual value of $\Delta n_{\text{II I}}$ may also change a little from one glass host to another. The theoretical model used here can accurately explain all of the observed results by assuming that this change is very small so that its contribution to the change in total refractive index is negligible.

On the basis of free-ion wave-functions and the assumption that the 4f-5d transitions make the dominant contribution to the change in polarizability between the two configurations, we calculated a shift in transition energy from configuration I to configuration II of 3.14 × 10^{4} cm^{-1}. This is a physically reasonable energy level shift but the actual value may be different due to the change in the value of the radial integral between the two configurations. Previous results on other types of samples indicate that this latter effect makes the dominant contribution to the polarizability change in different host environments.[ ] It is interesting to note that the value of $\Delta n_{\text{II I}}$ found for Pr^{3+}-doped glasses is the same as that found for Eu^{3+} in the same hosts.[ ] Since the 5d levels for Pr^{3+} are at lower energies than those of Eu^{3+}, these results imply that the change in radial integral is more important than the change in the position of the 5d levels in determining the polarizability of the rare-earth ions in glass hosts.

Unfortunately, there is still very little known on the atomic scale concerning the local environment of rare-earth ions doped into glass hosts. It is thought that ions such as Eu^{3+} in silicate glasses occupy interstitial sites and distort
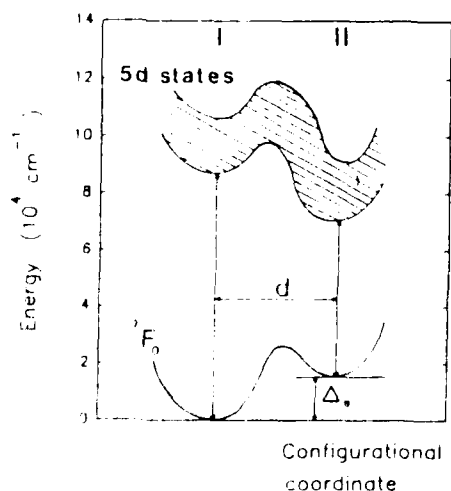
the local environment of the host by their Coulomb attraction of the nonbridging oxygen ions. This results in local environments with high nearest neighbor coordination numbers caused by the distortion of the rare earth ion on its surroundings. In producing this distortion, the trivalent rare-earth ion is in competition with the modifier ions of the host in attracting the nonbridging oxygen ions. Modifier cations in the second coordination sphere increase the rigidity of the host, thus hindering the free formation of the rare-earth ion environment. The success of this competition for attracting the nonbridging oxygen ions is determined by the relative field strengths of the rare earth and modifier ions. Thus, the larger the charge-to-radius ratio is for the rare-earth ion compared to that of the modifier ions, the more the rare earth ion will be able to distort its surroundings.

The above discussion can be used to understand the results listed in Table II. The asymmetry factor Δ_c for the double potential well is a measure of the ability of the rare earth ion to distort its local environment. If the rare-earth ion is able to freely distort its environment, it will form a very similar local environment at each site resulting in a small value for the asymmetry parameter. This is reflected in Table II which shows that the hosts with large modifier ions and thus low effective fields have small values for Δ_c whereas the hosts having small modifier ions with high electric fields have large values of Δ_c. This is also consistent with the results published previously for hosts with monovalent modifier ions.[2] The Δ_c values are larger for the glasses with divalent modifier ions compared to those found in similar glasses with monovalent modifier ions due to the higher local field strength of the former.

Although the results described here extend our under-standing of the formation of laser-induced permanent gratings in rare-earth-doped glasses, there are still several aspects of this phenomenon that require further investigation. The exact nature of the local surroundings of the rare earth ion on the atomic scale is still not known and finding the right rare earth-host glass combination to optimize this effect is still an important area of research. Further experiments are currently being performed using fluorescence line narrowing and micro-Raman spectroscopy.

[1] F. M. Durville, E. G. Behrens, and R. C. Powell, Phys. Rev. B 34, 4213 (1986); F. M. Durville, E. G. Behrens, and R. C. Powell, Phys. Rev. B 35, 4109 (1987); E. G. Behrens, F. M. Durville, and R. C. Powell, Opt. Lett. 11, 653 (1986).

[2] E. G. Behrens, F. M. Durville, and R. C. Powell, Phys. Rev. B 39, 6076 (1989).

[3] E. G. Behrens, R. C. Powell, and D. H. Blackburn, Appl. Opt. 29, 1619 (1990).

[4] H. Kogelnik, Bell System Tech. J. 48, 2909 (1969).

[5] R. C. Powell, S. A. Payne, L. L. Chase, and G. D. Wilke, Phys. Rev. B 41, 8593 (1990).

[6] L. Brewer, J. Opt. Soc. Am. 61, 1666 (1971).

[7] W. F. Krupke, Phys. Rev. 145, 325 (1966).

[8] V. I. Arbuzov, L. V. Viktorov, E. I. Galant, A. K. Przhevuskii, and M. N. Tolstoi, Sov. J. Phys. Chem. Glass 8, 223 (1982).

[9] E. G. Behrens, R. C. Powell, and D. H. Blackburn, J. Opt. Soc. Am. B 7, 1437 (1990).

A comparison of the spectroscopic properties of Eu³⁺-doped fluoride and oxide glasses under high-power, picosecond-pulse excitation

Gregory J. Quarles, Andrzej Suchocki,[a] and Richard C. Powell

Physics Department, Oklahoma State University, Stillwater, Oklahoma 74078-0444

The frequency harmonic outputs of a Nd:YAG laser were used to excite Eu³⁺ ions in fluoride and oxide glasses with high-power, picosecond pulses. Time-resolved fluorescence spectra, fluorescence lifetimes, and rise times were measured on the fluoride glass to obtain information about the two-photon absorption transitions and the radiative and radiationless decay processes. The results show the importance of coherence in the intermediate state of the two-photon transition observed with 532.0-nm pumping. Multiphoton pumping with 345.7-nm excitation results in spectral shifts and lifetime changes which are attributed to local polarization effects. Similar experiments were performed on the oxide glass, and the results were found to be significantly different because of the more efficient radiationless decay processes in the oxide host compared to the fluoride host.

I. INTRODUCTION

Time-resolved spectroscopy, with the use of high-power, picosecond-pulse excitation, has been shown to be an important technique for studying the spectral dynamics of trivalent rare-earth ions in solids.[1-6] We report the results of a detailed investigation of the spectroscopic properties of BZLT fluoride glass doped with Eu³⁺ ions with the use of the picosecond pulses from the primary and various harmonics of the output of a Nd:YAG laser as the source of excitation. In addition, similar measurements were made on Eu³⁺-doped lithium phosphate (LP) oxide glass to determine the effects of the host lattice on the spectroscopic properties with this type of excitation. The time-resolved fluorescence spectra, fluorescence lifetimes, and rise times were measured as a function of laser power for the various e···ation frequencies. The spectral properties are analyz.. in terms of single- and two-photon absorption processes and fluorescence from four different metastable states. These results are especially interesting, since little spectroscopic work has been reported on rare-earth ions in this type of fluoride glass host. The results obtained on the oxide glass differ greatly from those obtained on the fluoride glass because of higher efficiency of radiationless decay in the former type of material. These results on two-photon absorption processes in Eu³⁺ ions are significantly different than those reported previously for Nd³⁺. This is due to the fact that the initial and final states of the transition are of the same parity in the latter case, but not in the former one, and thus different types of intermediate states play an important role.

The nomenclature for different types of multiphoton absorption precesses has become somewhat confusing. In this work we use STEP to refer to a sequential two-photon excitation process in which the first photon causes a transition to a real intermediate state, and before relaxation can occur, the second photon excites the ion from this state to a higher state. VTEP is used for virtual two-photon excitation processes in which the intermediate state is a virtual state of the system. Finally, ESA is used to refer to excited-state absorption, which occurs when the first photon excites the ion to a real level, but relaxation to a metastable state occurs before the second photon is absorbed. All three types of processes have been observed in trivalent rare-earth ions in solids, and it is important to identify the specific type of process in order to determine the cross section for two-photon absorption (TPA).

The cross section for TPA processes can be expressed through second-order perturbation theory as[7]

$$\sigma = \sum_{\alpha,\beta} \left| \sum_j (C/\hbar)\langle f|p_\alpha|j\rangle \langle j|p_\rho|0\rangle / [\Delta\omega_j - i\Gamma_j] \right|^2, \quad (1)$$

where C contains various constant parameters and the density of final states, p is the electron momentum operator, α,β represent the states of polarization, $\Delta\omega_j$ is the detuning of the laser frequency from the peak of the transition from the ground state $|0\rangle$ to the intermediate state $|j\rangle$, and Γ_j is the natural linewidth of the intermediate state. The absolute magnitude of the denominator represents the upper limit of the interaction time for the TPA process. The type of process involved in TPA to a specific final state is determined by the matrix elements and interaction times involved with the different possible intermediate states included in the sum over $|j\rangle$. For trivalent rare-earth ions, the initial state has a $4f^n$ electron configuration, and the final state can either be another state of the same configuration or a state of the $4f^{n-1}5d$ configuration. For the former case, parity selection rules strongly favor virtual transitions to $5d$ intermediate states, despite close resonances of real transitions to $4f$ intermediate states. However, if the final state is part of the $4f^{n-1}5d$ configuration, real transitions to resonant $4f$ intermediate states or virtual transitions to $4f$ intermediate states with small detuning parameters can be important in the sum over $|j\rangle$. In this case the matrix elements are approximately the same for the different types of intermediate states, and the dominant terms in the sum depend on the interaction times. For virtual intermediate states, this is determined by

[a] Permanent address: Institute of Physics, Polish Academy of Sciences, Al. Lotnikow 32/46, 02-668 Warszawa, Poland.

the detuning from resonance and is typically of the order[7] of 10^{-14}–10^{-15} s. For real resonant intermediate states, the maximum interaction time can range between 10^{-5} and 10^{-9} s. If coherence is important in the overall TPA process, it is the dephasing time of the intermediate state that determines the maximum interaction time instead of the fluorescence lifetime of the level. Finally, if the laser excitation pulse is shorter than the maximum interaction, then the interaction time of the TPA process is given by the temporal pulse width of the laser. Each of these possibilities must be considered in determining the specific type of process involved in a TPA transition.

The experimental apparatus used for this work has been described previously.[1] A passively mode-locked Nd:YAG oscillator/amplifier laser with a pulse selector provided single excitation pulses with widths selectable between 25 and 200 ps in duration. The energy per pulse was approximately 25 mJ, and the appropriate frequency-doubling, -tripling, or -quadrupling crystals were used to obtain output at the various harmonic frequencies. The time-resolved spectroscopy measurements were made with two different experimental arrangements. One involved a combination of a monochromator, photomultiplier tube, and boxcar-signal averager combination, with the output sent to a strip-chart recorder. The second arrangement involved a monochromator, reticon detector, and an optical multichannel analyzer (OMA). All measurements were performed at room temperature.

The fluoride glass sample investigated in this work had dimensions of $1.82 \times 1.25 \times 0.18$ cm^3. Its composition[8] in mole percent was 27 ZnF$_2$, 19 BaF$_2$, 26 LuF$_3$, 27 ThF$_4$, and 1 EuF$_3$. The common designation for this glass is BZLT:Eu^{3+}. The oxide glass sample used for comparative studies had the dimensions $1.46 \times 1.25 \times 0.36$ cm^3. The composition of this sample in mole percent is 30 Li$_2$O, 52.3 P$_2$O$_5$, 10 CaO, 4.7 Al$_2$O$_3$, and 3.0 Eu$_2$O$_3$. It is designated as LP:Eu^{3+}.

II. EXPERIMENTAL RESULTS

Figures 1 and 2 show the energy levels and absorption spectrum for Eu^{3+} ions in BZLT glass along with the positions of the various laser frequencies used for pumping. The lower, sharp levels are associated with states of the 4f^6 electron configuration. The broad, overlapping bands above 27 000 cm^{-1} may either be due to states of the 4f^{5}5d electron configuration or to charge transfer states. For the fluoride glass host, the former seems more likely. The charge transfer bands should be very close to the band edge, while the 5d bands have been previously identified in Eu^{3+}-doped crystals with their peaks near 200 and 240 nm.[9] The latter is in agreement with the bands observed in this fluoride glass, and thus we refer to these bands as 5d bands, although the charge transfer assignment cannot be ruled out at this time. The absorption spectra for Eu^{3+} in the oxide glass in the visible region of the spectrum is similar to the fluoride glass. However, in this case the host band edge is at lower energy, and thus the charge transfer bands are shifted below the 5d bands[10] and appear as bands above 24 500 cm^{-1}.

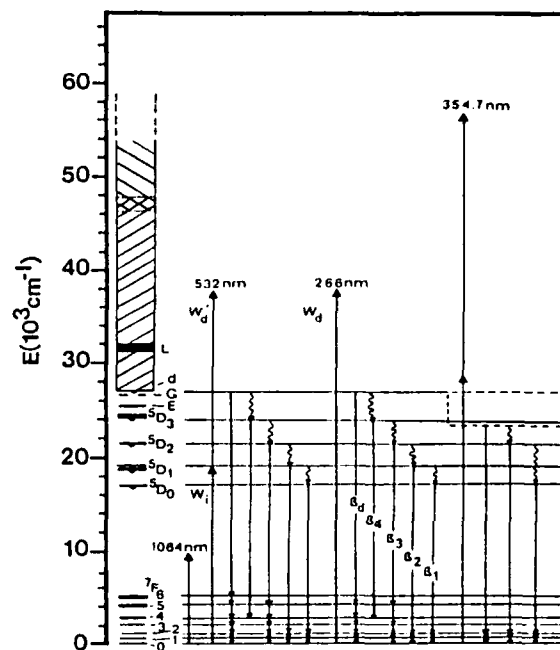The formulation of crystal-field-induced electric dipole

FIG. 1. Energy levels of the 4f^n and 4f^{5}5d configurations of Eu^{3+} in BZLT glass. The semicircles label the metastable states. The important absorption and emission transitions for the different excitation wavelengths used in this work are also shown. The solid lines represent excitation processes or radiative decay processes. The wavy lines denote the nonradiative decay processes. The broken horizontal lines show the shift in the position of the 5d level after very high-energy excitation. The β_i's denote the fluorescence decay rates and the W_j's the excitation rates.

transitions in the 4f^n configurations, as developed by Judd[11] and Ofelt,[12] was applied to the room-temperature absorption spectrum of the BZLT sample to determine parameters useful in the modeling of multiphoton spectroscopy. These parameters include the branching ratios, oscillator strengths, and radiative decay rates. The oscillator strength of a given transition of average frequency $\bar{\nu}$ from a level J to a level J' is expressed as

$$f(aJ;bJ') = (8\pi^2mc/3h)(\bar{\nu}/2J + 1)[XS_{ed}(aJ;bJ') + X'S_{md}(aJ;bJ')], \quad (2)$$

where the electric dipole and magnetic dipole line strengths are

$$S_{ed}(aJ;bJ') = \Sigma_{t=2,4,6}\Omega_t|\langle f^nJ||\bar{U}^{(t)}||f^nJ'\rangle|^2 \quad (3)$$

and

$$S_{md}(aJ;bJ') = (\hbar/2mc)^2|\langle f^nJ||\bar{L} + 2\bar{S}||f^nJ'\rangle|^2, \quad (4)$$

respectively. a and b represent other quantum numbers designating the states, f^n represents the electronic configuration, $\bar{U}^{(t)}$ is the tensor operator for electric dipole transitions, $\bar{L} + 2\bar{S}$ is the operator for magnetic dipole transitions, and the Ω_t are the Judd–Ofelt parameters that are associated with the crystal-field environment of the ion in the host lattice, which are determined by the analysis of the absorption spectrum. X and X' are the correction terms for the effective field in the crystal for electric and magnetic dipole transitions, defined, respectively, as

862   J. Appl. Phys., Vol. 63, No. 3, 1 February 1988
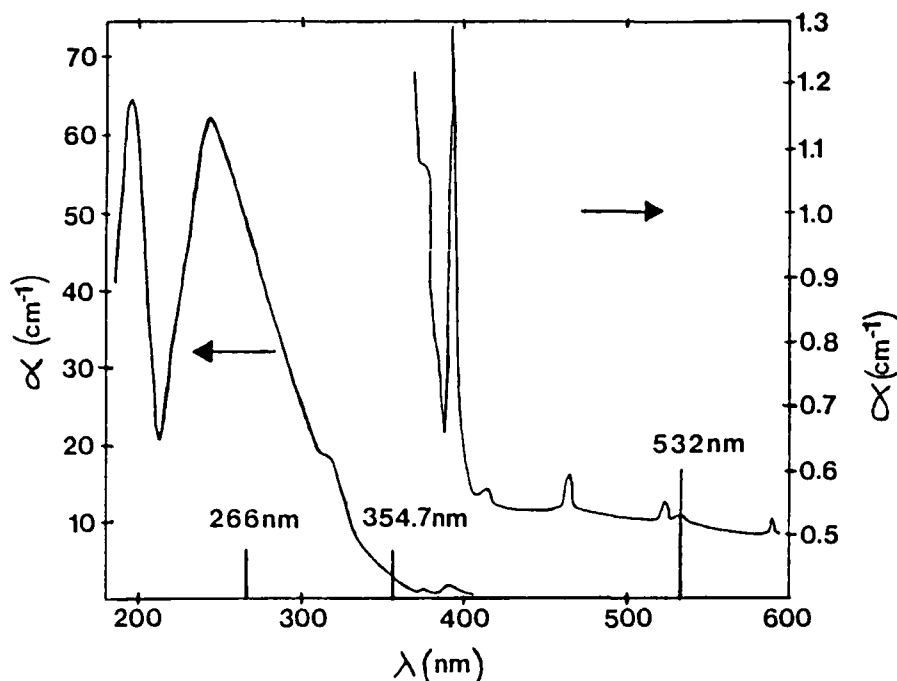
Quarles, Suchocki, and Powell   862

FIG. 2. Absorption spectrum of Eu^{3+} with the positions of the various laser excitation wavelengths shown. The BZLT sample used was 0.18 cm thick with a composition of 1.0 mol % of EuF$_3$.

$$X = (n^2 + 2)^2/9n$$

and

$$X' = n^3,$$

with n being the index of refraction of the host at the associated transition frequency. The reduced matrix elements in Eqs. (3) and (4) have been calculated previously[13–15] and are essentially invariant from host to host.

It is extremely difficult to make use of the Judd–Ofelt treatment for Eu^{3+} ions because of the exceedingly weak absorption and number of bands associated with totally forbidden and electric dipole forbidden transitions. Because of the limited number of weak absorption peaks in the fluoride glass sample, the Judd–Ofelt parameters for a very similar Eu^{3+}-doped fluoride glass were used in this evaluation.[13] These were found to be $\Omega_2 = 0.93 \times 10^{-20}$ cm^2, $\Omega_4 = 2.61 \times 10^{-20}$ cm^2, and $\Omega_6 = 2.17 \times 10^{-20}$ cm^2. By using these results, the spontaneous emission probability can be obtained for each transition from

$$A(aJ;bJ') = (64\pi^2\bar{\nu}^3)/[3hc^3(2J+1)]$$

$$\times [XS_{ed}(aJ;bJ') + X'S_{md}(aJ;bJ')]. \quad (5)$$

The branching ratios for transitions from each emitting level can then be related to the spontaneous emission coefficient through

$$\beta_{ij} = A_{ij}/\Sigma_j A_{ij}, \quad (6)$$

where the summation is over electric and magnetic dipole transitions to the final states j. The radiative lifetime for each emitting level can then be determined from

$$(\tau_i^{rad})^{-1} = \Sigma_j A_{ij}. \quad (7)$$

Table I lists the branching ratios, spontaneous emission coefficients, and radiative lifetimes of the excited states of Eu^{3+} ions in the fluoride glass.

TABLE I. Spectroscopic parameters of Eu^3 in BZLT fluoride glass (A_{ij} = spontaneous emission coefficient; β-branching ratio; T^{rad} = radiative lifetime).

Transition		A_{ij}(s^{-1})	β	T^{rad}(10^{-3}s)
$^5D_3$	$> {}^5D_2$	0.532	0.007	
	$^5D_1$	1.827	0.0244	
	$^5D_0$	0.0	0.0	
	$^7F_6$	0.0	0.0	
	$^7F_5$	10.662	0.1427	
	$^7F_4$	14.122	0.1890	
	$^7F_3$	9.866	0.1320	
	$^7F_2$	21.914	0.2933	
	$^7F_1$	15.797	0.2114	
	$^7F_0$	0.0	0.0	13.383
$^5D_2$	$> {}^5D_1$	0.095	0.0013	
	$^5D_0$	0.516	0.0070	
	$^7F_6$	0.485	0.0066	
	$^7F_5$	9.820	0.1331	
	$^7F_4$	8.638	0.1171	
	$^7F_3$	30.290	0.4105	
	$^7F_2$	20.378	0.2762	
	$^7F_1$	0.426	0.0058	
	$^7F_0$	3.143	0.0426	13.552
$^5D_1$	$> {}^5D_0$	0.163	0.0024	
	$^7F_6$	0.624	0.0090	
	$^7F_5$	4.344	0.0627	
	$^7F_4$	21.124	0.3050	
	$^7F_3$	29.002	0.4188	
	$^7F_2$	3.006	0.0434	
	$^7F_1$	10.988	0.1587	
	$^7F_0$	0.0	0.0	14.440
$^5D_0$	$> {}^7F_6$	1.951	0.0138	
	$^7F_5$	0.0	0.0	
	$^7F_4$	42.958	0.3038	
	$^7F_3$	0.0	0.0	
	$^7F_2$	30.224	0.2137	
	$^7F_1$	66.384	0.4694	
	$^7F_0$	0.0	0.0	37.267

Attempts to excite fluorescence of the BZLT:Eu^{3+} glass with multiphoton absorption of the primary 1064-nm radiation were unsuccessful. The doubled output at 532.0 nm resulted in single-photon absorption to the $^5D_1$ level and two-photon absorption into the $5d$ configuration band for this sample. The quadrupled output at 266.0 nm results in single-photon absorption into the $5d$ configuration band of this sample and no observed two-photon absorption. The tripled output at 354.7 nm gives a single-photon absorption into the $5d$ configuration band followed by multiphoton absorption above the band edge of the fluoride sample. For the oxide host, essentially no multiphoton processes were detected for any of the different excitation conditions. For the doubled, tripled, and quadrupled Nd-YAG laser excitation, the observed fluorescence of LP:Eu^{3+} originated almost entirely from the $^5D_0$ metastable state with very little higher-energy emission, even for the UV pumping. The fluorescence spectra and lifetimes observed with the various pumping wavelengths are described below

A. Results for 266.0-nm pumping

Figure 3 shows the BZLT:Eu^{3+} fluorescence spectra obtained at two different times after the 25-ps excitation pulse for quadrupled Nd-YAG laser pumping at 266.0 nm. The spectral resolution of the laser lines used for excitation is approximately $\pm$ 1 cm^{-1}. Observation of the emission in-
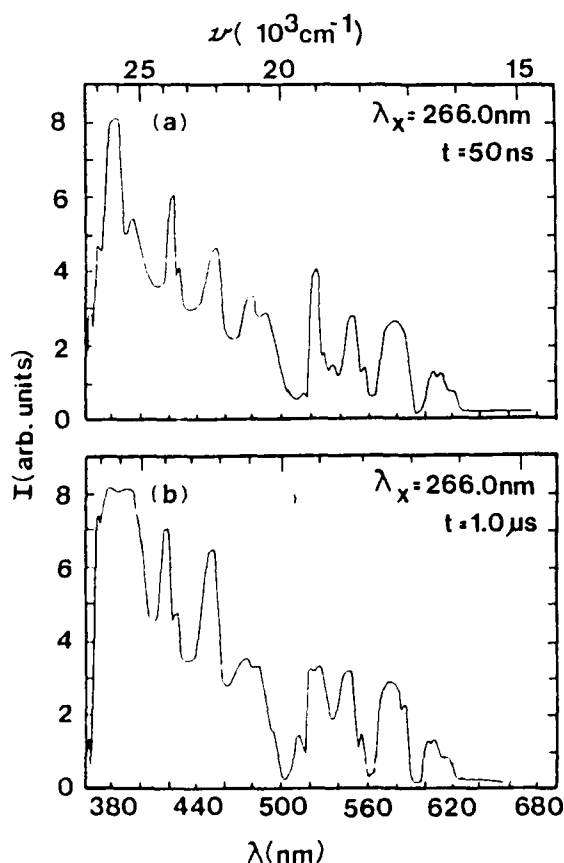

FIG. 3. Fluorescence spectra of BZLT:Eu^{3+} glass at two times after the excitation pulse at 266.0 nm, (a) 50 ns and (b) 1.0 µs.

tensity for all lines shows a linear dependence with pump power, thus indicating that single-photon absorption is responsible for exciting all of these transitions. The fluorescence emission includes transitions originating from all the various ^5D_J levels, as well as from the $5d$ configuration level. Each of the five groups of lines in Fig. 3, corresponding to the five different fluorescing states, has its own characteristic lifetime.

Figures 1 and 2 show that the 266.0-nm excitation directly pumps the $5d$ configuration level. Part of the excitation energy decays radiatively from the $5d$ level to the various ^7F_J multiplets of the ground-state term, while the rest of the excitation energy cascades down to the ^5D_J levels by fast radiationless relaxation processes. The fluorescence lifetime of the $5d$ level is measured to be 70 ns. The $^5D_{3,2,1,0}$ levels all have radiative transitions to the ground-state multiplets with fluorescence lifetimes of 1.57, 1.42, and 1.24 µs, and 5.94 ms, respectively. All of the lifetimes plotted were single exponential over two decades and have maximum error bars of $\pm$ 2%. The fast nonradiative decay rate from $^5D_3$ to $^5D_2$ is determined from the rate equations described below to be 6.1×10^5 s^{-1}. This value is almost identical to the rate of 6.3×10^5 s^{-1} given by the Judd–Ofelt analysis. For 266.0-nm pumping, a rise time of approximately 2 µs occurs when observing the $^5D_0$-$^7F_2$ emission transitions. With the use of Weber's model[16] for a cascading decay process, the theoretical estimate of this rise time should be < 10 µs, which is consistent with the observed result. Fluorescence from the $^5D_{2,1,0}$ levels of Eu^{3+} is well known in other hosts, but the observation of fluorescence from the $^5D_3$ and $5d$ levels is unusual. The fluorescence lifetimes and rise times for each of the metastable states are listed in Table II for these pumping conditions.

The time evolution of the fluorescence spectra shown in Fig. 3 can be described by the rate model shown in Fig. 1. The rate equations describing the time evolution of the excited-state populations are given by

$$\frac{dn_d}{dt} = W_d - \beta_d n_d, \tag{8}$$

$$\frac{dn_4}{dt} = \beta_d^{nr} n_d - \beta_4 n_4, \tag{9}$$

$$\frac{dn_3}{dt} = \beta_4^{nr} n_4 - \beta_3 n_3, \tag{10}$$

$$\frac{dn_2}{dt} = \beta_3^{nr} n_3 - \beta_2 n_2, \tag{11}$$

$$\frac{dn_1}{dt} = \beta_2^{nr} n_2 - \beta_1 n_1. \tag{12}$$

The n_i's represent the concentrations of ions in the various excited states, the β_i's are the fluorescence decay rates of these levels, the β_i^{nr}'s refer to the nonradiative decay rates, and W_d is the pumping rate of the $5d$ configuration level. Table I shows from the Judd–Ofelt analysis that nonradiative decay is dominant between the $^5D_3$, $^5D_2$, and $^5D_1$ metastable states, whereas radiative decay is the dominant process from the $^5D_0$ state to the ground-state components.

With the assumption of a delta function excitation pulse, these equations can be solved to give the time evolu-

864   J. Appl. Phys., Vol. 63, No. 3, 1 February 1988

Quarles, Suchocki, and Powell   864

TABLE II. Characteristics of metastable states of Eu^{3+} in BZLT ($\Delta t = 25$ ps; $T = 300$ K).

Parameter	Level				
	$^5D_0$	$^5D_1$	$^5D_2$	$^5D_3$	$5d$
Fluorescence lifetimes $\tau_f (\mu s)$					
$\lambda_{ex} = 266$ or	5940	1.24	1.42	1.57	0.07
532 nm					
$\lambda_{ex} = 354.7$ nm[a]	0.57		0.71		0.82
	0.26		0.34		0.18
Fluorescence rise times $t_m (\mu s)$					
$\lambda_{ex} = 266$	1.8	<0.35	0.28	0.06	0.03
532 nm	2100				0.03
$\lambda_{ex} = 354.7$ nm	...		0.05		0.03

[a] The fluorescence consisted of the superposition of sharp lines and a broadband.

tion of the excited-state populations. The observed fluorescence intensities from the ith level can be expressed as the product of the population of the level and its radiative decay rate β_i'. The solution of Eqs. (8) and (9) gives the ratio of intensities of the $5d$ and $^5D_3$ levels as

$$I_d(t)/I_4(t) = K(\beta_4 - \beta_d)\{1 - \exp[(\beta_d - \beta_4)t]\}^{-1},$$
(13)

where $K = [\beta_d'/(\beta_d^{nr}\beta_4')]$. Figure 4 shows the ratios of the integrated fluorescence intensities of all of the $5d$ transitions to the ground state and the visible transitions from the $^5D_3$ metastable state. By fitting Eq. (13) to the measured time evolution of the ratios of the fluorescence intensities, after correcting for quantum efficiencies, branching ratios, and the spectral sensitivity of the equipment, the value of K can

be determined The best fit shown by a solid line in Fig. 4 was obtained with a value of $K = 3.4 \times 10^{-6}$ s.

From the value of K obtained from the TRS results, it is possible to obtain the radiative decay rate from the $5d$ configuration level. The values needed for evaluation are the branching ratios for the $^5D_3$ metastable state, and these are available through the Judd–Ofelt analysis of the absorption spectrum. Use of the branching ratios, along with the measured value of the fluorescence lifetime of the $5d$ level, gives an estimate for the radiative decay rate for the $5d$ level of $9.72 \pm 2.14 \times 10^6$ s^{-1}.

Figure 5(a) shows the LP:Eu^{3+} fluorescence spectrum at 50 μs after the 266.0-nm excitation pulse. The fluorescence from the $^5D_0$ metastable state to the $^7F_{0,1,2,3,4}$ multiplets of the ground term is much stronger in the oxide glass than in the fluoride glass. The measured fluorescence lifetime of the $^5D_0$ level is 3.15 ms for this sample and is also purely single exponential. There is some very weak fluorescence from the $^5D_2$ and $^5D_1$ metastable states, as well as some weak broadband fluorescence at higher energies, which may be associated with charge transfer transitions. The signal from the weak fluorescence transitions was too small to obtain accurate fluorescence lifetime measurements. A comparison of the Eu^{3+} fluorescence in the oxide and fluoride glass hosts for this type of excitation shows that radiationless relaxation processes are more efficient in the oxide glass, which is consistent with previous results obtained by using other types of excitation.[17-19]
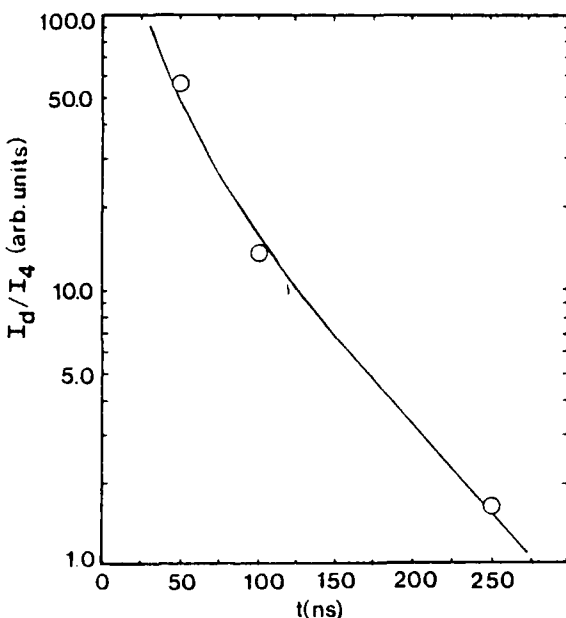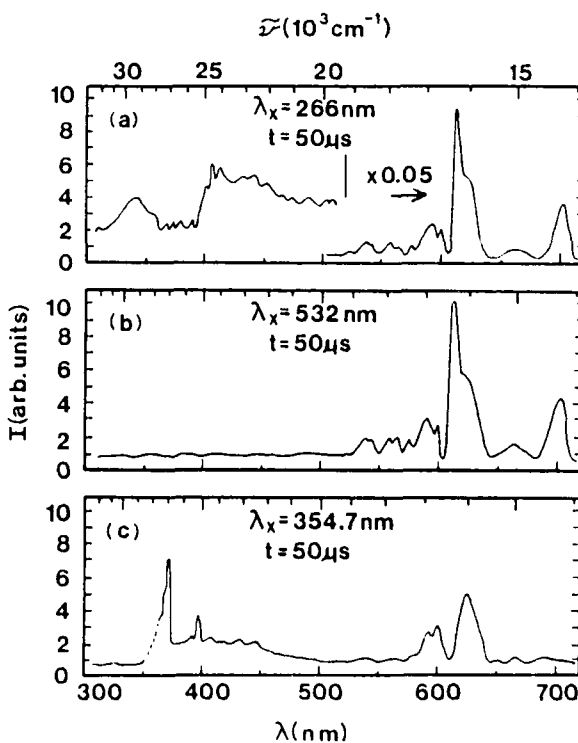

FIG. 4 Theoretical fitting and experimental points for the time evolution of the ratios of the integrated fluorescence intensities of the emission from the $5d$ level and $^5D_3$ metastable state after 266.0-nm excitation.

FIG. 5 Fluorescence spectra of LP:Eu^{3+} glass at 50 μs after the pulse for excitation at (a) 266 nm, (b) 532 nm, and (c) 354.7 nm.

B. Results for 532.0-nm pumping

Figure 6 shows the fluorescence spectra at two different times after the laser excitation pulse for doubled Nd-YAG laser pumping at 532.0 nm. The same lines appear in the spectra as seen in Fig. 3, but their relative intensities are different and change with excitation power. Figure 7 shows the variation in the integrated fluorescence intensity of the emission line near 515.0 nm as a function of excitation energy per pulse. The observed quadratic dependence indicates that this fluorescence transition is excited under these pumping conditions by two-photon absorption terminating on a level of the $5d$ configuration. The fluorescence transitions from all of the metastable states are the same as those discussed in the preceding section following single-photon pumping of the $5d$ level. As seen in Fig. 1, the intermediate state for this two-photon transition is one of the Stark components of the $^5D_1$ level, which can be directly pumped through one-photon absorption processes at this excitation wavelength. Only part of the ions excited to this intermediate state will absorb a second photon, while the rest will decay either radiatively to the ground state or radiationlessly to the $^5D_0$ level from which fluorescence emission occurs to the ground-state multiplets.

As shown in Table II, the rise time of the fluorescence decay profiles for the $^5D_0$-$^7F_2$ transition is measured to be 2.1 ms, with a 5.9-ms decay time. The decays occurring after the

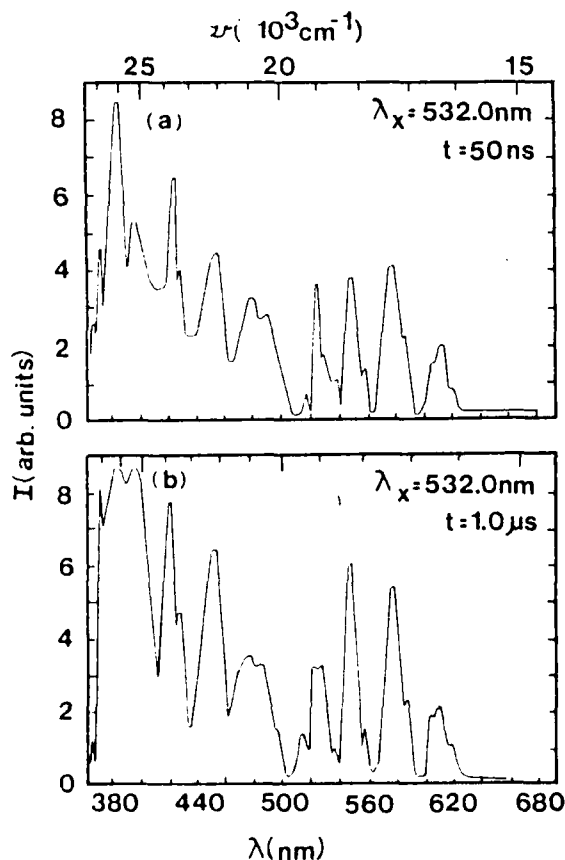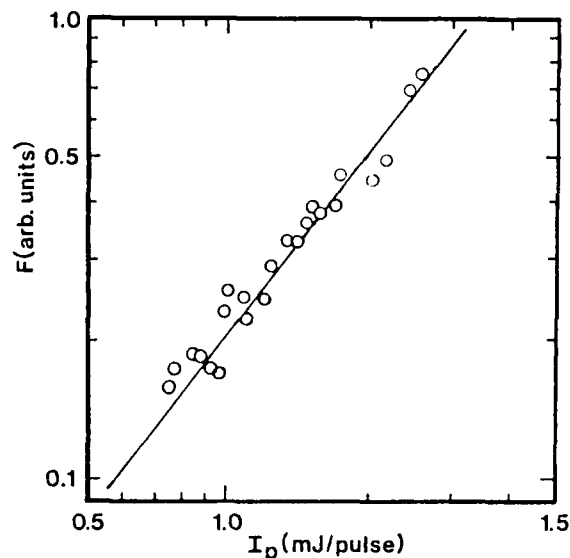FIG. 7. Integrated fluorescence intensity of the 515.1-nm spectral line as a function of laser energy at 532.0-nm excitation with a 25-ps pulse.

FIG 6 Fluorescence spectra of BZLT Eu^{3+} glass at two different times after the excitation pulse at 532.0 nm. (a) 50 ns and (b) 1.0 μs.

initial rise were observed to be single exponential. The observed rise time is much longer than expected for a direct nonradiative transition from the $^5D_1$ level. Longer than normal rise times of fluorescence from the $^5D_0$ level have been observed previously[19,20] and have been attributed to intersite energy transfer. Similar processes could also be important for the glass host. The laser excitation in resonance with the absorption transition to the $^5D_1$ level can selectively excite ions in specific host environments.[20] This is possible since the laser linewidth (< 0.5 Å) is much less than the widths of the excited electronic levels (approximately 100 Å). The long rise time was found to be independent of the power of the laser excitation, indicating that it is not specifically associated with multiphoton processes.

Figure 5(b) shows the LP:Eu^{3+} fluorescence spectrum at 50 μs after the 532.0-nm excitation pulse. As with 266.0-nm excitation, there is a strong fluorescence from the $^5D_0$ level and only weak emission from the $^5D_1$ level. No fluorescence can be observed from any of the higher levels, indicating that no multiphoton absorption processes are occurring. The fluorescence lifetime of the $^5D_0$ levels is 3.15 ms, also found to be single exponential, and the rise time is 600 μs. The latter is again anomalously long for simple radiationless relaxation processes. The LP glass and a similar Eu^{3+}-doped fluoride glass were studied previously[21] under different excitation conditions. The results indicated that the lifetimes remained single exponential and fairly constant across the fluorescence band. The energy transfer among the Eu^{1+} ions was measured to be weak and thus did not strongly effect the observed decay kinetics, although it can contribute to the initial rise of the fluorescence.

A simplified rate diagram for describing the pumping and decay dynamics under these excitation conditions is similar to that shown for 266.0-nm pumping in Fig. 1. The parameters are the same as those previously used, except there are the additional parameters W_i to describe the initial

single-photon pumping rate of the $^5D_1$ level and the second photon rate of the $5d$ level given by W'_d. Thus Eqs. (8) and (11) now become

$$\frac{dn_d}{dt} = W'_d - \beta_d n_d,\qquad(14)$$

$$\frac{dn_2}{dt} = W_t + \beta_3^{nr} n_3 - \beta_2 n_2,\qquad(15)$$

with Eqs. (9)–(11) remaining the same. Once again, the solutions of Eqs. (14) and (15) for δ-function excitation can be related to the measured relative fluorescence intensity ratios through

$$I_2(t)/I_3(t) = \{A + B\}/C,\qquad(16)$$

where the variables A, B, and C are given by

$$A = n_2(0)\beta'_2 \exp(-\beta_2 t),\qquad(17)$$

$$\begin{aligned}B = n_d(0)\beta'_2\beta_3^{nr}\beta_4^{nr}\beta_d^{nr}\{[\exp(-\beta_3 t)]/[(\beta_2-\beta_3)(\beta_4-\beta_3)(\beta_d-\beta_3)]\\ + [\exp(-\beta_4 t)]/[(\beta_2-\beta_4)(\beta_3-\beta_4)(\beta_d-\beta_4)] + [\exp(-\beta_d t)]/[(\beta_2-\beta_d)(\beta_3-\beta_d)(\beta_4-\beta_d)]\},\end{aligned}\qquad(18)$$

$$\begin{aligned}C = n_d(0)\beta'_3\beta_4^{nr}\beta_d^{nr}\{[\exp(-\beta_3 t)]/[(\beta_d-\beta_3)(\beta_4-\beta_3)]\\ + [\exp(-\beta_4 t)]/[(\beta_3-\beta_4)(\beta_d-\beta_4)] + [\exp(-\beta_d t)]/[(\beta_3-\beta_d)(\beta_4-\beta_d)]\}.\end{aligned}\qquad(19)$$

A simplified expression describing the ratio of the initial populations of the $5d$ and $^5D_1$ levels is given by evaluating Eq. (16) at long times after the excitation pulse. This evaluation is made possible with a few minor assumptions. Since it is experimentally determined that $\beta_2 \approx \beta_3 \approx \beta_4 \ll \beta_d$, then as $t \to \infty$, the exponentials involving β_d will become negligible, and we can assume that $\beta_2 \doteq \beta_3 \doteq \beta_4$. Likewise, since $\beta_2 \approx \beta_3$ and the Judd–Ofelt analysis shows that $\{\beta'_2/\beta'_3\} \approx 1$, our expression simplifies to

$$[I_3(t)/I_2(t)]|_{t\to\infty}$$
$$= \gamma\beta_d^{nr}\beta_4^{nr}\{[n_d(0)/n_2(0)] - \alpha\beta_3^{nr}\},\qquad(20)$$

where $\gamma = 3.9\times10^{-15}$ s^2 and $\alpha = 3.7\times10^{-2}$ s. We may then use the values of the intensity ratios at long times after the pulse to find the initial populations of the levels.

Figure 8 shows the ratios of the integrated fluorescence intensities of all of the $5d$ transitions and the visible transitions from the $^5D_1$ level in the fluoride glass for two different pulse widths. The data indicate that the relative values of the initial populations of the $5d$ and $^5D_1$ levels are approximately independent of the excitation pulse width. This indicates either that the maximum possible interaction time for the TPA process is much longer than the laser pulse width, so that no change in the intermediate state occurs during the time of the experiment, or that any transient changes in the properties of the intermediate state occur very rapidly with respect to the excitation pulse width.

By using the measured asymptotic values for the intensity ratios and Eq. (20), the initial population ratios are determined. These values of the initial population ratios can then be used to calculate the cross section for the second part of the TPA transition. The expression for this is[1]

$$\sigma_{2d}(\text{cm}^2) = [n_d(0)/n_2(0)](h\nu_2/h\nu_d)$$
$$\times [\Delta t/(0.375)I_p](\xi),\qquad(21)$$

where Δt is the laser pulse width, and I_p is the photon flux per pulse. A major simplification used in Eq. (21) is the use of the simplified expression $P(t) = (0.375/\Delta t)$ for the pulse-time dependence, instead of the full Gaussian expression

$$P(t) = (0.375/\Delta t)\exp\{-2.77[(t-t_0)/\Delta t]^2\}.\qquad(22)$$

In order to evaluate the cross section for the second step in the TPA process, it is necessary to estimate a value for the rate of interaction in the intermediate state, ξ. The fluorescence lifetimes of the ^5D_J metastable states are all much greater than the laser pulse widths. Use of either of these lifetimes or the time of the laser pulse as the effective interaction time gives values for the cross sections which are several orders of magnitude smaller than the values expected for f-f transitions. Thus ESA and STEP transitions with incoherent intermediate states can be eliminated as the type of TPA
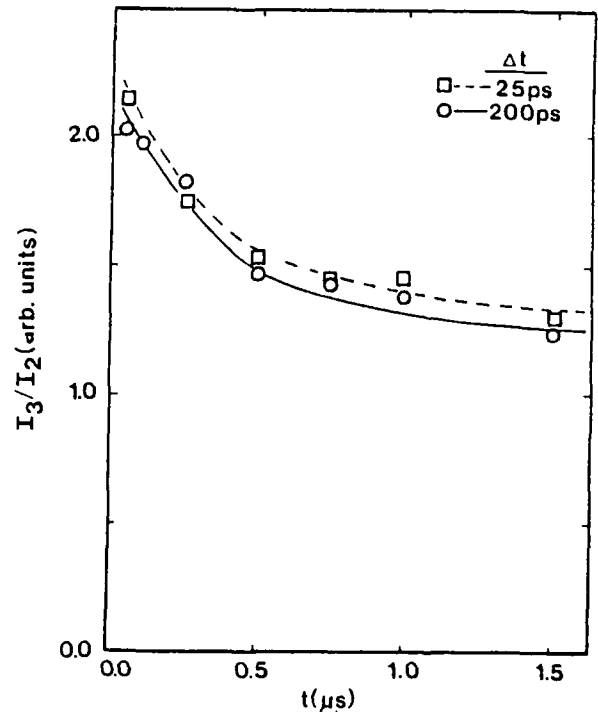

FIG. 8. Time evolution of the ratios of the integrated fluorescence intensities of the emission from the $^5D_2$ and $^5D_1$ metastable states after 532.0-nm excitation for two different pulse widths Δt.

867   J. Appl. Phys. Vol. 63, No. 3, 1 February 1988

Quarles, Suchocki, and Powell   867

process. For a transition involving a virtual intermediate or coherent TPA process with a real resonant intermediate state, the coherence times have been found to be in the range 10^{-12}–10^{-15} s.[22] This can be estimated by considering the spectral line shape of the absorption transition from the ground state to the possible intermediate states. According to Eq. (1), the dephasing time will then be the maximum time for TPA involving a real intermediate state. For transitions involving virtual intermediate states, the maximum interaction time is less than the coherence time by an amount determined by the detuning from resonance. In our case the single-photon absorption terminates on the edge of an absorption band due to a transition terminating on one of the Stark-split components of the $^5D_1$ metastable state. However, there are other levels with small detuning parameters, such as the other Stark components of $^5D_1$, which can have interaction times equal to or greater than that of the resonant interaction and thus cannot be neglected in the sum over intermediate states in Eq. (1). The measured transition linewidths in the absorption spectrum were used to estimate the coherence times.

This analysis gives a value of $\xi = 4.6 \times 10^{13}$ Hz for the resonant transition, which provides an upper limit for the interaction time, since at room temperature the linewidths should be a combination of homogeneous broadening due to phonon processes and inhomogeneous broadening due to the disorder in the glass host. For nearby off-resonance transitions, the measured coherence time is somewhat greater, but inclusion of the detuning parameter leads to similar interaction times. Thus the value found for ξ is used as an estimate of the interaction time. By using this value along with the values of the population ratios obtained from Eq. (20) and the excitation pulse intensity and width, Eq. (21) gives the values of the cross secitons for the second transitions in the TPA processes. The magnitudes are somewhat larger than those of ground-state absorption transitions, because they are parity allowed. This indicates that the TPA processes are either VTEP processes or a coherent STEP process in which fast phonon dephasing processes that broaden the intermediate level without shortening its lifetime are important in determining the cross section of the second step in the TPA processes.

Figure 9 shows the variation of σ_{2d} with excitation pulse width for the BZLT sample. The linear relationship between the cross section and laser pulse width is consistent with Eq. (21), and the magnitude is consistent with having a fast interaction time compared to the pulse width.

C. Results for 354.7-nm pumping

Figure 10 shows the fluorescence spectra at two different times after the excitation pulse for tripled Nd:YAG laser pumping at 354.7 nm. The lifetimes of the transitions are listed in Table II. This emission is quite different from that observed with 532.0- or 266.0-nm pumping. The wavelengths of the emission transitions are at different positions, and the lifetimes are different. Each of the three sets of fluorescence peaks involves a double exponential decay with a very fast rise time. For example, the 410-nm peaks have a
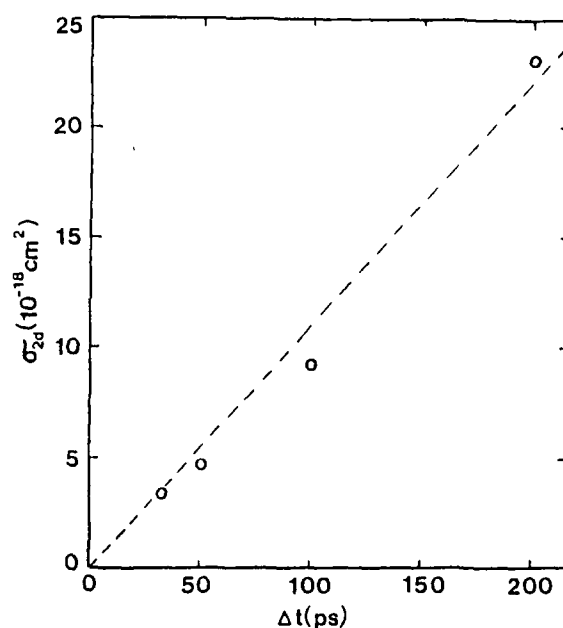

FIG. 9. Variation of the absorption cross section of the excited-state part of the STEP transition vs laser pulse width for 532.0-nm excitation.

longer decay component of 819 ns, a faster component of 179 ns, and a rise time of approximately 30 ns. The other two sets of peaks show similar lifetimes and rise times, which are listed in Table II.
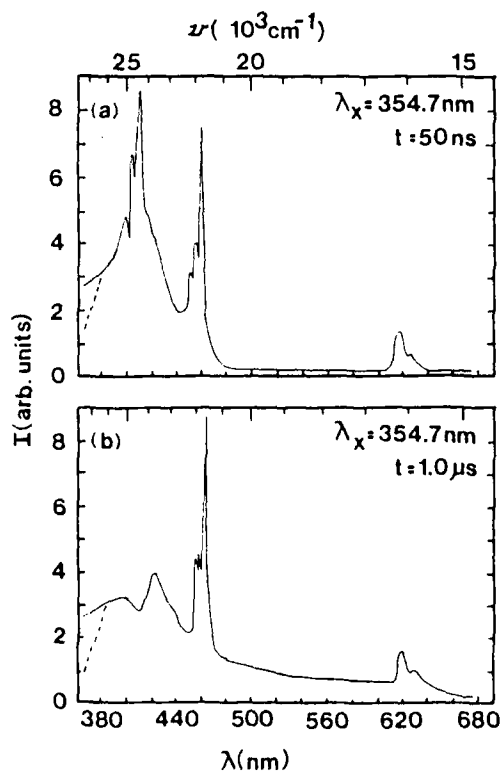

FIG. 10. Fluorescence spectra of BZLT:Eu^{3+} glass at two different times after the excitation pulse at 354.7 nm, (a) 50 ns and (b) 1.0 μs. The dashed line on the high-energy edge denotes the corrected spectra after the overlap with the 354.7-nm exciting light is taken into account.

The double exponential decays, rise times, shift in transition wavelengths, and reduction in the number of emission peaks indicate that there is a change in the configuration coordinates describing the energy levels for these pumping conditions. This may be associated with a multiphoton excitation process terminating at an energy far above the band edge. During the time the electron is in this highly excited state, the interaction of the ion with its surroundings will change through local polarization effects. The electron decays back down to the various metastable states, and fluorescence occurs before the surrounding lattice has time to relax back to its equilibrium condition. It appears that in this polarized state of the local site of the ion, the $5d$ configuration level is shifted, so that the bottom of its potential well falls below that of the $^5D_3$ metastable state. With these conditions, no fluorescence comes from the latter level. Likewise, it is possible that multiphoton excitation with 354.7 nm lifts the electron into the charge transfer band located above 200 nm. Following this excitation, radiative transitions come from either the charge transfer states of the $5d$ band, in addition to the ^5D_J levels. If there is a combination of radiative relaxation from both the charge transfer states and $5d$ bands, this could account for the double exponential decay curves observed with each transition. Single-photon excitation by 354.7-nm light in the LP:Eu^{3+} glass directly pumps the charge transfer state and gives a similar spectra to that seen in the fluoride glass. This spectrum, shown in Fig. 5(c), is taken at 50 μs after the 25-ps pulse. One difference is that the lifetimes in the oxide glass remain single exponential, indicating that there is no transfer or overlap between the $5d$ and charge transfer states. A schematic drawing of this model describing the change in the configuration coordinates is shown in Fig. 11. This model is a qualitative model for describing the changes after 354.7-nm excitation. More work needs to be done to better understand the shifts in emission and changes in lifetimes. Future work is planned when the addition of a picosecond dye laser attachment is completed.

III. DISCUSSION AND CONCLUSIONS

Picosecond-pulse excitation is an important experimental method for characterizing the spectral dynamics of ions in solids. The time-resolved spectroscopy technique provides a useful means through which two-photon absorption cross sections can be determined. These results, coupled with measurements of the excitation pulse-width dependence of the cross section, allow the mechanism of two-photon absorption to be identified.

The results show that Eu^{3+} ions in BZLT fluoride glass emit fluorescence from higher metastable states of the $4f^6$ configuration and from the lowest level of the $5d$ configuration. This implies weak electron-phonon interaction in BZLT:Eu^{3+} compared to many oxide glass hosts that exhibit fluorescence only from the $^5D_0$ level, or the $^5D_1$ and $^5D_0$ levels after radiationless relaxation from higher excited states.[23] Characterizing the properties of the $4f^5 5d$-$4f^6$ interconfigurational transition is especially interesting, since this has not been extensively studied, whereas the CTS of oxide glasses similar to the LP glass have typically been more closely studied. High-power, picosecond-pulse excitation
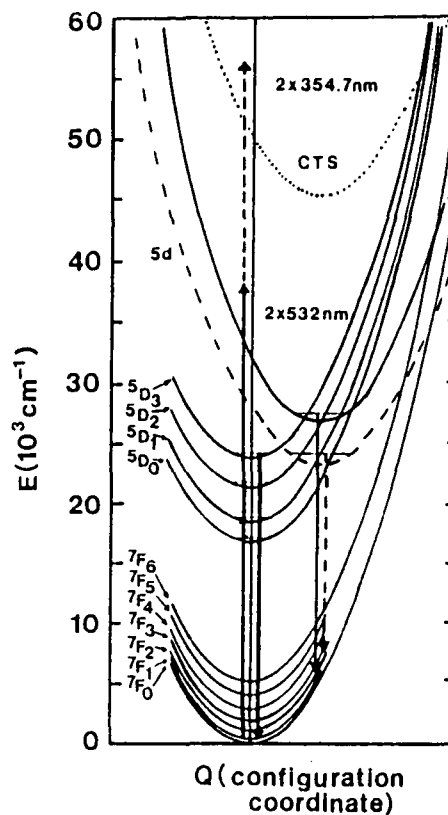

FIG. 11. Configuration coordinate diagram describing the changes in the BZLT:Eu^{3+} fluorescence after multiphoton, 354.7-nm pumping. The solid lines represent the location of the levels after 266.0- and 532.0-nm excitation. The broken line schematically represents the shift in the $5d$ potential well due to local polarization effects following the multiphoton 354.7-nm pumping. The dotted line indicates the position of the charge transfer band above the $5d$ level.

produces two-photon absorption in the BZLT glass, which was shown to take place through a mechanism involving a coherent intermediate state. The cross section for the second photon absorption in the TPA process is found to be significantly greater than that of the first photon absorption. This is because the former involves an f-d transition with a large density of final states, while the latter is an f-f transition with a small density of final states.[24] The results obtained on Eu^{3+} in the oxide glass provide less information on the spectral dynamics associated with high-power, picosecond pumping. This is due to the fact that the faster radiationless decay processes in the oxide host result in strong fluorescence emission only in the lowest metastable state. This demonstrates one limiting aspect of the time-resolved spectroscopy technique used here: it depends on having fluorescence emission from levels pumped only by two-photon absorption transitions as well as emission from levels pumped by one-photon absorption.

No evidence of ESA processes was found for the fluoride glasses under these excitation conditions, and no VTEP were observed when the excitation wavelength was not very close to resonance with a real single-photon transition. Multiphoton excitation to energies well above the band gap of the host allows a local distortion of the lattice to occur which leads to

Eu^{3+} fluorescence from a distorted crystal-field environment, giving rise to very different spectral properties. These types of spectral shifts and lifetime changes have been observed in other types of materials under conditions of high-energy excitation.[25]

Comparison of the results obtained on Eu^{3+} with those reported previously on Nd^{3+} shows that the type of TPA process taking place in trivalent rare-earth ions under similar excitation conditions can be quite different, depending on the nature of the final state of the transition. The latter case involved *f-f* transitions, and a resonant transition to a real *f* intermediate state was found to dominate the sum over intermediate states. The former case involves *f-d* transitions, and virtual or coherent real *f* intermediate states were found to be important in the TPA transition.

ACKNOWLEDGMENTS

[1]G. J. Quarles, G. E. Venikouas, and R. C. Powell, Phys. Rev. B **31**, 6935 (1985); G. E. Venikouas, G. J. Quarles, J. P. King, and R. C. Powell, Phys. Rev. B **30**, 2401 (1984).

[2]M. A. Kramer and R. W. Boyd, Phys. Rev. B **23**, 986 (1981).

[3]T. Y. Fan and R. L. Byer, J. Opt. Soc. Am. B **3**, 3454 (1986).

[4]A. Lezama and C. B. De Araujo, Phys. Rev. B **33**, 3221 (1986).

[5]L. E. Kholodenkov and A. G. Makhanek, Phys. Status Solidi B **125**, 365 (1984).

[6]O. K. Moune-Minn and P. Procher, C. R. Acad. Sci. (Paris) **300**, 203 (1985).

[7]I. Tanaka and M. Kawasaki, in *Advances in Multiphoton Photon Processes and Spectroscopy*, edited by S. H. Lin (World Scientific, Singapore, 1984), Vol. 1, p. 239.

[8]M. G. Drexhage, O. H. El-Bayoumi, C. T. Moynihan, A. J. Bruce, K.-H. Chung, D. L. Gavin, and T. J. Loretz, Commun. Am. Ceram. Soc. **5**, C-166 (1982).

[9]N. C. Chang, J. Appl. Phys. **34**, 3500 (1963).

[10]R. Reisfeld, Struct. Bonding **13**, 30 (1973).

[11]B. R. Judd, Phys. Rev. **127**, 750 (1962).

[12]G. S. Ofelt, J. Chem. Phys. **37**, 511 (1962).

[13]W. T. Carnall, P. R. Fields, and K. Rajnak, J. Chem. Phys. **49**, 4450 (1968).

[14]R. Reisfeld, E. Greenberg, R. N. Brown, M. G. Drexhage, and C. K. Jorgensen, Chem. Phys. Lett. **95**, 91 (1983).

[15]B. Blanzant, L. Boehm, C. K. Jorgensen, R. Reisfeld, and N. Spectro, J. Solid State Chem. **32**, 185 (1980).

[16]M. J. Weber and R. F. Schaufele, J. Chem. Phys. **43**, 1702 (1965).

[17]L. A. Riseberg and M. J. Weber, Prog. Opt. **14**, 89 (1972).

[18]C. Layne and M. J. Weber, Phys. Rev. B **16**, 3259 (1972).

[19]C. Brecher and L. A. Riseberg, Phys. Rev. B **21**, 2607 (1980).

[20]R. B. Hunt, Jr. And R. G. Pappalardo, J. Lumin. **34**, 133 (1985).

[21]X. Gang and R. C. Powell, J. Appl. Phys. **57**, 1227 (1985).

[22]S. Yatsiv, W. G. Wagner, G. S. Picus, and F. M. McClung, Phys. Rev. Lett. **15**, 614 (1965).

[23]Yu. V. Denisov, I. V. Kovaleva, V. P. Kolobkov, and V. V. Rastoskuev, Opt. Spectrosc. **38**, 54 (1975).

[24]J. D. Axe, Jr., Phys. Rev. **136**, A42 (1964).

[25]D. S. McClure and C. Pedrini, Phys. Rev. B **32**, 8465 (1985); S. A. Payne, A. B. Goldberg, and D. S. McClure, J. Chem. Phys. **81**, 1529 (1984); C. Pedrini, F. Rogemond, and D. S. McClure, J. Appl. Phys. **38**, 2379 (1986).

Photorefractive properties of KNbO₃

Roger J. Reeves, Mahendra G. Jani, Bahaeddin Jassemnejad,* and Richard C. Powell

Center for Laser Research, Oklahoma State University, Stillwater, Oklahoma 74078-0004

Greg J. Mizell and William Fay

Virgo Optics, Inc., 6736 Commerce Avenue, Port Richey, Florida 34668

(Received 25 January 1990)

Several experimental techniques were used to characterize the photorefractive properties of KNbO₃. Continuous-wave excitation was used to study two-beam coupling and creation times of photorefractive gratings for both undoped and doped samples. The results show how different types of dopants affect the photorefractive sensitivity and material properties relevant to the photorefractive effect such as carrier mobility, trapping time, effective trap density, effective electro-optic coefficient, Debye length, and the sign of the dominant photocarrier. Picosecond pulse excitation was used to study fast nonlinear responses of undoped KNbO₃. Along with the trapped-charge photorefractive response observed at long times after the excitation pulses, it was also possible to observe nonlinear responses due to absorptive changes at intermediate times and an ultrafast response that may have contributions associated with bound-electron nonlinearities and with scattering from Nb⁵⁺-ion hopping modes.

I. INTRODUCTION

Displacive ferroelectric crystals have the electro-optic properties necessary for producing photorefractive effects (PRE's). These light-induced changes in the refractive index of the material are the basis for many important devices in optical technology involving holographic storage, optical data processing, and phase conjugation.[1] KNbO₃ is predicted to have a high photorefractive sensitivity for materials of this class, but its properties have not been fully characterized.[2] The purpose of the research described here is to present new information about the photorefractive response of KNbO₃ crystals. The two most important aspects of this work are determining how the material properties change with different types of doping ions and showing how the nonlinear-optical response of the material evolves with time after picosecond pulse excitation.

The material properties associated with the PRE's are characterized using a spatial light intensity grating generated by the interference[3] of two coherent laser beams. The photorefractive response is associated with mobile charge carriers which are produced by photoionization of trap levels in the bright regions and through drift and diffusion are subsequently retrapped at new regions in the crystal. This leads to the buildup of a space-charge field in the material which modulates the refractive index through the electro-optic effect. Since the magnitude of the index change is proportional to the absorbed energy, the PRE can be generated with weak light sources on long-time scales, but it requires very high fluences to produce the PRE's with fast laser pulses. Other mechanisms associated with free carriers, bound charges, absorption changes, and vibrational properties can produce competing nonlinear-optical responses. To understand the PRE response of a material, it is necessary to characterize the

charge generation, relocation, and trapping processes as well as the effects of the competing nonlinear-optical processes. This can be accomplished by using a variety of experimental techniques which provide information over a wide range of response times and for samples with several different trap compositions. The results of this type of comprehensive *investigation of KNbO₃ are* described in the following sections.

Potassium niobate is a ferroelectric material with the perovskite type of crystal structure. At room temperature it has orthorhombic crystal symmetry of point group $mm2$, and the electro-optic coefficients of this material have been determined.[3] The various structural phases of KNbO₃ can be thought of as being derived from the cubic paraelectric phase by a series of distortions of the original cubic cell. For example, the orthorhombic distortion consists of a stretch of the original cube along one of the face diagonals (the cubic |110| direction). The |110| direction suffering a slight elongation is the direction of spontaneous polarization and is designated as the c axis of the principal cell. The remaining principal axes coincide with the other twofold rotation axes. Using the convention of previous work, we label the orthorhombic b axis as the direction parallel to the [010] axis of the original cubic cell. This is the only axis conserved through the phase transitions of the material.

Single crystals of high-optical-quality KNbO₃ were grown from high-temperature solutions using established techniques.[4] Both undoped crystals and crystals containing up to 1 mol % of Ta⁵⁺, Na⁺, Rb⁺, or Fe³⁺ were grown and cut into samples of approximate dimensions 3×3×5 mm. A discolorization was observed in all doped samples with the exception of Na:KNbO₃. Preliminary studies indicate that each dopant was uniformly incorporated in the crystal lattice at concentrations up to the 1 mol % level used in this study. The crystals were

x-ray oriented and poled.[4] Slight variations were observed in the x-ray Bragg angles and Curie temperature for the Ta:KNbO$_3$ sample. The most probable location of Ta^{5+} in the KNbO$_3$ lattice is the Nb^{5+} site while the Na$^+$ and Rb$^+$ ions are believed to occupy the K$^+$ site. Fe^{3+} has been previously studied and reported to occupy the Nb^{5+} site with the creation of free charge carriers.[5] Prior to poling, chemical polishing of doped and undoped samples revealed various domain-wall structures which could be readily observed on the surface with 8× magnification. In some cases, these observed surface pits and steps corresponded to visible domain imperfections within the bulk and in close proximity to the surface. After poling and repolishing, no evidence of domain structures at the surface could be observed.

II. RESULTS FOR CONTINUOUS WAVE EXCITATION

Laser-induced photorefractive gratings were written in undoped and doped KNbO$_3$ crystals using the 514.5-nm emission of a continuous-wave (cw) argon-ion laser. The photorefractive characteristics of the samples were studied using two types of experimental measurements: two-beam coupling and transient four-wave mixing (FWM).

A. Experimental

The experimental setup used for the beam coupling experiments is shown in Fig. 1(a). In these experiments one of the two beams used to write the grating is reduced in intensity and is designated as the probe beam. The pump- and probe-beam intensities were 820 mW/cm^2 and 5.3 mW/cm^2, respectively, and the pump beam was expanded to eliminate problems associated with nonuniformities of the light interference pattern. This experimental arrangement results in a grating thickness that is always equal to the crystal thickness independent of the crossing angle between the two beams. The intensity of the transmitted probe beam was measured with a photomultiplier tube and recorded on a strip chart recorder. The photorefractive gain was determined by recording the intensity change of the transmitted probe beam as the pump beam was cycled on and off.

In the four-wave mixing arrangement [Fig. 1(b)], the laser-induced grating was produced by two equal intensity pump beams with the same beam diameters. The grating properties were determined by using a weak (50 μW/cm^2) HeNe laser for the probe beam. The probe beam enters the sample in the opposite direction from the pump beams and is aligned for Bragg diffraction off the grating. A photomultiplier tube was used to detect the intensity of the diffracted probe beam and the signal was recorded on a digital oscilloscope. By chopping the pump beams on and off, the dynamics of grating formation were studied.

B. Results of two-beam coupling measurements

For some samples and experimental conditions, the charge relocation properties cause the refractive index grating to be out of phase with the incident light pattern.
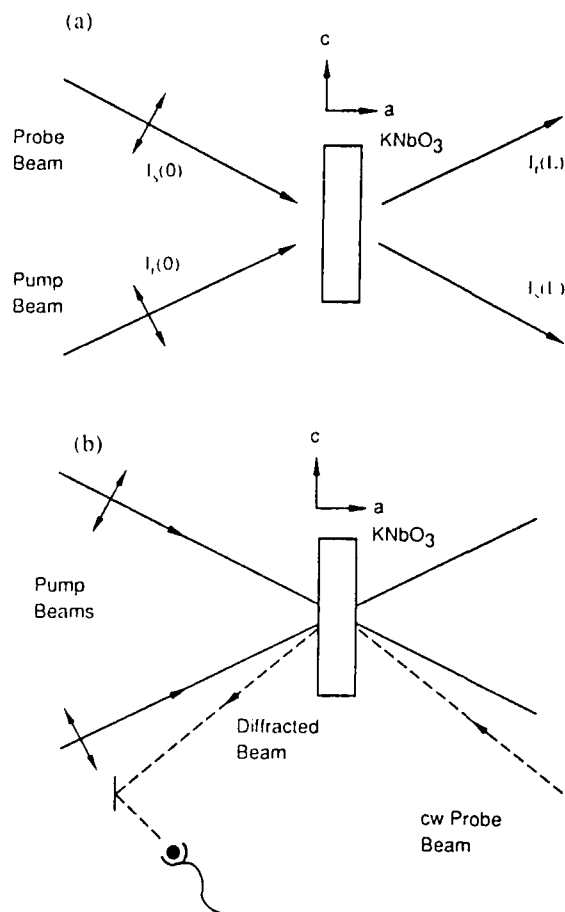

FIG. 1. Crystal and beam arrangements for (a) two-beam coupling experiments and (b) nondegenerate four-wave-mixing experiments.

Under these conditions energy can be transferred from one beam to the other. The direction of the energy transfer is determined by the crystal orientation and the sign of the dominant charge carrier. With the crystal oriented for maximum gain, the intensity of the signal beam can be written in terms of the gain coefficient Γ as[6]

$$\frac{I_s(L)}{I_s(0)} = \frac{[I_s(0) + I_r(0)]\exp[(\Gamma - \alpha)L]}{I_r(0) + I_s(0)\exp(\Gamma L)}, \quad (1)$$

where α is the absorption coefficient, L the interaction length, and I_r and I_s are the intensities of the pump and signal beams. Equation (1) reduces to

$$I_s(L) = I_s(0)\exp[(\Gamma - \alpha)L] \quad (2)$$

if $I_r(0) \gg I_s(0)$ and the pump beam is assumed to suffer negligible depletion traversing the length of the crystal. Experimentally we measure the effective gain[6] γ_0 given by

$$\gamma_0 = I_s(L)_{\text{with pump}}/I_s(L)_{\text{without pump}} = \exp(\Gamma L) \quad (3)$$

if the depletion of the pump beam is neglected.

The beam coupling gain can be expressed in terms of

material parameters as

$$\Gamma = 2\pi n^3 r_{eff} E_{SC}/\lambda ,$$ (4)

where n is the effective refractive index, r_{eff} is an effective electro-optic tensor component, and E_{SC} is the space-charge field. By including factors that account for the relative contributions of electrons and holes to the photorefractive effect, r_{eff} can be related to the electro-optic tensor component of a fully poled crystal as[7]

$$r_{eff} = F r_{ang} \sigma' .$$ (5)

F is a fractional poling factor, σ' is a normalized conductivity, and r_{ang} is the appropriate combination of electro-optic tensor components and angular and polarization factors for a fully poled crystal. For the two cases of only one type of charge carrier, $\sigma' = +1$ for holes and $\sigma' = -1$ for electrons. In the experiments performed here the two input beams were incident on the $\langle a \rangle$ surface of the crystal and were p-polarized so that r_{ang} can then be written as

$$r_{ang} = (n_3^4 r_{33} \cos^2\theta - n_1^4 r_{13} \sin^2\theta)/n^4 ,$$ (6)

where

$$n = [(\cos^2\theta/n_3^2) + (\sin^2\theta/n_1^2)]^{-1/2} .$$ (7)

The space-charge field takes the form

$$E_{SC} = [2\pi k_B T/e][\Lambda_g/(\Lambda_g^2 + \Lambda_0^2)] ,$$ (8)

where Λ_g is the grating spacing and

$$\Lambda_0 = [4\pi^2 \epsilon\epsilon_0 k_B T/(e^2 N_E)]^{1/2}$$ (9)

is the Debye screening length. Substituting for E_{SC} in Eq. (4) yields the expression for the photorefractive gain

$$\Gamma = [2\pi n^3 k_B \mathrm{Tr}_{eff}/(e\lambda)][K_g/(K_g^2 + K_s^2)] ,$$ (10)

where $K_g = 2\pi/\Lambda_g$ and $K_s = 2\pi/\Lambda_0$. By measuring the beam gain Γ as a function of grating spacing Λ_g and applying Eq. (10), two material properties can be determined: r_{eff} and $N_E = N N^+/(N + N^+)$, the effective density of empty traps.

In all the beam coupling experiments on undoped and doped KNbO$_3$, the grating normal was aligned parallel to the c axis and the crystal and beam geometry were arranged to give gain to the signal beam. At each angle of the input beams, the effective gain γ_0 was measured and the photorefractive gain Γ determined using Eq. (3). The experimental values for Γ were fit to a straight line form[7] of Eq. (10),

$$K_g/\Gamma = [e\lambda/(2\pi n^3 k_B \mathrm{Tr}_{eff})][1 + (K_g^2/K_s^2)] ,$$ (11)

with K_g/Γ plotted versus K_g^2. This presupposes that r_{eff} is independent of K_g. Examination of Eq. (5) shows that this assumption implies that σ' is independent of K_g, a situation that exists only if one type of photocarrier is dominant. When displayed in this manner, a value for r_{eff} can be obtained from the intercept and a value for K_s can be obtained from the slope and intercept of the straight-line plots. The experimental points are shown in

Fig. 2(a) for the five crystals studied and the values of r_{eff} and N_E obtained from these results are summarized in Table I. Figure 2(b) shows theoretical curves of the photorefractive gain Γ as a function of grating spacing calculated using the values of r_{eff} and N_E in Table I. In calculating N_E from K_s and Eq. (9) a value of $\epsilon = 55$ was used.[8] Using a value[3] of $r_{ang} = r_{33} = 64$ pm/V, estimates of $F\sigma$ can be obtained giving some idea of the relative contributions of electrons and holes.

The direction of the photorefractive coupling is determined by the sign of the dominant photocarrier and the crystal and beam geometry. For each of the crystals studied the polarity of the c axis was determined in a pyroelectric cooling experiment[9] and the sign of the photocarrier determined from the results is listed in Table I.

C. Results of transient response measurements

Another important parameter of a photorefractive crystal is the time required to build up the refractive index grating. Reduced KNbO$_3$ has been shown to have a microsecond response time which greatly enhances its
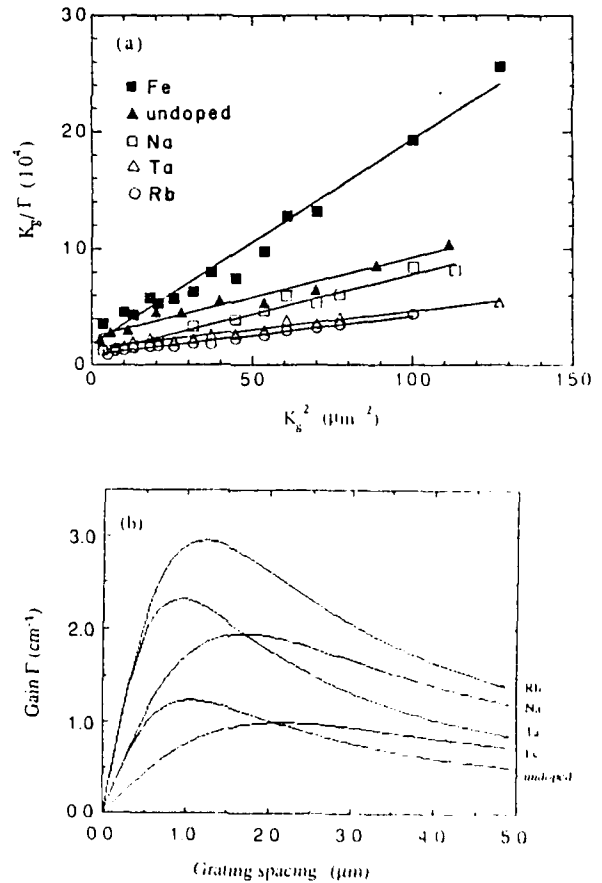

FIG. 2. (a) Grating wave vector K_g divided by beam coupling gain Γ as a function of K_g^2 for the five KNbO$_3$ crystals studied, and (b) theoretical curves of beam coupling gain Γ as a function of grating period using material parameters determined from least-squares fits to the data.

TABLE I. Material parameters obtained from two-beam coupling measurements on $KNbO_3$ crystals.

Crystal	Sign of dominant photo-carrier	Λ_0 (μm)	N_E (10^{16} cm^{-3})	r_{eff} (pm/V)	$F\sigma = r_{eff}/r_{33}$
$KNbO_3$ (undoped)	+	1.05	0.28	10.0	+0.20
$KNbO_3$:Ta	+	0.94	0.35	16.7	+0.33
$KNbO_3$:Rb	+	1.22	0.21	27.6	+0.55
$KNbO_3$:Fe	−	2.15	0.07	−16.4	−0.33
$KNbO_3$:Na	+	1.69	0.11	25.3	+0.15

potential for real time applications.[5]

Kukhtarev and co-workers[10,11] developed a mathematical analysis of the time evolution of the grating formation. This analysis has recently been extended for the case of dual charge carriers.[12,13] For fringe spacings large compared to both the charge diffusion length and the Debye screening length, the dielectric relaxation time

$$\tau_{di} = \epsilon\epsilon_0/(\sigma_d + \sigma_{ph}) \qquad (12)$$

is a good approximation to the grating buildup time.[1] In Eq. (12) σ_d is the dark conductivity and σ_{ph} is the photoconductivity given by

$$\sigma_{ph} = ea\Phi\mu\tau I/(h\nu) . \qquad (13)$$

e is the electronic charge, α is the absorption coefficient, Φ is the quantum efficiency for exciting a charge carrier, μ is the mobility, I is the optical intensity, and $h\nu$ is the photon energy. Inverting Eq. (12) to give the grating buildup rate

$$\delta = (1/\tau_{di}) = (\sigma_d + \sigma_{ph})/(\epsilon\epsilon_0) \qquad (14)$$

provides a linear relationship between I and δ. Using this approximation for the grating formation rate allows σ_{ph} to be determined from the slope of the fit of Eq. (14) to the data.
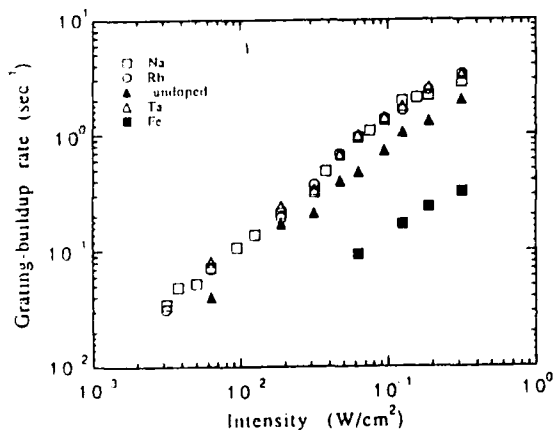
The grating buildup time was measured for all five crystals at one angle as a function of incident intensity. The buildup rate is plotted against light intensity in Fig. 3 for each crystal and the results are observed to qualitatively follow the straight-line model predicted by Eq. (14). The values of the product $\Phi\mu\tau$ obtained from the slopes are listed in Table II.

A useful figure of merit for characterizing the photorefractive sensitivity of a given material is how much optical energy is needed to produce a given refractive index change. Expressed in mathematical terms the sensitivity is[2]

$$S_n = \frac{dn}{d(\alpha W_0)} , \qquad (15)$$

where n is the refractive index, α the absorption coefficient, and W_0 the incident optical energy. For a phase grating the diffraction efficiency is given by[14]

$$\eta = e^{(-\alpha d/\cos\theta)}\sin^2(d\pi\Delta n/\lambda\cos\theta) \qquad (16)$$

and the induced refractive index change can be determined by measuring the absolute diffraction efficiency. The intensity of the scattered HeNe beam was calibrated to yield the absolute diffraction efficiency for all five crystals and combined with the grating buildup times to give the photorefractive sensitivity. The results obtained are given in Table II.

The results from the cw laser experiments show that doping $KNbO_3$ with Na^+, Rb^+, or Ta^{5+} at the 1 mol. % level enhances the photorefractive performances of the crystal. The maximum beam coupling gain and photorefractive sensitivity increases for these crystals over an

FIG. 3. Photorefractive grating buildup rate as a function of input light intensity for the five $KNbO_3$ crystals studied.

TABLE II. Material parameters obtained from FWM transient signal buildup rates measured on $KNbO_3$ crystals.

Crystal	S_n (10^{-5} cm^3/J)	$\Phi\mu\tau$ (10^{-10} cm^2/V)
$KNbO_3$ (undoped)	2.45	3.74
$KNbO_3$:Ta	3.79	6.46
$KNbO_3$:Rb	7.93	6.51
$KNbO_3$:Fe	0.41	0.53
$KNbO_3$:Na	3.22	6.07

undoped sample. The iron-doped crystal used in this
study was observed to have an inferior photorefractive
performance when compared to an undoped crystal.
Also the predominant charge carrier was determined to
be electrons in contrast to holes observed in the other
crystals. Medrano et al.[15] found that the charge carriers
in their iron-doped samples were holes and that there was
an increase in photorefractive gain over a pure crystal
that had been reduced and contained electrons as photo-
carriers. It is expected that it is the same Fe^{2+}-Fe^{3+}
donor-trap system that produces the photorefractive
effect in pure and iron-doped samples. Taken together,
the results above suggest that it is the Fe^{2+}-Fe^{3+} ratio
rather than absolute amounts that is important in pre-
dicting the photorefractive performance of a particular
crystal.

III. RESULTS FOR PICOSECOND
PULSE EXCITATION

The nonlinear optical response of $KNbO_3$ was investi-
gated using picosecond pulses to establish laser-induced
gratings. These gratings were probed using both pi-
cosecond and cw probe beams and the measurements ob-
tained provide information on the time evolution of the
gratings from a time scale of picoseconds out to many
minutes.

A. Experimental

Single pulses with durations of 30 psec full width at
half maximum (FWHM) at 532 nm were produced by a
frequency-doubled, mode-locked Nd:YAG laser. After
being split into two pump beams, the pulses were recom-
bined in the crystal with an external crossing angle of 2θ.
This angle could be varied from 16° to 44° corresponding
to grating spacings varying from 1.91 to 0.71 μm. Typi-
cal incident energies of the two pump beams were 0.11
and 0.06 mJ giving an intensity modulation index of

$$m = 2(E_1 E_2)^{1/2}/(E_1 + E_2) = 0.95 . \tag{17}$$

The diameter of each of the two pump beams was mea-
sured with a traveling knife edge and found to be 0.54
mm at the $1/e^2$ points of the on-axis peak intensity. The
Gaussian radius of each beam is 0.27 mm and the in-
cident fluences are 39 and 21 mJ/cm² for the two pulses.
The temporal overlap of the two pump pulses was
achieved with an optical delay line in one beam path.

A degenerate four-wave-mixing experiment was used
to investigate the fast grating formation and decay. The
experimental arrangement is shown in Fig. 4. A less in-
tense, third picosecond pulse that was exactly counter-
propagating to one of the pump beams acts as a probe
beam. This probe pulse was s-polarized to be orthogonal
to the pump-pulse polarization and was focused to the
same diameter in the crystal. From phase matching con-
siderations the diffracted signal is counterpropagating to
the other pump beam and was extracted with a beam
splitter. The arrival of the probe pulse in the crystal
could be varied by an optical delay line. Delay times
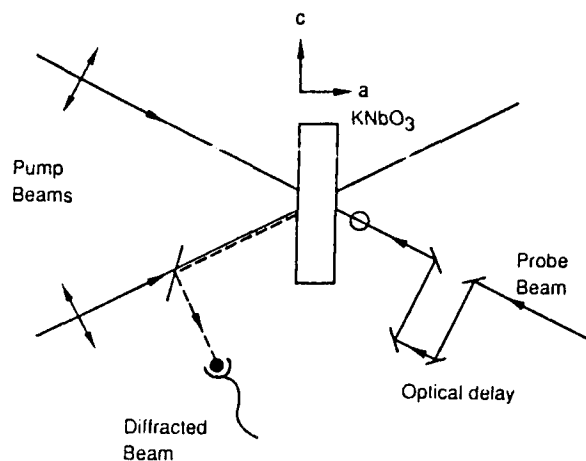ranging from several hundred picoseconds before to

FIG. 4. Crystal and beam arrangements for the picosecond
pulse-probe experiments on photorefractive gratings in $KNbO_3$.

several nanoseconds after the arrival of the pump pulses
could be obtained. The diffracted signal was detected by
the photodiode, recorded on a signal averager, and aver-
aged over several thousand laser pulses.

In order to follow the signal to longer times, the probe
pulse was replaced by a 1-mW cw He-Ne laser beam.
The intensity of this laser was attenuated by three orders
of magnitude to keep its influence below that required for
grating erasure. The incident angle of the probe beam
was adjusted to satisfy the Bragg scattering condition.

B. Results of pulse-probe measurements

The absolute diffraction efficiency was measured for
gratings produced in $KNbO_3$ as a function of probe-pulse
delay with the crystal in a photorefractive and in a non-
photorefractive geometry. The results are shown in Fig.
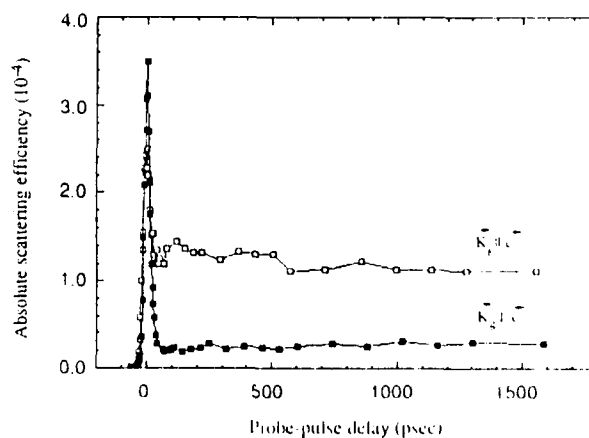5 for a grating spacing that is 1.9 μm. In the pho-

FIG. 5. Time evolution of the absolute scattering efficiency
from a laser-induced grating written by two 30-psec pulses mea-
sured by an optically delayed weak probe pulse.

torefractive geometry the crystal is oriented with the grating wave vector K_g aligned parallel to the c axis of the crystal so the write beams produce an internal space-charge field that is also parallel to the c axis and the s polarized probe pulse senses the photorefractive effect through the r_{31} electro-optic tensor component. In the other geometry the crystal is rotated 90° ($K_g \perp c$) and any space-charge field produced will be in the direction of the crystallographic b axis. Due to the symmetry elements of the electro-optic tensor any index change produced will not be detected by an s-polarized probe pulse.

Two features are apparent in the data of Fig. 5 and they appear to be similar to results recently reported for BaTiO$_3$.[16,17] First a sharp peak is observed centered at a probe delay of $t=0$ psec. The real time width of this peak is close to the expected autocorrelation width of our three pulses. The origin of this signal is the fast physical processes contributing to the third-order susceptibility $\chi^{(3)}$ associated with the FWM of the two pump beams, probe beam, and signal beam. Possible contributions to the susceptibility include nonlinearities associated with bound electrons, free carriers, and any phonon or thermal effects with characteristic relaxation times comparable or less than the optical pulse width. In BaTiO$_3$, free carriers generated by single-photon absorption were thought to be the dominant contribution to the nonlinear susceptibility.[16,17]

The second feature apparent in Fig. 5 is a long-lived signal lasting for probe-pulse delays of several nanoseconds. It is more pronounced in the $K_g \| c$ orientation than in the $K_g \perp c$ orientation. This suggests that it may be photorefractive in origin. For this interpretation to be correct, impurity donor centers would have to be photoionized to produce free charge carriers that migrate far enough to establish a significant space-charge field during the time of the pump pulses. However, the small free carrier mobilities and fast trapping times that are typical of the ferroelectric oxides would allow the free carriers to diffuse only a small fraction of a grating spacing before being trapped. Thus there is some question about the origin of this component of the signal.

The intensity of the conjugate peak shows little change with grating spacing which is not the case for the signal at long probe-pulse delays. Figure 6 shows the intensity of the diffracted signal for four grating spacings. As the spacing decreases, the intensity of the nanosecond time component decreases. Such a decrease in a photorefractive grating is expected in high-mobility, long-trapping-time materials where the free carriers are able to destroy the grating by diffusing over a full grating period at small spacings before being trapped. However, in ferroelectric oxides the low mobilities coupled with the fast trapping times for charge carriers make this process unlikely. For the grating periods used in Fig. 6 the charge migration is expected to be diffusion dominated and the space-charge fields will be limited by the diffusion field

$$E_D = 2\pi k_B T /(e \Lambda_g) . \tag{18}$$

Thus the photorefractive effect will cause the intensity of the scattered signal to increase as the grating spacing de-
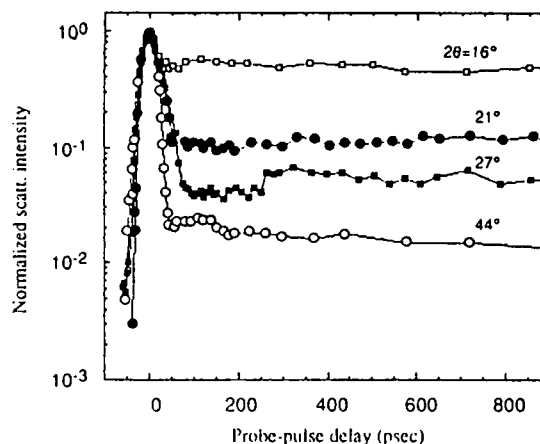

FIG. 6. Picosecond time evolution of the normalized scattering intensity for four grating spacings in KNbO$_3$.

creases, which is exactly opposite to the results observed in Fig. 6. This casts further doubt on attributing this signal contribution to a photorefractive effect.

In the results from the nonphotorefractive orientation shown in Fig. 5 there is a nonzero scattering background for long probe delays. This component may be associated with scattering from an absorption or photochromic grating generated by the photoexcitation and subsequent trapping of charge carriers. The diffraction efficiency for an absorption grating is given by[14]

$$\eta_a = (1 - e^{-\alpha d}) \sinh^2[\Delta \alpha d /(2 \cos\theta)] . \tag{19}$$

The change in absorption coefficient $\Delta \alpha$ is just

$$\Delta \alpha = Ns , \tag{20}$$

where N is the density of displaced charges and s is the absorption cross section of the defect centers. The cw photorefractive beam coupling experiments showed that the concentration of donor centers in the crystal used here is $N_E = 3 \times 10^{15}$ cm^{-3}. Since the input photon rate is somewhat greater than this, we can approximate $N = N_E$. The absorption cross section of the donor levels is not known in KNbO$_3$, but some idea of its magnitude can be obtained from results in the literature. It is known that the most common defect center leading to photorefractive effects in as-grown ferroelectrics is the Fe^{2+}-Fe^{3+} system where the deep-level donor is Fe^{2+} and the acceptor is Fe^{3+}. The deep-level absorption cross section has been measured for this defect in InP:Fe and found to be[18] $s = 1 \times 10^{-17}$ cm^2. Using this value of s for KNbO$_3$ we obtain $\Delta \alpha = 0.03$ cm^{-1}. Substituting for $\Delta \alpha$ in Eq. (19) yields a diffraction efficiency of $\eta_a = 10^{-5}$ which is in good agreement with the observed scattering efficiency of about $\eta = 2 \times 10^{-5}$ for this signal component. The consistency of this interpretation of the $K_g \perp c$ results suggests that the $K_g \| c$ results might be associated with a directional-dependent change in the absorption coefficient.

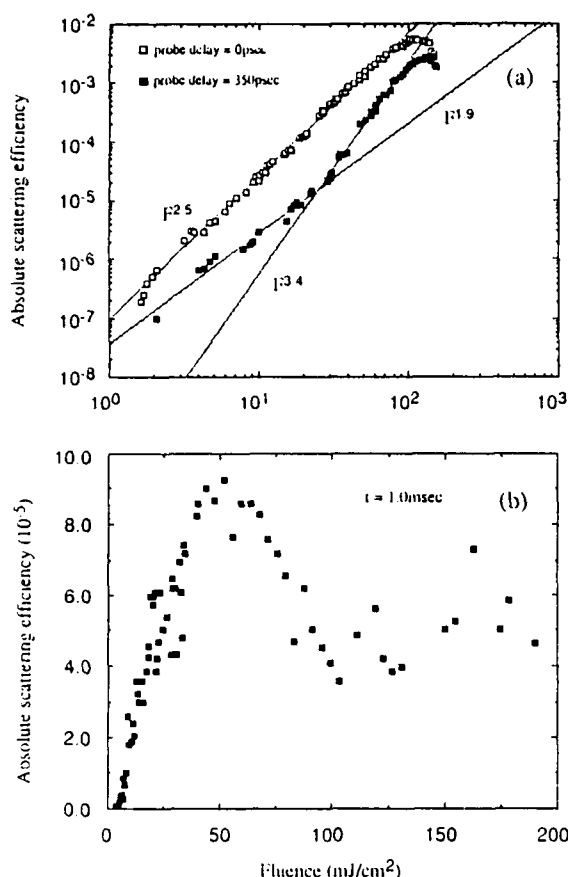Figure 7(a) shows the results of measuring the scatter-

FIG. 7. Absolute scattering efficiency as a function of the fluence of two 30-psec writing pulses at (a) probe delays of 0 and 350 psec after the writing pulses and (b) at a time of 1.0 msec after the writing pulses as measured by a cw probe beam.

Fig. 8. Ratio of the probe-pulse intensity with the pump beam on T and the pump beam off T_0, as a function of incident fluence in a picosecond-pulse two-beam coupling experiment on KNbO₃. The closed and open squares represent the two photorefractive crystal orientations that are related by a 180° rotation about a line bisecting the two input beams.

ing efficiency as a function of incident fluence. At a probe-pulse delay of 0 psec, the diffraction efficiency follows a power-law dependence on the total fluence F of $F^{2.5}$, slightly greater than the quadratic dependence expected. At a delay time of 350 psec, a single power-law dependence is not observed. In the low-intensity region with fluences below 10 mJ/cm² a least-squares fit to the data yields a dependence of $F^{1.9}$. Above 10 mJ/cm² a power-law dependence of $F^{3.4}$ is observed. At both of these delays there is a saturation of the signal around an incident fluence of 100 mJ/cm².

A definite signature of the photorefractive effect is the observation of two-beam coupling. An experiment was performed to detect two-beam coupling in KNbO₃ using picosecond pulses and the results are shown in Fig. 8. The crystal was oriented in the photorefractive geometry with a grating spacing of 1.9 μm and a pump-beam- -to-probe-beam intensity ratio of 9:1. The experimental quantity measured and plotted in Fig. 8 is the ratio T/T_0 as a function of the incident fluence, where T is the intensity of the transmitted probe beam with the pump beam on and T_0 is the intensity with the pump beam off. Energy transfer through photorefractive gain will increase the
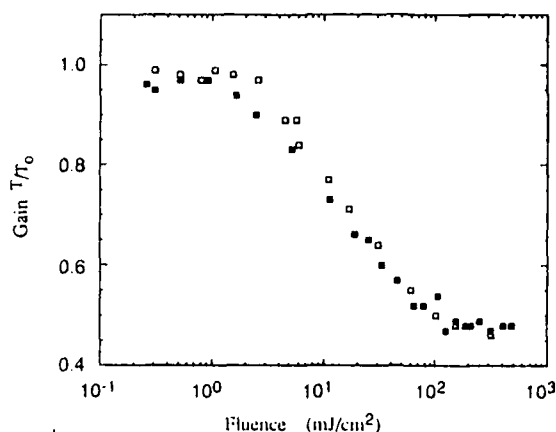
intensity of the probe beam in the presence of the pump beam. The points represented by closed and open squares correspond to the two photorefractive crystal orientations that are related by a 180° rotation about a line bisecting the two input beams. The photorefractive contribution to the signal will reverse direction when the crystal is rotated and be seen as a difference between the points for the two orientations in Fig. 8. Such a difference is not observed in these results suggesting that the free carriers do not diffuse the required half grating spacing on picosecond time scales. The decay in the ratio T/T_0 as a function of fluence is most probably associated with two-photon absorption.

In conjunction with these two-beam coupling measurements, the probe-pulse transmission was recorded as a function of the arrival time of the pump pulse. The results obtained are shown in Fig. 9 where the ratio T/T_0 is plotted against probe-pulse delay for the two crystal orientations $K_g \| c$ and $K_g \perp c$. This experiment was performed at the same crossing angle as the beam coupling results and the intensity of the pump beam was 80 mJ/cm². For negative probe-pulse delays, i.e., the probe pulse arrives before the pump pulse, the ratio T/T_0 is close to unity and there is no interaction between the beams. As the pulses start to overlap in time the probe is attenuated through two-photon absorption which peaks at zero delay. For both crystal orientations the probe pulse continues to be attenuated at long delay times after the pump pulse. The extend of the attenuation is significantly greater in the $K_g \| c$ orientation than in the perpendicular $K_g \perp c$ orientation. At these long-time scales there is no temporal overlap of the pulses and the effects are not grating or photorefractive in origin. A reasonable explanation of these results is the anisotropy of the absorption coefficient relative to the crystal c axis. Thus we conclude from these results that the contribu-
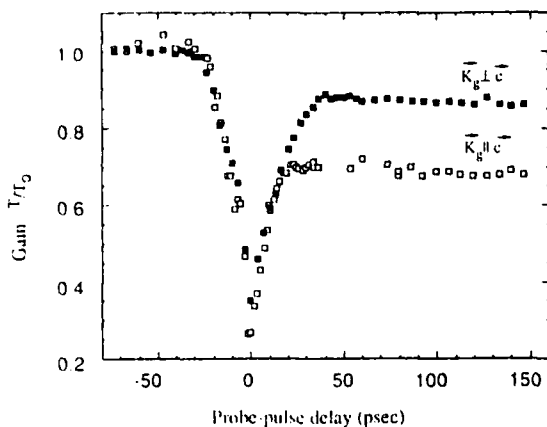
FIG. 9. The quantity T/T_0 as a function of the arrival time of the probe pulse for two orientations of a $KNbO_3$ crystal.

tion to the FWM signal on the time scale of several hundred picoseconds to nanoseconds after picosecond pulse excitation is due to a laser-induced absorption grating.

C. Results of cw probe measurements

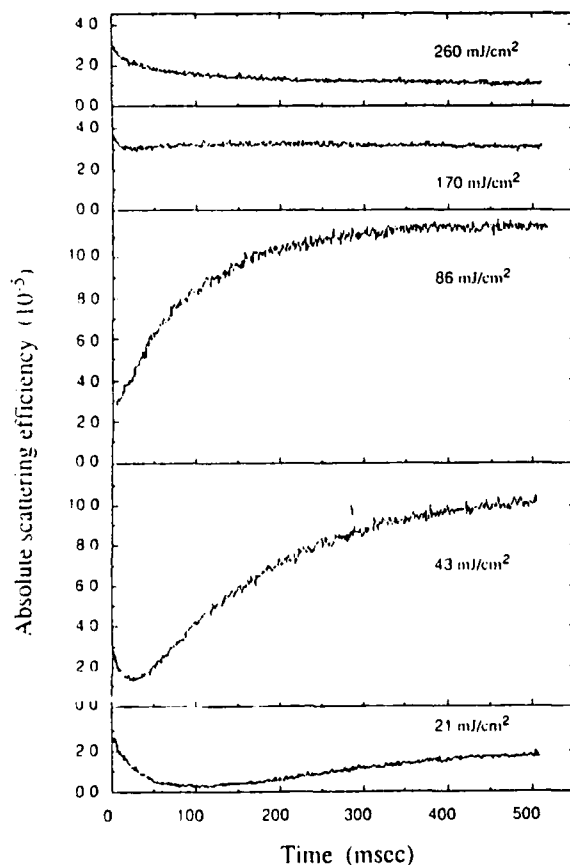The picosecond pulse experiments were repeated using a cw probe beam. In this case, the fast-time resolution of

the pulse-probe experiments described in the previous section is lost, but the evolution of the signal can be followed to very long times. The transient signals obtained show the decay of the fast nonlinear responses and the buildup and dark decay of the photorefractive grating. The crystal a axis and the polarization of the probe beam were aligned in the plane of incidence (p polarization) so the effective electro-optic coefficient is given in Eq. (6). The signal was followed in time after a single 30-psec pulse of excitation from the crossed write beams.

Figure 10 shows the time evolution of the scattering efficiency for different excitation fluences. The intensities of the fast- and long-time components of the signal change differently with fluence and the buildup time of the long-time signal decreases as fluence is increased. Figure 7(b) shows the results of measuring the signal strength at 1 msec after the write pulses as a function of write-beam fluence. The data show a very different behavior than the signals measured at faster times shown in Fig. 7(a). The observed behavior does not fit a single power-law dependence but is close to linear below 50 mJ/cm^2 at which point the scattering efficiency is observed to saturate.

Figure 11 shows the dark decay of photorefractive

FIG. 10. Time evolution of the absolute scattering efficiency of laser-induced gratings in $KNbO_3$ as a function of time after the arrival of the two 30-psec writing pulses measured by a cw probe beam.
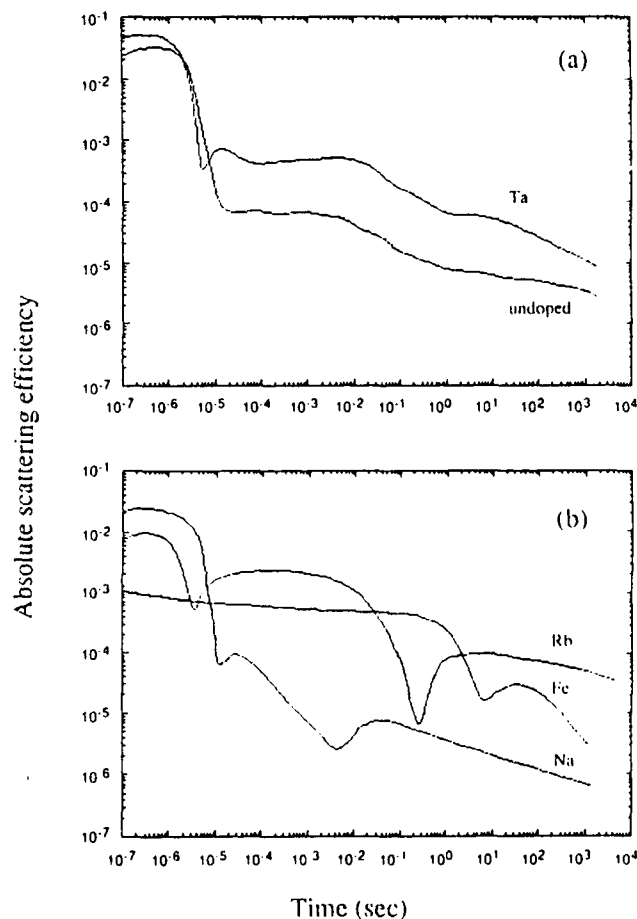

FIG. 11. Dark decay of photorefractive gratings in doped $KNbO_3$ crystals induced by two single 30-psec writing pulses.

gratings written by single laser pulses in the doped and undoped KNbO₃ crystals. The signal for the undoped crystal has at least two decay components with very different relaxation times. Nonexponential erasure decays have been observed in $Bi_{12}SiO_{20}$ (Ref. 19) and LiNbO₃ (Ref. 20) and were explained by the participation of several trapping centers in the photorefractive charge migration. Steady-state beam coupling results presented earlier show that both electrons and holes are involved in the photorefractive processes in the crystals used here. The decay results observed demonstrate that the trapping mechanism involves two types of acceptors that have two distinct relaxation times. One trap may be associated with the creation of holes in the valence band by photoexcitation of electrons to midgap impurity levels, while the other may be associated with photoexcitation of electrons to the conduction band. It is well known that mobilities of electrons and holes are different in these types of materials and multiple components to the decay of a grating involving both electrons and holes should be expected.

The doped KNbO₃ crystals show more complicated dark decays. In some cases the intensity of the scattered beam is observed to undergo several dips where one component of the grating decays while another component with a longer relaxation time still contributes to the intensity. Theoretical modeling of these features will require incorporation of multiple trapping levels in describing the dynamics of charge relocation.

Figure 12 shows the dark decay of the photorefractive grating in undoped KNbO₃ for five different grating spacings. The decay time decreases with grating spacing reflecting the shorter time charge carries require to diffuse a half grating period. The nonexponential nature of the decay is more pronounced for the smaller grating spacings. For the larger spacings the decay is expected to be dominated by the carrier with the highest mobility and a single exponential decay would result. As the spacing decreases both carriers and their respective trapping

FIG. 12. Dark decay of photorefractive gratings in KNbO₃ for five different grating periods.

centers are able to contribute to the decay and nonexponential transients appear.

IV. DISCUSSION AND CONCLUSIONS

Characterization of the photorefractive effect using cw excitation has been reported previously for KNbO₃ crystals where the response time for reduced KNbO₃ was measured to be 100 μsec.[5] Also, doping with iron has been shown[15] to result in a substantial increase in the photorefractive efficiency over that of undoped samples. The results described here using cw excitation give a further understanding of the photorefractive effect in doped and undoped KNbO₃ by determining various material parameters associated with laser-induced charge relocation. The mobility-lifetime products given in Table II show that doping KNbO₃ with either Ta, Rb, or Na decreases the time required to form a photorefractive grating by a factor of 2 over an undoped crystal. This increase in the buildup rates carries over to an enhancement in the photorefractive sensitivity for these crystals with the Rb dopant producing the highest. In the Fe-doped sample electrons were found to be the dominant charge carrier while holes were the dominant carriers in all other samples.

It is only recently that picosecond pulses have been used to study nonlinear responses of materials such as $Bi_{12}SiO_{20}$,[21] BaTiO₃,[16,17] GaAs,[22] and CdTe.[23] In the picosecond work reported here on KNbO₃, three different types of nonlinear effects were identified due to their different time responses. Utilizing both pulsed and cw probe beams, picosecond laser-induced grating techniques were used to follow the evolution of the nonlinear response from the picosecond time scale out to times of many minutes. On the time scale of milliseconds and longer, the photorefractive response which was observed with cw excitation is seen. This is associated with the space-charge field built up by photoinduced charge relocation and the interaction of this field with the electro-optic tensor components of the material. The dark decay of the signal is highly nonuniform indicating that different types of traps are taking part in the charge relaxation back to an equilibrium configuration.

On the time scale of 100 psec out to nanoseconds, the nonlinear response has properties that are better described by a laser-induced change in the absorption coefficient associated with two-photon absorption. The time scale and magnitude of this signal are consistent with a relocation of charge carriers. For example, since the dominant photoinduced charge carriers are holes, the first photon might create a hole by promoting an electron in the valence band into a midgap acceptor. The second photon might promote this electron into the conduction band. The electrons and holes created in this way will migrate to different types of traps before finally recombining.

The variation of the signal in this time regime for different crystal orientations is associated with the anisotropy of the absorption coefficient. The absorption coefficient for KNbO₃ is a tensor quantity with different values for different propagation and polarization direc-
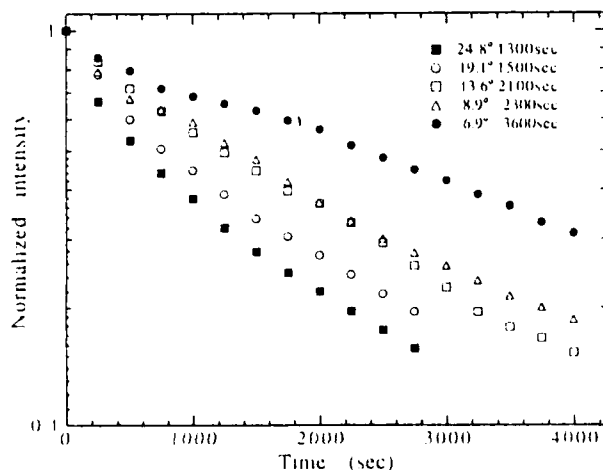
tions. If a, b, and c are the crystallographic axes, then the absorption coefficient can be represented by the tensor

$$\alpha = \begin{vmatrix} 0 & \alpha_{ab} & \alpha_{ac} \\ \alpha_{ab} & 0 & \alpha_{ac} \\ \alpha_{ca} & \alpha_{ca} & 0 \end{vmatrix} , \qquad (21)$$

where α_{ij} is the absorption coefficient for a beam propagating in the ith direction with polarization along the j axis. If the crystal is oriented with $K_g \| c$, the probe-pulse polarization is always perpendicular to the c axis and the apparent absorption coefficient is given by the linear combination

$$\alpha = \alpha_{ab}\cos\theta + \alpha_{ca}\sin\theta , \qquad (22)$$

where θ is the half-angle between the intersecting pump and probe beams. In the orthogonal orientation $K_g \perp c$, the appropriate combination for the absorption coefficient is

$$\alpha = \alpha_{ac}\cos\theta + \alpha_{ac}\sin\theta . \qquad (23)$$

For the data in Fig. 9, $\theta = 8°$ and the attenuation of the probe in the $K_g \perp c$ orientation is due mainly to the first term in Eq. (23). The first term in Eq. (22) is expected to be of this same magnitude and the extra attenuation of the probe in the $K_g \| c$ orientation is due to the component $\alpha_{ca}\sin\theta$. As the angle θ increases the probe beam in both the two-beam coupling experiment and in the FWM experiment will undergo an increasing absorption as it propagates more along the c axis. This is consistent with the results shown in Fig. 5. Based on this analysis, the longer-lived signal in the picosecond pulse-probe FWM experiments is the scattered beam from an absorption grating. The photoexcited charge carriers are trapped on a time scale comparable with the optical pulse width but their redistribution among different trapping levels sets up an absorption grating that is anisotropic with crystallographic directions.

The physical origin of the fast conjugate peak observed in the picosecond FWM experiments is difficult to determine unambiguously because its time response cannot be resolved with 30-psec pulses used here. This signal is associated with the third-order susceptibility of the material and can have contributions from electronic and vibrational mechanisms that respond on a picosecond time scale. The extend of each contribution can be estimated from the nonlinear refractive index for the effect. If the induced change in the refractive index is Δn, the nonlinear refractive index n_2 is defined as[24]

$$\Delta n = n_2 \langle E^2 \rangle , \qquad (24)$$

where E is the electric field of the optical wave. n_2 is related to the third-order susceptibility by[24]

$$n_2 = (12\pi/n_0)\chi^{(3)} , \qquad (25)$$

where n_0 is the background refractive index which equals 2.35 for $KNbO_3$. For a refractive index grating, the theory of Kogelnik[14] can be used to obtain the refractive

index change induced from the absolute scattering intensity by

$$\Delta n = (\lambda\cos\theta/\pi d)\sqrt{\eta} . \qquad (26)$$

The maximum diffraction efficiency recorded in these experiments at $\Delta t = 0$ was $\eta = 5.5 \times 10^{-3}$ obtained at an intensity of 100 mJ/cm^2. The electric-field intensity of the incident wave is related to the fluence F by[25]

$$\langle E^2 \rangle = (8\pi/cn_0)F = 1.19 \times 10^7 \qquad (27)$$

for the above fluence, in cgs units. The value of $\chi^{(3)}$ measured in this case is calculated to be 2.3×10^{-13} esu.

Two of the electronic contributions to the conjugate peak will be scattering from a free-carrier index grating that is generated by single-photon absorption and scattering from the induced polarization of bound charges in the material. The change in the refractive index associated with scattering from a free-carrier grating is given in the Drude model by[26]

$$\Delta n = 2\pi N_c e^2/(n_0 \nu^2 m_c) , \qquad (28)$$

where N_c is the density of free carriers of effective mass m_c. N_c (in cm^{-3}) can be approximated by the absorbed photon flux

$$N_c = (\lambda\alpha/hc)I = 5.4 \times 10^{16} . \qquad (29)$$

Using this value in Eq. (28) predicts the free-carrier grating index change and third-order susceptibility contribution to be $\Delta n = 3.0 \times 10^{-6}$ and $\chi^{(3)} = 1.5 \times 10^{-14}$ esu. These are an order of magnitude smaller than the measured values.

The value of $n_2 = 29 \times 10^{-13}$ esu measured[27] for $KTaO_3$ can be used as an approximation for the bound-charge contribution to $\chi^{(3)}$ for $KNbO_3$. Using Eq. (25) the third-order nonlinear susceptibility from this effect is calculated to be 1.8×10^{-13} esu, which is the same order of magnitude as the measured value.

Recent Raman-scattering experiments on $KNbO_3$ have shown central peaks in the scattering spectrum that are associated with relaxation modes involved in the successive cubic-tetragonal-orthorhombic-rhombohedral phase transitions.[28,29] While there is some question about an additional contribution to the signal from a soft phonon mode, this is not relevant to the results described here.[30,31] It is beyond the scope of our experiments to resolve the specific contributions due to the relaxation modes and soft modes. However, it is clear that the Nb^{5+} relaxation modes are responsible for a contribution to the dielectric constant of the material and thus will contribute to the nonlinear refractive index measured as a conjugate signal peak in our FWM experiments.

The multiwell potential surface involved with the hopping modes is the eight-site order-disorder model used to describe the successive phase transitions in displacive ferroelectric crystals.[28] This model has the Nb^{5+} ions located in one of eight potential wells which have potential minima displaced from the cubic unit cell center along the $\langle 111 \rangle$ directions. The different structural phases of the crystal are a consequence of the preferential occupation by the Nb^{5+} ion of a certain set of potential wells.
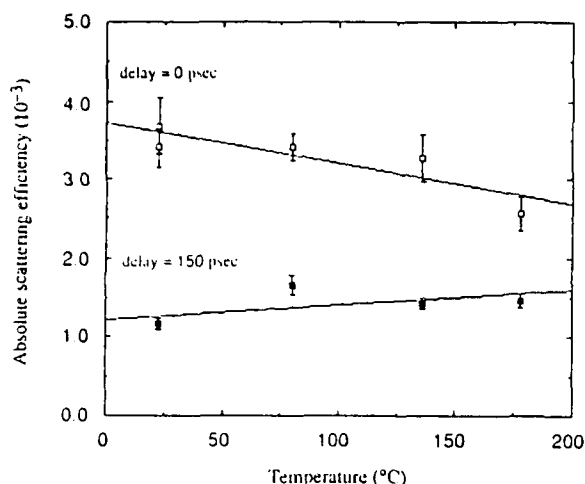
FIG. 13. Absolute scattering efficiency of a laser-induced grating in KNbO₃ as a function of temperature for probe-pulse delays of 0 and 150 psec after the 30-psec writing pulses.

For example, in the cubic phase each of the eight sites is equally occupied, while tetragonal ordering arises below the first phase transition temperature due to a set of four wells perpendicular to a particular axis becoming preferentially occupied.

The influence of this polar hopping mode on the laser-induced gratings is very similar to the analysis of stimulated Raman scattering. However in this case the low frequency of the mode means the effect is seen in a degenerate mixing configuration. The contribution to $\chi^{(3)}$ can be calculated using fluctuation-dissipation theory arriving at the result[32]

$$\chi^{(3)} = -(N/8h)[(\nu\alpha_k^2)/(\nu^2+\omega^2)] \ . \tag{30}$$

The polarizability change for this mode can be calculated from the Clausius-Mossotti relation

$$\alpha = (3\epsilon_0/N)[(n^2-1)/(n^2+2)] \ . \tag{31}$$

The refractive index change arising from a Nb⁵⁺ ion hopping between the two nonequivalent potential wells is inferred from the linear birefringence for KNbO₃ crystals.[33]

At 300 K Δn is approximately 0.18 and it decreases to about 0.15 at 500 K. Substituting for the measured Raman peak linewidth and the calculated value of $\Delta\alpha$ the contribution to $\chi^{(3)}$ is 9×10^{-13} esu. Stimulated hopping between two of the equivalent potential wells will make a similar contribution to $\chi^{(3)}$.

The intensity of the diffracted signal was measured as a function of temperature for undoped KNbO₃ and the results are shown in Fig. 13. The signal was measured at two delay times of the probe pulse, 0 and 150 psec. The results at zero delay show the signal strength to decrease as temperature is increased while the signal at 150 psec increases very slightly. A larger temperature range could not be studied because of the phase transitions of the crystal at 250 K. The intensity of the Raman-scattering peak was observed to increase with temperature.[28] This peak is associated with relaxations from the higher-energy potential well to the lower well which will become more probable as the upper well is thermally activated. In terms of the zero-delay signal observed in our laser-induced grating experiment where the light pattern is driving the modes in the bright regions, the detected signal intensity depends on the contrast in the refractive index between the bright and dark regions of the sample. As the temperature is increased this contrast decreases as the Nb⁵⁺-phonon modes become more occupied in the dark regions. Also the linear birefringence between the two phases decreases as the temperature increases.[33] The decrease in Δn is about 17% over the temperature range between 300 and 500 K while the signal decrease in the same range is close to 28%.

Thus from the above discussion it appears that the bound electron and Nb-hopping mode both contribute to the observed FWM signals at zero time delay in KNbO₃. Further experiments using different samples and faster excitation pulses will be done to separate these contributions.

ACKNOWLEDGMENTS

---

*Permanent address: Department of Physics, Central State University, Edmond, Oklahoma 73060.

[1]P. Gunter, Phys Rep. 93, 199 (1982).

[2]P. Gunter and J. P. Huignard, in *Photorefractive Materials and their Applications I*, edited by P. Gunter and J. P. Huignard (Springer-Verlag, Berlin, 1988), p. 65.

[3]P. Gunter, Opt. Commun. 11, 285 (1974).

[4]G. J. Mizell, W. R. Fay, and Y. Shimoji, SPIE 968, 88 (1988).

[5]E. Voit, M. Z. Zha, P. Amrhein, and P. Gunter, Appl. Phys. Lett. 51, 2079 (1987).

[6]J. P. Huignard and A. Marrakchi, Opt. Commun. 38, 249 (1981).

[7]M. B. Klein and G. C. Valley, J. Appl. Phys. 57, 4901 (1985).

[8]E. Wiesendanger, Ferroelectrics 6, 263 (1974).

[9]G. D. Boyd, R. C. Miller, K. Nassau, W. L. Bond, and A. Savage, Appl. Phys. Lett. 5, 234 (1964).

[10]N. Kukhtarev, V. Markov, and S. Odulov, Opt. Commun. 23, 338 (1977).

[11]N. V. Kukhtarev, Pis'ma Zh. Tekh. Fiz. 2, 1114 (1976) [Sov. Tech. Phys. Lett. 2, 438 (1976)].

[12]G. C. Valley, J. Appl. Phys. 59, 3363 (1986).

[13]F. P. Strohkendl, J. M. C. Jonathan, and R. W. Hellwarth, Opt. Lett. 11, 312 (1986).

[14]H. Kogelnik, Bell Syst. Tech. J. 48, 2909 (1969).

[15]C. Medrano, E. Voit, P. Amrhein, and P. Gunter, J. Appl. Phys. 64, 4668 (1988).

[16]A. L. Smirl, G. C. Valley, R. A. Mullen, K. Bohnert, C. D. Mire, and T. F. Boggess, Opt. Lett. 12, 501 (1987).

[17]A. L. Smirl, K. Bohnert, G. C. Valley, R. A. Mullen, and T. F. Boggess, J. Opt. Soc. Am. B 6, 606 (1989).

[18]R. B. Bylsma, D. H. Olson, and A. M. Glass, Opt. Lett. 13, 853 (1988).

[19]R. A. Mullen, Ph.D. thesis, University of Southern California, 1984 (unpublished).

[20]K. Tyminski and R. C. Powell, J. Opt. Soc. Am. B 2, 440 (1985).

[21]J. M. C. Jonathan, G. Roosen, and Ph. Roussignol, Opt. Lett. 13, 224 (1988).

[22]G. C. Valley, A. L. Smirl, M. B. Klein, K. Bohnert, and T. F. Boggess, Opt. Lett. 11, 647 (1986).

[23]M. S. Petrovic, A. Suchocki, R. C. Powell, G. Cantwell, and J. Aldridge, J. Appl. Phys. 66, 1359 (1989).

[24]A. Yariv and R. A. Fisher, in Optical Phase Conjugation, edited by R. A. Fisher (Academic, London, 1983), p. 14.

[25]J. D. Jackson, in Classical Electrodynamics, 2nd ed. (Wiley, New York, 1975), p. 272.

[26]R. K. Jain, Opt. Eng. 21, 199 (1982).

[27]R. Adair, L. L. Chase, and S. A. Payne, Phys. Rev. B 39, 3337 (1989).

[28]J. P. Sokoloff, L. L. Chase, and D. Rytz, Phys. Rev. B 38, 597 (1988).

[29]M. D. Fontana, A. Ridah, G. E. Kugel, and C. Carabatos-Nedelec, J. Phys. C 21, 5853 (1988).

[30]M. D. Fontana, G. E. Kugel, and C. Carabatos-Nedelec, Phys. Rev. B 40, 786 (1989).

[31]J. P. Sokoloff, L. L. Chase, and D. Rytz, Phys. Rev. B 40, 788 (1989).

[32]L. L. Chase (private communication).

[33]W. Kleemann, F. J. Schafer, and M. D. Fontana, Phys. Rev. B 30, 1148 (1984).